SISSA
Scuola
Internazionale
Superiore di
Studi Avanzati

Physics Area – PhD course in
Statistical Physics

Slow dynamics and ergodicity breaking in many-body systems

Candidate:
Federico BALDUCCI

Advisor:
Prof. Antonello SCARDICCHIO

Academic Year 2021–2022

"...in questo seguitare una muraglia
che ha in cima cocci aguzzi di bottiglia."

Eugenio Montale

Acknowledgements

At last, this long journey has come to an end. Looking back on the last four years, I barely recognize the version of myself that arrived to Trieste, full of expectations and desire to learn. Strangely enough, I am going to leave the city with the same spirit: a lot of expectations, and the sensation of having still much more to learn. But, for all the rest that has changed, I have to thank profoundly the people that both have guided me, or just came along a parallel path.

Let me start with the most obvious credit: if it were not for my supervisor Antonello Scardicchio, I would not be here writing this Thesis. Antonello has been a mixture of a determined boss, a helpful collegue, and a paternal figure in these years of pandemic and difficult human contact. Being sometimes harsh and way too direct, and other times supportive and yielding, he taught me a most important piece of advice for physics and for life in general: to count on one own's resources, and work hard one own's way. A sincere thanks goes also to Giuseppe Mussardo: even if we did not work together after the master's, his experienced mentorship has helped me navigate through the idiosyncrasy of the academic world.

Let me acknowledge also all the collaborators of these years. First (in chronological order), Claudia Artiaco: it was her to lure me into the physics of glasses and disordered systems, and together we underwent all sorts of emotions, from despair to delight. Second (not for importance), Carlo Vanoni: besides being a relentless physicist, he has been also a great buddy in all adventures, that are too many to list. Then, a word of thanks goes also to the less-close collaborators: especially Markus Heyl, who helped me a great deal, but also Claudio Arezzo, Nicole Fabbri, Andrea Gambassi, Santiago Hernánded-Gómez, Alessio Lerose, Adam McRoberts, Roderich Moessner, Giorgio Parisi, Riccardo Piergallini and Angelo Russomanno.

Moving on to my colleagues and friends in Trieste, it is impossible to acknowledge them all: it was also thanks to them that life has been so enjoyable in these years. A special word, however, goes to the ones with whom we also discussed physics: Alessio Ansuini, Luca Capizzi, Giuliano Chiriacò, Giuseppe Del Vecchio Del Vecchio, Pierpaolo Fontana, Guido Giachetti, Sara Murciano, Rajat Kumar Panda, Silvia Pappalardi, Alessandro Santini, and Vittorio Vitale. Outside Trieste, yet another thanks goes to Federica Ferretti, for her stochastic help and active exchange of views.

Finally, I take the occasion to thank Claudio Castelnovo and Andrea De Luca, for having accepted to referee this Thesis, and Aurélia Chenu and Adolfo del Campo, for having offered me a postdoc position: I am really looking forward to work with you!

List of Publications

This thesis is based on the following publications (in chronological order):

[1] C. Artiaco, F. Balducci, G. Parisi, and A. Scardicchio, "Quantum jamming: Critical properties of a quantum mechanical perceptron", Phys. Rev. A **103**, L040203 (2021).

[2] C. Artiaco, F. Balducci, and A. Scardicchio, "Signatures of many-body localization in the dynamics of two-level systems in glasses", Phys. Rev. B **103**, 214205 (2021).

[3] C. Arezzo, F. Balducci, R. Piergallini, A. Scardicchio, and C. Vanoni, "Localization in the Discrete Non-linear Schrödinger Equation and Geometric Properties of the Microcanonical Surface", J. Stat. Phys. **186**, 24 (2022).

[4] C. Artiaco, F. Balducci, M. Heyl, A. Russomanno, and A. Scardicchio, "Spatiotemporal heterogeneity of entanglement in many-body localized systems", Phys. Rev. B **105**, 184202 (2022).

[5] S. Hernández-Gómez, F. Balducci, G. Fasiolo, P. Cappellaro, N. Fabbri, and A. Scardicchio, "Optimal control of a quantum sensor: A fast algorithm based on an analytic solution", arXiv:2112.14998 (2021).

[6] F. Balducci, A. Gambassi, A. Lerose, A. Scardicchio, and C. Vanoni, "Localization and melting of interfaces in the two-dimensional quantum ising model", Phys. Rev. Lett. **129**, 120601 (2022).

[7] S. Hernández-Gómez, F. Balducci, P. Cappellaro, A. Scardicchio, and N. Fabbri, "Optimal quantum control of a spin qubit in diamond for biosensing", in Proceedings of the 2022 IEEE International Workshop on Metrology for Industry 4.0 & IoT (2022), pp. 115–120.

[8] F. Balducci, A. Scardicchio, and C. Vanoni, "Slow melting of a disordered quantum crystal", arXiv:2207.11246 (2022).

The following forthcoming publications will treat subjects close to the ones presented in this thesis:

[9] C. Artiaco and F. Balducci, "Slow thermalization of strongly-coupled two-level systems in glasses", (to be published).

[10] F. Balducci, A. Gambassi, A. Lerose, A. Scardicchio, and C. Vanoni, "Interface dynamics in the two-dimensional quantum Ising model", (to be published).

Contents

Acknowledgements **v**

List of Publications **vii**

1 Introduction **1**

2 The quantum perceptron and its jamming transition **7**
2.1 The classical model . . . 8
2.2 The quantum partition function . . . 11
2.3 Extremization of the free energy . . . 13
2.4 Results from the path-integral Montecarlo . . . 14
2.5 Conclusions and outlook . . . 17

3 Weak ergodicity breaking in the DNLSE **21**
3.1 The model . . . 22
3.2 Presentation of the results . . . 24
3.3 Infinite temperature limit . . . 25
3.4 Large connectivity limit . . . 26
3.5 Solution of the fully-connected model . . . 28
3.6 Topological structure of the equipotential surface . . . 31
3.7 A Brownian exploration of the equipotential surface . . . 35
3.8 Conclusions and outlook . . . 38

4 Spatiotemporal heterogeneity of entanglement in MBL systems **41**
4.1 Description of the protocol . . . 43
4.2 Methods of analysis . . . 44
4.3 Distribution of the relaxation times . . . 47
4.4 Spatial correlations of the relaxation times . . . 48
4.5 Conclusions and outlook . . . 50

5 Signatures of MBL in the dynamics of TLS in glasses **53**
5.1 The TLS model . . . 55
5.2 Strong-coupling renormalization . . . 57
5.2.1 A polaron-like transformation . . . 57
5.2.2 Debye-Waller factor . . . 60
5.2.3 Normal ordering . . . 60
5.2.4 Relaxation of the TLS via Fermi's Golden Rule . . . 61
5.3 Dissipative dynamics at weak coupling . . . 64
5.3.1 GKSL master equation . . . 64
5.3.2 Free TLS evolution . . . 65
5.3.3 Coupling to phonons . . . 65
5.3.4 Dynamical phases from the GKSL equation . . . 67
5.4 Numerical simulations . . . 69

5.4.1 Disorder distributions of the parameters . . . 69
5.4.2 Initial state and dynamical observables . . . 70
5.4.3 Unitary evolution of the TLS . . . 71
5.4.4 Full evolution of the TLS . . . 73
5.5 Conclusions and outlook . . . 76

6 Interface dynamics in the 2d quantum Ising model 79
6.1 Model . . . 82
6.1.1 Constrained dynamics in the strong-coupling limit . . . 83
6.1.2 Hilbert space fragmentation . . . 85
6.2 Infinite coupling dynamics . . . 85
6.2.1 Strip-like configurations . . . 85
6.2.2 Smooth domain walls . . . 88
6.3 A particular initial condition: the infinite corner . . . 91
6.3.1 Average of the interface and its continuum limit . . . 92
6.3.2 Fluctuations of the interface . . . 93
6.3.3 Entanglement dynamics . . . 94
6.3.4 Connection with the asymptotics of the Plancherel measure . . . 96
6.4 Mechanisms of integrability breaking . . . 98
6.4.1 Finite bubbles . . . 98
6.4.2 Finite coupling . . . 100
6.4.3 Arguments in favour of Stark many-body localization . . . 101
6.5 Melting in presence of quenched disorder . . . 104
6.5.1 Modifications in the holographic mapping . . . 105
6.5.2 Perturbation theory estimates . . . 107
6.5.3 Spectral statistics via exact diagonalization . . . 110
6.5.4 Dynamics . . . 113
6.5.5 Comparison with classical corner growth models . . . 117
6.5.6 Limits of validity of the approximations . . . 118
6.6 Conclusions and outlook . . . 118

7 Optimal control of a spin qubit for quantum sensing 121
7.1 Optimized dynamical decoupling for sensing . . . 122
7.2 A variational approach . . . 124
7.2.1 Spherical approximation . . . 125
7.2.2 Time discretization and Simulated Annealing . . . 126
7.3 Comparison with experiments . . . 129
7.3.1 An application to magnetic field sensing . . . 129
7.3.2 An application to biological signals sensing . . . 132
7.4 Conclusions and outlook . . . 133

A Addendum to Chapter 2 135
A.1 Replicated and disorder-averaged free energy . . . 135
A.2 Replica-symmetry-breaking ansatz for the overlap matrix . . . 137
A.3 Replica-symmetric free energy . . . 137
A.4 Perturbation theory at zero temperature . . . 139
A.5 Quadratic approximation for the propagator . . . 140

B Addendum to Chapter 4 **143**
B.1 Energy of the initial states . . . 143
B.2 Finite-size and finite-sample effects . . . 143
B.2.1 Relaxation times within the XXZ model . . . 143
B.2.2 Relaxation times within the *l*-bit model . . . 144
B.3 Heterogeneity in the ergodic regime . . . 144
B.4 Analytical estimates of local timescales . . . 145
B.5 Self-averaging property of the correlation function . . . 148

C Addendum to Chapter 5 **151**
C.1 Estimate of the dipole tensor . . . 151
C.2 Computation of the interaction strength . . . 152
C.3 Computation of the Debye-Waller factor . . . 154
C.3.1 Considering sound polarization differences . . . 154
C.3.2 Disregarding sound polarization . . . 155
C.4 Fermi's Golden Rule . . . 156
C.5 Computations for the master equation . . . 158
C.6 Two-site observables within the diagonal unitary evolution . . . 159
C.7 Concurrence in a random state . . . 160
C.8 Integration of the GKSL master equation . . . 161

D Addendum to Chapter 6 **163**
D.1 Magnetization in the linear strip . . . 163
D.2 Two-point functions . . . 164
D.3 Continuum limit of the interface . . . 165
D.4 Second order Schrieffer-Wolff and integrability breaking . . . 167
D.4.1 First order corrections: PXP Hamiltonian . . . 168
D.4.2 First order corrections: corner Hamiltonian . . . 169
D.5 Participation ratio and localization length . . . 170
D.6 Useful properties of the Bessel functions . . . 172

E Addendum to Chapter 7 **175**
E.1 Definition of the sensitivity . . . 175
E.2 Details on the experimental platform . . . 176
E.2.1 Characterization of the amplitude of the target signal . . . 177
E.3 Additional test cases . . . 177
E.3.1 Monochromatic target signal . . . 177
E.3.2 7-chromatic target signal . . . 179

Bibliography **181**

Ai miei genitori Lucia e Roberto

1 Introduction

In this Chapter, I briefly introduce the research themes that will be explored in this Thesis. First, I digress on the ergodic hypothesis, and its reconsideration in the current trends of statistical mechanics. Then, I move on to introduce the physics of glasses and of many-body localization, explaining how together they represent the leitmotif of the Thesis. Finally, I present the scheme that tries to lock in the different works I have been carrying out during the PhD.

The fathers of statistical mechanics, Ludwig Boltzmann above all, understood too well that the equations of motion for a generic macroscopic system cannot be integrated explicitly. This factual impossibility led a certain disuse of the tools of dynamics at the microscopic level, in favor of the statistical description of ensembles in thermal equilibrium, which proved so fruitful in the years. The job of every physicist is, however, to come back and question every day the assumptions that have been made along the way—no surprise then of our perennial restlessness and sense of unease. Therefore, even after the (wrong) proof by Fermi [11], the (rather useless for physicists) one by Birkhoff [12], and the one by Von Neumann [13], the validity of the ergodic hypothesis continued to be disputed over time. This defiant attitude paid well—it always does—as came the surprise of the Fermi-Pasta-Ulam-Tsingou experiment [14], which was followed by the surge in the field of integrability [15–17]; not to forget all the developments from the Kolmogorov-Arnol'd-Moser theorem [18–20] to classical [21, 22] and quantum [23–26] chaos theory.

Of course, it is not my intent to review here all the history of statistical mechanics: I wanted just to highlight how, in the field, a great deal of effort has been devoted to the continuous questioning of the very founding hypotheses. Most importantly, this research trend is becoming more and more significant in the last years. One could wonder whether we have all forgotten the wisdom of the giants on whose shoulders we stand, but clearly this is not the case. Rather, now it is really the time to resume again the tools of dynamics, especially in the context of quantum mechanics, to investigate the multitude of physical systems that may or may not thermalize.

I say it is the time to study the dynamics of complex systems for at least three reasons. First, in the laboratories it is becoming possible to manipulate individually the components of many-body systems, attaining a degree of control that was unimaginable from the perspective of the founders of both statistical and quantum mechanics [27–33]. Such a control is disclosing an incredibly vast panorama of possibilities for investigations, both at the practical and at the fundamental level [34, 35]. Second, for the purpose of building a universal quantum computer in some future time [36–39], the need for a system to *avoid* going to equilibrium is of central importance. So, the ergodic hypothesis is seen as detrimental, and systems that defy it are eagerly looked for. Notice that this happens also in basically any instance of quantum technology application, from quantum sensing [40] to quantum simulators [41–44]. Third—which in part is a consequence of the two before—in the last 20 years

or so, several theoretical models have been devised, that do not go to thermal equilibrium on any reasonable timescale, or even at infinite time [45–51]. These models, together with the classical- and quantum-integrable models already known before [17, 26], are beginning to constitute a sort of "zoo", and people are looking both for a classifying principle, and for new exotic "beasts" to be included in the collection.

In the light of what I have been saying, it is becoming clear that quantum, out-of-equilibrium systems play an important role both at the fundamental level of investigations, and in fruitful applications to futuristic devices. It is in this context that, in the years of my PhD, I have tried to deliver some infinitesimal, yet non-zero contribution. In order to give a self-consistent presentation of such results, let me start by identifying the two bearing pillars that underpin all of them: the theory of classical glasses, and of quantum many-body localization (MBL). Even if these two phenomena arise in rather different situations, they both revolve around the breaking of ergodicity: therefore, it is natural to expect that they may also share some trait. I will now broadly introduce each of the two separately, while leaving to the main body of the Thesis some considerations on their common features. Also, I will not provide a pedagogical introduction to any of the two, leaving it to the excellent reviews that I will mention.

Glasses, and more in general amorphous solids, are a state of matter that is known to basically everybody, for their versatile applications and common uses. Nonetheless, a deep theoretical understanding—say, to the level we understand gases or crystals—is still lacking, as it is missing a widely accepted description of their transition from the liquid phase [52–55]. This is true to the point that the very existence of a standard thermodynamic transition is still debated, see for instance Refs. [56, 57]. What is known from experiment is that, for a huge class of a materials, a cooling rapid enough to avoid the first-order crystallization transition drives the system to a non-crystal, yet solid phase. This phase is characterized by the absence of definite Bragg peaks (the structure factor is substantially identical to that of the corresponding liquid), but also by a rigidity typical of crystals. Moreover, sound waves are present, and they behave in many respects similarly to those of crystals, even in the absence of long-range order [58]. I will treat more in depth the physics of amorphous solids in Chaps. 2 and 5, where I will specialize the discussion to their ultra-low temperature properties. Indeed, not only the alleged glass transition is poorly understood, but also the nature of the effective quantum excitations above the ground state is.

All the above features can be traced back to the fact that the phenomenon of glassiness is *dynamical in nature*, so that the use of statistical ensembles should be taken with care from the beginning. It is therefore natural that many of the tools to tackle many-particle, out-of-equilibrium systems were developed exactly in this field. Among all of those tools and ideas, some abstract theoretical models stand out distinctly: for instance, the introduction by Edwards and Anderson of the eponimous spin-glass model [59] brought a whole new energy to the field. The celebrated solution by Parisi [60–63] of its mean-field version, the Sherrington-Kirkpatrick model [64], did not close all the relevant questions: instead, it spurred an even stronger interest in the physics of disordered systems. The introduction of the simulated annealing algorithm [65, 66], the theoretical framework of rugged energy landscapes [67] and ultrametricity [68], and the formulation of the random first-order transition [69–73], are just examples of the pay-off that came from such investigations. Both analytical results and convinicing evidence from numerical simulations continue to point at new connections and unexpected phenomena even in these last years: I am

referring, for example, to the surprising super-universality of the jamming transition in dimensions $d \geq 2$ [74, 75], and to the exact solution of the thermodynamics of infinite-dimensional hard-sphere systems [76–79].

In this Thesis, some of the tools developed for classical glasses will be used to inspect various out-of-equilibrium systems. Without going into much detail, I anticipate that the use of a spherical model [80, 81] and of simulated annealing [65, 66] will be crucial to the solution of the control problem of a spin qubit sensor in Chap. 7. Then, the concept of entropic barriers will play a central role in understanding the slow dynamics of the discrete non-linear Schrödinger equation [82] in Chap. 3. Finally, the framework of dynamical heterogeneity [53, 83, 84] will be used to inspect entanglement spreading in the MBL phase in Chap. 4. At the same time, insight developed on the quantum side—especially in the theory of MBL—will be applied to problems that are investigated typically in the glass community. For instance, the issue of low-temperature anomalies of thermodynamic observables in structural glasses [85] will be dealt with in Chap. 2 using a quantum, mean-field model, and mathematical tools inspired by the physics of *spin* glasses. Then, the two-level system (TLS) model [86–91] for the low-temperature excitations in amorphous solids will be inspected from the viewpoint of quantum localized dynamics in Chap. 5.

Moving on to the second pillar, the name of Phil W. Anderson appears again in a milestone work about non-ergodic behaviour [92], in which he argued that quenched disorder, combined with quantum interference, can lead to suppression of transport and, ultimately, to the absence of thermalization. Such phenomenon was first thorougly investigated for non-interacting quantum matter [93–97], and also observed experimentally using various platforms [98–101]. Then, the investigation moved on to genuinely many-body systems [45, 46, 102, 103]: it was in particular the work of Basko, Aleiner and Altshuler on weakly interacting metals [46], followed by the intuition of Oganesyan and Huse to look at the same physics in spin chains [47], that really spurred a huge interest in this *many-body localization* (MBL). Such interest came from different sides: from the practical one, it was thought that MBL could help the creation of quantum hardware resilient to noise—but later this idea fell in disuse, because of residual interactions leading to dephasing. From the theoretical side, instead, MBL represented a novel, purely quantum, non-ergodic phase, with no classical counterpart, and characterized by an emergent integrability. Such integrability was found to be utterly different from the well-known Bethe ansatz [16, 17, 104], and instead to be characterized by *local integrals of motion* (LIOM), interacting via a particular effective Hamiltonian, called the *l-bit model* [105–109].

Even if the introduction of the l-bit model solved the problem of describing the localized phase [110, 111], the problem of the transition to MBL was left open. Indeed, the very existence of MBL represented a challenge to the celebrated eigenstate thermalization hypothesis (ETH) [24–26], i.e. a predictive form of the ergodic hypothesis, specified to many-body quantum systems. On the basis of quantum chaos and ETH, indeed, several authors repeatedly argued that MBL cannot be a stable phase of matter [112–119]. Others [120] tried to reconcile the analytical results on the transition [107–109, 114, 121–128] with the numerical results [48, 49, 129–135], the latter showing contrasting evidence, critical exponents that do not comply well-established bounds, and a substantial disagreement on the critical disorder strength. Experiments, unfortunately, do not meet the required level of precision to settle these questions [136–142], which therefore remain open to date.

In this Thesis, the issue of stability of MBL will not be tackled directly. The results that concern MBL will be either focused on the phase itself—about which there is

solid analytical evidence—and not on the transition (Chap. 4), or investigate models in which localization lasts for some finite time only (Chap. 5). The point of view adopted here will be thus rather pragmatic: like there is no definitive proof of the classical glass transition, but everybody agrees on the phenomenology, the same can be said for MBL, as long as one does not care about the thermodynamic and infinite-time limits. Moreover, the validity and interest of the results presented will be motivated regardless of the existence of a true, stable MBL phase.

To elaborate further, it is interesting to notice that, despite all the controversy, the physics of localization in many-body interacting systems has been developed well beyond the original scope. In the last years, numerous quantum many-body models have been proposed, that avoid going to equilibrium for extremely long timescales: the role of quenched disorder, indeed, can be played by configurational disorder [143–151], kinetic constraints [152–158], long-range interactions [159–163], or confinement of elementary excitations [164–174]. As a consequence of the above features, or because of similar mechanisms, some models also display Hilbert-space fragmentation [175, 176], or quantum many-body scars (i.e. non-thermal eigenstates at the center of the spectrum) [177, 178]. While in all of the previous examples the systems are believed to thermalize in the long run, the timescale after this takes place may become incredibly long, thus being irrelevant in any practical situation.

It is also necessary to mention that there are systems for which MBL is instead firmly believed to hold in the original form. It is the case of Floquet systems [179–183], for which in particular a recent numerical study [184] has shown the consistency of the MBL transition at moderate values of disorder, or of quasi-periodic systems [185–189], for which the presence of locally ergodic regions (that are thought to cause an avalanche instability, leading to ETH) are suppressed. The stability of the MBL phase of quasi-periodic systems is thought to be so strong, that it may be possible also to find a localized phase in two dimensions, as some recent studies argue [190–192].

On the other hand, systems have been found that escape the localization mechanism even in $1d$. For instance, the presence of a continuous symmetry is thought to be incompatible with MBL, because of the presence of resonances among states forced by the symmetry to be degenerate in energy [193–195]. Also, kinetically constrained "PXP" models [196–198], while displaying a slow dynamics *per se*, become thermal in the presence of a generic disorder, because the constraints make the disordered potential effectively non-local [199].

I am describing all of these possibilities, because in Chap. 6 I will present a work that shares common traits with many of them: a two-dimensional model with emerging dynamical constraints that both hosts MBL, starting from certain initial conditions, and that delocalizes upon the introduction of disorder. The interest in the problem, in view also of the discussion above, stems from the fact that much insight on non-ergodic behavior is usually gained from one-dimensional systems, for which advanced analytical [16, 200] and numerical [201] techniques are available. On the other hand, the non-equilibrium (and possibly non-ergodic) evolution of higher-dimensional quantum systems is a largely uncharted territory: therefore, I believe that the results presented will really be of interest.

Since it would be difficult, if not impossible, to organize the different works that I have carried out during my PhD in well-defined categories, I opted for a simple division in chapters, without a real developing thread. The scheme is the following.

- In Chap. 2 I describe the quantum jamming transition of the perceptron model, with implications for the low-temperature, thermodynamic anomalies of structural glasses.
- In Chap. 3 I show how a mean-field approximation, followed by a geometrical analysis, sheds light on the localization mechanism taking place in the discrete non-linear Schrödinger equation at high energies.
- In Chap. 4 I show how in many-body localized systems there is a complex entanglement spreading dynamics, that is reminiscent of the dynamical heterogeneity found in classical glasses.
- In Chap. 5 I consider the two-level system (TLS) model for the low-temperature properties of glasses, showing that a transient many-body localization takes place for the TLS. Such phenomenon is proposed as an explanation for the very slow thermalization found in experiments.
- In Chap. 6 I describe how the dynamics of the two-dimensional Ising model can in some cases be reduced to that of simple, one-dimensional effective models, under some assumptions. The consequences are multiple, and are discussed at the beginning of the Chapter.
- In Chap. 7 I show how tools coming from spin glass theory can be successfully applied to solve the optimal control problem of a simple quantum sensor of magnetic fields.

2 The quantum perceptron and its jamming transition

In this Chapter, I present some results on the quantum jamming transition of the perceptron model. After having introduced and motivated the problem, in Sec. 2.1 I show the known results for the corresponding classical system. Then, in Secs. 2.2 and 2.3 I show how to get to a set of equations, that fully capture the thermodynamics of the quantum problem, while in Sec. 2.4 I show what can be found from the numerical solution of those equations. Finally, in Sec. 2.5 I summarize the results and indicate some future directions. The Chapter is based on the publication [1].

In the Introduction it was hinted at why glasses constitute an interesting research area in physics. Systems that exhibit glassiness of some type range from amorphous solids, whose properties measured in the labs are not thoroughly understood yet, to abstract problems in computer science, that typically are hard to solve. In this Chapter, we will present a problem that sits in between those two extrema: the jamming transition of the perceptron model, when endowed with quantum dynamics.

Let us start from one side of the story: constraint satisfaction problems (CSP). By definition, a CSP consists, given a set of states and a set of constraints, in determining the subset of states compatible with all the constraints. In general CSP are hard problems; the Boolean satisfiability (SAT) CSP was indeed the first one to be proved NP-complete [202, 203]. In the years, it has become clear that tools from the statistical physics of disordered systems could be fruitfully applied to the field of CSP [204]. For instance, the origin of their computational difficulty was investigated within the framework of phase transitions [205–208], and efficient algorithms inspired by glass physics were devised [209–211].

While CSP defined in terms of discrete variables map naturally to spin glasses, CSP with *continuous* variables have shown a deep connection with *structural* glasses [74, 212–214]. A prominent example of CSP with continuous variables is the sphere packing problem [215, 216]. Sphere systems have gained plenty of attention among the glass physics community, and their jamming transition has been studied with the mathematical tools coming from structural glasses [217, 218], as well as from mean-field *spin* glasses [79, 212]. A result of the investigation was the quite surprising finding that the critical behaviour of hard-sphere jammed packings is independent of dimensionality for $2 \leq d \leq 10$ [74, 75], and presents features typical of the mean-field solution [219, 220]. This superuniversality led to the development of a simple toy model, presenting a jamming transition in the same universality class of infinite-dimensional hard-sphere systems, and that could be analytically solved: the perceptron [221–225]. The interest in the perceptron model comes also from the fact that it supports several applications in learning protocols [226–230], and it constitutes the building block of deep neural networks.

In this scenario of interplay between statistical mechanics and computer science, many authors have been also looking at ways to use quantum dynamics to speed up

the solution of classical problems, thus putting into play the issue of quantum computation as well [36]. In the specific case of discrete-variable CSP, a growing body of literature has investigated the impact of quantum dynamics on the spin-glass transition [231–237]. It is worth to stress that the effect of quantum fluctuations may be also detrimental in a quantum computing or annealing context, since phenomena as many-body localization could take place [238–242]. The study of CSP with continuous variables and a quantum dynamics, surprisingly, has not received the same kind of attention so far, but it promises to be equally far-reaching. In this Chapter, we are exactly going to take a step in this direction, building on the few known results in the field [243, 244].

Finally, in view of the connection with structural glasses, the study of quantum continuous CSP might as well provide clues for the anomalous (i.e. non-Debye) behavior of thermodynamic quantities in glasses at ultra-low temperatures. As said in the Introduction, this is currently an open problem in the glass physics community, and is eagerly looked at. Such anomalies, as $C_V \sim T$ at $T \sim 0$ [85], have received a phenomenological explanation in terms of quantum mechanics [86–88] (see also Chap. 5), but no firm result exist.

The purpose of this Chapter is to address the jamming transition deep in the quantum regime through the perceptron model. We show that quantum mechanical effects change the nature of the critical phase radically. We find that, for any $\hbar \neq 0$, the critical exponents are different from the classical ones and independent of the temperature. We also find that $C_V(T \sim 0) \sim e^{-\Delta/T}$ at small T, while at higher temperatures the specific heat has a power-law behavior. Remarkably, the latter result, valid in the deep quantum regime, resembles the semiclassical results of Ref. [244], connecting the physics on the two sides of the jamming transition.

2.1 The classical model

The perceptron model can be formulated as a particle living on a N-dimensional sphere, subjected to $M = \alpha N$ randomly placed obstacles. The parameter α represents the density of contraints, and it will be central in understanding the phase diagram of the model.

The vector $\vec{X}$ represents the position of the particle on the sphere $\vec{X}^2 = N$, and the obstacles are represented by the N-dimensional vectors $\vec{\xi}^\mu = (\xi_1^\mu, \dots, \xi_N^\mu)$, where $\mu = 1, \dots, M$ and ξ_i^μ are i.i.d. Gaussian random variables with zero mean and unit variance[1]. For each obstacle, one defines the constraint

$$h^\mu(\vec{X}) = \frac{1}{\sqrt{N}} \vec{\xi}^\mu \cdot \vec{X} - \sigma > 0. \tag{2.1}$$

Geometrically, it corresponds to asking the particle to be localized on one spherical cap, since the constraint is cutting away a half N-dimensional space. The parameter σ controls the convexity of the problem, a quantity of great importance in CSP, as will become clear soon. One can easily check that if $\sigma > 0$ the spherical cap is smaller than half sphere, thus the intersection of all the constraints always leads to a convex shape (see also Fig. 2.1a). On the other hand, if $\sigma < 0$ then the *removed* spherical caps are smaller than half sphere, and the intersection of the constraints leads to a sphere with several holes punched in it: this is clearly a non-convex set

[1] One does not need to enforce the normalization of the vectors $\vec{\xi}^\mu$, since they lie on the N-sphere of radius $N^{1/2}$ by the central limit theorem. Also in the following, all the statements concerning the geometry of the problem will refer to the limit $N \to \infty$, where fluctuations are suppressed.

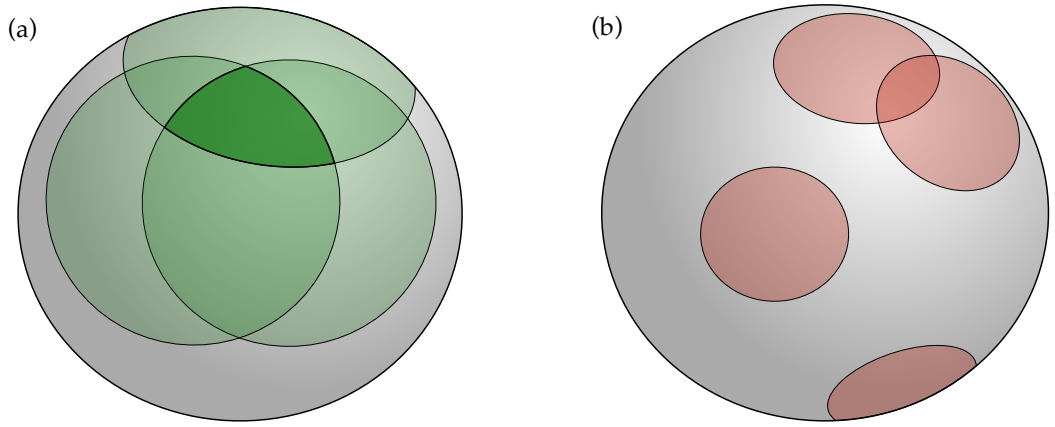

FIGURE 2.1: Sketch of the perceptron configuration space. (a) Case $\sigma > 0$: the green area is the allowed region, and it is convex since it comes from the intersection of spherical caps smaller than half sphere. (b) Case $\sigma < 0$: now spherical caps smaller than half sphere define instead the *excluded* region (red shaded areas). Thus, the allowed region (i.e. the complementary) is a non-convex set.

(see Fig. 2.1b). The connection with hard spheres in very high dimensionality is now quite easy to grasp, at least pictorially: the particle in the perceptron model moves in a space that has spherical holes carved out, as if it were a single sphere in $N-1$ dimensions, moving in a background constituted by other frozen spheres[2]. It is natural to expect that in high dimensions a mean-field picture should emerge for the many-body problem as well; that it is to say, the problem should reduce to a single-particle one, that moves in a self-consistently-induced background [79]. With all of this in mind, the connection of hard spheres with the perceptron does not come unexpected.

The constraints may be implemented through a cost function of the form

$$V = \sum_{\mu=1}^{M} v\left(h^{\mu}\left(\vec{X}\right)\right), \tag{2.2}$$

where the function v is such that $v(h) \equiv 0$ if $h \geq 0$, and $v(h) \neq 0$ if $h < 0$. The choice of v does not influence the jamming point, defined to be the highest density point (in configuration space) at which $V = 0$, but it does modify the behaviour in the jammed phase at higher densities. For instance, a hard-wall potential

$$v(h) = \begin{cases} +\infty & h < 0 \\ 0 & h \geq 0 \end{cases} \tag{2.3}$$

makes the jammed phase disappear altogether, while a soft-wall potential allows for non-zero energy configurations, weighted according to the form of v. Here, we will concentrate on the hard-wall case, leaving to the end a discussion of the implications for the soft case.

The perceptron model with classical, commuting variables was addressed and solved in Refs. [222–225]. The phase diagram relative to the hard-wall potential

[2]The point-like particle of the perceptron model can be interpreted as the center of the sphere under consideration, moving in a space where the other frozen spheres have been carved out with twice their radius.

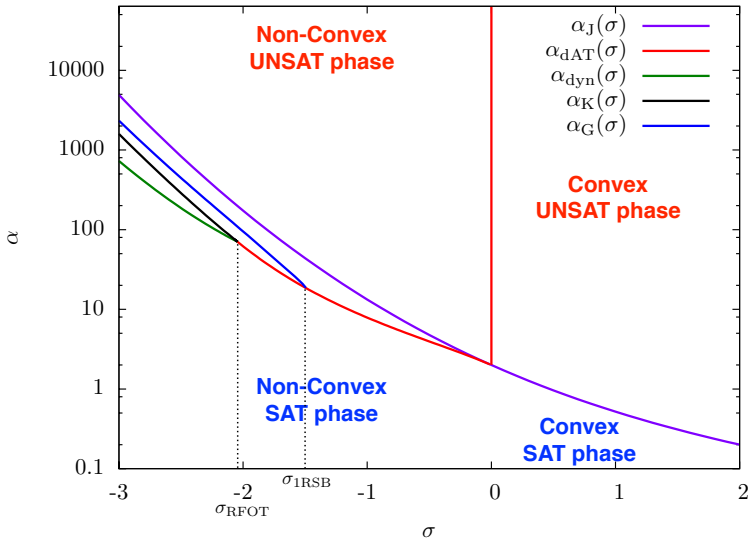

FIGURE 2.2: Phase diagram of the perceptron model, as derived in Ref. [224]. In the convex region $\sigma > 0$ there is only one phase transition, the jamming one (delimited by the curve α_J). When $\sigma \leq 0$, instead, the RS solution becomes unstable on the de Almeida-Thouless line α_{dAT}, and the correct solution presents either one-step RSB ($\sigma_{1RSB} < \sigma < 0$) or full RSB ($\sigma < \sigma_{1RSB}$). The line α_G represents the Gardner transition [214] from one-step RSB to full RSB. For $\sigma < \sigma_{RFOT}$ the phenomenology of the random first-order transition (RFOT) of glasses [55, 69–73] is present, and both a dynamical transition α_{dyn} and a Kauzmann transition α_K take place. This figure is taken from Ref. [224], where also more details can be found.

case is independent of the temperature (in fact there is no finite energy scale) and is shown in Fig. 2.2; see also the figure caption for a detailed description. The two main phases, i.e. constraints satisfied (SAT) or unsatisfied (UNSAT), are determined by whether there is or there is not any volume left by the intersection of the M constraints. More precisely, one has to consider the limit of the set

$$\mathcal{W}_{N,M} := \{\vec{X} \in \mathbb{R}^N,\ \vec{X}^2 = N \ \mid\ h_\mu(\vec{X}) > 0\ \ \forall\, \mu = 1, \dots, M\} \tag{2.4}$$

as $N, M \to \infty$, with $\alpha = M/N$ fixed. In the SAT phase, a position $\vec{X}$ for the particle satisfying all the constraints can be found with probability 1; in the UNSAT phase, instead, $\mathcal{W}_{N,M}$ becomes empty and the CSP problem has no solution. The sharp SAT-UNSAT transition is induced by increasing the constraint density α up to some $\alpha_c(\sigma)$. As anticipated, the convexity parameter σ determines the features of the SAT-UNSAT transition [222, 224]. For $\sigma > 0$, the constraints can be thought to force the particle $\vec{X}$ to be closer than some distance to each obstacle: this is the convex regime for the allowed region. It is found that the free energy has a single minimum and the replica-symmetric (RS) solution is everywhere stable. On the contrary, when $\sigma < 0$ the constraints are satisfied if the particle is away from each obstacle, thus the allowed region is non-convex and can be even composed of disconnected islands. The SAT-UNSAT transition falls within a phase where the landscape is rugged and marginally stable. In this Chapter, we will concentrate only on the value $\sigma = 0$, at the border of the RS stable region, for which the jamming point correponds to $\alpha_c(0) = 2$. In this way, the jamming point can be reached within the RS ansatz, but the physics of the glassy phase ($\sigma < 0$) is captured as well.

2.2 The quantum partition function

The perceptron model is quantized by imposing the canonical commutation relations $[X_i, P_j] = i\hbar\delta_{ij}$. The Hamiltonian reads[3]

$$H = \frac{\vec{P}^2}{2m} + \sum_{\mu=1}^{M} v\big(h^\mu(\vec{X})\big). \tag{2.5}$$

To inspect the phase diagram of the quantum model, it is necessary to compute the quenched disorder average of the free energy:

$$F = -\frac{1}{\beta}\overline{\log Z}, \qquad Z = \operatorname{Tr} e^{-\beta H}. \tag{2.6}$$

The procedure is very similar to the one employed in the context of quantum spin glasses [231, 232, 234, 237], and can be found in Refs. [244]. Since it is impossible to provide any simple sketch of the computation, because of the profusion of indices and rather long expressions, we will defer all the details to App. A.1. Here, we just summarize with words the meaning of the computation.

The first thing to do is to represent the partition function as a path integral in imaginary time (Eq. (A.1)), and use a Lagrange multiplier $\lambda(t)$ to enforce the spherical constraint. To compute the average of the logarithm, the replica trick should be used:

$$\log Z = \lim_{n\to 0} \frac{Z^n - 1}{n} = \lim_{n\to 0} \frac{\partial}{\partial n} Z^n, \tag{2.7}$$

where Z^n is computed for integer n and then analytically continued to real values. Therefore, after having introduced replicas $X_a(t)$, $a = 1, 2, \ldots, n$, the average over disorder should be performed. Such average is carried out more easily if one introduces the auxiliary process

$$r_a^\mu(t) := \frac{\vec{X}_a(t)\cdot\vec{\xi}^\mu}{\sqrt{N}}. \tag{2.8}$$

At this point, the expressions depend on $X_a(t)$ only through the *overlap*

$$Q_{ab}(t,s) := \frac{\vec{X}_a(t)\cdot\vec{X}_b(s)}{N}, \tag{2.9}$$

which physically measures the similarity between two replicas. Performing the change of variables from $\vec{X}_a(t)$ to $Q_{ab}(t,s)$ (and taking care of the Jacobian of the transformation), leads finally to the expression (cf. Eqs. (A.15)–(A.16))

$$\overline{Z^n} = \oint \left[\prod_{a=1}^{n} D\lambda_a \prod_{b\geq a} DQ_{ab}\right] \exp\left\{N\mathcal{A}(Q_{ab}, \lambda_a)\right\}, \tag{2.10}$$

[3] The choice of the kinetic term $P^2/2m$, typical of flat space, gives no significant difference from the correct one the sphere, that should be expressed in terms of the angular momentum (see for instance the appendices of Ref. [244]).

where the symbol $\oint$ indicates that $\vec{X}(0) = \vec{X}(\beta\hbar)$, and the effective action is

$$\mathcal{A} = \frac{1}{2}\log\det Q(t,s) + \frac{\beta m}{2}\sum_a \int_0^{\beta\hbar}\frac{dt}{\beta\hbar}\,\partial_s^2 Q_{aa}(t,s)\Big|_{s=t} - \frac{\beta m}{2}\sum_a\int_0^{\beta\hbar}\frac{dt}{\beta\hbar}\,\lambda_a(t)[Q_{aa}(t,t)-1] + \alpha\log\left\langle e^{-\beta\sum_a\int_0^{\beta\hbar}\frac{dt}{\beta\hbar}\,v(r_a-\sigma)}\right\rangle_Q . \quad (2.11)$$

Above, we have also introduced the (normalized) averages over the effective degree of freedom $r_a(t)$:

$$\langle F\rangle_Q := \frac{1}{\sqrt{\det Q}}\oint\left[\prod_{a=1}^n Dr_a\right] e^{-\frac{1}{2}\sum_{a,b}\int\int_0^{\beta\hbar}\frac{dt}{\beta\hbar}\frac{ds}{\beta\hbar}r_a(t)Q_{ab}^{-1}(t,s)r_b(s)}F[r]. \quad (2.12)$$

The functional integrals over $Q_{ab}(t,s)$ and $\lambda_a(t)$ can now be evaluated via the saddle point method in the limit $N\to\infty$. However, solving the equation $\delta\mathcal{A}/\delta Q = 0$, which yields the matrix $Q^{\rm sp}$, is not possible in full generality, and an ansatz is needed. Following Refs. [234, 244], it makes sense to assume (see also App. A.2)

$$Q_{ab}^{\rm sp}(t,s) = q_d(t-s)\delta_{ab} + Q_{ab}^* \quad (2.13)$$

where q_d is some function, and Q_{ab}^* is a hierarchical matrix. Thus, the time dependence is kept only in the diagonal term, while the permutational symmetry of the replicas manifests only in a time-independent term.

At this point, let us specify the computation to the replica-symmetric (RS) phase. Assuming replica symmetry, the overlap becomes

$$Q_{ab}^{\rm RS}(t,s) = q_d(t-s)\delta_{ab} + q(1-\delta_{ab}), \quad (2.14)$$

so that it is q_d for the same replica, and q for any two different replicas. Substituting $Q^{\rm RS}$ is Eqs. (2.10)–(2.11), the expressions simplify significantly, as shown in App. A.3. The first main point is the introduction of the autocorrelation function

$$G(t) := q_d(t) - q, \quad (2.15)$$

whose Fourier components are denoted as

$$G_n := \tilde{G}(\omega_n) := \int_0^{\beta\hbar}\frac{dt}{\beta\hbar}\,G(t)e^{-i\omega_n t}, \qquad G(t) = \sum_{n\in\mathbb{Z}}\tilde{G}(\omega_n)e^{i\omega_n t}, \quad (2.16)$$

with the Matsubara frequencies

$$\omega_n = \frac{2\pi n}{\beta\hbar}, \qquad n\in\mathbb{Z}. \quad (2.17)$$

Then, on the same line of Eq. (2.12) we introduce the averages

$$\langle F\rangle_G := \frac{1}{\sqrt{\det G}}\oint Dr\, e^{-\frac{1}{2}\int\int_0^{\beta\hbar}\frac{dt}{\beta\hbar}\frac{ds}{\beta\hbar}r(t)G^{-1}(t-s)r(s)}F[r], \quad (2.18)$$

and define also the Gaussian kernel

$$\gamma_q(h) := \frac{e^{-\frac{h^2}{2q}}}{\sqrt{2\pi q}}. \quad (2.19)$$

With these ingredients, the free energy (per dimension and per replica) can be expressed as

$$-\beta f \overset{\text{RS}}{=} \frac{1}{2}\sum_{n\in\mathbb{Z}} \log G_n + \frac{q}{2G_0} - \frac{\beta m}{2}\sum_{n\in\mathbb{Z}} \omega_n^2 G_n - \frac{\beta\mu}{2}\left[\sum_{n\in\mathbb{Z}} G_n - (1-q)\right] + \alpha\gamma_q \star \log\left\langle e^{-\beta\int_0^{\beta\hbar}\frac{dt}{\beta\hbar}\, v(r(t)+h)}\right\rangle_G (-\sigma). \quad (2.20)$$

Above, we have absorbed the mass m in the Lagrange multiplier λ, thus defining

$$\mu := m\lambda, \quad (2.21)$$

and we have denoted the convolution over h by $\star$. Unfortunately, the notation is quite heavy; however, we think that bearing in mind that the convolutions are always computed over the dummy variable h, and finally evaluated at $-\sigma$, everything should be clear.

2.3 Extremization of the free energy

The free energy Eq. (2.20) needs to be extremized wrt. G_n, q and μ. The resulting saddle-point equations are very easy to obtain, so we skip the derivation altogether and give the result:

$$G_n^{-1} = \beta m\omega_n^2 + \beta\mu + \beta\Sigma_n \quad (2.22)$$

$$\sum_{n\in\mathbb{Z}} G_n = 1 - q \quad (2.23)$$

$$q = \alpha\gamma_q \star \langle r_0\rangle_v^2\,(-\sigma) \quad (2.24)$$

with the self-energy

$$\Sigma_n := \frac{\alpha}{\beta}\left\{G_n^{-1} - G_n^{-2}\gamma_q \star \left[\langle r_n^* r_n\rangle_v - \delta_{n0}\langle r_0\rangle_v^2\right](-\sigma)\right\} \quad (2.25)$$

and the averages

$$\langle F\rangle_v := \frac{\left\langle e^{-\beta\int_0^{\beta\hbar}\frac{dt}{\beta\hbar}\, v(r(t)+h)} F[r]\right\rangle_G}{\left\langle e^{-\beta\int_0^{\beta\hbar}\frac{dt}{\beta\hbar}\, v(r(t)+h)}\right\rangle_G}. \quad (2.26)$$

Notice that the averages $\langle\cdots\rangle_v$ are a function of h (over which then the convolution acts), and that $r_n = \tilde{r}(\omega_n)$ according to Eq. (2.16).

The equations above are quite complicated, and have evaded our attempts of solving them analytically so far. The main difficulty is the presence of the quantum averages $\langle\cdots\rangle_v$, which involve both a non-local (in time) kernel $G^{-1}(t-s)$, and a hard-wall potential at position h. On the contrary, for the Sherrington-Kirkpatrick model the corresponding equations could be solved at $T = 0$ using a sensible ansatz for the self-energy [237], since the effective degree of freedom in that case is a two-level system. Here, even using a similar ansatz we were not able to close the equations (2.22)–(2.24) self-consistently; nevertheless we hope to address this issue in some future work.

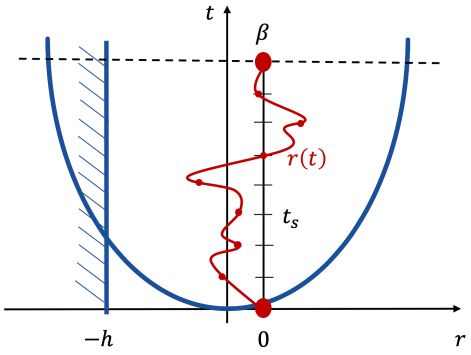

FIGURE 2.3: Sketch of the Path Integral Montecarlo (PIMC) used to simulate the dynamics of the $\beta\hbar$-periodic process $r(t)$ in the potential generated by $G^{-1}(t-s)$ and $v(r(t)+h)$. The first step consists in discretizing time in S slices; then, the PIMC algorithm proposes a move $r(t_s) \to r(t_s) + \delta(t_s)$ for every time step t_s, which is accepted or rejected according to the Metropolis algorithm. The presence of the hard-wall potential makes the convergence of the Montecarlo very demanding, and it is not sufficient to reject the attempted moves with $r < -h$ to have a good numerical protocol. Thus, we implemented an improved Montecarlo sampling which exploits the method of images. We modified the free particle kinetic term of the Hamiltonian and, instead of sampling the probability $P(r_0, 0 \mid r_0, \beta)$ of the free particle, we used $P(r_0, 0 \mid r_0, \beta) - P(\mathrm{Im}(r_0), 0 \mid r_0, \beta)$ where $\mathrm{Im}(r_0) = -r_0 - 2h$ is the image of r_0 when the wall is in $-h$. Another expedient is to add a move which translates rigidly the time chain $r(t_s)$, i.e. $r(t_s) \to r(t_s) + \delta$ with δ independent of t_s. The presence of the convolution implies the evaluation of the averages $\langle \cdots \rangle_v$ for many positions $-h$ of the wall. We approximate this Gaussian integral with the Gauss-Hermite quadrature, with always at least 10 sample points. This first step of the iterative method stops when G_n has converged for every n within a fixed tolerance (we fixed the relative difference between G_n^{old} and G_n^{new} to be $< 0.1\%$). The second step is to check if the converged G_n verifies the identity in Eq. (2.23). If it does so, one can move on to the third step; otherwise, μ is changed via the bisection method and the first step is performed again. The third step consists in computing the r.h.s. of Eq. (2.24) with the converged G_n and μ, and check if the identity in Eq. (2.24) is verified. If it is so, one has found the parameters which solve the self-consistency equations; if not, q is changed and one has to repeat all the procedure from the first step. This figure is taken from Ref. [1].

2.4 Results from the path-integral Montecarlo

The only analytical progress made from Eqs. (2.22)–(2.24) was in the semiclassical regime $\beta\hbar \to 0$ (explored in great detail in Ref. [244]), and a variational computation that we will present soon. For the rest, Eqs. (2.22)–(2.24) must be solved self-consistently via some numerical procedure. Since they have the form of typical dynamical mean-field theory (DMFT) equations [245], it is reasonable that an iterative procedure, accompanied by a path-integral Montecarlo (PIMC) for the evaluation of the averages $\langle \cdots \rangle_v$, would suffice. In Fig. 2.3 it is shown a sketch of how the PIMC was implemented for the effective degree of freedom r.

Now, we present some results that have been obtained via PIMC simulations. The investigation was performed on the line $\sigma = 0$ in the phase diagram, from $\alpha = 0$ to $\alpha_c(\sigma = 0) = 2$, because we wanted to retain the simplicity of the RS equations, without going in the RSB regime, but still accessing the physics of the non-convex phase, which is confined to $\sigma \leq 0$.

As a first thing, the value of the order parameter q as a function of α and β was found; it is plotted in Fig. 2.4a against the classical counterpart $q_{\mathrm{cl}}(\alpha)$ (that was considered in Ref. [224]). Unlike the quantum case, $q_{\mathrm{cl}}(\alpha)$ is independent of the temperature—indeed, there is no finite energy scale in the classical problem, while

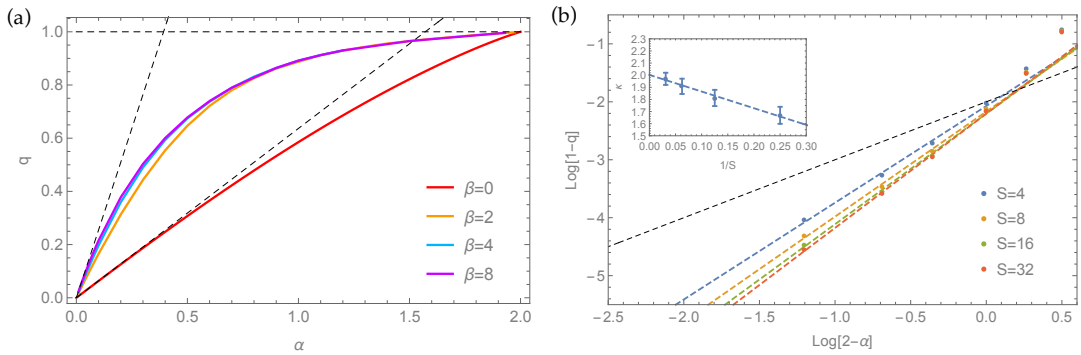

FIGURE 2.4: (a) Edwards-Anderson order parameter q as a function of the constraint density α for various temperatures. From bottom to top: infinite temperature classical dynamics (red line) to finite temperature quantum dynamics ($\beta = 2, 4, 8$). The $O(\alpha)$, $\beta = \infty$ results are shown as dashed black lines (while the horizontal black line is a reference for the value $q = 1$). Notice how, as soon as $\alpha \gtrsim 1$, the temperature dependence of q is effectively lost (it is $\sim e^{-c\beta/(2-\alpha)^2}$). (b) Edwards-Anderson order parameter close to the critical point $\alpha = 2$. From top to bottom, increasing the number of Trotter slices $S = 4, 8, 16, 32$ for sufficiently large β, the slope increases. For reference, the classical value of the slope (from $(1 - q) \sim (2 - \alpha)$) is shown as the diagonal dashed black line. In the inset are shown the values of the slope with their errors, and its extrapolation to $S \to \infty$ to the value $\kappa = 2.0 \pm 0.1$, quoted in the text. This figure is taken from Ref. [1].

$\hbar \neq 0$ introduces a new finite scale. Moreover, the critical behaviour around the jamming transition is, in the classical case,

$$1 - q_{\rm cl}(\alpha) \simeq \frac{2-\alpha}{4} + O\left((2-\alpha)^2\right) : \tag{2.27}$$

this defines a critical exponent $\kappa_{\rm cl} = 1$, that is valid in all the region $\sigma \geq 0$. We recall that, instead, $\kappa_{\rm cl} = 1.41574\cdots$ if $\sigma < 0$.

From Fig. 2.4a one can see that the quantum value of q is always larger than the classical one, and this can be easily understood. Recalling that q represents how much two different replicas are similar (cf. Eq. (2.9)), if the space at disposal of the particle is smaller, necessarily the overlap will be larger. But this is exactly the case, since the ground state of a quantum particle in a billiard is more concentrated than a flat distribution on the same billiard, because of Dirichlet boundary conditions at the walls. Moreover, the particle becomes more concentrated the larger the aspect ratio of the billiard, namely if one of the sides is larger than the others.

To be more quantitative, one finds $q > q_{\rm cl}$ already at the lowest order in α: from the self-consistency equation (2.24),

$$q = \alpha \langle r_0 \rangle^2_{v,h=0} + O(\alpha^2) \tag{2.28}$$

since γ_q concentrates to a delta function for small q. The average $\langle \cdots \rangle_{v,h=0}$, when $\beta \to \infty$, reduces to the expectation value over the ground state of a harmonic oscillator with a wall in the origin. The problem is easily solved in App. A.4, and the result is

$$q = \frac{8}{\pi m^2}\alpha + O(\alpha^2), \tag{2.29}$$

that has to be compared with $q_{\rm cl} = 2\alpha/\pi m^2 + O(\alpha^2)$.

Another interesting dependency of the quantum order parameter q is that on

the temperature $T = 1/\beta$: in particular, from Fig. 2.4a it is evident that q becomes independent of T through a crossover at $\alpha \lesssim 1$. From the classical calculation, it is expected that the typical linear size ℓ of the allowed region for the particle on the sphere vanishes as

$$\ell \sim \sqrt{1 - q_{\mathrm{cl}}} \sim \sqrt{2 - \alpha} \tag{2.30}$$

for $\alpha \to 2$. Thus, as soon as the energy gap to the first excited state becomes larger than the temperature, i.e. roughly when

$$\frac{\hbar^2}{m\ell^2} \sim \frac{\hbar^2}{m(2-\alpha)} \gtrsim T, \tag{2.31}$$

the quantum dynamics is *effectively at zero temperature* and the order parameter q becomes independent of T. This estimate should be corrected by the fact that the gap, deep in the quantum regime, grows even faster than $(2-\alpha)^{-1}$ when $\alpha \to 2$, as will become clear soon.

Since the quantum dynamics recovers the classical dynamics only when the de Broglie wavelength $\lambda_T \sim \hbar/\sqrt{mT} \ll \ell$, on approaching jamming it is quantum mechanics that dominates. Hence, for any $T, \hbar, m$, as $\alpha \to 2$ one eventually enters a quantum critical regime, where quantum mechanics controls the dynamics and defines, among other things, novel critical exponents. The classical result is recovered only by taking the limit $T \to \infty$ *before* $\alpha \to 2$.

The value of the critical exponent κ regulating the relation $(1-q) \sim (2-\alpha)^{\kappa}$ in the quantum regime can be extracted by looking at the low-temperature, large-α data from the PIMC. As usual, a sufficiently large number of Trotter slices S must be taken (see Fig. 2.3), and S should be increased even more when $\alpha \to 2$, making the numerical simulations rather demanding. However, fortunately, the asymptotic region is reached already at $\alpha \gtrsim 1$. The data in Fig. 2.4b clearly show that the critical exponent of the quantum theory is not the classical one, $\kappa_{\mathrm{cl}} = 1$, and it departs more and more from it as the number of Trotter slices is increased. Performing a log-log fit to extract such critical exponent, in a region $1 \leq \alpha \leq 1.7$, and extrapolating $S \to \infty$, it is found $\kappa = 2.0 \pm 0.1$.

That $\kappa > 1$ in the quantum case can be understood also from a simple variational calculation. Using in the scaling region $\alpha \to 2$ the (uncontrolled) approximation

$$G_n^{-1} = \frac{\beta m}{1-q}\left(\omega_n^2 + \frac{\hbar^2}{4m^2}\right), \tag{2.32}$$

the self-consistency equations can be solved explicitly for $\beta \to \infty$, as detailed in App. A.5, finding $\kappa = 3/2$. The value $\kappa \simeq 2$ from the Montecarlo simulations presumably comes once the true behavior of $\Sigma(\omega)$ is considered.

Another quantity of interest is the regularized internal energy per degree of freedom

$$u = \frac{1}{2\beta}\sum_{n\in\mathbb{Z}} \frac{\mu + \Sigma_n}{m\omega_n^2 + \mu + \Sigma_n}, \tag{2.33}$$

cf. Ref. [244] for the regularization procedure. Like q, it becomes independent of β already at $\alpha \gtrsim 1$. Extrapolating its behavior for an infinite number of Trotter slices, the internal energy diverges as (see also Fig. 2.5a)

$$u \sim \frac{\hbar^2}{m(2-\alpha)^2} \tag{2.34}$$

for $\alpha \to 2$. This can be again interpreted in terms of reduced volume and uncertainty principle, and confirms the previous result $\kappa \simeq 2$.

All the results presented above show that, at fixed temperature, in the quantum regime the critical properties of the system are essentially determined by the ground state, and the gap to the first excited state grows as

$$\Delta \sim \frac{\hbar^2}{m(1-q)} \qquad \text{for } \alpha \to 2. \tag{2.35}$$

This implies that, if one focuses on frequencies $\omega \ll \Delta/\hbar$, or times $t \gg \hbar/\Delta$, there is no dynamics. In order to see some dynamical behavior, one should consider instead $\omega \gtrsim \Delta/\hbar$. As shown in Fig. 2.5b, at these large frequencies the form of the self-energy $\Sigma(\omega)$ changes significantly. Indeed, at any $\alpha < 2$, the self-energy is an analytic function of ω^2 in a neighborhood of the origin $\omega = 0$ (see the inset of Fig. 2.5b). As $\alpha \to 2$, this behavior becomes extended to increasing values of ω. At larger frequencies, however, $\Sigma(\omega)$ develops a linear behavior. Moreover, for any $\alpha < 2$, it must hold $\lim_{\omega\to\infty} \Sigma(\omega) = 0$, as can be seen from the definition Eq. (2.25). Performing a log-log fit, it is found that the constant contribution to the autocorrelation function scales as $\beta\mu \sim (1-q)^\delta$ where $\delta \simeq -0.9$. From a quadratic fit of $\Sigma(\omega)$ at small ω, the coefficient of the quadratic term is found to be instead almost independent of $(1-q)$.

The behavior of $\Sigma(\omega)$ defines the effective dynamics of the theory, and its analytical properties around the origin determine the low-temperature behavior of thermodynamical observables. Both the analyticity of $\Sigma(\omega)$ around $\omega = 0$ and the independence from β of all the observables, including the internal energy u, show that the specific heat is non-analytic in T when $\alpha \to 2$. More precisely, our findings show that the specific heat

$$C_V(T) \sim e^{-\Delta/T}, \qquad \text{for } T \sim 0, \tag{2.36}$$

due to the presence of the gap, Eq. (2.35). However, since at not-so-small ω it holds $\Sigma(\omega) \sim |\omega|$, the specific heat presents a power-law behavior at high enough temperatures:

$$C_V(T) \sim T^\gamma, \qquad \text{for } T > T_{\text{cutoff}}. \tag{2.37}$$

Since $\Delta \to \infty$ as $\alpha \to 2$, $T_{\text{cutoff}} \to \infty$ too.

It is interesting to conclude noticing that the linear dispersion $\Sigma(\omega) \sim |\omega|$, observed in the critical regime, is similar to the results of Ref. [244], where the authors performed a semiclassical analysis to investigate the UNSAT phase with soft potentials. In particular, they sent $\hbar \to 0$ with $\beta\hbar$ kept fixed, while in this study it is $\hbar$ to be kept finite. They found the linear dispersion $\Sigma(\omega) \sim |\omega|$ in a neighborhood of the origin $\omega = 0$, implying a power-law behavior of the specific heat $C_V(T)$ at small T near the jamming point. The similarities between the two results are surprising, since the regimes considered are different, and suggest that the linear dispersion $\Sigma(\omega) \sim |\omega|$ might be a universal feature of quantum models near jamming.

2.5 Conclusions and outlook

In this Chapter we have shown how the perceptron with hard-wall potentials can be used as a model for reaching the quantum jamming transition with analytical control. Studying the replicated, quenched free energy in the RS approximation, a quantum critical point corresponding to the classical jamming point $\alpha_c = 2$ at $\sigma = 0$

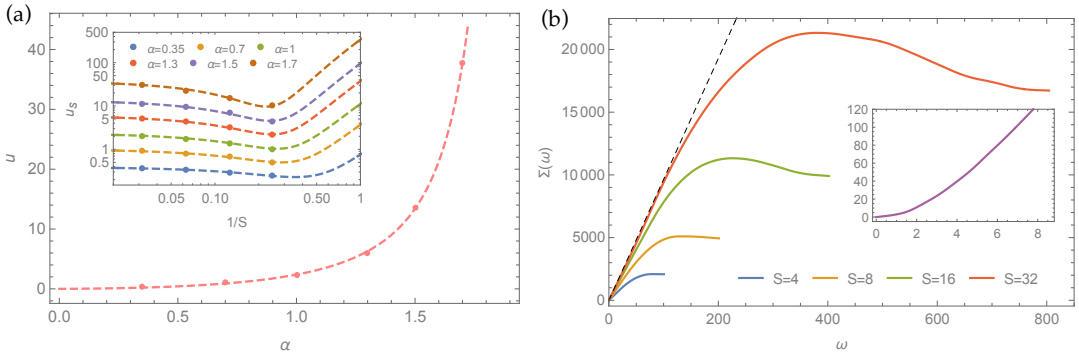

FIGURE 2.5: (a) Internal energy u as a function of the density of constraints α. The dashed line is a fit of the form $u = A(2-\alpha)^{-\kappa}(1 + B(2-\alpha) + C(2-\alpha)^2)$ with $\kappa = 2.0$ obtained from the behavior of order parameter q. This confirms $u \sim (1-q)^{-1} \sim (2-\alpha)^{-2}$ as discussed in the main text. In the inset one can see, from bottom to top for $\alpha = 0.35, 0.5, 0.7, 1, 1.3, 1.5, 1.7$, the extrapolation of the values of $u_S = u + a/S + b/S^2$ as a function of the number of Trotter slices S (in log-log scale). (b) Self-energy $\Sigma(\omega)$ at $\alpha = 1.7$, $\beta = 1/2^3$ as a function of the Matsubara frequency ω, for increasing number of Trotter slices (accessing higher and higher frequencies). We see that $\Sigma(\omega)$ develops a linear ω behavior (black, dotted line) for intermediate ω's, while retaining its analyticity in terms of ω^2 around the origin for any $q < 1$ (inset). In the inset, it is shown $\Sigma(\omega)$ at small ω's for $\alpha = 1.5$, $\beta = 8$. This figure is taken from Ref. [1].

is found. Usually, quantum critical points are confined and influence the physics around $T = 0$ [233]; here, instead, the quantum jamming critical point exists *for any temperature*, and the classical results are recovered only by taking $T \to \infty$ *before* $\alpha \to \alpha_c$. In other words, it is the classical critical point to be confined to $T = \infty$.

Using tools from RSB theory and DMFT, we were able to find quantum critical exponents different from the classical ones, and an exponentially small specific heat C_V at small T. For frequencies higher than the gap but not asymptotically large, there is instead a dispersion relation $G(\omega)^{-1} \sim |\omega|$, which implies a power-law specific heat for $T > T_{\text{cutoff}}$, where T_{cutoff} diverges at the critical point. This shows a connection with the semiclassical analysis of Ref. [244], where a different region of parameters was considered, and this surely deserves to be investigated further.

An appealing extension of this work would be to consider soft potentials, having a finite $v' \equiv \partial v/\partial r|_{r=0}$ [4], as in the case of typical models of structural glasses. Employing soft potentials, it is possible to access the UNSAT phase deep in the quantum regime. While it is reasonable to expect that the quantum jamming transition will turn into a crossover (like the classical one does), the same phenomenology outlined in this Chapter should be observed as far as the change in the potential on length scales $O((1-q)^{1/2})$ is large with respect to the gap $\Delta \sim (1-q)^{-1}$. This means that for $(1-q) \gtrsim (v')^{-2/3}$, or $\alpha \lesssim 2 - c(v')^{-1/3}$, the physics is dominated by the hard-wall quantum jamming critical point. The robustness with temperature of the quantum critical point, shown in the above results, implies that the quantum character of the system even with soft potentials cannot be neglected. Therefore, it suggests that standard approaches used to study glassy systems at ultra-low temperatures, which add quantum effects on top of the classical landscape [246–248], might be inadequate.

Another interesting extension of this study would be to move to the regions with $\sigma \neq 0$. For the case $\sigma > 0$, studied in learning protocols, the same methods adopted

[4] A similar reasoning applies for the case $v' = 0$ but $\partial^k v/\partial r^k|_{r=0} \neq 0$ with $k > 1$.

in our study can be implemented, and one can directly investigate the effects of the quantum dynamics. In the region $\sigma < 0$, instead, it is also necessary to solve the self-consistency equations in the RSB framework. As the allowed volume becomes clustered, quantum effects may play a double role: for low disorder, tunneling may help the particle to explore many disconnected flat regions, and speed up the search of solutions (as it happens in the quantum random energy model [241, 242]); for high disorder, quantum localization may take place, breaking ergodicity and changing significantly the classical phase diagram. The interplay of these behaviors, hard to be guessed, deserves a complete investigation, which we hope will be object of a future study.

3 Weak ergodicity breaking in the discrete non-linear Schrödinger equation

In this Chapter, the mechanism of localization in the discrete non-linear Schrödinger equation is inspected. In Sec. 3.1 I introduce the DNLS model, and then in Sec. 3.2 I put in perspective the results wrt. the known literature. In Secs. 3.3 –3.5 I show the solution of the mean-field version of the model, which motivates the independence on dimensionality at high energy densities. In Sec. 3.6 a rigorous geometrical analysis of the potential energy surface is performed, and in Sec. 3.7 I present the results of numerical simulations for the dynamics on such surface. Finally, in Sec. 3.8 I draw the conclusions and indicate future directions. The Chapter is based on the publication [3].

As mentioned in the Introduction, the seminal work of Fermi, Pasta, Ulam and Tsingou (FPUT) [14] spurred a renewed interest in the ergodic hypothesis, and in particular in the dynamics of thermalization for nonlinear systems. Since then, a huge amount of work has been accumulated, ranging from numerical studies of several microscopic models (see e.g. Refs. [249–252] and references therein), to beautiful analytical constructions for the hydrodynamic description in the continuum [15, 17, 253]. This fruitful field of nonlinear studies, however, has remained quite distinct from the one of structural and spin glasses, despite in both cases the object of study are systems that find some obstruction in their way to thermalization. This is perfectly understandable, since FPUT-like systems are mainly one-dimensional toy models used in fundamental investigations, while the physics of glasses has to deal with compelling experimental observations, and therefore to use realistic models amenable of little analytical control. Nevertheless, it is reasonable to expect that some tools and insights developed on one side may reveal very fruitful on the other side, as was put forward by a few studies [254–258]—even if the original hypothesis of metastability in FPUT systems was seriously challenged [252].

In this Chapter, we will describe a work that goes exactly in this direction. The starting point is the *discrete non-linear Schrödinger equation* (DNLSE) [82], one of the prominent models in the field of nonlinear oscillators. It is the lattice version of the eponymous nonlinear wave equation [17, 259]; however the lattice discretization in general breaks the symmetries leading to integrability [260], and the model is expected to be ergodic. The model was indeed observed to be ergodic, in numerical simulations, for moderate values of the energy density; however, erogidicity was found to break down for highly energetic initial conditions [261–264]. This feature was quite surprising, since the configurations that showed localization were as far as they could from the continuum (integrable) description: rather, they seemed to be constituted by few sites accumulating a finite fraction of the total charge. Because of this observation, numerous works have tried to ascribe the lack of ergodicity

at high energy density to the presence of very-long-lived, breather-like excitations [265–271], but the rigorous results are still few[1] [274]. On the other hand, some experiments have reported that Rubidium atoms on one-dimensional lattices—in the Bose-Einstein condensate phase well described by the DNLSE—survive very close to the initially prepared, localized configurations [29, 275], thus confirming the prediction of the numerical simulations.

Another reason for interest in the ergodicity breaking in the DNLSE are the similarities with the *quantum* MBL phenomenon. In particular, some works put forward the idea that MBL-like physics could be observed in Josephson junction chains [276, 277]—a model very similar to the DNLSE. The non-ergodicity in this case is due to an initial state with sufficiently large charge fluctuations, that play the role of quenched disorder in an otherwise clean system. A natural question that follows is then what would happen in a semiclassical setting for such models: of course MBL, like Anderson localization, cannot survive when $\hbar \to 0$. Therefore, the origin of the phenomena are definitely not the same, and it would be interesting to find out what is the crossover between the two, as $\hbar$ is tuned[2].

An explanation for the weak ergodicity breaking in the DNLSE, different from the presence of breathers, was recently proposed in Refs. [281–283]. The argument is based on the inequivalence of the microcanonical and canonical Gibbs ensembles at high energy density, and a point central to the computation is the complete disregard for the geometry of the lattice on which the problem is set. This feature is very interesting, as it suggests that a *mean-field* description could perfectly apply. In this Chapter it is shown that this is exactly the case: the problem is set on a graph with large connectivity, and it is proven how in the limit of infinite connectivity the construction of Refs. [282, 283] is perfectly justified. Since the mean-field limit is known to be a very good approximation in many statistical mechanics problems, and it is (in the description of phases and transition between them) *exact* above a certain critical dimension, we believe that our results are able to describe *qualitatively* also the experimentally relevant situation of 1, 2 or 3-dimensional lattices.

To introduce better the results obtained and the way the proof is reached, let us first introduce some notation in the next Section. We will then summarize the results in more detail in Sec. 3.2, and finally move on to the computation.

3.1 The model

As anticipated above, we want to propose a mean-field-like description to the mechanism of ergodicity breaking at high energy density in the DNLSE. For this reason, let us consider the DNLS model on an arbitrary, regular graph $\mathcal{G}$:

$$H = -\frac{g}{\kappa} \sum_{i,j=1}^{N} A_{ij} \left(\psi_i^* \psi_j + \psi_j^* \psi_i \right) + \frac{v}{2} \sum_{i=1}^{N} |\psi_i|^4. \tag{3.1}$$

Here, the ψ_i, ψ_i^* are complex fields that live on the vertices i of $\mathcal{G}$, and are canonically conjugated: their Poisson brackets read $\{\psi_i^*, \psi_j\} = i\delta_{ij}$. Then, g,v are non-negative

[1] Some rigorous, mathematical works deal instead with the quantum version of the problem [272, 273].

[2] Please pay attention to the fact that the interplay between disorder, quantum-mechanical localization and nonlinear effects in the DNLSE has been the subject of vast research (see e.g. Refs. [278–280] and references therein), but the physics behind it is appreciably different from the one discussed here.

parameters, which will be eventually set to $g = 1$ and $v = 2$; for the time being, however, it is convenient to leave them unspecified. Finally, κ is the connectivity of $\mathcal{G}$ and A its adjacency matrix, so each entry A_{ij} is either 0 (ij disconnected) or 1 (ij connected). Notice that, thanks to the $1/\kappa$ normalization of the kinetic term (known as *Kac rescaling*), $H = O(N)$ for any $\mathcal{G}$, even in the limit of fully connected graph $\kappa \sim N \to \infty$, without having to rescale g.

The Hamiltonian (3.1) can be rewritten in a more convenient form by means of the canonical transformation

$$\begin{cases} \psi_i = \sqrt{q_i}\, e^{i\phi_i} \\ \psi_i^* = \sqrt{q_i}\, e^{-i\phi_i} \end{cases} \tag{3.2}$$

with $q_i \geq 0$ and $\phi_i \in [0, 2\pi]$. Equation (3.1) becomes

$$H = -\frac{2g}{\kappa} \sum_{i,j=1}^{N} A_{ij} \sqrt{q_i q_j} \cos(\phi_i - \phi_j) + \frac{v}{2} \sum_{i=1}^{N} q_i^2. \tag{3.3}$$

Apart from the energy, there is another natural conservation law to take into account: defining the *charge*

$$Q := \sum_i |\psi_i|^2 = \sum_{i=1}^{N} q_i, \tag{3.4}$$

it holds $\{Q, H\} = 0$. Without loss of generality, we choose to work with fixed $Q \equiv N$ from now on (or, more generally, with the *average* charge fixed).

We take the chance to fix some conventions for the computation of the partition function: let us employ a dimensionless chemical potential μ, call the inverse temperature $\beta := 1/T$ (so that $k_B \equiv 1$), and

$$Z(N, \beta, \mu) = \int [d\psi\, d\psi^*] e^{-\beta H + \mu Q}, \tag{3.5}$$

with the measure chosen to be

$$[d\psi\, d\psi^*] := \prod_i \frac{1}{2\pi} d\psi_i\, d\psi_i^* = \prod_{i=1}^{N} \frac{1}{2\pi} dq_i\, d\phi_i =: [dq\, d\phi]. \tag{3.6}$$

The energy density is defined as $\varepsilon := H/N$. The previous works [261, 282, 283], from which this one takes inspiration, have shown that $\varepsilon = \varepsilon_c = v$ corresponds to the $T = \infty$ limit of the model on a $1d$ chain when coupled to a thermal reservoir at temperature T, and that at ε_c the Gibbs distribution ceases to be valid: the states with energy density $\varepsilon > \varepsilon_c$ remain well-defined only in the microcanonical ensemble. Moreover, other works have shown that the dynamics of a chain ceases to be ergodic in this non-Gibbs phase, with the charges localizing on isolated sites in solitons rather than moving around. This has been seen both by using a simplified stochastic evolution algorithm, for all $\varepsilon \geq \varepsilon_c$ [269, 270], and with Hamiltonian dynamics [262] (although in this latter work the threshold is put at $\varepsilon \simeq 1.25\, v$).

Now, we will present our results, putting them in perspective wrt. the previous literature, and then move on to the proof.

3.2 Presentation of the results

Now that we have introduced the model, we can present with more precision the results obtained. They can be summarized in the following points:

1. the equilibration time for the DNLSE at high energy density is exponentially long in N, where N is the number of sites composing the lattice;

2. this is not due to a breakdown of connectivity of the topology of the microcanonical surface (when only the potential energy is taken into account), i.e. there is no trace of *strong* ergodicity breaking;

3. the origin of the localization phenomenon at high energy density can be traced to the behaviour of the gap of the Laplace operator on the $(N-2)$-dimensional microcanonical energy manifold.

To prove these points, we proceed as follows.

The first issue is about the possibility of neglecting the term containing phase variables in the Hamiltonian, i.e. the first term on the r.h.s. of Eqs. (3.1) or (3.3). Such term allows the exchange of charges between different sites, and the analysis of Refs. [282, 283] started exactly with the assumption that it can be simply dropped off. This is a fundamental point, since the partition function does not factorize in a form $Z = Z_{\text{momentum}} Z_{\text{position}}$, as it happens for example when looking at gases or liquids, where typically the phase-space variables (p, x) appear each in its own term: $H(p, x) = K(p) + V(x)$. We therefore show that expansion around infinite temperature of the free energy (and, consequently, of all relevant observables) gets contributions from the kinetic term only at $O(1/\kappa)$, where κ is the connectivity of the graph on which the DNLSE is set. Therefore, if one considers a fully connected model, the assumption of neglecting the kinetic term is completely justified. As said before, this is a first approximation to the physics of finite-connectivity lattices.

We then solve the fully connected model finding that the "infinite temperature phase", in which the free energy becomes essentially given by the potential term alone, extends all the way down to a finite temperature $T_s = 2g$ (g is the strength of the kinetic term and v that of the potential). This is in stark contrast with the $1d$ model, where there is no mathematical proof showing that the kinetic term plays no role around infinite temperature. At temperatures lower than T_s, or equivalently energy densities $\varepsilon < \varepsilon_s = 1.481\ldots$ (with the parameters $g = 1$, $v = 2$ used throughout this Chapter), the fully-connected model enters a *synchronized phase* in which the phases ϕ_i stop rotating independently from each other and eventually move together at $T = 0$ (energy density $\varepsilon_{GS} = v/2 - 2g = -1$). Conversely, for temperatures higher than T_s the motion of the phases ϕ_i is incoherent and the charges move randomly on the microcanonical, potential energy surface. The phase diagram described so far is shown in Fig. 3.1.

Subsequently, after having highlighted the importance of the potential energy surface, we study the topology of such manifold. We prove, using tools from stratified Morse theory, that the manifold undergoes a series of critical points (critical in the language of Morse theory, not of statistical physics) but it remains connected until energy densities $\varepsilon = vN/4 = N/2$, which means *super-extensive* energy. The infinite-temperature localization phase transition, described in the introduction to this Chapter and taking place at energy density $\varepsilon_c = v = 2$, is therefore *not* due to a breakdown of connectivity in such manifold. Rather, we attribute it to the change in the scaling with N of the smallest, non-zero eigenvalue λ_1 of (minus) the Laplace operator on the microcanonical surface (the smallest eigenvalue $\lambda_0 = 0$ corresponds

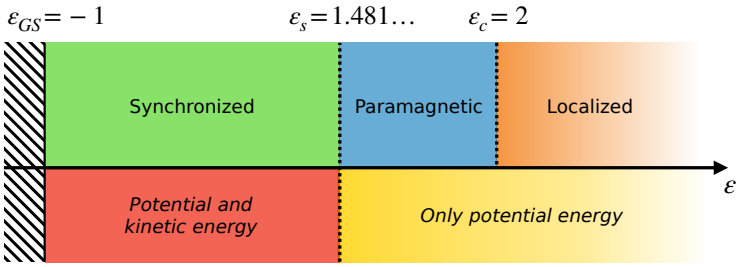

FIGURE 3.1: Phase diagram of the fully connected DNLS model for $v = 2$ and $g = 1$. The region $\varepsilon > \varepsilon_c$ corresponds to non-positive temperatures and localized dynamics; the region $\varepsilon_s < \varepsilon < \varepsilon_c$ to ergodic incoherent dynamics for the phases ϕ_i (Eq. (3.2)); the region $\varepsilon < \varepsilon_s$ to coherent dynamics for the same phases. Notice that in the $1d$ model the syncrhonized region is confined to zero temperature, and the paramagnet/localized transition coincides with the full Hamiltonian/only potential transition. This figure is taken from Ref. [3].

to the uniform distribution on the manifold). Namely, for $\varepsilon < \varepsilon_c = 2$ (the numerics agrees with the thermodynamic calculation within errors) we have $\lambda_1 = O(1)$, while for $\varepsilon > \varepsilon_c$ we have $\lambda_1 \sim e^{-\gamma N}$. The function $\gamma(\varepsilon) \geq 0$ and vanishes as $\varepsilon \to \varepsilon_c^+$ with critical exponent close to 2.

We conjecture that this transition is related to an entropic effect for the motion of a particle on the microcanonical energy surface. In other words, the volume of the regions of phase space close to an imbalanced configuration (i.e. when a few charges are considerably larger than the others) becomes bigger, at energies $\varepsilon > \varepsilon_c$, than the volume of balanced configurations. We suggest that this mechanism, and the link with the behaviour of the smallest eigenvalue of the Laplacian on the microcanonical surface, is generic for DNLSE with different choices of graphs and potentials (as also indicated by the results of Refs. [284, 285]).

3.3 Infinite temperature limit

Let us start exploring the limit $T \to \infty$. Assuming ergodicity, the computation of the canonical partition function for the Hamiltonian (3.1) should describe the behavior of the system for $\varepsilon \leq 2$.

Denoting the thermal average of an observable A as

$$\langle A \rangle_{\beta,\mu} := \frac{1}{Z} \int [dq\, d\phi]\, e^{-\beta H + \mu Q} A, \tag{3.7}$$

one can inspect the infinite temperature limit, $\beta \to 0$, by considering the expansion

$$\langle A \rangle_{\beta,\mu} = \langle A \rangle_{0,\mu} - \beta \Big[\langle AH \rangle_{0,\mu} - \langle A \rangle_{0,\mu} \langle H \rangle_{0,\mu} \Big] + O(\beta^2). \tag{3.8}$$

The first thing to do is to adjust the chemical potential to have a fixed average charge (recall the choice in Sec. 3.1):

$$\begin{aligned} N \equiv \langle Q \rangle_{\beta,\mu} &\simeq \langle Q \rangle_{0,\mu} - \beta \Big[\langle QH \rangle_{0,\mu} - \langle Q \rangle_{0,\mu} \langle H \rangle_{0,\mu} \Big] \\ &\simeq N \langle q \rangle_{0,\mu} - \beta \Big[\frac{v}{2} \big(N \langle q^3 \rangle_{0,\mu} + N(N-1) \langle q \rangle_{0,\mu} \langle q^2 \rangle_{0,\mu} \big) - N \langle q \rangle_{0,\mu} \frac{v}{2} N \langle q^2 \rangle_{0,\mu} \Big] \\ &\simeq -\frac{N}{\mu} + \beta \frac{2Nv}{\mu^3} \end{aligned} \tag{3.9}$$

so that $\mu \simeq -1 + 2\beta v$. In the computation above, it was used that the averages involving the kinetic energy vanish by symmetry, and $\langle q^k \rangle_{0,\mu} = k!/(-\mu)^k$.

Now focus on the internal energy. It was already found $\langle H \rangle_{0,\mu} = Nv/\mu^2$; thus just $\langle H^2 \rangle_{0,\mu}$ is needed. The only non-zero angular integrals in $\langle H^2 \rangle_{0,\mu}$ are

$$\int [d\phi] \, \cos(\phi_i - \phi_j) \cos(\phi_k - \phi_l) = \frac{1}{2}(\delta_{ik}\delta_{jl} + \delta_{il}\delta_{jk}); \tag{3.10}$$

therefore

$$\langle H^2 \rangle_{0,\mu} = \frac{4g^2}{\kappa^2} N\kappa \langle q \rangle_{0,\mu}^2 + \frac{v^2}{4}\left[N\langle q^4 \rangle_{0,\mu} + N(N-1)\langle q^2 \rangle_{0,\mu}^2\right] \tag{3.11}$$

where recall κ is the connectivity of the graph. The final result is

$$\varepsilon(\beta) = v - \beta\left(v^2 + \frac{4g^2}{\kappa}\right) + O(\beta^2) \tag{3.12}$$

From this expression one can see that the result of the non-interacting case $\varepsilon(\beta = 0) = v$ is not modified by the presence of the hopping on any graph geometry. Notice also that the kinetic energy term (measured by g) contributes only with $O(g^2/\kappa)$ and therefore vanishes to this order in the mean-field, fully connected limit $\kappa \to \infty$. Such limit will be explored in the next section.

3.4 Large connectivity limit

As noted at the end of the last section, in Eq. (3.12) the $O(\beta)$ correction to the internal energy density becomes independent of g in the limit of large connectivity $\kappa \to \infty$. Indeed, one can verify that *all the terms* in the expansion involving the hopping are subleading in κ. The situation is reminiscent of the Thouless-Anderson-Palmer (TAP) high temperature expansion of the Sherrington-Kirkpatrick model [286]. Alongside with TAP, one can expand the free energy density $f := -\log(Z)/\beta N$ in powers of $1/\kappa$:

$$f = f_0 + \frac{1}{\kappa} f_1 + O\left(\frac{1}{\kappa^2}\right), \tag{3.13}$$

where f_0 is the free energy density at $\kappa \to \infty$, or $g = 0$, while one can express f_1 (and successive orders too) as a sum of diagrams.

To see it, start by expanding in powers of g the full free energy density:

$$-\beta f N = \log \int [dq\, d\phi] e^{-\beta H_0 + \mu Q} \sum_{k=0}^{\infty} \frac{1}{k!}\left[\frac{2g\beta}{\kappa}\sum_{ij} A_{ij}\sqrt{q_i q_j}\cos(\phi_i - \phi_j)\right]^k \tag{3.14}$$

$$=: -\beta f_0 N + \sum_{\ell=1}^{\infty}\left(\frac{2g\beta}{\kappa}\right)^{\ell} \sum_{\Lambda \in \mathcal{D}_\ell} \Lambda \tag{3.15}$$

where consistently quantities evaluated at $g = 0$ are denoted by a "0" subscript. Equation (3.15) represents the definition of the diagrams $\Lambda \in \mathcal{D}_\ell$, that are also shown graphically in Fig. 3.2. More precisely, at each order ℓ of the effective coupling constant g/κ there are averages

$$\int [d\phi] \, \cos(\phi_{i_1} - \phi_{i_2}) \cos(\phi_{i_3} - \phi_{i_4}) \cdots \cos(\phi_{i_{2\ell-1}} - \phi_{i_{2\ell}}) \prod_{j=1}^{N} \langle q^{n_j/2} \rangle_0, \tag{3.16}$$

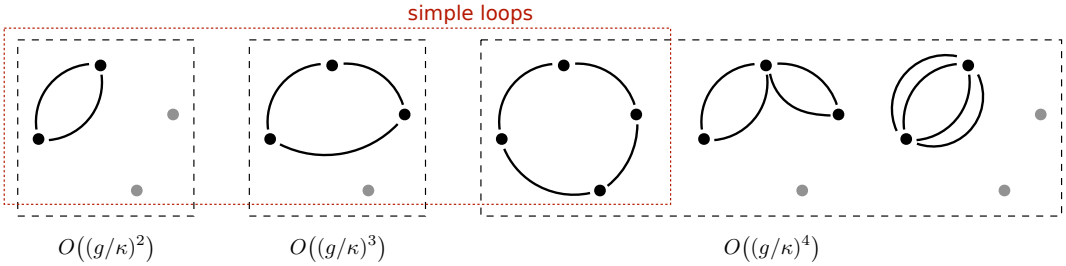

FIGURE 3.2: Allowed diagrams $\Lambda \in \mathcal{D}_\ell$ in the expansion (3.15) up to order $\ell = 4$. Including counting factors, they evaluate (from left to right) to $N\kappa/2$, $N\kappa(\kappa-1)/3$, $N\kappa(\kappa-1)(\kappa-2)/4$, $N\kappa(\kappa-1)/3$, and $N\kappa/8$. Circled in red are the one-loop, connected diagrams of which there are one per each order ℓ: these contribute to lowest order in $1/\kappa$. Notice also that there is no watermelon diagram at $O((g/\kappa)^3)$ because of point 2 in the text. This figure is taken from Ref. [3].

where n_j is the multiplicity with which index j appears in the string $i_1 i_2 \cdots i_{2\ell}$. Notice that

1. since we are expanding a logarithm, by the linked-cluster theorem each diagram $\Lambda \in \mathcal{D}_\ell$ must consist of one connected piece only;
2. for the angular integration not to yield 0, each ϕ_i must appear an even number of times; in particular this means that all the diagrams in $\mathcal{D}_\ell$ must be closed and each vertex must have an even number of legs (see Fig. 3.2);
3. the permutation symmetry of the couples $i_{2p} i_{2p+1}$ yields a factor $\ell!/S_\Lambda$, where S_Λ is the symmetry factor of the diagram Λ. Therefore, according to the usual arguments this cancels the $1/\ell!$ in the expansion of the exponential, leaving the symmetry factor in the denominator;
4. the permutation symmetry within each couple $i_{2p} i_{2p+1}$ of the two indices yields a factor 2 for each pair, and so a factor 2^ℓ in total;
5. the angular integration for simple loops evaluates to $2^{1-\ell}$, while multiple loops give a result depending on the geometry (e.g. in Fig. 3.2 the first three diagrams are simple loops and receive respectively a factor $1/2$, $1/4$ and $1/8$, while the fourth receives a factor $1/4$ and the last a factor $3/8$).

By using the previous rules, and having a look at Fig. 3.2, one can get convinced that at fixed order ℓ the simple loops (e.g. the diagrams circled in red in Fig. 3.2) are the least suppressed by κ. Indeed, since they are composed by the maximum number of *distinct* points, the factor κ^ℓ in the denominator of Eq. (3.15) is compensated by the $\sim N\kappa^{\ell-1}$ possible choices of the points. Having noted this feature, we can explicitly compute f_1: the angular integration yields a factor $2^{1-\ell}$ (as noted in point 5 before), the symmetry factors are $S_\Lambda = 2\ell$, and only the averages $\langle q^1 \rangle_0 = 1$ appear. Therefore one has

$$-\beta f_1 = \frac{\kappa}{N} \sum_{\ell=2}^{\infty} \left(\frac{2g\beta}{\kappa} \right)^\ell N\kappa^{\ell-1} \frac{1}{2\ell} 2^\ell \frac{1}{2^{\ell-1}} = -2g\beta - \log(1-2g\beta), \tag{3.17}$$

with the sum starting from $\ell = 2$ because there is no diagram at order 1.

At this point, one can give a physical interpretation to Eqs. (3.13)–(3.17). In the large connectivity limit $\kappa \to \infty$, the extensive contribution to the free energy is always regular and independent of the hopping between different sites. Moreover, as

long as $\beta < \beta_s := (2g)^{-1}$, the sub-extensive contribution f_1 can be forgotten, while at $\beta = \beta_s$ it diverges and there is a phase transition: interactions must be taken into account and to go beyond one needs to address the problem non-perturbatively.

3.5 Solution of the fully-connected model

To go beyond perturbation theory, one can compute the partition function of the fully-connected model $\kappa = N-1$ using saddle-point methods. Dropping sub-leading terms in N:

$$Z_{MF}(N,\beta,\mu) = \int [dq\, d\phi] \exp\Big\{ -\frac{\beta v}{2}\sum_i q_i^2 + \mu \sum_i q_i + \frac{2\beta g}{N}\Big(\sum_i \sqrt{q_i} e^{i\phi_i}\Big)\Big(\sum_i \sqrt{q_i} e^{-i\phi_i}\Big)\Big\}. \quad (3.18)$$

We expand

$$\Big(\sum_i \sqrt{q_i} e^{i\phi_i}\Big)\Big(\sum_i \sqrt{q_i} e^{-i\phi_i}\Big) = \Big(\sum_i \sqrt{q_i}\cos\phi_i\Big)^2 + \Big(\sum_i \sqrt{q_i}\sin\phi_i\Big)^2, \quad (3.19)$$

so that a Hubbard-Stratonovich transformation can be performed:

$$Z_{MF}(N,\beta,\mu) = \frac{N}{2\pi}\int [dq\, d\phi] \int dy_1 dy_2 \exp\Big\{ -\frac{\beta v}{2}\sum_i q_i^2 - \frac{N}{2}(y_1^2+y_2^2) + \mu\sum_i q_i + 2\sqrt{\beta g}\, y_1 \sum_i \sqrt{q_i}\cos\phi_i + 2\sqrt{\beta g}\, y_2 \sum_i \sqrt{q_i}\sin\phi_i\Big\}. \quad (3.20)$$

Now all the q,ϕ integrals are factorized, and the basic constituents are of the form

$$\frac{1}{2\pi}\int dq\, d\phi\, \exp\Big[-\beta v q^2/2 + \mu q + \sqrt{\beta g q}\,(y_- e^{i\phi} + y_+ e^{-i\phi})\Big] \quad (3.21)$$

with $y_\pm = y_1 \pm i y_2$. One can perform first the angular part:

$$\begin{aligned}\frac{1}{2\pi}\int_0^{2\pi} d\phi\, e^{z(y_- e^{i\phi} + y_+ e^{-i\phi})} &= \frac{1}{2\pi}\int_0^{2\pi} d\phi \sum_{k\geq 0}\frac{z^k y_-^k}{k!} e^{ik\phi}\sum_{\ell\geq 0}\frac{z^\ell y_+^\ell}{\ell!} e^{-i\ell\phi} \\ &= \sum_{k\geq 0}\frac{(z^2 y_+ y_-)^k}{(k!)^2} = I_0(2z\sqrt{y_+ y_-}), \end{aligned} \quad (3.22)$$

I_0 being the modified Bessel function of the first kind. Thus, defining

$$J(\beta,\mu,Y) := \int_0^\infty dq\, e^{-\beta v q^2/2 + \mu q} I_0\big(2\sqrt{\beta g q Y}\big) \quad (3.23)$$

with $Y := y_+ y_- = y_1^2 + y_2^2$, one arrives at

$$Z_{MF}(N,\beta,\mu) = N\int_0^\infty dY e^{-NY/2 + N\log J(\beta,\mu,Y)}. \quad (3.24)$$

When performing this integral in the $N\to\infty$ limit, if the saddle point is within the domain of integration $Y \geq 0$, one can use the saddle point method, otherwise one needs to integrate by parts around the lower limit of integration $Y = 0$ (see Fig. 3.3).

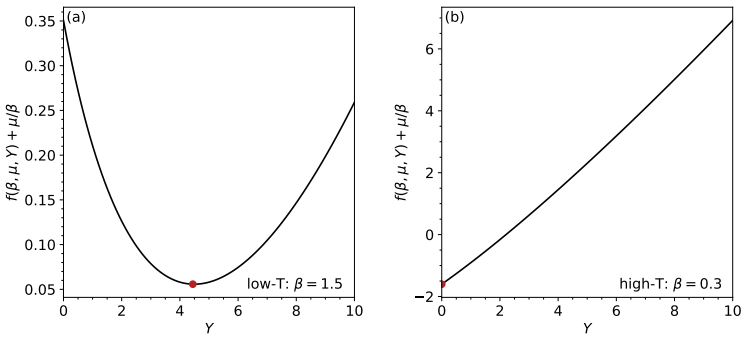

FIGURE 3.3: Plot of the free energy density $f(\beta,\mu,Y)+\mu/\beta$, with $g=1$, $v=2$, and μ fixed so that $\langle Q\rangle = N$. The red dot is the solution of Eq. (3.26), i.e. the extremal point. It moves from the bulk of the allowed region $Y>0$ at low temperature (panel (a)), to the boundary $Y=0$ at high temperature (panel (b)). This figure is taken from Ref. [3].

In any case, the free energy density is

$$f(\beta,\mu,Y) = \beta^{-1}(Y/2 - \log J), \tag{3.25}$$

where Y solves the saddle-point equation (with the above proviso)

$$\frac{1}{2} = \frac{1}{J}\frac{\partial J}{\partial Y}. \tag{3.26}$$

It also is convenient to trade μ for the (average) total charge $\langle Q\rangle = N$:

$$1 = \frac{1}{J}\frac{\partial J}{\partial \mu}. \tag{3.27}$$

Equations (3.26)–(3.27) can be easily solved numerically by iteration for any desired β.

Another way of rewriting Eqs. (3.26)–(3.27) is by interpreting $J(\beta,\mu,Y)$, defined in Eq. (3.23), as a partition function for the variable q, which thus acquires the probability density

$$p(q) = \frac{1}{J} e^{-\beta v q^2/2 + \mu q} I_0\left(2\sqrt{\beta g q Y}\right). \tag{3.28}$$

Then, the two equations (3.26)–(3.27) take (respectively) the form

$$\sqrt{\frac{Y}{4\beta g}} = \left\langle \sqrt{q}\,\frac{I_1(2\sqrt{\beta g q Y})}{I_0(2\sqrt{\beta g q Y})} \right\rangle_p \tag{3.29}$$

$$1 = \langle q\rangle_p\,. \tag{3.30}$$

These last expressions are convenient to control the limits $\beta\to\infty$ and $\beta\to 0$. Indeed, as $\beta\to\infty$ the problem simplifies and the probability concentrates around the saddle point $q=1$ (Eq. (3.30)). One can also expand the Bessel functions (as long as, self-consistently, $Y \gg 1/\beta$) for large arguments, and substituting $q=1$ in Eq. (3.29) gives

$$\sqrt{\frac{Y}{4\beta g}} = \langle \sqrt{q}(1+\cdots)\rangle_p \implies Y = 4g\beta + O(\beta^0). \tag{3.31}$$

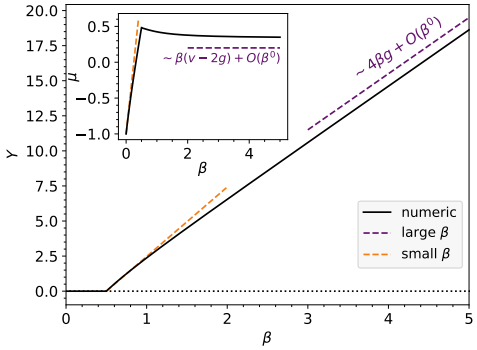

FIGURE 3.4: Saddle-point value of Y found upon solving Eqs. (3.26)–(3.27) by iteration, with $g = 1$ and $v = 2$ (black solid line). For $\beta < (2g)^{-1} = 0.5$ the correct solution is Y_1, while at larger values of β it becomes Y_2 (see Eq. (3.35)). For comparison, we show the approximate solutions at $\beta \to \infty$ and $\beta Y \to 0$ as dashed lines. Note that the $\beta \to \infty$ approximation, to the order obtained in Eqs. (3.31)–(3.32), still needs a $O(\beta^0)$ term to be fixed. *Inset:* Corresponding values found for μ. This figure is taken from Ref. [3].

Also, imposing Eq. (3.30) explicitly on Eq. (3.28), one gets

$$\mu = \beta(v - 2g) + O(\beta^0). \tag{3.32}$$

For small β, instead, one can expand the Bessel functions for small argument (as long as this returns self-consistently $\beta Y \ll 1$), and obtain

$$\sqrt{\frac{Y}{4\beta g}} = \left\langle \sqrt{q}\left[(\beta g q Y)^{1/2} - \frac{1}{2}(\beta g q Y)^{3/2} + \cdots\right]\right\rangle_p \tag{3.33}$$

$$= (\beta g Y)^{1/2}\langle q\rangle_p - \frac{1}{2}(\beta g Y)^{3/2}\langle q^2\rangle_p + \cdots . \tag{3.34}$$

There are two solutions:

$$Y_1 = 0, \qquad Y_2 = \frac{2\beta g - 1}{(\beta g)^2\langle q^2\rangle_p}. \tag{3.35}$$

The second solution is negative for $\beta < \beta_s = (2g)^{-1}$, so in this region one must stick with Y_1 (since the Y integral in Eq. (3.24) is on the positive domain). As $\beta \gtrsim \beta_s$, instead, Y_2 becomes the correct solution, until the condition $\beta Y \ll 1$ is no more valid and the approximation breaks down. In Fig. 3.4, the comparison of the numerically exact solutions with the small-β and large-β approximations is presented.

To connect with the diagrammatic expansion done in Sec. 3.4, notice that the critical value $\beta_s = (2g)^{-1}$ is the same given by the radius of convergence of perturbation theory for f_1, the sub-extensive contribution to the free energy. We are now in position to give an interpretation to the phase transition taking place at $T_s = 1/\beta_s$: it is the temperature below which the angles ϕ_i no more average to zero, but start acquiring a common orientation. Indeed, on one hand

$$-g\frac{\partial}{\partial g}(\beta f) = \beta\frac{2g}{N^2}\sum_{i\neq j}\left\langle\sqrt{q_i q_j}\cos(\phi_i - \phi_j)\right\rangle; \tag{3.36}$$

on the other hand, by differentiating the saddle-point free energy,

$$-g\frac{\partial}{\partial g}(\beta f) = g\frac{1}{J}\frac{\partial J}{\partial g} = Y\frac{1}{J}\frac{\partial J}{\partial Y} = \frac{Y}{2}. \tag{3.37}$$

The comparison of the last two equations implies

$$Y = \frac{4\beta g}{N^2}\sum_{i\neq j}\left\langle \sqrt{q_i q_j}\cos(\phi_i - \phi_j)\right\rangle. \tag{3.38}$$

We conclude that, as $\beta \to \infty$, the angles must all point in the same direction (albeit the latter can change in time). Indeed, recalling that q concentrates around 1, in order to find the asymptotic, low temperature behaviour $Y \simeq 4\beta g$ one needs that all the phases align: $\langle\cos(\phi_i - \phi_j)\rangle \to 1$, so $\phi_i \to \phi_0$ for all $i = 1, 2, \ldots, N$. This is the statistical mechanics signature of a synchronized phase [287, 288], in which all fields have a common phase and the fluctuations of the amplitudes are negligible. The synchronization phase transition is second-order, with the order parameter Y growing linearly close to $\beta_s = (2g)^{-1}$.

One can also express the above observations in terms of the energy density ε. At $T = 0$ the system is in the ground state, with energy density $\varepsilon_{GS} = v/2 - 2g$: this readily follows from the $\beta \to \infty$ expansion of the free energy. At the synchronization transition $T = T_s = 2g$, instead, the energy density can be found numerically by imposing $Y = 0$ and fixing μ from Eq. (3.27): for $g = 1$ and $v = 2$ we find $\varepsilon_s = 1.481\ldots$ (see also Fig. 3.1).

Finally, one can identify the order parameter Y with the average interaction energy density (see Eq. (3.38)), which vanishes at temperatures $T > T_s$.

3.6 Topological structure of the equipotential surface

It's time to start focusing on the region $\varepsilon \geq \varepsilon_c = v$. Having completely lost the spatial structure given by the hopping *for any graph geometry*, the model has become *effectively non-interacting*. For this reason, we can also fix $v \equiv 2$ wlog. from now on.

The microcanonical surface is non-trivial, because of the presence of two conservation laws: energy ($H = N\varepsilon$) and charge ($Q = N$). For large energy density, the bulk of the volume of the microcanonical surface is concentrated in the region where a few charges get a large share of the total charge (the participation ratio is $O(1)$ [282, 283]). These are localized charge configurations. However, these configurations are not isolated from each other, and a continuous charge rearrangement can move any localized lump anywhere else in space, passing through regions of equally distributed charges. In this Section, we show that this can be done by moving continuously on the microcanonic surface for any $\varepsilon = O(1)$.

Let us summarize here what is proven as a theorem in this Section: *The microcanonical surface remains a connected manifold for all the energy densities $\varepsilon < N/2$ (extensive energy density), in particular through the dynamical transition observed numerically at $\varepsilon_c = 2$, which then cannot be imputed to a deficiency in connectivity.* Moreover, as ε increases, the surface passes a series of critical points, according to stratified Morse theory. *At the dynamical transition $\varepsilon_c = 2$, the number of transverse dimensions of the pipe connecting two regions corresponding to localized charges equals the number of longitudinal dimensions.* What this topological proof cannot tell is *how* the equilibration time depends on N. That is a property of the dynamics, which one can only conjecture is

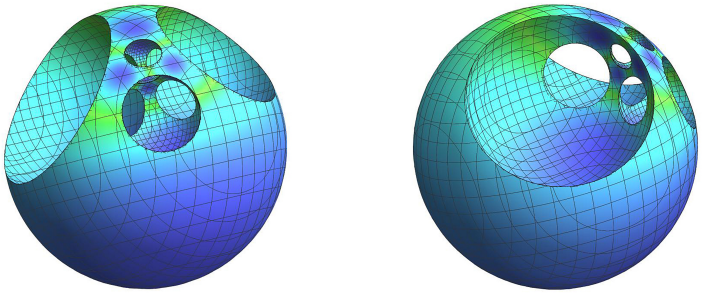

FIGURE 3.5: Two different views of the same stereographic projection of the manifold $\mathcal{M}_\varepsilon$ (Eq. (3.39)), for $N = 5$ and $\varepsilon = 2$. While this projection respects the topology of the manifold, clearly its metric structure is altered. Colors depend on the distance from the vertices of Δ^{N-1}, varying from blue for the five 0-handles around those vertices to green for the median sections of the ten 1-handles. This figure is taken from Ref. [3].

due to the shape of the pipes linking the "fat" regions of localized charge, and it is presented at the end of this Section as a *Problem*.

In order to prove these two results, let us introduce the manifold and some relevant results of Morse theory. Again, change variables from the ψ_i's to the local charges $q_i = |\psi_i|^2$ (Eq. (3.2)), that are the only combinations of the ψ_i's entering in the conservation laws. Thus, one is left with the equations

$$\begin{cases} \frac{1}{N}\sum_{i=1}^{N} q_i = 1 \\ \frac{1}{N}\sum_{i=1}^{N} q_i^2 = \varepsilon \\ q_i \geq 0 \quad \forall i = 1, 2, \ldots, N. \end{cases} \tag{3.39}$$

These equations define a $(N-2)$-dimensional manifold with boundary and corners $\mathcal{M}_\varepsilon$ (see Fig. 3.5 for a visual impression of the case $N = 5$), naturally embedded in $\mathbb{R}^N$, whose central role was recognized already in Ref. [289]. The topology of this manifold undergoes a series of changes as ε varies, which can be outlined by stratified Morse theory in the following way.

The first and the last equation in (3.39) represent the affine simplex $\Delta^{N-1} \subset \mathbb{R}^N$ spanned by the vectors $Ne_1, \ldots, Ne_N$, where $e_1, \ldots, e_N$ is the canonical base of $\mathbb{R}^N$. Hence, $\mathcal{M}_\varepsilon$ is non-empty for $1 \leq \varepsilon \leq N$. Moreover, $\mathcal{M}_\varepsilon$ is a small $(N-2)$-sphere around the barycenter of Δ^N when ε approaches 1, while it is the disjoint union of N small $(N-2)$-disks, each near to a vertex of Δ^{N-1}, when ε approaches N.

In order to see what happens for the intermediate values of ε, think of the boundary $\partial\Delta^{N-1}$ as a stratified space, whose strata are its open sub-simplices of Δ^{N-1}, and observe that $\varphi : \partial\,\Delta^{N-1} \to \mathbb{R}$ given by $\varphi(q) = \|q\|^2/N$ is a stratified Morse function, meaning that it restricts to a Morse function on every stratum. Then, for every $1 < \varepsilon < N$, the radial projection from the barycenter of Δ^{N-1}, that is the vector $e_1 + \cdots + e_N$, induces a stratified diffeomorphism between $\mathcal{M}_\varepsilon$ and the suplevel set $M^\varepsilon(\varphi) = \{q \in \partial\Delta^{N-1} \mid \varphi(q) \geq \varepsilon\} \subset \partial\Delta^{N-1}$, according to the second equation in (3.39).

Morse theory tells us that the topology of $\mathcal{M}_\varepsilon \cong M^\varepsilon(\varphi)$ changes only at the critical values of the restrictions of φ to the strata of $\partial\Delta^{N-1}$. Such critical values have the form N/k with $1 < k < N$. Indeed, for each k we have $\binom{N}{k}$ corresponding non-degenerate critical points of index $N-k-1$ located at the barycenters of the $(k-1)$-dimensional faces of Δ^{N-1}. This implies that for $\delta > 0$ small enough $M^{N/k-\delta}(\varphi)$

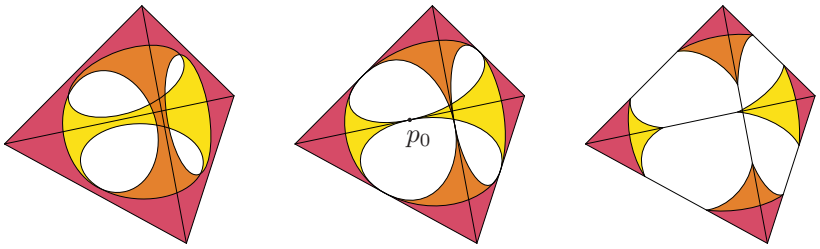

FIGURE 3.6: The last critical point, at which the microcanonic manifold splits into N disconnected pieces each representing a different set of localized configurations, close to each of the vertices of Δ^{N-1}. The figure concerns the case $N = 4$. Everything is depicted in the $(N-1)$-dimensional affine subspace A^{N-1} given by the first equation in (3.39). In yellow $\mathcal{M}_\varepsilon \subset \mathbb{S}^{N-2}_\varepsilon$ and in red the suplevel set $M^\varepsilon(\varphi) \subset \mathrm{Bd}\,\Delta^{N-1}$. This figure is taken from Ref. [3].

can be obtained by attaching $\binom{N}{k}$ narrow $(k-1)$-handles to $M^{N/k+\delta}(\varphi)$. Each of these $(k-1)$-handles is an $(N-2)$-cell C^{N-2} which is the product of a $(k-1)$-cell $C^{k-1} = \mathrm{Cl}(\Sigma - M^{N/k+\delta}(\varphi))$ (where Cl stands for the closure operator) for a $(k-1)$-dimensional face Σ of Δ^{N-1} and a small $(N-k-1)$-cell C^{N-k-1} such that $C^{N-2} \cap M^{N/k+\delta}(\varphi) = \partial\, C^{k-1} \times C^{N-k-1}$.

As a consequence, for every $k = 1, \ldots, N-1$ and $N/(k+1) < \varepsilon < N/k$ the $(N-2)$-manifold $M^\varepsilon(\varphi)$ is a regular neighborhood, meaning an $(N-2)$-dimensional thickening, of the $(k-1)$-skeleton of Δ^{N-1} in $\partial\Delta^{N-1}$. In particular, recalling the homeomorphism $\mathcal{M}_\varepsilon \cong M^\varepsilon(\varphi)$, we can conclude that $\mathcal{M}_\varepsilon$ has N connected components for $N/2 < \varepsilon \leq N$, while it is connected for $1 \leq \varepsilon \leq N/2$.

The above discussion shows that, for $N > 4$, at $\varepsilon = 2$ the manifold $\mathcal{M}_\varepsilon$ has gone through a series of gluing handles procedures described above, yet remaining connected. This raises the intriguing problem of characterizing $\mathcal{M}_2$ also from a purely geometrical point of view. Of course the simplest geometrical invariant of $\mathcal{M}_\varepsilon$ is its volume. Since $\mathrm{vol}(\mathcal{M}_1) = \mathrm{vol}(\mathcal{M}_N) = 0$, we know by continuity that there exists $\varepsilon_0(N) \in (1, N)$ which maximizes $\mathrm{vol}(\mathcal{M}_\varepsilon)$. Recall that Boltzmann's law entails $S(\varepsilon) = \log(\mathrm{vol}(\mathcal{M}_\prime))$, and also that it holds

$$\frac{1}{T} = \frac{1}{N}\frac{dS}{d\varepsilon}. \tag{3.40}$$

At infinite temperature clearly $\frac{dS}{d\varepsilon}|_{\varepsilon=2} = 0$. So, the stationary point for the microcanonical manifold volume arises at $\varepsilon = 2$ (value that is correct only in the limit $N \to \infty$), as already argued before. This classical observation has been significantly strengthened in [282, 283] for the model under consideration, where it is observed that $\varepsilon = 2$ is indeed $\lim_{N\to\infty} \varepsilon_0(N)$ and moreover $\varepsilon_0(N) = 2 + O(N^{-1/3})$. We believe that a direct geometric analysis of the behaviour of $\mathrm{vol}(\mathcal{M}_\varepsilon)$ would be very interesting by itself since it could shed light on various other aspects of the problem studied.

While we leave this task for future investigation, we now observe that thanks to the Morse-theoretic description above, we can quantify the volume contribution of each handle attachment through any critical value of $\varepsilon = N/k$, $1 < k < N$. Indeed, given $\varepsilon = N/k - \delta$ and p_0 a singular point in $\mathcal{M}_{N/k}$, we can look at the projection Π from the barycenter B of the symplex of a neighborhood of p_0 in the sphere $\mathbb{S}^{N-2}$ inside the $(N-1)$-dimensional affine subspace A^{N-1} given by the first equation in (3.39) onto the tangent space to this sphere (see Figs. 3.6 and 3.7).

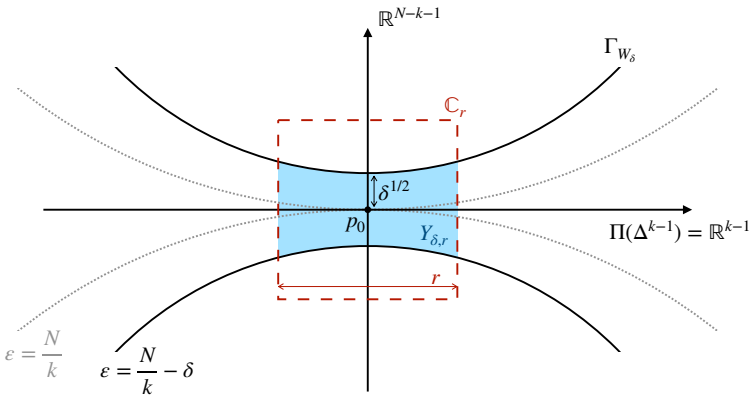

FIGURE 3.7: Image of the projection via Π on $T_{p_0}(\mathbb{S}^{N-2})$ of a neighborhood of a singular point p_0 in $\mathcal{M}_{N/k}$. Γ_{W_δ} is the profile of $\Pi(\mathcal{M}_{N/k-\delta})$ in $T_{p_0}(\mathbb{S}^{N-2})$. In blue the handle attachment $Y_{\delta,r}$. This figure is taken from Ref. [3].

As argued above, p_0 is a non-degenerate critical point of index $N-k-1$ located at the barycenter of a $(k-1)$-dimensional face Δ^{k-1} of Δ^{N-1} and hence we can choose coordinates $(x_1,\dots,x_{k-1},y_1,\dots,y_{N-k-1})$ on $T_{p_0}(\mathbb{S}^{N-2})$ in such a way that $\underline{x} = (x_1,\dots,x_{k-1})$ parametrize $\Pi(\Delta^{k-1})$, and $\underline{y} = (y_1,\dots,y_{N-k-1})$ span its orthogonal complement. By intersecting $\Pi(\mathcal{M}_\varepsilon)$ with a $(N-2)$-cube $\mathbb{C}_r$ centered in the origin of $T_{p_0}(\mathbb{S}^{N-2})$ with faces parallel to the coordinate axis, we are led to estimate the rate change of the local effect on the volume of the handle-attachment procedure ($\mathrm{vol}(Y_{\delta,r})$ as shown in Fig. 3.7). This can be done observing that such region is bounded by a function $W_\delta(|\underline{x}|)$, which is at first order quadratic in $|\underline{x}|$, being the image via Π of the profile of the sphere, and s.t. $W_\delta(0) = \delta^{1/2} + O(\delta)$. It is now a straightforward computation to see that

$$\mathrm{vol}(Y_{\delta,r}) = C(N,k)\, r^{k-1}\delta^{(N-k-1)/2} + \text{h.o.} \tag{3.41}$$

for some constant $C(N,k)$. The above computation holds for any $k = 2\dots N-1$, and singles out yet another peculiarity of the value $\varepsilon = 2$, corresponding to $k = N/2$ (for even values of N). In fact, this is the only situation in which the contributions coming from the two factors of the handle $C^{k-1}\times C^{N-k-1}$ are of the same order.

Having established that nothing worth of notice in the topology of $\mathcal{M}_\varepsilon$ occurs at $\varepsilon = 2$, we will see in the next Section that a simple Brownian motion on $\mathcal{M}_\varepsilon$ does change its behavior precisely at $\varepsilon = 2$. The dynamics of the Brownian motion is notoriously linked to another natural geometric invariant of $\mathcal{M}_\varepsilon$, namely its first non-zero eigenvalue of the Laplacian for the curved metric induced on $\mathcal{M}_\varepsilon$ (with Neumann boundary conditions). We will then provide in the next Section strong evidence for the following intriguing (and hard) geometric

Problem. *Having set* $\gamma(\varepsilon) := -\lim_{N\to\infty}\frac{1}{N}\log\lambda_1$, *it holds*

$$\begin{cases}\gamma = 0 & \varepsilon \le 2\\ \gamma > 0 & \varepsilon > 2.\end{cases} \tag{3.42}$$

Providing fine estimates for the first eigenvalue of the Laplacian is well known to be a subtle (and important) problem in geometric analysis. The present situation seems particularly interesting and original also from a purely mathematical point of view for the concurrence of the value $\varepsilon = 2$ as special value both for the volume and

λ_1, a coincidence that certainly deserves further understanding on the mathematical side.

We believe, however, that the simple observation in Eq. (3.41) could be a first step towards the understanding of the coincidence stated above. Indeed, a very much conjectural, and simplified picture of why the charges become localized could be based on the counting of "useful" and "useless" directions when crossing the handles connecting two different localized configurations. One can make as well a connection with the question of *entropic barriers* in spin-glass dynamics (on this topic see e.g. [208, 290–292]). We leave this connection for future investigations.

3.7 A Brownian exploration of the equipotential surface

In order to extract the first non-zero eigenvalue of the Laplacian, we resorted to studying the correlation functions of a Brownian motion on the surface $\mathcal{M}_\varepsilon$. Indeed, being the diffusion equation described by the Laplacian, it is known that the late decay of the correlation functions of coordinates (e.g. the charges q_i) gives its first non-zero eigenvalue. Hence, we pick as a starting point a random vector $\vec{q}$ that satisfies all the conditions in (3.39) (this can be easily done by repeatedly projecting on the three distinct manifolds defined by each constraint, until they are all obeyed), and let it evolve by free diffusion on $\mathcal{M}_\varepsilon$ up to a final time T_f. Specifically, at each Monte Carlo step we update the position as $\vec{q}(t+dt) = \vec{q}(t) + d\vec{W}$, where dW_i are i.i.d. Gaussian random variables s.t. $\langle dW_i \rangle = 0$ and $\langle dW_i^2 \rangle = dt$, dt being small[3]; and then we enforce again the constraints until they are all satisfied.

We believe it is important to emphasize that our dynamics is fundamentally different from that of [264, 269, 270, 282]. In these works, the basic Monte Carlo step was the redistribution of charge within a triplet of sites. Specifically, a triplet (q_i, q_j, q_k) was updated to a randomly chosen new triplet (q_i', q_j', q_k'), with the constraint that the transformation $(q_i, q_j, q_k) \longmapsto (q_i', q_j', q_k')$ could be performed continuously in the subsystem defined by the three charges only, and without violating the (local) charge and energy constraints. In the case of *consecutive* triplets $i = j-1 = k-2$, this Monte Carlo algorithm provides a good description for the dynamics of a chain. The case of generic i, j, k, instead, addresses a mean-field situation like the one considered in this work. We believe nevertheless that it would be difficult to connect this "triplet" dynamics to the Brownian motion (which instead is related to the eigenvalues of the Laplacian), so we decided to simulate directly the latter.

In Fig. 3.8 we show the time evolution of the (connected) correlation function

$$G(t) := \frac{1}{N}\sum_{i=1}^{N} \langle q_i(t+t')q_i(t') \rangle_{t'} - \frac{1}{N}\sum_{i=1}^{N} \langle q_i(t+t') \rangle_{t'} \langle q_i(t') \rangle_{t'} \tag{3.43}$$

where the angular brackets denote averaging wrt. the time variable in the subscript:

$$\langle A(t') \rangle_{t'} := \lim_{T_f \to \infty} \frac{1}{T_f} \int_0^{T_f} A(t')\, dt'.$$

[3] Notice that with this normalization $\|\vec{q}(t+dt) - \vec{q}(t)\| = O(\sqrt{N})\sqrt{dt}$ and the relative Fokker-Plank equation is Eq. (3.44), which does not contain any explicit factor of N. Different scalings of dq can be easily obtained by rescaling time.

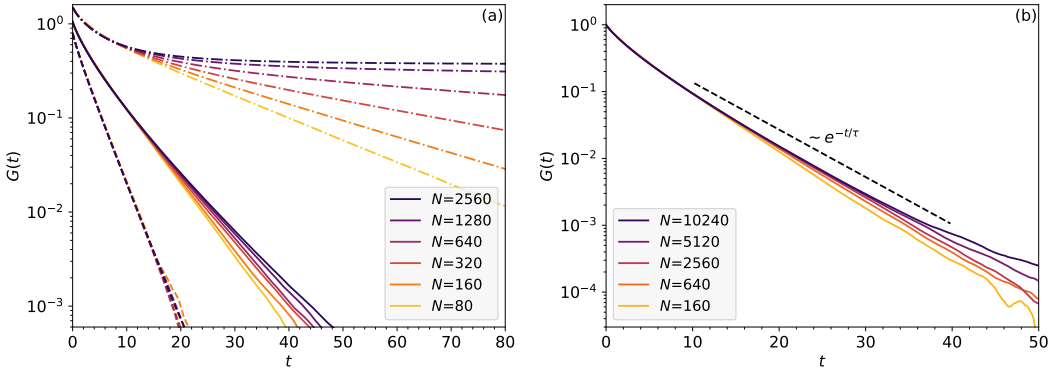

FIGURE 3.8: (a) Correlation function, Eq. (3.43), as a function of physical time t with $dt = 0.01$. Dashed lines refer to $\varepsilon = 1.9$ (ergodic region), solid lines to $\varepsilon = 2.05$ (near-critical region) and dashed-dotted lines to $\varepsilon = 2.5$ (localized region). One can see that, except in the critical region, the decay has a wide simple exponential window. Each curve is obtained by averaging over at least 5000 different runs. (b) Correlation function at the critical point $\varepsilon = 2$. The decay is slower than an exponential (and becomes slower as N is increased), as shows the comparison with the black dashed line. For each N we performed a fit $\log G(t) = -t/\tau - \log(1 + (t/t_1)^z)$, finding values of τ, t_1 and z that we report in Fig. 3.10. Each curve is obtained by averaging over at least 50000 different runs. This figure is taken from Ref. [3].

At $t = 0$, $G(0) = (\varepsilon - 1)$ because of the second constraint in Eq. (3.39). Taking $t \to \infty$, instead, *if the dynamics on the manifold is ergodic* it holds $G(\infty) = 0$. Conversely, if ergodicity is broken either because $\mathcal{M}_\varepsilon$ is disconnected in pieces or because the dynamics is effectively confined in a smaller region, it holds $G(t) \to const > 0$. According to the discussion before, $\mathcal{M}_\varepsilon$ becomes disconnected for $\varepsilon > N/2$. At this point there is a geometric obstruction to ergodicity: a trajectory starting in a neighborhood of, say, $q_1 = O(N)$ cannot reach the neighborhood of any other $q_i = O(N)$ with $i \neq 1$. Therefore, for these (large) values of ε the correlation function does not get to 0 as $t \to \infty$. Before then (viz. for any finite N, and any $\varepsilon < N/2$) there is always a finite time scale τ, after which the function $G(t)$ does get close to 0. This correlation time is a good proxy for an equilibrium time (since the charges q_i are the only observables of the systems).

We also note that $G(t)$ must decay exponentially in t (after, of course, a possible initial transient). This is due to the fact that a diffusion equation is associated to the Brownian motion:

$$\partial_t P(q,t) = \frac{1}{2}\Delta P(q,t), \tag{3.44}$$

where the Laplacian has the usual definition in curvilinear coordinates:

$$\Delta := g^{-1/2}\partial_a(g^{1/2}g^{ab}\partial_b). \tag{3.45}$$

The smallest eigenvalue of $-\Delta$ is $\lambda_0 = 0$, and the corresponding (properly normalized) eigenvector is nothing but the uniform (microcanonical) distribution $P(q, t \to \infty) = \phi_0(q)$. Since the Laplacian on a compact Riemannian manifold has a pure point spectrum, the first eigenvalue $\lambda_1 > 0$ and the gap, which we will denote as $\lambda_1 =: 1/\tau$, controls the asymptotic decay of $P(q,t) \simeq \phi_0(q) + c_1\phi_1(q)e^{-t/\tau} + ...$ In particular, this means that $G(t) \sim e^{-t/\tau}$ for large t, as claimed before.

The exponential decay can be seen clearly in Fig. 3.8a. Within the exponential form, one can distinguish two cases: for $\varepsilon < 2$ the curves fall approximately on a

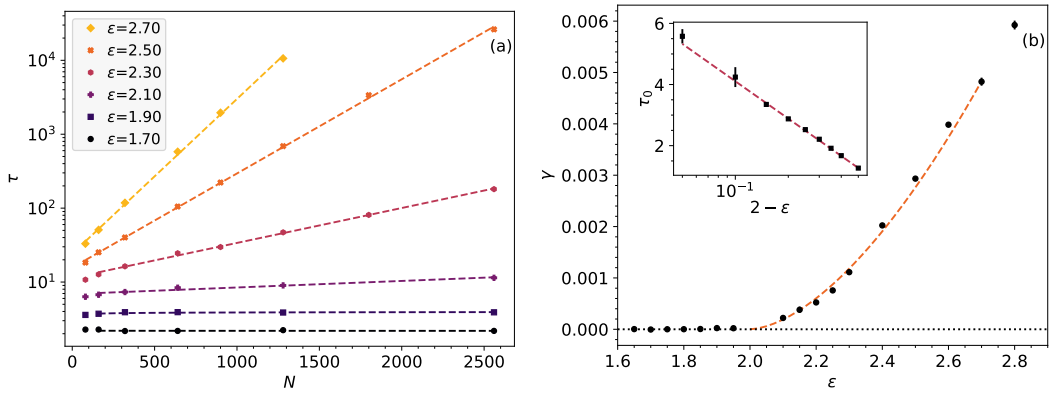

FIGURE 3.9: (a) Correlation times τ extracted from the exponential decay of the correlation function, Eq. (3.43): we can see that τ diverges in the thermodynamic limit as ε becomes greater than 2 (not all datasets are shown here to improve readability). We have also performed fits (dashed lines): for $\varepsilon > 2$, we employed $\log \tau = \gamma N + c$, from which we extracted the γ's presented in the right panel. For $\varepsilon < 2$, instead, since τ is almost constant with N we found that finite-size effects are well accounted for by the fitting function $\tau = w/\log(N) + \tau_0$. The τ_0's obtained are displayed in the inset of the right panel. (b) Exponent γ as a function of ε (black dots). It can be clearly seen that $\gamma = 0$ within errors for $\varepsilon < 2$, while $\gamma > 0$ for $\varepsilon > 2$. The orange, dashed line is a fit of the form $\log \gamma = \eta \log(\varepsilon - 2) + h$, yielding $\eta = 1.7 \pm 0.1$ and $h = -4.7 \pm 0.1$. (Inset) The value of $\tau \simeq \tau_0$ diverges logarithmically in the limit $\varepsilon \to 2^-$ (see, for a comparison at the critical point, Fig. 3.10a). The dashed line is a fit $\tau_0 = -\zeta \log(2 - \varepsilon) + u$, from which we find $\zeta = 1.76 \pm 0.02$ and $u = 0.05 \pm 0.01$. This figure is taken from Ref. [3].

universal curve, which is the limit $N \to \infty$; for $\varepsilon \geq 2$ various system sizes have different decays: larger systems decay on a *longer* timescale and there is no obvious limit $N \to \infty$. This corresponds to the following statement on the spectrum of the Laplacian: for $\varepsilon < 2$ the gap remains finite when $N \to \infty$, while for $\varepsilon \geq 2$ the gap closes with N. We find numerically that the gap closes exponentially with N: $\tau \simeq e^{\gamma N}$ for some rate $\gamma > 0$, see Fig. 3.9. This fact implies that $\varepsilon = 2$ is a *dynamical* critical point, at which the dynamics becomes scale-invariant [293].

More precisely, for $\varepsilon < 2$ the timescale τ is constant with N and grows with ε, ultimately diverging logarithmically as $\varepsilon \to 2^-$ (see the inset of Fig. 3.9b). For $\varepsilon > 2$, it is $\gamma(\varepsilon)$ which grows with ε: $\gamma \sim (\varepsilon - 2)^\eta$ with $\eta \simeq 1.7 \pm 0.1$ (see Fig. 3.9b).

To sum up: to the left of the critical point $\varepsilon = 2$ the dynamics is ergodic and $G(t) \to 0$ for any N *and also for the limit* $N \to \infty$; to the right, instead, the relaxation becomes progressively slower as N increases and in the limit $N \to \infty$ it holds $G(t) \to const > 0$. The limiting functional form at $\varepsilon = 2$ must be a function decaying to 0, but slower than an exponential. We checked that, in a small right neighborhood of $\varepsilon = 2$, the fitting function $G(t) = (\varepsilon - 1)e^{-t/\tau}/(1 + (t/t_1)^z)$ works pretty accurately with $z \in [0.7, 1.0]$ depending on the values of N used (see Figs. 3.8b and 3.10 for the details). Indeed, for this estimate to be useful one must have $t_1 \ll \tau \to \infty$, to ensure a sufficiently large fitting window. Since τ grows with N (albeit only logarithmically) while t_1 decreases (see Fig. 3.10a), it will eventually hold $t_1 \ll \tau$. Unfortunately, this crossover takes place roughly at the largest system sizes we were able to simulate, so the values of z we can extract cannot be considered precise. By using only the points in the "asymptotic region" (shaded region in Fig. 3.10), $z \simeq 1.0$, while smaller values of N (non-shaded region) we have a considerably smaller $z \simeq 0.75$. The precise

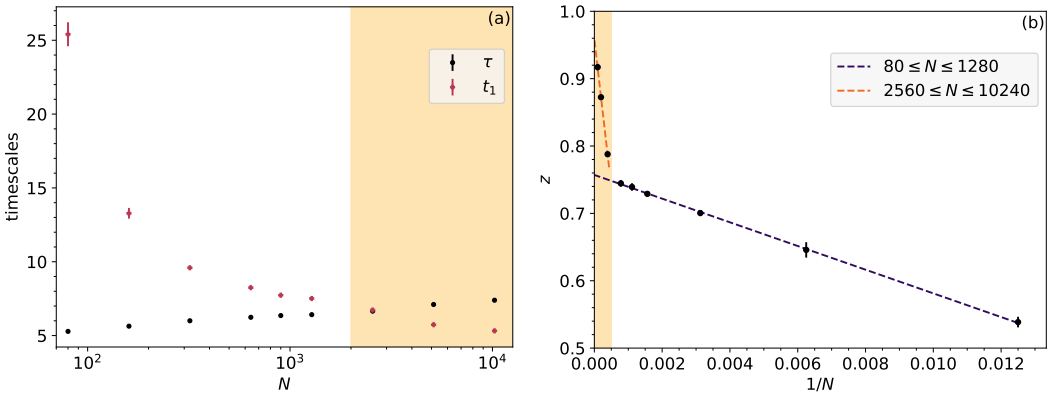

FIGURE 3.10: (a) Typical timescales of the exponential (τ) and power-law (t_1) decay of the correlation function at the critical point $\varepsilon = 2$, found from the fits of the correlation function $G(t)$ (Fig. 3.8b). We see that the crossover to power-law decay takes place at $N \gtrsim 2000$ (shaded region), so much larger system sizes are needed to extract a clean dynamical critical exponent z. (b) Corresponding values of the dynamical critical exponent z. The errorbars represent the fit errors, that surely underestimate the strong fluctuations at finite N (see also Refs. [282, 283]). Therefore, we can only present two possible fits, one excluding the smallest N points and one the largest, and give a value of z respectively $z \simeq 1.0$ and $z \simeq 0.75$. Since the smallest N points have $t_1 > \tau$ (as seen in panel (a)), which is a clear pre-asymptotic behavior, we would tend to discard them in favour of the 3 largest N points in the dataset. This figure is taken from Ref. [3].

values of the critical exponents clearly requires further numerical investigations. We end by noticing that the form of $G(t)$ at criticality can be related to the distribution $\rho(\lambda)$ of the eigenvalues of the Laplacian at $\varepsilon = 2$, which must be of the form $\rho(\lambda) \sim \lambda^{z-1}$ near $\lambda = 0$.

3.8 Conclusions and outlook

We studied the mechanism for weak ergodicity breaking at high energy densities in a fully connected DNLSE model. We showed that, whatever the interactions between sites (kinetic energy term) are, they can be neglected for $\varepsilon \geq \varepsilon_s = 1.481...$ that corresponds to a finite temperature $T_s = 2g = 2$. We are left therefore with a purely potential model, whose physical properties reflect the geometrical properties of the potential energy surface and therefore are subject to a localization transition at infinite temperature (corresponding to $\varepsilon_c = v = 2$). We proved that the microcanonical, potential energy surface is connected for all extensive energies (energy densities of $O(1)$), thus showing that the ergodicity breaking must be of the *weak* form. This is quite remarkable, given that the model is fully connected: for mean-field spin-glass models, in fact, it was recently argued that the ergodicity breaking must be strong [294].

Then, we showed that the localization transition is due to a phase transition in the order parameter $\gamma = -(\log \lambda_1)/N$, where λ_1 is the smallest non-zero eigenvalue of $-\Delta$, the Laplacian on the (curved) equipotential surface. For $\varepsilon < 2$ we have $\gamma = 0$ and for $\varepsilon > 2$ we have $\gamma \sim (\varepsilon - 2)^\eta$ with η around 2. This puts on firmer grounds the connection between the works on thermodynamics (like Refs. [282, 283]) and those on the dynamics (like Refs. [264, 269, 270]). The approximation in which one can

neglect the kinetic energy is exact on the fully connected model, and one can imagine that it is a good approximation for a finite-dimensional lattice, therefore making our results qualitatively compelling for the experimental observations [29, 275] and the numerical works [262]. Making a quantitative connection, and computing a possible $1/\kappa$ series of corrections to our results is left for future work, as is the validation of our predictions using a genuine mean-field Hamiltonian dynamics.

The transition taking place at $\varepsilon_c = 2$ makes the equilibration time τ change from $O(1)$ to exponentially large in N, $\tau \sim e^{\gamma N}$: the phenomenology is very similar to that observed in the MBL-like phase of Josephson junction arrays [276, 277], and of quantum glasses as well [239, 241]. However, the nature of the transition in the DNLSE seems to be of entropic origin: the volume of the region of phase space around any given localized configuration is exponentially larger than the volume connecting two localized configurations, therefore making the passage from one localized configuration to another exponentially unlikely. Quantum mechanical localization, in contrast, is a consequence of interference and it vanishes when $\hbar \to 0$. It is also tempting to notice that the lowest eigenvalue of $-\Delta$ becoming exponentially small in a large parameter is precisely what happens in localized quantum-mechanical Schrödinger equations. However, given these elements, we cannot argue more than a similarity at a formal level.

We also refrain from speculating on the effect of turning on $\hbar$. Previous works have shown that, for $\hbar \neq 0$ and at least in a 1d geometry, transport is strongly suppressed as $T \to \infty$ [272] and non-Gibbs state exist for $\varepsilon \geq 2$ as well [281]. In a more general setting, on the one hand one would expect that a charge localized on a site could tunnel quantum-mechanically towards a neighboring site; on the other hand the effects of interference should be taken into account [276, 277]. Sorting out the leading effects of quantization upon the system (3.1), at least at the semiclassical level, is left out for future work.

To conclude, it is worth stressing that topology was already used in some studies related to equilibration or phase transitions. For instance, the slow dynamics of p-spin models was related to the structure of saddles of the free energy landscape [290, 291, 295–297] (please notice that here, instead, all the computations were performed in the microcanonical ensemble). Other authors argued that generically phase transitions are accompanied by a change in topology in the phase space (see e.g. Refs. [298–300] and other references therein). While leaving aside for now the possible connections, it is immediate to understand that the topological nature of our results implies that they are quite general, since the same phenomenology holds for any convex potential $V(q)$. This conclusion sheds light also on the numerical evidence for localization in similar models [284, 285], which so far was left unaddressed by any quantitative means.

4 Spatiotemporal heterogeneity of entanglement in many-body localized systems

In this Chapter, I present some results concerning how entanglement spreading is heterogeneous, both in space and in time, deep in the MBL phase. In Sec. 4.1 I describe the models under study, while Sec. 4.2 I introduce the quantities and methods used for the investigation. In Sec. 4.3 I show the results for one-site observables, and in Sec. 4.4 the results for the correlation functions. Finally, in Sec. 4.5 I draw the conclusions and discuss future research perspectives. The Chapter is based on the publication [4].

With this Chapter and the following, we move on to discuss some instances of the interplay between the physics of glasses, and of many-body localization (MBL). As motivated in the Introduction, MBL is an interesting phenomenon, as it realizes a non-thermal, stable quantum phase of matter. Despite the tremendous effort of the last 15 years or so, many of its features still remain mysterious: for instance, neither consensus has been reached on what is the universality class of the transition [112–114, 121–128], or on what is the order of magnitude for the critical disorder strength [133–135], or even on whether MBL is a phase or just a transient regime in finite-size systems, or finite-time experiments [115–120]. What is pretty clear instead from perturbation theory [46, 107], non-perturbative computations [108, 109] and a body of numerical works [301–307] is instead the nature of the localized phase (or regime), which is characterized by the presence of local integrals of motion (LIOM, or l-bits), making MBL a particular instance of integrability.

In this Chapter—as well as in this whole thesis—we do not want to enter the diatribe on all the open issues about MBL. Rather, we want to present some results that have a validity *regardless* of what is the nature of the transition, or of what happens in the thermodynamic limit at infinite times, somewhat on the lines of Ref. [308]. That is to say, the results presented here are valid even if the localization lasts only for a finite, yet long time.

What we did was to investigate the MBL phase with the idea that interactions and disorder, when put together, can lead to heterogeneity that bears clear signatures of the many-body nature of the dynamics of the system, and can help characterizing it. It is well known, in fact, that *classical* glassy dynamics—both in structural and spin glasses—can be characterized by the presence of so-called *dynamical heterogeneity* [53, 56, 83, 84, 309–311]. One speaks about dynamical heterogeneity when each local degree of freedom presents an autocorrelation function that decays in time with a different functional form, thus strong spatiotemporal fluctuations are present in the system.

It was already argued that dynamical heterogeneity in classical glass models has

a quantum counterpart and, at ultra-low temperatures, can be induced by quantum fluctuations [51, 153, 243, 312]. However, previous studies have investigated quantum glass systems modeled on a classical counterpart. Here we adopt a different approach: we borrow the theoretical tools of classical glass theory in order to explore the quantum MBL phase, and we study the properties of entanglement. In this perspective, the observed similarities in the heterogeneous behavior of local correlations, which are quantum in the MBL case and classical for glasses, appear unexpected.

Another reason for interest in the phenomenon treated in this Chapter is the physics of entanglement itself. While entanglement can be completely characterized for two qubits [36, 313, 314], this becomes more challenging in the many-body context, which presents a multitude of facets [315–318]. The numerous studies on the entanglement growth in the MBL phase [48, 129, 319, 320] are mainly focused on global properties, employing measures such as the entanglement entropy, purity, quantum Fisher (or mutual) information, or total correlations [137, 321–324]. In this Chapter, we go beyond those approaches, focusing on the local properties of entanglement, therefore aiming at characterizing its spreading in a more detailed way. The focus is on the combined temporal and spatial behavior of the local entanglement as measured by the concurrence, which has been used to characterize entanglement in MBL before (but only at the global level) [325], and which can be measured experimentally [326, 327].

The starting point is the finding that the dynamics of the concurrence among couples of spins or l-bits is highly heterogeneous, with a wide range of different relaxation times. To quantify this observation, the distribution of the relaxation times τ_i of the concurrence is investigated within the l-bit model, and its properties are described in a wide range of parameters and initial-state energies. The main findings are the following:

1. The strong fluctuations of entanglement at the local level manifest as a power-law-tailed probability distribution for τ_i which, in turn, is at the origin of the known power-law decay of the *average* concurrence [325].

2. The width of such distribution increases as disorder increases or energy decreases.

3. The local relaxation times τ_i are spatially correlated, with the correlations growing as disorder increases or energy decreases: this is a counter-intuitive result, since, naively, one might expect the correlations to increase when approaching the delocalization transition by *lowering* the disorder.

It is worth stressing that this latter result suggests that the associated entanglement correlation length represents a previously unrecognized length scale in the MBL phase.

Finally, but not less importantly, entanglement heterogeneity persists also outside the MBL phase. Here, we choose to focus on the deep MBL phase only because, thanks to the l-bit model, the numerics can reach larger system sizes, and one can also get some analytical insight. The detailed study of entanglement heterogeneity out of the MBL phase, and across the MBL-thermal transition, is deferred to future studies.

4.1 Description of the protocol

The aim of this Chapter is to study the general properties of the spatiotemporal entanglement dynamics of MBL systems. For this purpose, let us use an effective description in terms of LIOMs, which allows to access the nonequilibrium real-time dynamics of MBL systems for long times and large system sizes. Deep in the MBL phase, Hamiltonians of short-range interacting, quantum, spin-1/2 degrees of freedom can be diagonalized through a quasi-local unitary transformation [108, 109, 328], yielding a representation of the model in so-called l-bit form:

$$H_{\text{l-bit}} = \sum_{i=1}^{L} h_i \sigma_i^z + \sum_{i,j=1}^{L} J_{ij} \sigma_i^z \sigma_j^z + \dots \tag{4.1}$$

where $\{\sigma_i^x, \sigma_i^y, \sigma_i^z\}$ are the localized spin-1/2 operators associated with the LIOMs. We neglect further terms in the Hamiltonian which comprise n-body interactions with $n \geq 3$, which is a controlled approximation for weakly interacting spins in the original microscopic model. From analytical results [105, 107–109, 328], it is known that the interactions J_{ij} are exponentially suppressed with the distance r_{ij} between localization centers. To achieve a model-independent effective description, let us parameterize the l-bit model as follows. Assume that the h_i are independent identically distributed random fields, with a uniform distribution over $[-h, h]$, and that the J_{ij} are uncorrelated Gaussian variables of zero average and standard deviation $J_0 e^{-r_{ij}/\kappa}$. For numerical purposes, set also $h = J_0 = 1$.

The particular advantage of the l-bit model (4.1) is that it allows to perform analytical estimates of few-body observables, and to efficiently compute them numerically, reaching system sizes up to $L = 140$ spins for very long times. To give an example, Eq. (B.2) in App. B.4 shows how to compute a two-site correlation function in $O(N)$ steps; cf. Refs. [110, 111, 319, 325] for other examples.

It is worth stressing that the l-bits become closer and closer to the physical spins as the disorder increases, ultimately coinciding asymptotically at infinite disorder [307, 329]. Thus, at small values of κ (i.e. large disorder strength), one can safely consider the l-bits as uniformly spaced on a chain, and compute the distances among them as $r_{ij} = |i - j|$, $i, j = 1, 2, \dots, L$. The numerical results presented in the following are obtained exactly in this strongly localized regime, deep in the MBL phase. It is important to note that the effective model allows to tune: i) the interaction decay length κ (equivalent to varying the disorder strength); and ii), the initial condition, i.e. the energy density at which we probe the system's properties. Concerning the latter parameter, it is reasonable to choose as initial state of the dynamics a product state in the *effective* spin basis:

$$|\psi_0\rangle = \bigotimes_{i=1}^{L} \left(A_i |\Uparrow\rangle_i + B_i |\Downarrow\rangle_i \right), \tag{4.2}$$

where $|\Uparrow\rangle_i, |\Downarrow\rangle_i$ are the eigenstates of σ_i^z, and $|A_i|^2 + |B_i|^2 = 1$. The reasons for this choice are multiple. First, in this way the initial state is factorized, and the evolution of entanglement can be followed more easily, as it starts from zero. Second, employing Eq. (4.2), the system is initially prepared in a superposition of eigenstates, so the dynamics is non-trivial. Third, Eq. (4.2) allows to tune the coefficients A_i and B_i such that the initial-state energy expectation value $E := \langle \psi_0 | H_{\text{l-bit}} | \psi_0 \rangle$ can be varied at will. This tuning can be achieved using a classical simulated annealing

algorithm (see App. B.1 for details), and allows to explore different regions of the energy spectrum. Let us measure E in units of the standard deviations of h_i and $\sum_j J_{ij}$, defining the dimensionless energy density

$$\varepsilon := \frac{E}{N}\left[\frac{h^2}{3} + \frac{2J_0^2}{e^{2/\kappa}-1}\right]^{-1/2}. \tag{4.3}$$

Notice that $\varepsilon = 0$ corresponds to the center of the spectrum, while $\varepsilon \approx -1$ to the ground state (more details in App. B.1). Let us remark that the localization properties of MBL systems depend on the energy of the considered state and are stronger near the edges of the spectrum [131, 330].

For small system sizes, the results of the effective model can be compared with a full microscopic calculation for the spin-1/2 XXZ chain with random fields:

$$H_{\mathrm{XXZ}} = \sum_{i=1}^{L-1}\left[\frac{J}{2}(S_i^+ S_{i+1}^- + \mathrm{h.c.}) + V S_i^z S_{i+1}^z\right] + \sum_{i=1}^{L}\Delta_i S_i^z, \tag{4.4}$$

where $J = V = 1$ (unless otherwise stated) and Δ_i are random variables uniformly distributed over $[-\frac{W}{2}, \frac{W}{2}]$. For $W_c \simeq 7 \pm 2$, this model exhibits an MBL transition [49–51, 331] (see Refs. [307, 329] for the relation between W and the effective model parameters h, κ and J_0). When employing (4.4), we probe the centre of the energy spectrum initializing the system in a Néel state $|\psi_0\rangle = |\uparrow\downarrow\uparrow\downarrow\ldots\rangle$ where $\uparrow,\downarrow$ indicates the physical spin basis, and average the results over different disorder realizations. Notice that the XXZ model can be employed to explore the presence of entanglement heterogeneity also in the thermal phase; however, due to the smallness of the accessible system sizes, we will not investigate thoroughly the thermal phase in the present Chapter. We defer such investigation to future studies.

4.2 Methods of analysis

For the purpose of exploring the spatiotemporal heterogeneity of entanglement in MBL systems, we concentrate on the two-site concurrence, which quantifies the pairwise entanglement between two qubits [313, 314, 317, 325]. For two spins-1/2 located at lattice sites i and j, the concurrence is defined as [314, 317]

$$C_{i,j} := \max\{0,\, \lambda_1 - \lambda_2 - \lambda_3 - \lambda_4\}. \tag{4.5}$$

λ_a^2 are the eigenvalues of the matrix $R_{ij} = \rho_{ij}(\sigma_y \otimes \sigma_y)\rho_{ij}^*(\sigma_y \otimes \sigma_y)$ sorted in descending order, where ρ_{ij} is the two-site reduced density matrix, and the complex conjugation is done in the standard computational basis.

While the general formula (4.5) must be applied to the l-bit model, for the microscopic XXZ Hamiltonian the concurrence can be computed more easily. Since the dynamics conserves the z component of the total magnetic field, S^z_{tot}, and we initialize the system in the Néel state, having $S^z_{\mathrm{tot}} = 0$, Eq. (4.5) can be simplified as [332]

$$C_{i,j} = 2\max\left[0, \left|\langle S_i^+ S_j^-\rangle - \sqrt{P_{++}P_{--}}\right|\right] \tag{4.6}$$

with

$$P_{\pm\pm} \equiv \frac{1}{4} \pm \frac{1}{2}\left(\langle S_i^z\rangle + \langle S_j^z\rangle\right) + \langle S_i^z S_j^z\rangle. \tag{4.7}$$

and $\langle\bullet\rangle := \langle\psi(t)|\bullet|\psi(t)\rangle$, where $\psi(t)$ is the state of the system at time t.

It has been shown that in MBL systems the concurrence averaged over all couples i, j decays in time as a power law [325], while it decays exponentially fast in ergodic systems. Our key goal is to establish a more detailed spatiotemporal analysis of the concurrence beyond its averaged value. Specifically, we wish to investigate, in MBL systems, the relationship between the late-time, power-law behavior of the average concurrence and the relaxation of the concurrence at the local level. Because of the presence of quenched disorder, we expect to observe that the relaxation of the two-site entanglement is *heterogeneous*, i.e. it has a different functional form and characteristic time scale in distinct spatial regions. We aim at verifying and quantifying such entanglement heterogeneity. Similar questions have been already explored in the framework of classical glasses; in this Chapter, we will adapt some tools and ideas developed in that context to the case of quantum localized systems.

In this perspective, we define a local *on-site* concurrence as

$$C_i(t) := \sum_j C_{i,j}(t)\,, \tag{4.8}$$

quantifying the total amount of two-qubit entanglement of i with all the other lattice sites. In the case of the XXZ model, we find that $C_{i,j} \simeq 0$ for $|i-j| > 1$, so that we can trade the sum in Eq. (4.8) with the nearest-neighbour term: $C_i(t) := C_{i,i+1}(t)$ (see also [325]).

For large systems and for a single disorder realization, we find that the local concurrence defined in Eq. (4.8) typically decays to zero on a certain time scale, and then definitely remains so (see Fig. 4.1). This motivates us to define the local relaxation time as

$$\tau_i := t_0\, e^{\langle \log(t/t_0)\rangle_C} := t_0 \exp \frac{\int_0^{t_{\rm fin}} \log(t/t_0)\, C_i(t) dt}{\int_0^{t_{\rm fin}} C_i(t) dt}, \tag{4.9}$$

where $t_0 = J_0^{-1}$. Notice that $C_i \geq 0$, so the averages above are well-defined and independent of t_0 (in the thermodynamic limit). The definition (4.9) employs the logarithm $\log(t/t_0)$; this ensures that τ_i is a good estimator of the *typical* time scale of the relaxation time of the concurrence even if $C_i(t)$ decays very slowly[1]. Notice that typically, for *finite* systems, $C_i(\infty) \simeq O(2^{-L})$ (see App. C.7): thus, the function $C_i(t)$ might be interpreted as a probability distribution over $\mathbb{R}$ only in the thermodynamic limit.

Our aim is to estimate the distribution function of τ_i exactly in the thermodynamic limit. Such limit can be approached by fixing the maximum simulation time of the dynamics $t_{\rm fin}$ and increasing L, until convergence is reached. We find from our numerics that this typically happens for $L \gtrsim 30$, which is achievable in the l-bit but not for microscopic Hamiltonians by means of exact diagonalization. Indeed, for the microscopic XXZ Hamiltonian in the MBL phase and for finite L, one finds a spurious peak in the distribution of τ_i due to those realizations of $C_i(t)$ which are still nonzero at the final evolution time $t_{\rm fin}$. This is precisely due to the fact that, for small L and whatever the choice of $t_{\rm fin}$, there will be always a finite number of such nonvanishing realizations. Unfortunately, for the XXZ model, we cannot consider

[1] We verified that, upon changing the definition of τ_i, e.g. with

$$\tau_i := \langle t \rangle_C = \frac{\int_0^{t_{\rm fin}} t\, C_i(t) dt}{\int_0^{t_{\rm fin}} C_i(t) dt} \tag{4.10}$$

or $\tau_i := \max\{t | C_i(t) > 0\}$, our findings do not qualitatively change.

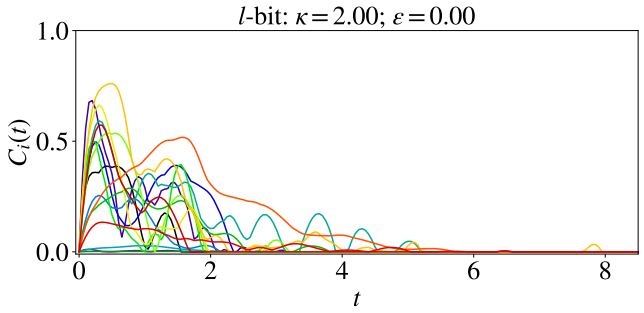

FIGURE 4.1: Single instance for the on-site concurrences $C_i(t)$, defined in Eq. (4.8). Heterogeneity in the entanglement spreading can be clearly seen: the curves $C_i(t)$ are described by different functional forms, and decay to zero on different time scales. The chain length is of $L = 80$ sites. The concurrence of one site every three is plotted to enhance readability. This figure is taken from Ref. [4].

system sizes larger than $L = 20$. This represents a crucial argument for the use of the effective l-bit model.

Let us emphasize again that the average concurrence in the MBL phase decays as a power law, while the on-site concurrence vanishes after a finite time, as depicted in Fig. 4.1. Thus, the power-law decay of the average is nothing but a consequence of the heterogeneous behavior at the local level. This can be also captured by a simple analytical model, as sketched in the following. Let us schematize the on-site concurrence as a step function $f_\tau(t) = \theta(\tau - t)$, where τ is a random variable drawn from a power-law-tailed distribution. Assuming $P(\tau) = \mathcal{N}\theta(\tau - \tau_0)\tau^{-\gamma}$, with $\gamma > 1$ and $\mathcal{N}$ a normalization constant, one gets a disorder average $\langle f(t)\rangle = (\tau_0/t)^{\gamma-1}$ that decays as a power law. This shows that, when $f_\tau(t)$ has a simple form and vanishes after a finite time in each disorder realization, and when the relaxation times have a long-tailed power-law distribution, the average $\langle f(t)\rangle$ decays as a power law. We expect this argument to be at the origin of the power-law decay of the average concurrence in MBL systems.

While the τ_i's provide temporal information of the entanglement dynamics, we are further interested in the spatial component. For that purpose we quantify the spatial correlations of the local relaxation time via (see also Ref. [309])

$$G_\tau(r) := \overline{\left[\frac{\langle \tau_i \tau_j\rangle_{\text{is}} - \langle \tau_i\rangle_{\text{is}}\langle \tau_j\rangle_{\text{is}}}{\langle \tau_i^2\rangle_{\text{is}} - \langle \tau_i\rangle_{\text{is}}^2}\right]_{|i-j|=r}}, \tag{4.11}$$

where $\langle\bullet\rangle_{\text{is}}$ denotes the average over different initial states, $[\bullet]_{|i-j|=r}$ the average over all sites i, j separated by a distance r, and $\overline{\bullet}$ the average over different disorder realizations[2]. In App. B.5, we show that $G_\tau(r)$ as defined in Eq. (4.11) is very robust to finite-size effects and disorder fluctuations: it is a self-averaging quantity. From our numerical simulations, we find that $G_\tau(r)$ experiences in general a stretched-exponential decay as a function of r. This allows to define a length scale η_τ by performing a fit of the form $\log G_\tau(r) \sim a + (r/\eta_\tau)^b$ for some suitable a and b. The length η_τ quantifies the distance over which the local entanglement relaxation is spatially correlated, i.e. it gives the size of the typical clusters of fast or slow entangling spins. In App. B.5, we show also that η_τ is almost independent of the system size for $L \geq 40$.

[2]Notice that the averages have to be taken in the proper order: first $\langle\bullet\rangle_{\text{is}}$, second $[\bullet]_{|i-j|=r}$, finally $\overline{\bullet}$.

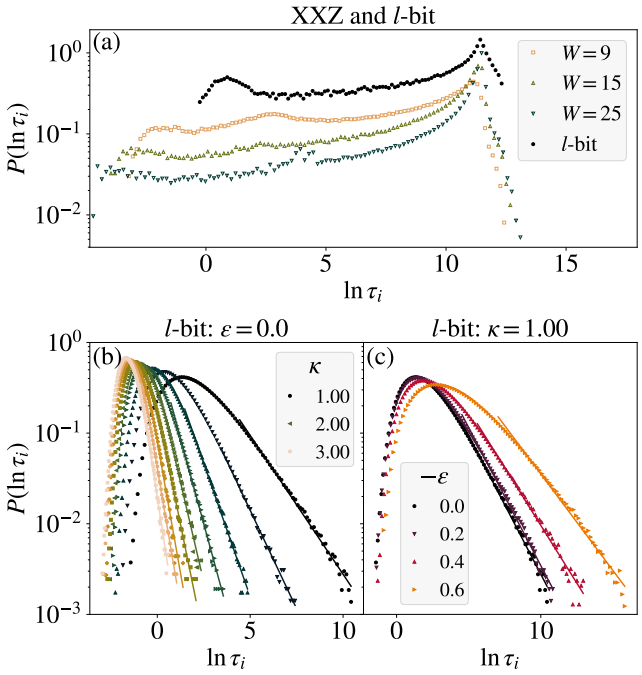

FIGURE 4.2: Probability distribution functions of $\log(\tau_i)$. (a) Results for the XXZ model (4.4), for $L = 16$, $t_{\rm fin} = 10^3$, and various W. We performed the XXZ unitary dynamics using the Krylov technique [333], with dimension of the $M = 40$, and at least 8000 disorder realizations. For comparison, the l-bit model at $L = 10$, $\kappa = 1$, $\varepsilon = 0$ is shown as well (300 disorder realizations). J_0 has been fixed to make the pdf's maximum coincide with the XXZ ones. (b)-(c) Results for the l-bit model (4.1) at $L = 80$, for various κ (in steps of $\Delta\kappa = 0.25$) and ε, averaged over at least 4000 disorder realizations and 20 initial states for each of them. As κ decreases, i.e. disorder increases, the distributions broaden; the same when ε decreases, in analogy with classical amorphous materials approaching the glass transition. We performed power-law fits on the tails of the pdf's, obtaining the exponents β whose behavior is shown in Fig. 4.3b. This figure is taken from Ref. [4].

4.3 Distribution of the relaxation times

We show in Fig. 4.2 the probability distribution function (pdf) of $\log \tau_i$, obtained within both the XXZ and the l-bit model. We see that within the XXZ model (Fig. 4.2a) the pdf's show a peak at large relaxation times, corresponding to the final simulation time of the dynamics $t_{\rm fin}$. In App. B.2 we argue that this feature is due to the (typical) asymptotic value $C_i(\infty) \simeq O(2^{-L})$; see also the discussion below Eq. (4.9). If the time spent in such asymptotic region is too large, the relaxation time is heavily influenced by the final time of the dynamics. This is a finite-size effect, and it does disappear upon considering larger system sizes, as we show for the l-bit model in App. B.2.2 (larger system sizes for the XXZ model cannot be presently considered).

The pdf's obtained considering the l-bit model for $L = 80$ and for different values of κ, and ε are shown in Figs. 4.2b–4.2bc. Thanks to the large system size, these plots do not present any peak at large times, and clearly show that the the pdf of $\log \tau_i$ has a power-law tail; thus the distribution of τ_i has a power-law tail as well. We see that the pdf's become broader as the disorder is increased (both in the XXZ and the l-bit model), or the energy is lowered (in the l-bit model).

We define the typical value of τ_i as $\mathrm{typ}[\tau_i] := t_0 \exp\langle \log(\tau_i/t_0)\rangle_{\tau_i}$, where $\langle \bullet \rangle_{\tau_i}$ is the average over the pdf of τ_i. In Fig. 4.3a, we show the behavior of $\mathrm{typ}[\tau_i]$ as a

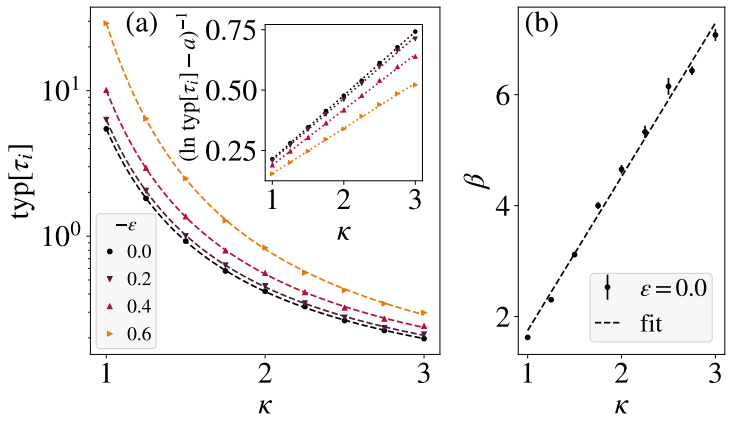

FIGURE 4.3: (a) The typical value of τ_i, defined in the main text, is shown as a function of κ for different ε (dots). The dashed lines are fits with the function $\exp[a + (b\kappa + c)^{-1}]$. From a, we performed the linear fits depicted in the inset: $\log(\text{typ}[\tau_i] - a)^{-1}$ as a function of κ is found to be linear, as expected (see App. B.4). (b) Slope β as a function of κ, obtained from the linear fits of the tails of $\log P(\log \tau_i)$ in Fig. 4.2b. $\beta(\kappa)$ is consistent with a linear behavior; with a linear fit we obtain: $\beta = 2.8(5)\kappa - 1.(2)$. This figure is taken from Ref. [4].

function of the parameters κ and ε. Following usual arguments for the l-bit model [110, 111, 319], in App. B.4 we derive the rough estimate

$$\log(\text{typ}[\tau_i]/t_0) \approx (2\kappa \log 2 - 1)^{-1}. \tag{4.12}$$

Fig. 4.3a depicts the fits of typ$[\tau_i]$ with this functional relation with respect to κ, showing that our numerical results are in reasonable agreement with the functional form of the prediction, even if the coefficients of the fit do not match those in Eq. (4.12).

We performed fits $\log P(\log \tau_i) \sim -\beta(\log \tau_i)$, shown in Fig. 4.2b, and from there extracted the power-law exponents β, that we report in Fig. 4.3b. We see that β has a roughly linear dependence on κ, a property which will help us interpreting the behavior of the correlation function in the next Section.

Before moving to the study of the correlation function, let us emphasize that dynamical heterogeneity is not restricted to the MBL phase. In App. B.3, we present some qualitative results also in the ergodic regime. Further investigations in this direction promise to be fruitful; however, they go beyond the scope of this Chapter and will be discussed in forthcoming publications.

4.4 Spatial correlations of the relaxation times

Fig. 4.4 shows the spatial correlations between τ_i's. Due to the strong finite-size effects for the XXZ model, we restrict ourselves to the l-bit model. In Fig. 4.4a we report the spatial distribution of the τ_i's for a disorder realization. As κ decreases, i.e. the disorder increases, the relaxation times of the local entanglement become spatially correlated over longer distances. The correlation function $G_\tau(r)$, defined in Eq. (4.11), is shown in Figs. 4.4b–4.4c: $G_\tau(r)$ decays more slowly upon decreasing κ and ε, confirming the pattern observed in Fig. 4.4a. The same result is also supported by the (qualitative) behavior of the dynamical correlation length η_τ as a function of κ.

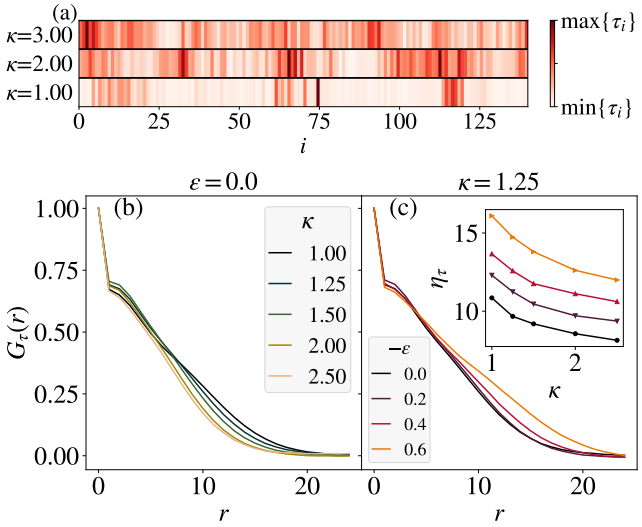

FIGURE 4.4: Spatial correlation of the τ_i's in the l-bit model. (a) Snapshot of the spatial distribution of the τ_i's at three different values of κ (in one realization of disorder), showing the emergence of dynamically correlated clusters as the disorder increases. (b)–(c) The correlation function $G_\tau(r)$, defined in Eq. (4.11), for $L = 140$, and various κ and ε. We see that the spatial correlation among τ_i's increases for decreasing κ and ε. Data averaged over at least 1000 disorder realizations, and 20 initial states each. (Inset of (c)) The dynamical correlation length η_τ, from stretched exponential fits of $G_\tau(r)$, as a function of κ. η_τ decreases as κ increases: for larger disorder, larger clusters of dynamically correlated spins emerge. This figure is taken from Ref. [4].

We see in the inset of Fig. 4.4c that η_τ decreases when κ increases, i.e. when disorder decreases.

The implications are twofold. Recall that the local entanglement spreading slows down when κ decreases (i.e. the disorder increases) or the energy decreases (Fig. 4.2). Therefore, first, increasingly larger clusters of spins emerge, in which the entanglement relaxation is correlated (Fig. 4.4). Second, since the distribution of relaxation times becomes broader as disorder increases, more clusters are likely to assume an extreme value of the relaxation time in the slow, as well as in the fast tail.

These findings might seem surprising in the quantum case, as a more localized structure might be expected when disorder increases. Remarkably, a similar growth of dynamical heterogeneous clusters takes place in classical amorphous materials and spin glasses [309], suggesting a connection between the phenomenology close to the glass transition and to the MBL one.

We can provide an analytical argument to justify why the correlation length should increase for increasing disorder as follows. An MBL system develops increasing correlations as the time goes on, as witnessed by the entanglement entropy [48, 129, 319]. It is well established that, for finite systems, there is a time t_c at which the system becomes fully correlated: therefore, one can roughly assume that relaxation times $\tau_i \geq t_c$ are more spatially correlated with each other than the times $\tau_i < t_c$. If, decreasing κ, the fraction of times larger than t_c increases, then one can argue that the relaxation times become more correlated, in agreement with the increasing relaxation-time correlation length η_τ that we observe.

Let us substantiate the above argument. First, we estimate t_c by quantifying the degree of correlation in the system via the half-system entanglement entropy: it increases in time as $S(t) \sim \kappa \log(t)$ [48, 129, 319] and, for a finite system of size L, it

saturates to a value of order L at a time $t_c \simeq \exp(L/\kappa)$. For times $\tau_i \geq t_c$, the system has reached its maximum correlation, as we have stated before. Now, let us evaluate the fraction $f_>$ of relaxation times $\tau_i > t_c$ as

$$f_> := \int_{\log t_c}^{\infty} P(\log \tau_i) d(\log \tau_i), \tag{4.13}$$

i.e. $f_>$ quantifies the weight of the relaxation-time distribution $P(\log \tau_i)$ corresponding to relaxation times τ_i larger than t_c. Finally, we can show that $f_>$ increases with decreasing κ, meaning that the relaxation times become more correlated for increasing disorder. This simply follows from the results of Sec. 4.3, for which $\log P(\log \tau_i) \simeq -\beta \log \tau_i$, with exponent $\beta = A\kappa - B$ ($A \simeq 2.8$ and $B \simeq 1$, see Fig. 4.3b). Thus, Eq. (4.13) reads

$$f_> = \int_{L/\kappa}^{\infty} \frac{1}{(\log \tau_i)^{A\kappa - B}} d(\log \tau_i) \sim \left(\frac{L}{\kappa}\right)^{1 - A\kappa + B} \tag{4.14}$$

and $f_>$ increases with decreasing κ. This means that the weight of the relaxation-time distribution associated with a maximally correlated system increases when increasing the disorder. This conclusion agrees with the behavior found for the relaxation-time correlation length, η_τ. Finally, let us notice that the limit $\kappa \to 0$ is singular (since $t_c \to \infty$), and the argument above ceases to be valid.

4.5 Conclusions and outlook

In this Chapter, we studied the spatiotemporal spreading of entanglement in MBL systems by monitoring the on-site concurrence. We showed that in the MBL phase the on-site concurrence behaves heterogeneously, with different functional forms and relaxation times for each site of the lattice. Using the tools developed for dynamical heterogeneity in classical glasses, we quantified such heterogeneous behavior of entanglement by investigating the on-site concurrence relaxation times τ_i, which display a non-trivial spatiotemporal structure.

First, we observed that the local relaxation times τ_i increase upon increasing the disorder, or upon lowering the energy of the initial states. Specifically, their distribution broadens significantly, as the exponent β, dictating the decay $P(\log \tau_i) \sim (\log \tau_i)^{-\beta}$ increases as $\kappa \to 0$. This can be understood in terms of the slowing down of the dynamics, due to the stronger disorder or the vicinity to the edges of the spectrum.

In addition, taking into account the spatial correlations among the τ_i's, we observed that, as disorder increases or energy decreases, increasingly larger dynamically correlated clusters arise. Within a cluster, the relaxation times are similar among sites and, due to the broadness of the τ_i distribution, are likely to assume an extremely small or large value. We defined a correlation length of the relaxation times, η_τ, which quantifies the typical extension of the correlated clusters. It represents a new length scale characterizing the MBL phase.

The emergence of increasingly large clusters of correlated spins is somewhat surprising since one might naively expect the clusters to grow in size upon decreasing the disorder strength, i.e. when the delocalization transition is approached. A possible explanation lies in the fact that the concurrence quantifies only the entanglement shared by two qubits: therefore, at lower disorder, it may miss the tri-partite, or generally multi-partite, entanglement growth.

Our analysis was mainly focused on the deep, many-body localized phase, where the l-bits are close to the physical spins. Similar properties for the entanglement heterogeneity are expected in all systems that present a long, localized transient before they reach a thermal state. Such systems include MBL systems coupled to a bath [51, 334–340], MBL systems in $d \geq 2$ [113, 308, 323, 341–346], and two-level systems in structural glasses (see Chap. 5). In addition, it is worth emphasizing that entanglement heterogeneity should be present also in the ergodic phase; however, we leave its characterization to future studies.

Our findings open up future research directions towards the characterization of spatiotemporal entanglement properties. A next crucial step is to explore the spatial correlation of local relaxation times in observables less affected by finite-size effects and disorder fluctuations. It would be desirable to define suitable *macroscopic* observables, in the way the four-point susceptibility $\chi_4(t)$ is for classical glasses [53, 56, 83, 84]. In the MBL case, such observables need to detect only local entanglement fluctuations and be experimentally measurable (if possible). A further interesting extension of our contribution could be to consider entanglement heterogeneity for two subsystems consisting of more than one spin, which could provide additional information on the multipartite spatiotemporal structure of quantum entanglement. Finally, we note that the observed entanglement correlated clusters, which grow in size for increasing disorder strength, might be linked to the *localized bubbles* which have been the subject of numerous recent studies [112, 114]. Exploring such connections promises to be an interesting research direction for future studies.

5 Signatures of many-body localization in the dynamics of two-level systems in glasses

In this Chapter, I show how tools developed in the context of many-body localization can explain the slowness of thermalization for two-level systems in glasses. I start by introducing the model in Sec. 5.1, and then in Sec. 5.2 I show how a non-perturbative transformation can be used to put the model in a form amenable of analytical treatment. Then, in Sec. 5.3 I show how to derive from first principles a Gorini-Kossakowski-Sudarshan-Lindblad equation for the relaxational dynamics of the TLS, which predicts a very long, localized transient for the TLS. In Sec. 5.4 I show that the presence of such transient is confirmed by numerical simulations, and what are its features in terms of entanglement spreading. Finally, I draw the conclusions in Sec. 5.5. The Chapter is based on the publications [2, 9].

While in Chapter 4 I have shown how tools developed in the context of classical glasses can be fruitfully applied to *quantum* disordered systems, and in particular many-body localization (MBL), in this one I will show how the physics of MBL may be realized to some extent in structural glasses at ultra-low temperatures.

The starting point is the celebrated two-level system (TLS) model. The story begins in 1971, when Zeller and Pohl, in a famous study [85], noticed that there was a surprising degree of universality in the low-temperature properties of many different amorphous solids. Few months later, Anderson, Halperin and Varma [86], and independently Phillips [87], introduced the TLS model as an explanation for such universality. The main point was the postulation of existence of low-temperature, localized excitations in structural glasses, basically coming from the presence of multiple equilibria for some atoms or molecules. With a minimal set of assumptions on the shape of such equilibrium configurations, the TLS model was able to reproduce the temperature dependence of the specific heat, thermal conductivity, sound attenuation, and other quantities [88, 89]. However, the model left unaddressed several questions, the most important of which probably is the super-universality of the so-called Q factor [347]: within the TLS model, such dimensionless factor acquires an astonishingly consistent value for all known glass formers, but only because of a precise cancellation of small and large, independent quantities. It was in particular Leggett [348–350] to recognize this puzzle, and since then many works have tried to put forward some explanation, usually by modifying in some respect the original TLS model [90, 91, 351]. The most promising of these explanations for the universality of Q is the presence of interactions among TLS, generated by phonons (and, if the TLS have an electric dipole, also photons). While the presence of interactions was recognized long ago [352–354], and also observed experimentally at the level of the single TLS [355, 356], the study of the consequences has proven difficult, since the model becomes many-body.

A first consequence of the presence of a phonon bath is, as just said, that TLS-TLS interactions are generated, in the form of dipole-dipole interactions $\sim 1/r^3$ [353, 354]. On the other hand, the phonon bath is also responsible for the equilibration of the TLS at the bath temperature. While the former have been subject of extensive studies [357–365], the issue of thermalization has been overlooked so far. Namely, TLS are always assumed thermal on all experimentally accessible timescales, and standard thermodynamic ensembles are applied. The purpose of this Chapter is precisely to investigate the quantum dynamics of TLS coupled to phonons, and to discuss how they reach thermal equilibrium. We idealize the system composed of TLS and phonons as an isolated system, and we analytically derive the Gorini-Kossakowski-Sudarshan-Lindblad (GKSL) master equation for the reduced density matrix of the TLS, tracing out the phonons under the assumption of weak coupling (more on this later). We find that the TLS unitary evolution (the so-called Liouvillian) is governed by a Hamiltonian with an extensive number of local conserved quantities, as the effective l-bit Hamiltonian of MBL systems; the dissipative term (the so-called Lindbladian) destroys localization and drives the system to a thermal state. We show that, considering the typical values of the TLS disorder parameters, dissipation is much slower than any other timescale of the problem, and TLS relaxation dynamics shows the fingerprint of localization for a long time window.

The work presented here shares many traits with a growing body of recent literature, that has investigated the impact of dissipation and dephasing on MBL systems [51, 334–340, 366]. The research question underlying these works concerns how the imperfect isolation from the environment enters the experimental measurements on MBL systems [136–138, 367]. Even though dissipative baths necessarily lead to delocalization, it has been found that at intermediate and long timescales the relaxation dynamics of MBL systems coupled to heat baths shows clear signatures of the localized phase, and differs from the one of ergodic systems. Such findings are in agreement with the results of the present Chapter, as will become evident in the following.

We focus in particular on the creation and spreading of entanglement as measured by the concurrence [313, 314, 317] and the entanglement entropy. The former measures the amount of entanglement between two TLS; under time evolution it grows to a maximum, and then decays and vanishes. The latter instead increases monotonically with time to reach a thermodynamic value. We simulate both the artificially isolated TLS system (i.e. dissipation is set to zero), and the open system. For the artificially isolated system, we can confidently investigate the thermodynamic limit (our numerics goes up to $N = 60$ TLS). We observe that, for long timescales, the concurrence decays as a power law $C \sim t^{-\beta_i}$, down to a plateau value which is exponentially small in the number of TLS. This slow power-law decay is the signature of localization, and contrasts with the exponentially fast decay one would observe for an ergodic system. In the open system we find that the concurrence always vanishes, never reaching the plateau observed in the unitary case. This is not surprising, since the phonon (and photon) bath to which TLS are coupled is effectively infinite, and entanglement can spread indefinitely. Moreover, for not-too-large dissipation, we find that the concurrence decays as a power law $C \sim t^{-\beta_o}$, as in the artificially isolated system, indicating that the signatures of TLS localization are observable even in this case for long time windows. The exponents $\beta_{i,o}$ in the two scenarios are of the same order of magnitude. Their comparison shows that, within the statistical errors and finite-size corrections, β increases in the presence of dissipation.

Before discussing the relaxational dynamics via the GKSL equation, however, we will digress on the issue of strong vs. weak coupling between the TLS and the

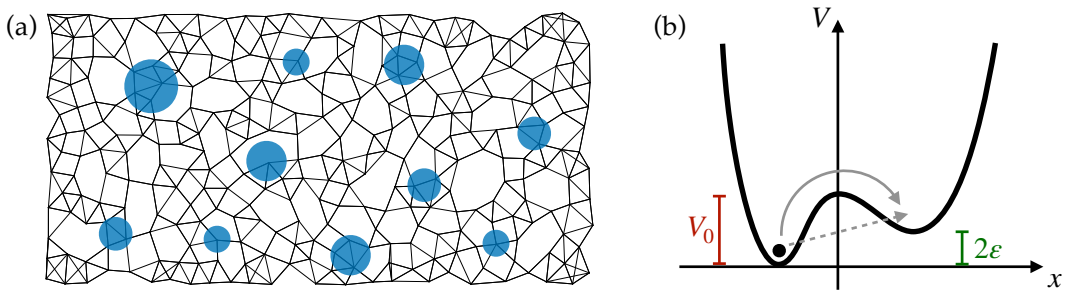

FIGURE 5.1: Sketch of the two-level system (TLS) model. (a) In the amorphous lattice structure, some groups of atoms (blue shaded circles) may have several equilibrium positions, that modify only locally the lattice. Because of thermal and quantum fluctuations, they oscillate among such positions, yielding a greater number of degrees of freedom wrt. a regular lattice. (b) For each of such groups of atoms, generalized coordinates may be introduced, that parametrize the displacement of the atoms. The simplest assumption is to take one only coordinate, with two minima at energy difference ε, separated by a potential barrier V_0. The tunnelling rate between the two minima (dashed arrow) is given by Eq. (5.5), while the activated process (full arrow) is completely negligible at ultra-low temperatures. The dynamics of the ensemble of TLS is then dominated by quantum mechanical effects.

phonons. Namely, in Sec. 5.2 we will show how a renormalization group transformation, when applied to strongly-coupled TLS, generates yet another TLS model, that is instead *weakly* coupled. The consequences are several. First, this will provide a justification of using the weak-coupling approximation when deriving the GKSL equation. Second, this will make manifest what is the nature of the localized impurities, and in what sense they undergo MBL. Third, this will pave the discussion for a more refined approach to the problem of relaxation, through a generalization of the Lindblad equation, which will be object of a future study [9].

5.1 The two-level system model

The standard Hamiltonian considered in the literature for the TLS model in presence of the phonon bath is [90, 357, 365]

$$H = H_{TLS} + H_{ph} + H_{int}. \tag{5.1}$$

The first term describes the TLS, and it is often parametrized by Pauli matrices:

$$H_{TLS} = \sum_i \left(\varepsilon_i \sigma_i^z + \Delta_i \sigma_i^x\right). \tag{5.2}$$

In the previous expression, ε_i is the asymmetry energy between the two states and Δ_i is the tunnelling strength, see also Fig. 5.1b. Both ε_i and Δ_i are random variables, whose microscopic distributions are very difficult to access experimentally. However, one can infer from experimental data their probability distributions using some tricks and assumptions, as will become clear in the following.

From *ab initio* numerical simulations [247, 248] and from simple physical reasoning [86, 88], it turns out that ε_i should be taken from a distribution with compact

support, typically[1]

$$p_\varepsilon(\varepsilon) = \begin{cases} W^{-1} & \text{if } 0 \le \varepsilon \le W \\ 0 & \text{otherwise.} \end{cases} \tag{5.3}$$

The tunneling rate Δ_i has instead a very broad distribution, usually taken to be log-uniform:

$$p_\Delta(\Delta) = \begin{cases} [\Delta \log(\Delta_{max}/\Delta_{min})]^{-1} & \text{if } \Delta_{min} \le \Delta \le \Delta_{max} \\ 0 & \text{otherwise.} \end{cases} \tag{5.4}$$

That Δ should have such a wide distribution can be understood at a semiclassical level: by WKB approximation

$$\Delta \sim \exp\left[\frac{\sqrt{2mV_0}\delta x}{\hbar}\right], \tag{5.5}$$

where m,V_0 and δx are respectively the mass, potential barrier and displacement in some generalized coordinates, parametrizing the potential well that defines a TLS (see Fig. 5.1b). Thus, even small fluctuations of m, V_0 or δx are strongly amplified at the level of Δ. In general we choose (see Table 5.1)

$$\Delta_{min} = 10^{-9}\, W, \qquad \Delta_{max} = 10^{-1}\, W. \tag{5.6}$$

It is important to stress that the *typical* value of Δ_i will be very small:

$$\Delta_{typ} = \exp \int d\Delta\, p_\Delta(\Delta) \log(\Delta) = 10^{-5}\, W. \tag{5.7}$$

The phonon Hamiltonian is

$$H_{ph} = \sum_{\mathbf{q}s} \hbar\omega_{\mathbf{q}s} b^\dagger_{\mathbf{q}s} b_{\mathbf{q}s}, \tag{5.8}$$

$\omega_{\mathbf{q}s}$ being the dispersion relation, and $b_{\mathbf{q}s}$ (resp. $b^\dagger_{\mathbf{q}s}$) the annihilation (resp. creation) operator for a phonon with wavevector $\mathbf{q}$ and polarization s. As usual, their commutator reads $[b_{\mathbf{q}s}, b^\dagger_{\mathbf{q}'s'}] = \delta_{s,s'}\delta_{\mathbf{q},\mathbf{q}'}$. Even in amorphous materials the dispersion relation $\omega_{\mathbf{q}s}$ can be roughly approximated by the Debye model: $\omega_{\mathbf{q}s} = v_s|\mathbf{q}|$. The only proviso is that the transverse (T) and longitudinal (L) velocities are slightly different, with $v_L/v_T \approx 1.5$; see Table 5.1 for the actual values.

For later convenience, introduce also the coordinate and momentum operators of the phonon field:

$$x_{\mathbf{q}s} = \sqrt{\frac{\hbar}{2\omega_{\mathbf{q}s}}}\left(b_{\mathbf{q}s} + b^\dagger_{-\mathbf{q}s}\right), \qquad p_{\mathbf{q}s} = i\sqrt{\frac{\hbar\omega_{\mathbf{q}s}}{2}}\left(b^\dagger_{\mathbf{q}s} - b_{-\mathbf{q}s}\right), \tag{5.9}$$

with commutator $[x_{\mathbf{q}s}, p_{\mathbf{q}'s'}] = i\hbar\delta_{s,s'}\delta_{\mathbf{q},-\mathbf{q}'}$. In these variables, the Hamiltonian reads

$$H_{ph} = \frac{1}{2}\sum_{\mathbf{q}s}\left(p_{\mathbf{q}s}p_{-\mathbf{q}s} + \omega^2_{\mathbf{q}s}x_{\mathbf{q}s}x_{-\mathbf{q}s}\right) \tag{5.10}$$

having dropped a zero-point constant.

[1] One is free to set $\varepsilon_i, \Delta_i \ge 0$ for all i by adjusting the sign of the Pauli matrices.

Finally, the interaction Hamiltonian that couples phonons to TLS is

$$H_{int} = \sum_{i\mathbf{q}s} \gamma_{is}\, \sigma_i^z\, \Xi_{i\mathbf{q}s}\, x_{\mathbf{q}s}\, : \tag{5.11}$$

γ_{is} is the site-dependent coupling strength, with the dimension of an energy, and $\Xi_{i\mathbf{q}s}$ parametrizes the spatial and angular form of the interaction:

$$\Xi_{i\mathbf{q}s} = \frac{1}{\sqrt{\rho V}}\,(-iq)\,\mathsf{D}_i^{ab} e_{\mathbf{q}s}^{ab} e^{i\mathbf{q}\cdot\mathbf{r}_i}. \tag{5.12}$$

In the above expression, V is the volume of the sample, ρ the material density, $\mathbf{r}_i$ is the position of the i-th TLS and D_j^{ab} a dimensionless, random elastic dipole tensor. Finally, there is the projector $e_{\mathbf{q}s}^{ab} := \frac{1}{2}\left(\hat{q}^a \hat{e}_{\mathbf{q}s}^b + \hat{q}^b \hat{e}_{\mathbf{q}s}^a\right)$, where $\hat{\mathbf{e}}_{\mathbf{q}s}$ are the polarization versors[2]. Notice that Eq. (5.11) entails that the phonons do not make the TLS flip from one state to the other, instead their presence modifies the imbalance between the two minima of the potential. Notice that this picture will get modified in Sec. 5.2, where the *renormalized* TLS will flip because of the emission or absorption of phonons.

In the following, we will set $\gamma_{is} \equiv \gamma_s$ for each site, and absorb in D_i^{ab} all the randomness. The experimentally correct form of D_i^{ab} is clearly inaccessible, therefore some approximations are in order. To our knowledge, there are two main ways of parametrizing D_i^{ab} (for a more detailed discussion see App. C.1).

1. Following the standard literature (e.g. Ref. [88]), one can just assume that D_i^{ab} is a random symmetric tensor with entries of $O(1)$.

2. Following Ref. [365], D_i^{ab} should be taken as the *difference* between two random tensors, one for each well of the TLS. Moreover, its entries should not be of $O(1)$, instead they should be fixed from self-consistent criteria for the stability of the amorphous lattice. This different choice boosts the entries from $O(1)$ to $O(10)$.

As shown in App. C.1, the two choices give rise to sensibly different results; however, the overall physical picture remains qualitatively the same for what concerns this study. Throughout the text, it will be made clear what type of dipole structure we will be using.

5.2 Strong-coupling renormalization

From Table 5.1, it is clear that the experimentally relevant situation for TLS is when $\varepsilon \lesssim \gamma$, i.e. when TLS and phonons are strongly coupled. It is convenient, then, to perform a *polaron transformation* that takes into account the strong-coupling effects, generating new renormalized couplings which, hopefully, can be treated perturbatively [357, 365]. In the next pages, such procedure will be laid out in detail.

5.2.1 A polaron-like transformation

To our knowledge, the easiest way to derive the correct form of the transformation is the following. Having a closer look at the interaction Hamiltonian (5.11), one sees

[2] Note that with our conventions $\hat{\mathbf{e}}_{\mathbf{q}s}^* = \hat{\mathbf{e}}_{-\mathbf{q}s}$, thus $\Xi_{i\mathbf{q}s}^* = \Xi_{i-\mathbf{q}s}$ and the interaction Hamiltonian is Hermitian, as it should be.

Parameter	*Physical meaning*	*SiO_2*	*BK7*	*PMMA*
ε_i	TLS asymmetry energy $\sim$ unif$[0, W]$	$W = 130$ meV	$W = 73$ meV	$W = 33$ meV
Δ_i	TLS tunneling stregth $\sim$ log-unif$[\Delta_{min}, \Delta_{max}]$	$\Delta_{max} = 10$ meV $\Delta_{min} = 100$ peV	$\Delta_{max} = 10$ meV $\Delta_{min} = 100$ peV	$\Delta_{max} = 3$ meV $\Delta_{min} = 30$ peV
$\bar{P}$	TLS density of states $= \rho_{TLS}/W \log(\Delta_{max}/\Delta_{min})$	0.8×10^{45} J^{-1}m^{-3}	1.1×10^{45} J^{-1}m^{-3}	0.6×10^{45} J^{-1}m^{-3}
ρ_{TLS}	TLS number density	0.30 nm^{-3}	0.24 nm^{-3}	0.058 nm^{-3}
v_L v_T	sound velocity	5800 m/s 3800 m/s	6200 m/s 3800 m/s	3150 m/s 1570 m/s
ρ	material density	2200 kg/m^3	2510 kg/m^3	1180 kg/m^3
T_D	Debye temperature	348 K	360 K	101 K
γ_L γ_T	TLS-phonon coupling	1.04 eV 0.65 eV	0.96 eV 0.65 eV	0.39 eV 0.27 eV
D_i^{ab}	elastic dipole tensor	$O(1-10)$ entries	$O(1-10)$ entries	$O(1-10)$ entries

TABLE 5.1: Parameters of the model, specifying the material to fused quartz (SiO_2), borosilicate glass (BK7) and plexiglass (PMMA). The values of $\bar{P}, v_L, v_T, \rho, T_D$ are unambiguous since they come from direct measurements [365, 368]. The values of $W, \Delta_{min}, \Delta_{max}, \rho_{TLS}$ are instead more difficult to extract, since they are inferred from the density of states (DOS) $\bar{P}$. One can reasonably set $W = k_B T_{glass}$: indeed, the TLS are formed at the glass transition [88]. One must then set $\Delta_{max} \approx 10^{-1} W$ in order to have a DOS that goes to zero above W [86], and $\Delta_{min} \approx 10^{-9} W$ to reproduce instead a flat DOS at low temperatures [89]. These values are to be considered the less precise, since they enter only logarithmically in the observables; in general there is a lot of confusion about them in the literature. With these estimates, ρ_{TLS} remains fixed as well to the values in the table. Finally, we need to specify γ_{is} and D_i^{ab}, which in truth always figure multiplied one by another. We fix $\gamma_{is} \equiv \gamma_s$ on every site, take γ_L, γ_T from Ref. [368], and we defer to App. C.1 for the form of D_i^{ab}.

that it is nothing but a linear term in the phonon coordinate operator. Thus, one can "complete the square" in Eq. (5.10) by shifting the origin of the $x_{\mathbf{q}s}$ fields. By inspection, this is accomplished by the unitary transformation

$$U = \exp\left[-\frac{i}{\hbar} \sum_{i\mathbf{q}s} \frac{\gamma_s}{\omega_{\mathbf{q}s}^2} \sigma_i^z \, \Xi_{i\mathbf{q}s} \, p_{\mathbf{q}s} \right]. \tag{5.13}$$

It is a simple exercise to verify that

$$U(H_{ph} + H_{int})U^\dagger = H_{ph} - \sum_{ij} \sum_{\mathbf{q}s} \frac{\gamma_s^2}{2\omega_{\mathbf{q}s}^2} \sigma_i^z \sigma_j^z \Xi_{i\mathbf{q}s} \Xi_{j\mathbf{q}s}^* : \tag{5.14}$$

indeed, the second term on the r.h.s. is just the "missing piece of the square". It is important to notice that the only interaction generated at this level is in the σ^z–σ^z channel, with couplings

$$J_{ij} := \sum_{\mathbf{q}s} \frac{\gamma_s^2}{2\omega_{\mathbf{q}s}^2} \Xi_{i\mathbf{q}s} \Xi_{j\mathbf{q}s}^*. \tag{5.15}$$

Already by dimensional analysis one finds

$$J_{ij} \sim \frac{\gamma^2}{\rho v^2 |\mathbf{r}_i - \mathbf{r}_j|^3}. \tag{5.16}$$

In App. C.2 the exact computation is reported, yielding

$$J_{ij} = \frac{\gamma^2 \mathbb{D}_{ij}}{16\pi\rho v^2 r_{ij}^3}, \tag{5.17}$$

where we defined the sound velocity averaged over polarizations v as

$$\frac{1}{v^3} := \frac{1}{3}\sum_s \frac{1}{v_s^3}\,, \tag{5.18}$$

and similarly an averaged coupling strength γ:

$$\gamma^2 := \frac{v^3}{3}\sum_s \frac{\gamma_s^2}{v_s^3}. \tag{5.19}$$

Also, $\mathbb{D}_{ij}$ are averages of the dipole moments D_i^{ab}, that are defined in Eq. (C.19), and whose distribution are shown in Fig. C.1b. It is interesting to notice that these interactions correspond exactly to the ones found via a weak-coupling expansion [353], but here they gain a non-perturbative justification. Putting in the formula the numbers of Table 5.1, using the choice 2 for the dipole tensors, and taking the i-th and j-th TLS at a distance $r_{ij} = \rho_{TLS}^{-1/3}$, one finds for our example glasses

$$\begin{aligned} \mathrm{SiO_2} &: J_{ij} \simeq 1.6\times 10^{-5}\ \mathrm{eV} \simeq 2.4\times 10^{10}\ \mathrm{Hz};\\ \mathrm{BK7} &: J_{ij} \simeq 3.1\times 10^{-5}\ \mathrm{eV} \simeq 4.8\times 10^{10}\ \mathrm{Hz};\\ \mathrm{PMMA} &: J_{ij} \simeq 4.2\times 10^{-5}\ \mathrm{eV} \simeq 6.5\times 10^{10}\ \mathrm{Hz}. \end{aligned} \tag{5.20}$$

It is also easy to transform the TLS Hamiltonian, that involves only Pauli matrices. Defining the phonon operators P_i from

$$U =: \exp\left[-i\sum_i P_i\,\frac{\sigma_i^z}{2}\right] \quad\Longrightarrow\quad P_i := \sum_{\mathbf{q}s}\frac{2\gamma_s}{\hbar\omega_{\mathbf{q}s}^2}\,\Xi_{i\mathbf{q}s}\,p_{\mathbf{q}s}, \tag{5.21}$$

—i.e. P_i is the amount of which the TLS basis has to be rotated—one finds

$$UH_{TLS}U^\dagger = \sum_i\left[\varepsilon_i\sigma_i^z + \Delta_i\sigma_i^x\cos(P_i) + \Delta_i\sigma_i^y\sin(P_i)\right]. \tag{5.22}$$

Putting everything together, one finds an equivalent Hamiltonian for the TLS in an elastic medium, that reads[3]

$$H' = UHU^\dagger = H_{ph} + \sum_i\left[\varepsilon_i\sigma_i^z + \Delta_i\sigma_i^x\cos(P_i) + \Delta_i\sigma_i^y\sin(P_i)\right] + \sum_{ij}J_{ij}\sigma_i^z\sigma_j^z \tag{5.23}$$

$$= H_{ph} + \sum_i\left[\varepsilon_i\sigma_i^z + \Delta_i\sigma_i^+ e^{-iP_i} + \Delta_i\sigma_i^- e^{iP_i}\right] + \sum_{ij}J_{ij}\sigma_i^z\sigma_j^z \tag{5.24}$$

with $\sigma^\pm = \frac{1}{2}(\sigma^x \pm i\sigma^y)$. In the equations above one sees that the polaron transformation has generated a direct coupling between TLS, and a new TLS-phonon coupling via $\sigma_i^x\cos(P_i) + \sigma_i^y\sin(P_i)$, or equivalently $\sigma_i^+ e^{-iP_i} + \sigma_i^- e^{iP_i}$. These phonon operators are complicated, yet have absolute value less than 1, and the hope is that by normal ordering they could be put in an easier form to deal with. Equation (5.24) also gives a clear physical interpretation of the whole transformation: the operators $e^{\pm iP_i}$ "shift the origin" of the phonon field as a TLS jumps between the up and down states.

[3] Notice that H' is *exactly* equivalent to H; no approximation has been made so far.

5.2.2 Debye-Waller factor

Let us pause a moment, and compute a quantity that will be useful in the following: it is the average on a thermal state

$$\langle e^{iP_i}\rangle_T = \exp\left\{-\sum_{\mathbf{q}s}\frac{\gamma_s^2}{\hbar\omega_{\mathbf{q}s}^3}\Xi_{i\mathbf{q}s}\Xi^*_{i\mathbf{q}s}\coth\left(\frac{\beta\hbar\omega_{\mathbf{q}s}}{2}\right)\right\} \tag{5.25}$$

$$=: e^{-\Gamma_i^2(T)/2}. \tag{5.26}$$

We will refer to Γ_i^2 as *Debye-Waller factor*, and denote its zero-temperature value as $\Gamma_{i,0}^2 := \Gamma_i^2(0)$. The Debye-Waller factor is computed explicitly in App. C.3, finding that at very low temperatures

$$\frac{\Gamma_i^2}{2} = \frac{\gamma^2 q_D^2\,\mathrm{Tr}(\mathsf{D}_i^2)}{12\pi^2\rho\hbar v^3} + O\big(e^{-T_D/2T}\big), \tag{5.27}$$

where again the average velocity v and coupling γ were used, since the polarization differences are not crucial. Hence, from Eq. (5.27) the Debye-Waller factor increases exponentially slowly with the temperature. One can rewrite

$$\frac{\Gamma_i^2}{2} = \frac{E_D^2}{4E_i^2} + O\big(e^{-T_D/2T}\big). \tag{5.28}$$

where E_D is the Debye energy and E_i is defined as

$$E_i := \sqrt{\frac{3\pi^2\hbar^3\rho v^5}{\gamma^2\,\mathrm{Tr}(\mathsf{D}_i^2)}}. \tag{5.29}$$

For the materials of Table 5.1, and parametrizing the dipole tensors according to point 2, one readily finds at zero temperature

$$\mathrm{SiO_2}: \frac{\Gamma_{i,0}^2}{2} \simeq 19; \qquad \mathrm{BK7}: \frac{\Gamma_{i,0}^2}{2} \simeq 19; \qquad \mathrm{PMMA}: \frac{\Gamma_{i,0}^2}{2} \simeq 19\,. \tag{5.30}$$

These values are very close to the ones found in Ref. [365] (parameter α, p. 3). We stress that Γ_i^2 does fluctuate also at zero temperature, since the TLS are coupled via the random dipole tensor D to the phonons. In particular, the distribution of the random variable $\mathrm{Tr}(\mathsf{D}_i^2)$ is plotted in Fig. C.1a. If the temperature is higher, it is shown in App. C.3 that the Debye-Waller factor grows slowly, gaining only a factor 4 at $T = T_D$.

5.2.3 Normal ordering

At this point, one can go back to Eq. (5.24), and find a more manageable expression for the operators $e^{\pm iP_i}$. Without making any approximation yet, they can be normal-ordered. Using the Baker-Campbell-Hausdorff formula (specified to creation and annihilation operators)

$$e^{c_i b_i + c_j^* b_j^\dagger} = e^{c_j^* b_j^\dagger} e^{c_i b_i} e^{\frac{1}{2}c_i c_j^* \delta_{ij}}, \tag{5.31}$$

one finds

$$e^{iP_i} = e^{i\Gamma_{i,0}\tilde{b}_i^\dagger} e^{-i\Gamma_{i,0}\tilde{b}_i} e^{-\Gamma_{i,0}^2/2}, \tag{5.32}$$

having defined

$$\tilde{b}_i := \frac{1}{\Gamma_{i,0}} \sum_{\mathbf{q}s} \gamma_s \sqrt{\frac{2}{\hbar \omega_{\mathbf{q}s}^3}} \Xi_{i\mathbf{q}s}^* b_{\mathbf{q}s}, \qquad \tilde{b}_i^\dagger := \frac{1}{\Gamma_{i,0}} \sum_{\mathbf{q}s} \gamma_s \sqrt{\frac{2}{\hbar \omega_{\mathbf{q}s}^3}} \Xi_{i\mathbf{q}s} b_{\mathbf{q}s}^\dagger. \tag{5.33}$$

Indeed, the normal ordering procedure generates the Debye-Waller factor on the vacuum state, i.e. at zero temperature. Notice also that, thanks to the definition with the factor $(\Gamma_{i,0})^{-1}$ in front, the operators $\tilde{b}$ and $\tilde{b}^\dagger$ can be considered of order 1.

At this point, one can rewrite *exactly*

$$H' = H_{ph} + \sum_i \left[\varepsilon_i \sigma_i^z + \overline{\Delta}_i \sigma_i^+ e^{-i\Gamma_{i,0}\tilde{b}_i^\dagger} e^{i\Gamma_{i,0}\tilde{b}_i} + \overline{\Delta}_i \sigma_i^- e^{i\Gamma_{i,0}\tilde{b}_i^\dagger} e^{-i\Gamma_{i,0}\tilde{b}_i} \right] + \sum_{ij} J_{ij} \sigma_i^z \sigma_j^z, \tag{5.34}$$

with renormalized tunneling rates

$$\overline{\Delta}_i := e^{-\Gamma_{i,0}^2/2} \Delta_i. \tag{5.35}$$

The physical interpretation is rather straightforward: the tunnelling rate of a TLS is *exponentially* suppressed, since it has to "bring along" a cloud of phonons, namely the polaron. Such suppression is regulated by the Debye-Waller factor, that by Eq. (5.30) is not a small number. It is for this reason that, as shown in Fig. 5.2, the paramters $\overline{\Delta}$ are pushed down to very small energies, providing a clear separation of timescales between the fast, coherent dynamics of the TLS alone, and the slow, decoherence-inducing influence of the phonon bath. This picture is in perfect agreement with the wide distribution of the tunneling strengths found in experiments, and for their considerably small values.

Before moving on, it is worth mentioning that already at the level of Eq. (5.34) one can begin to see the physics of MBL appearing. Indeed, ignoring for a moment the presence of phonons, that are only exponentially weakly coupled, the dynamics of the TLS is governed by an Hamiltonian that is *diagonal* in σ^z, and in the form of the l-bit model already discussed in Chap. 4. One therefore expects to see features, in the dynamics of TLS, that are similar to the ones predicted by the l-bit model. The influence of the phonons through the σ^x term will be the object of study of the next Section.

5.2.4 Relaxation of the TLS via Fermi's Golden Rule

In this Section, we provide some simple estimates for the relaxation dynamics of the TLS, when the phonons are considered as a bath. This will be the starting point for the more quantitative analysis of Sec. 5.3.1, where the relaxational dynamics will be investigated through the more sophisticated GKSL equation.

The first thing to do is to notice that the polaron transformation has taken into account the strong-coupling effects, generating new, small renormalized coupling. Roughly speaking, there are three energy scales in the Hamiltonian (5.34) (specifying the material to SiO_2; for the other materials the behaviour is the same):

$$SiO_2: \qquad \varepsilon_i \sim 10^{14}\ \text{Hz}, \qquad \overline{\Delta}_i \sim 10^5\ \text{Hz}, \qquad J_{ij} \sim 10^{10}\ \text{Hz}. \tag{5.36}$$

Since both $\varepsilon_i \gg \overline{\Delta}_i$ and $\varepsilon_i \gg J_{ij}$, one can integrate out the phonons in a system of *non-interacting* TLS. It is not important that $\overline{\Delta}_i \lesssim J_{ij}$, since the level spacing will be

of the order of ε_i. Anyway, we will also contemplate on the effect of adding the interactions at the end of this section.

Suppose to start from an infinite-temperature state: the "up" and "down" states of the TLS are equally populated. The main process one needs to consider is the decay of an "up" TLS into phonons. It is important to stress at this point that it will be the "up" and "down" states of the Hamiltonian (5.24) (or equivalently Eq. (5.34)) to be considered physical, that is to say the TLS states *after* having applied the polaron transformation. This point is subtle, since the distinction between TLS and phonons becomes blurry in the strong-coupling regime. However, since the interactions J_{ij} are small, one can safely consider the TLS one by one when they decay; moreover, since the phonons are a thermodynamically large system, the influence of just one TLS being flipped is negligible. For these reasons, one can safely assume that the phonon ground state is left unchanged in the asymptotically far regions, even if the operators $\overline{\Delta}_i \sigma_i^{\mp} e^{\pm i\Gamma_{i,0}\tilde{b}_i^\dagger} e^{-i\Gamma_{i,0}\tilde{b}_i}$ not only flip the TLS, but also shift locally the phonon ground state.

For the reasons outlined above, on can use Fermi's Golden Rule applied to only one TLS. The decay rate reads

$$Y_i = \sum_f \frac{2\pi}{\hbar} \left| \langle f, \downarrow | \, \overline{\Delta}_i \sigma_i^- e^{i\Gamma_{i,0}\tilde{b}_i^\dagger} e^{-i\Gamma_{i,0}\tilde{b}_i} \, |0, \uparrow\rangle \right|^2 \rho_f(2\varepsilon_i) \tag{5.37}$$

where $\rho_f(E)$ is the final density of states of the phonons at energy E. In particular, for the reasons above the final state can be thought as made of phonons of the *unperturbed* Hamiltonian H_{ph}. In App. C.4 it is determined

$$Y_i = \frac{\pi \overline{\Delta}_i^2 \varepsilon_i}{\hbar E_i^2} e^{-2\varepsilon_i/E_D} \, {}_0F_2\left(;\frac{3}{2},2;\frac{\varepsilon_i^2}{4E_i^2}\right) \tag{5.38}$$

where ${}_0F_2$ is a generalized hypergeometric function (see Eq. (C.53)), E_D is the Debye energy and E_i is defined in Eq. (5.29).

The expression above, in terms of the generalized hypergeometric function, is not very transparent: using its asymptotic expansions (Eq. (C.54)) everything becomes clear instead. For *weak* coupling between TLS and phonons, one needs to take the small argument expansion, and finds ${}_0F_2(;3/2,2;\varepsilon_i^2/4E_i^2) \simeq 1$: it follows

$$Y_i = \frac{\gamma_i^2 \overline{\Delta}_i^2 \varepsilon_i \, \mathrm{Tr}(\mathsf{D}_i^2)}{3\pi\hbar^4 \rho v^5} e^{-2\varepsilon_i/E_D}. \tag{5.39}$$

The meaning of this equation is made clear by the comparison with the *single-phonon* computation that will be performed in Sec. 5.3 in the framework of the GKSL equation, see Eq. (5.53): the two expressions are practically the same. In the strong-coupling limit, instead, Eq. (5.38) takes into account the emission of many real phonons, and this is reflected from an enhancement in the decay rate. However, for physical values of the parameters, such enhancement is not enough to overcome the exponential suppression $\propto e^{-2\varepsilon_i/E_D}$, due to the finite bandwidth of the phonons.

The decay rate of Eq. (5.38) is correct to order $O(\overline{\Delta}_i^2)$ (which is a small parameter), and to all orders in the phonon operators $\tilde{b}_i, \tilde{b}_i^\dagger$. Therefore, it is expected to give a pretty accurate result. Considering only the typical values for all the random parameters, and employing the choice 2 for the dipole tensors, one finds that the typical

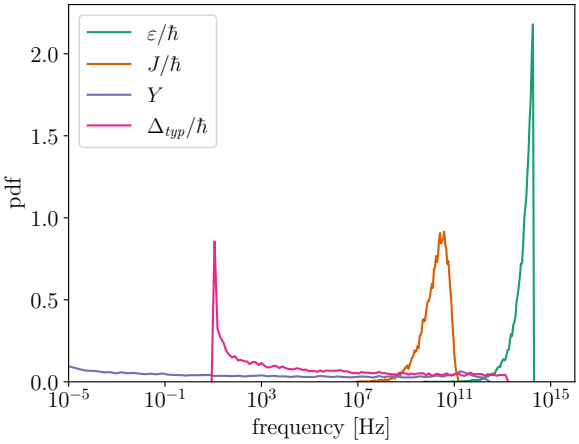

FIGURE 5.2: Probability distribution functions (pdf) for the (disordered) parameters of SiO_2. The distributions are computed following the prescriptions explained in the main text (in particular, point 2 at the end of Sec. 5.1 is used). One can see a clear separation of timescales: the single-site energies ε represent the fastest scale, and are followed by the interactions J_{ij}. Then there is the renormalized tunnelling $\overline{\Delta}$, which in the strong-coupling computation dictates also the coupling to phonons. Finally, the thermalization rates Y are the slowest, and are spread across many orders of magnitude.

values of Y_i are

$$Y_{SiO_2} \simeq 7.6 \times 10^{-1}\ \text{Hz}, \quad Y_{BK7} \simeq 3.7 \times 10^{-2}\ \text{Hz}, \quad Y_{PMMA} \simeq 7.2 \times 10^{-1}\ \text{Hz}\,. \quad (5.40)$$

Since $J_{ij} \gg \hbar Y_i$ (at least at the level of typical values), the coherent dynamics of the TLS should be observed for a wide time window, before thermalization ultimately takes place.

The values given above for the thermalization rates Y_i should be taken with a grain of salt. As can be seen in Fig. 5.2, the probability distribution of Y_i is *extremely* wide, spanning many orders of magnitude. Therefore, we do expect thermalization to be slow, but reasonably it will take place on timescales shorter than this average value. On the other hand, several experiments observe that a time of the order of minutes is necessary for the TLS to behave as thermal (see e.g. Refs. [355, 369]), so the distributions in Fig. 5.2 may explain well such experimental observation.

At this point, the last thing to do is to address what happens when the interactions among TLS are taken into account as well, when computing the decay rate. First of all, the rates of Eq. (5.38) are nearly unchanged if perturbation theory is done wrt. the interacting Hamiltonian $\sum_i \varepsilon_i \sigma_i^z + \sum_{ij} J_{ij} \sigma_i^z \sigma_j^z$. Indeed, the only difference that may take place is that a phonon-mediated process speeds up the decay of a *group* of "up" states. However, even if interactions may favour the energy matching condition for the decay, nevertheless more TLS in the configuration need to be flipped, and this happens at higher orders in $\overline{\Delta}_i$. In conclusion, we are confident that perturbation theory as we have developed it captures the essential features of the relaxation dynamics of the TLS, and is quantitatively accurate to a fair degree. In a forthcoming study [9], we will address the possibility of applying a GKSL framework to the *many-body* problem of Eq. (5.34), thus putting the results of this Section on firmer grounds.

5.3 Dissipative dynamics at weak coupling

In the previous Section we described in detail what is the effect of strong interactions between TLS and phonons. The overall picture is that each TLS is renormalized by a cloud of phonons (a version of the polaron problem) and, in terms of the renormalized operators, the Hamiltonian (5.34) presents a *weak coupling* between phonons and TLS. It is therefore customary in the literature to start *directly from the weakly-coupled Hamiltonian*, taking it as an alternative microscopic model. This is exactly what we are going to do in this Section, with the purpose of studying the out-of-equilibrium dynamics of the TLS in presence of the phonon bath. Working at weak coupling will enable one to get a rather intuitive picture of the TLS dynamcs, and we will comment again on the consequences of the underlying strong coupling in Sec. 5.5.

5.3.1 Gorini–Kossakowski–Sudarshan–Lindblad master equation

Let us start again from Eq. (5.1). We choose to work in the Gorini-Kossakowski-Sudarshan-Lindblad (GKSL) framework [370, 371], obtaining a master equation for the (reduced) density matrix of the TLS ρ, that must have the general form

$$\partial_t \rho(t) = -\frac{i}{\hbar}[H_{TLS} + H_{LS}, \rho(t)] + \sum_\kappa \mathcal{L}_\kappa \rho(t). \tag{5.41}$$

The first term on the r.h.s. describes the unitary evolution of the system, and it is called the *Liouvillian*. It is composed of H_{TLS}, which is the TLS Hamiltonian of Eq. (5.2), and H_{LS}, which is the *Lamb-Stark shift* Hamiltonian (it will be specified below in Eq. (5.48), and it basically contains the same interactions found from the strong-coupling treatment). The second term on the r.h.s., the so-called *Lindbladian*, describes instead dissipation and decoherence. The $\mathcal{L}_\kappa$ are Lindblad super-operators; in general, the label κ can assume $O(N^2)$ values but, as we will show in the following, in our system the dominant terms are on-site, reducing $\kappa \equiv i = 1, 2, \ldots, N$.

The GKSL master equation (5.41) relies on some approximations [370, 371]. First, one assumes weak coupling between TLS and phonons: this was already discussed at length; here we just remark that one can perform another consistency check *a posteriori*, by verifying that the energy scales of decoherence and dissipation induced by phonons are smaller than the TLS energy set by W. The GKSL framework consists in three further approximations:

1. *Born approximation:* at all times the influence of the TLS on the phonon thermal population is negligible. This is a consequence of weak coupling, and of the TLS being a dilute system in the (amorphous) lattice. Therefore, we expect the approximation to be valid to a good extent in our system.

2. *Markov approximation*: all the bath excitations decay on very fast timescales with respect to those of the TLS. This is not guaranteed when working at ultra-low temperatures, but it is still a good starting point.

3. *Rotating-wave approximation:* when considering two TLS, the *resonant* processes are dominant. Equivalently, the relaxation time of TLS in the open-system, τ_R, is long with respect to the timescale of the intrinsic evolution of the system [370]; in formulas: $\tau_R \gg |\nu_i - \nu_j|^{-1}$. We will validate a posteriori this assumption in Sec. 5.3.4.

Within these assumptions, the TLS-TLS interactions in H_{LS} commute with the isolated TLS Hamiltonian: $[H_{TLS}, H_{LS}] = 0$, ultimately leading to the MBL character

of the unitary dynamics. It is interesting to notice that MBL features appear from different, complementary computations, in the weak- and strong-coupling limits.

5.3.2 Free TLS evolution

In order to compute the Lamb-Stark shift H_{LS} and the Lindblad super-operators $\mathcal{L}_\kappa$, it is convenient to diagonalize the TLS Hamiltonian H_{TLS} 5.2 [370, 371]. We look for single-site operators S_i such that

$$[H_{TLS}, S_i] = -\hbar\nu S_i. \tag{5.42}$$

The linear problem is easily solved, finding eigenvalues

$$\hbar\nu_{i,0} = 0, \qquad \hbar\nu_{i,\pm} = \pm\hbar\nu_i = \pm 2\sqrt{\varepsilon_i^2 + \Delta_i^2}, \tag{5.43}$$

with corresponding eigenoperators

$$S_i^z = \vec{v}_{i,0}\cdot\vec{\sigma}_i, \qquad S_i^\pm = \vec{v}_{i,\pm}\cdot\vec{\sigma}_i, \tag{5.44}$$

where

$$\vec{v}_{i,0} = -\frac{2}{\hbar\nu_i}(\Delta_i, 0, \varepsilon_i), \quad \vec{v}_{i,\pm} = \frac{2}{\hbar\nu_i}(-\varepsilon_i, \pm i\hbar\nu_i/2, \Delta_i). \tag{5.45}$$

Notice that, since typically $\Delta_i \ll \varepsilon_i \sim W$, $\hbar\nu_i$ will be of order W. Also, defining $S_i^x = (S_i^+ + S_i^-)/2$ and $S_i^y = (S_i^+ - S_i^-)/2i$, the operators S_i^x, S_i^y, S_i^z form a Pauli basis. At this point, it is easy to verify that the TLS Hamiltonian reads

$$H_{TLS} = -\frac{1}{2}\sum_i \hbar\nu_i S_i^z. \tag{5.46}$$

5.3.3 Coupling to phonons

The coupling with phonons induces both dissipation and TLS–TLS interactions. Under the assumptions discussed above, they can be be modelled via the GKSL master equation. Its final form for TLS in glasses is given by:

$$\begin{aligned}\partial_t\rho(t) = -\frac{i}{\hbar}\Big[-\frac{1}{2}\sum_i \hbar\nu_i S_i^z + \sum_{ij} J_{ij}^w S_i^z S_j^z, \rho(t)\Big] \\ + \sum_i \Upsilon_i^w f_T(\hbar\nu_i)\Big(S_i^+\rho(t)S_i^- + S_i^-\rho(t)S_i^+ - 4\rho(t)\Big) \\ + \sum_i \Upsilon_i^w\Big(S_i^+\rho(t)S_i^- + \{\rho(t), S_i^z\} - 2\rho(t)\Big).\end{aligned} \tag{5.47}$$

In the previous equation, the first term on the r.h.s. corresponds to the commutator $-\frac{i}{\hbar}[H_{TLS} + H_{LS}, \rho(t)]$, where

$$H_{LS} = \sum_{ij} J_{ij}^w S_i^z S_j^z \tag{5.48}$$

is the Lamb-Stark shift Hamiltonian. With the notation J^w and Υ^w we are emphasizing that such quantities are derived via a weak-coupling computation, therefore they are in principle different from the ones obtained in Sec. 5.2.

The second term on the r.h.s. of Eq. (5.47) contains the dissipative terms: it is written separating explicitly the temperature dependent and independent contributions,

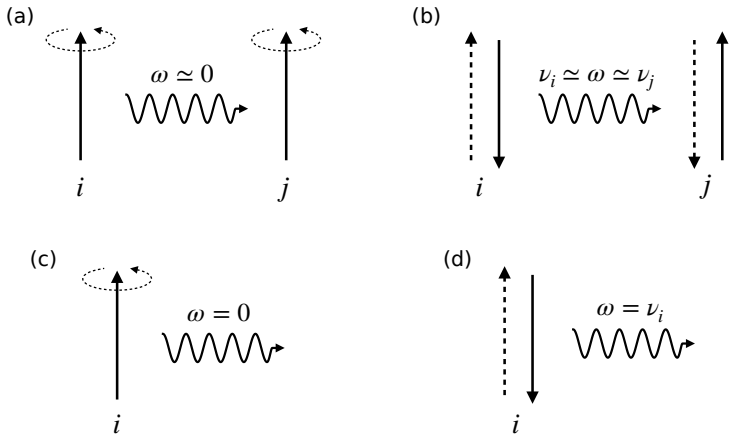

FIGURE 5.3: Virtual (a,b) and real (c,d) phonon processes that lead to TLS-TLS interactions and dissipation, respectively. (a) Interactions in the S^z–S^z channel are mediated by phonons of vanishing frequency ω, and take place among each couple ij, yielding H_{LS} of Eq. (5.48). (b) Flip-flop interactions can take place only if the two TLS resonate: this is a very rare event, because the ν_i's are widely distributed random variables. We disregard this possibility altogether throughout this study. (c) Dephasing of a single TLS under the action of the phonon bath. This process is negligible because there are no real phonons at $\omega = 0$. (d) Decay of a TLS into a phonon. Considering that resonating TLS are very rare and the phonon density of states vanishes at $\omega = 0$, as noted above, it is easy to see that non-unitary processes involving two TLS can be neglected. This figure is taken from Ref. [2].

indeed $f_T(\epsilon) := (e^{\epsilon/k_BT} - 1)^{-1}$ is the Bose-Einstein distribution function at temperature T. Considering that $\hbar\nu_i \sim W \sim 0.1$ eV, however, at ultra-low temperature ($T \sim 1$ K and below) $f_T \simeq 0$, and our system is effectively at *zero temperature*. Thus, in the following we will keep only the temperature-independent contributions.

Before introducing the expressions for Υ_i^w and J_{ij}^w, a few comments are in order. As depicted in Fig. 5.3, in general interactions can take place either in the S^z–S^z channel (panel (a)), or by flipping two spins with the emission and absorption of a virtual phonon (panel (b)). This latter case, for our system, can be neglected: since ν_i and ν_j are random variables, the matching condition $\omega = \nu_i = \nu_j$ (ω is the phonon frequency), entailed by the rotating wave approximation, is a rare event. Thus, the Lamb-Stark shifts are always diagonal in S^z[4]. Moreover, the Lindblad superoperators of Eq. (5.41) correspond only to the decay processes in Fig. 5.3d, since purely dephasing processes (panel (c)) are absent: this simply follows from the density of states of the phonons at zero frequency being zero.

Having understood what are the physical processes behind the GKSL evolution, we can compute explicitly the dissipation rates Υ_i^w and the interaction strengths J_{ij}^w. As stated above, they both come from phonon processes; therefore, one can treat them in a unified way. We start by rewriting the interaction Hamiltonian, Eq. (5.11), as

$$H_{int} =: \sum_i \sigma_i^z \mathcal{E}_i : \tag{5.49}$$

[4]Even accounting for rare interactions in the S^x–S^x channel, the picture is not modified. Indeed, terms of the form $K_{ij}S_i^xS_j^x$ will still decay with the distance r_{ij}: the probability of having a resonant ij couple that is *also close in real space* is vanishingly small. Therefore, the MBL-breaking effect of weak $S_i^xS_j^x$ terms [372–374] is negligible in comparison to the Lindblad dissipator.

$\mathcal{E}_i$ are the environment operators that need to be traced out. Then, following Refs. [370, 371], we define

$$\Gamma_{ij}^{\omega} := \frac{1}{\hbar^2}\int_0^{\infty} ds\, e^{i\omega s}\ \mathrm{Tr}_B\left[\rho_B^T\, \hat{\mathcal{E}}_i^{\dagger}(t)\, \hat{\mathcal{E}}_j(t-s)\right] \tag{5.50}$$

with the hat on $\hat{\mathcal{E}}_i(t)$ indicating the interaction picture. It then holds

$$\Upsilon_i^w = \left(\frac{\Delta_i}{\hbar\nu_i}\right)^2 \left[\Gamma_{ii}^{\nu_i} + \left(\Gamma_{ii}^{\nu_i}\right)^*\right]\Big|_{T=0}, \tag{5.51}$$

$$J_{ij}^w = \frac{2\varepsilon_i}{\hbar\nu_i}\frac{2\varepsilon_j}{\hbar\nu_j}\frac{\hbar}{2i}\left[\Gamma_{ij}^0 - \left(\Gamma_{ji}^0\right)^*\right]. \tag{5.52}$$

The prefactors $\Delta_i/\hbar\nu_i$ and $2\varepsilon_i/\hbar\nu_i$ come from the basis rotation in Eq. (5.44); for the rest, here below it will appear how Υ_i^w and J_{ij}^w are essentially the same of the ones found via the strong-coupling computations in Eqs. (5.39) and (5.15), respectively.

We leave to Appendix C.5 all the details of the computation of Γ_{ij}^{ω}, which is rather straightforward, while we present here the results obtained:

$$\Upsilon_i^w = \frac{\Delta_i^2\gamma_i^2\nu_i\,\mathrm{Tr}(D_i^2)}{12\pi\rho\hbar^3 v^5}, \tag{5.53}$$

$$J_{ij}^w = \frac{\gamma_i\varepsilon_i}{\hbar\nu_i}\frac{\gamma_j\varepsilon_j}{\hbar\nu_j}\frac{\mathbb{D}_{ij}}{4\pi\rho v^2 r_{ij}^3}. \tag{5.54}$$

Above, $\mathrm{Tr}(D_i^2) = \sum_{ab} D_i^{ab} D_i^{ba}$, and $\mathbb{D}_{ij}$ is again the contraction of the dipoles D_i^{ab} and D_j^{cd} defined in Eq. (C.19).

At this point, we can check *a posteriori* whether the weak-coupling and the rotating-wave approximations are valid. Plugging in Eqs. (5.53) and (5.54) the typical values of the parameters, we find $\hbar\Upsilon_i^w/W \sim 10^{-8}$ and $J_{ij}^w/W \sim 10^{-3}$. Therefore, even in the extreme case of a coupling constant comparable to the on-site energies $\gamma \sim W$, the assumption of weak coupling is perfectly justified *a posteriori*. Moreover, as anticipated at the beginning of this Section, the rotating-wave approximation is amply valid too: indeed, the relaxation time in the open system is much longer than the intrinsic timescale of TLS: $(\Upsilon_i^w)^{-1} \gg |\nu_i - \nu_j|^{-1} \sim \hbar W^{-1}$.

5.3.4 Dynamical phases from the GKSL equation

The GKSL equation (5.41) constitutes the starting point for exploring the quantum dynamics of the TLS. As a first thing, we notice that in the absence of dissipation the evolution would be unitary, governed by the Hamiltonian

$$H_{TLS} + H_{LS} = -\frac{1}{2}\sum_i \hbar\nu_i S_i^z + \sum_{ij} J_{ij}^w S_i^z S_j^z. \tag{5.55}$$

$H_{TLS} + H_{LS}$ is completely expressed in terms of the extensive set of local conserved quantities S_i^z. This is the same property of the effective Hamiltonian of MBL systems, known as the *l-bit Hamiltonian* [106–109, 302, 328]. Borrowing the terminology from MBL, we can refer to the S_i^z's as the l-bits, or local integrals of motion (LIOM); indeed, they are on-site operators whose values are conserved during time evolution. However, $H_{TLS} + H_{LS}$ presents two main differences with respect to the l-bit Hamiltonian of standard MBL systems. First, in the TLS Hamiltonian the l-bits are

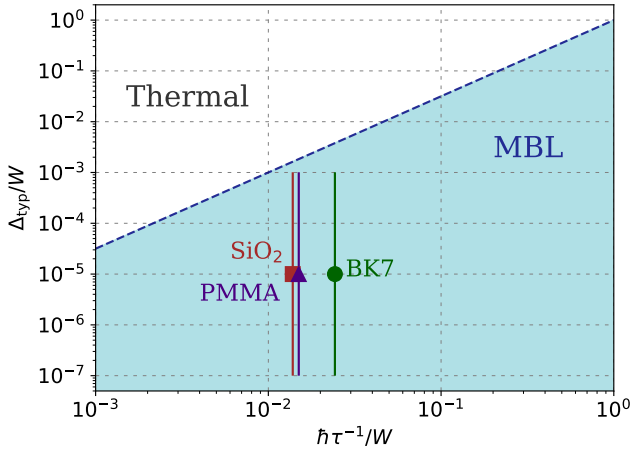

FIGURE 5.4: Sketch of the expected phase diagram for TLS in glasses. From Eq. (5.56) we see that an MBL transient regime can be observed before thermalization takes place, if the typical timescales of interaction are short with respect to the dissipation timescales (blue-shaded area). The three glassy materials reported in Table 5.1 lie well within the MBL region, even accounting for the large uncertainties in the parameter Δ_{typ} (the standard deviation of $\log(\Delta_i)$ is plotted as an errorbar). Thus, the localized regime should be experimentally observable. This figure is taken from Ref. [2].

formed by *single* spins, not exponentially localized groups of them. Second, the interaction between the TLS decays with distance as a power law, $J_{ij}^w \propto r_{ij}^{-3}$, rather than exponentially. We will comment more on this point later, in Sec. 5.4.3.

The diagonal interactions in H_{LS} are responsible for the dephasing of the spins. That is to say, if one artificially turns off the jump operators, i.e. if one sets the dissipation rates $\Upsilon_i^w \equiv 0$, diffusive transport is suppressed but the entanglement spreading persists. We will present numerical results on this artificial situation in Sec. 5.4.3, showing that the entanglement entropy grows slowly, but indefinitely in time, while the concurrence decays as a power law.

The picture described above is broken by the introduction of the jump operators: dissipative terms in the GKSL equation kill long-time coherence and drive the system to a thermal state. Nevertheless, one can observe an MBL transient regime in the relaxation dynamics, if the timescales of dissipation are appreciably longer than those of interactions. Such competition is quantified by the dimensionless ratio

$$\frac{\hbar \Upsilon_i^w}{J_{ij}^w} \sim \left(\frac{\Delta_{typ}}{W}\right)^2 \left(\frac{W}{\hbar \tau^{-1}}\right)^3, \tag{5.56}$$

where $\tau = r/v$, $r = \rho_{TLS}^{-1/3}$ being the typical distance between TLS and v the speed of sound in the glass. If this ratio is sensibly smaller than 1, the signatures of the localized phase should be observed in the dynamics of the system, and in particular in the spreading of entanglement. In Fig. 5.4, we show a tentative dynamical phase diagram for the TLS system.

Recalling that in experiments $\Delta_{typ} \sim 10^{-5}\, W$ while $W \sim 0.1$ eV and, considering $v \sim 5$ km/s and $r \sim 10$ nm, we have $\hbar\tau^{-1} \sim 1$ meV. Thus, the ratio is approximately $\hbar Y / J \sim 10^{-5} \div 10^{-4}$, making dissipation much slower than the interaction part of the unitary dynamics. Even if one allows Δ_{typ}—the most difficult parameter to infer from experiments—to vary few orders of magnitude, the system will still present an observable MBL transient regime.

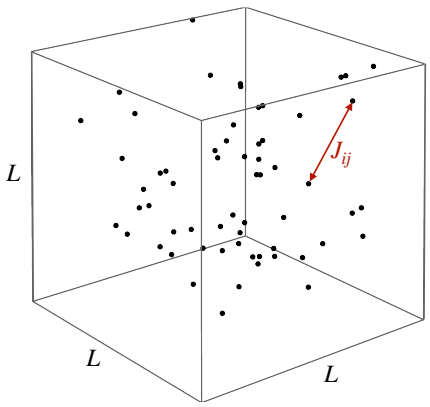

FIGURE 5.5: The TLS are uniformly distributed in a cube of size L, at constant density. The pairwise interactions J_{ij} in Eq. (5.54) are mediated by phonons. These are also responsible for the dissipation in Eq. (5.53). We employ periodic boundary conditions to minimize finite-size effects. This figure is taken from Ref. [2].

5.4 Numerical simulations

In this Section we present the results of our numerical simulations on the real-time evolution of the TLS. The analysis will be divided into two parts. In Sec. 5.4.3, we will consider the artificially isolated system (i.e. the one evolving only under the unitary dynamics given by the Liouvillian of the GKSL) governed by the Hamiltonian in Eq. (5.55). In Sec. 5.4.4, we will re-introduce the dissipative terms and consider the full TLS evolution governed by the GKSL master equation (5.47).

Before going through that, in Secs. 5.4.1–5.4.2 we will briefly discuss the assumptions involved in our numerical simulations, and define the dynamical observables.

5.4.1 Disorder distributions of the parameters

As discussed in Sec. 5.1, in the literature the parameters defining the TLS model are drawn from wide probability distributions (see p_ε and p_Δ in Eq. (5.3) and (5.4), respectively). It follows that the competing timescales in the GKSL master equation (namely ν_i^{-1}, $\hbar/J_{ij}^w$, and $(\Upsilon_i^w)^{-1}$) are distributed over several orders of magnitude and, even though their typical values are very different, they overlap one with another. In our numerical simulations we employ simplified and less broad distributions, arguing that this choice, if properly taken, does not qualitatively alter the physical content and predictions of the model.

We fix $W \equiv 1$, thus setting the (dimensionless) energy scale; $\Delta_{min}/W = 10^{-2}$ and $\Delta_{max}/W = 1$, thus $\Delta_{typ}/W = 10^{-1}$ (unless otherwise specified). We also set $\gamma_i \equiv W$, the material density $\rho = 2$ g/cm^3, and the speed of sound $v_{L,T} = 5$ km/s, irrespective of polarization. We consider $\mathrm{Tr}(D_i^2)$ to be the square of a Gaussian random variable of zero average and variance 1, since it must be positive, and $\mathbb{D}_{ij}$ to be a Gaussian random variable of zero average and standard deviation 1, since it can take both signs (see also App. C). Finally, we consider the TLS as uniformly distributed in a cube with side L, and compute their distances r_{ij} using periodic boundary conditions. The cube side depends on the number of TLS as $L = L_0 N^{1/3}$, with $L_0 \simeq \rho_{TLS}^{-1/3}$, so that we keep fixed the TLS number density ρ_{TLS}. For numerical purposes, we fix $L_0 = 1$ nm. See Table 5.1 for a comparison with the experimental values, and Fig. 5.5 for a sketch of the system.

In order to explore the phase diagram obtained in the GKSL framework, and shown in Fig. 5.4, we introduce two further artificial parameters to tune interaction and dissipation strengths:

$$J_{ij} \to \eta J_{ij}, \qquad Y_i \to \epsilon Y_i. \tag{5.57}$$

In Sec. 5.4.3 we study the artificially isolated system, setting $\eta = 10^5$ (in order to amplify the effects of interactions on the numerically accessible timescales) and $\epsilon = 0$. In Sec. 5.4.4 we re-introduce the dissipator in the GKSL master equation, and we set $\eta = 10^5$ and $\epsilon = 10^{-6}, 10^{-4}, 1$.

With these choices of the parameters, the on-site frequencies ν_i, the TLS-TLS interactions $\eta J_{ij}/\hbar$ (with $\eta = 10^5$), and the dissipation rates ϵY_i (for $\epsilon = 1$) are of comparable orders of magnitude and are much less widely distributed than originally. The latter feature is particularly useful for numerical purposes, since one can access only small system sizes and, hence, cannot sample well broad distributions. Our results will be discussed in view of these choices.

5.4.2 Initial state and dynamical observables

We always take the initial state of the dynamics to be a product state, in which each TLS is represented by a random vector on the Bloch sphere:

$$|\psi(0)\rangle = \bigotimes_{i=1}^{N} \left(\cos(\theta_i/2)|\uparrow\rangle_i + e^{i\phi_i}\sin(\theta_i/2)|\downarrow\rangle_i\right), \tag{5.58}$$

where $\theta_i \in [0, \pi]$ and $\phi_i \in [0, 2\pi)$. Thus, the system is initially at infinite temperature, and we can track precisely the entanglement growth and spreading.

The choice of the appropriate entanglement measure is not obvious: since we are dealing with an open quantum system, we wish to discriminate between quantum entanglement and thermal entropy. A reliable measure of (pairwise) quantum entanglement in open systems is the *concurrence* C_{ij} [313, 314, 317] (see also Chap. 4), where i and j are TLS indices. The concurrence quantifies the distance of the two-site reduced density matrix ρ_{ij} from the manifold of mixed, separable states whose reduced density matrix can be written as $\rho = \sum_a p_a \rho_a^{sep}$, where ρ_a^{sep} are separable, $p_a \geq 0$, and $\sum_a p_a = 1$. This implies that, if $C_{ij} > 0$, there is no mixture of separable states that can account for the correlations between sites i and j. For two spins-1/2, it can be shown [317] that

$$C_{ij} = \max\{0,\, \lambda_1 - \lambda_2 - \lambda_3 - \lambda_4\}, \tag{5.59}$$

where λ_a^2 are the eigenvalues of the matrix $R_{ij} = \rho_{ij}(\sigma_y \otimes \sigma_y)\rho_{ij}^*(\sigma_y \otimes \sigma_y)$ sorted in descending order, and the complex conjugation is done in the standard computational basis.

We define the average concurrence as

$$C(t) := \frac{1}{N} \sum_{1 \leq i < j \leq N} C_{ij}(t). \tag{5.60}$$

The normalization factor $1/N$ (instead of the seemingly natural $1/N^2$) is due to the *monogamy of entanglement*: each TLS can be highly entangled only with another TLS, so among the $N(N-1)/2$ terms in the sum, only $O(N)$ will be non-negligible.

Its particular definition allows the concurrence to quantify the entanglement between the two TLS considered, irrespective of how they are entangled with other degrees of freedom. Thus, it spots entanglement between two TLS even if they are thermal, i.e. also entangled with a heat bath. For this reason, we employ the concurrence as a well-defined entanglement measure both in the absence (Sec. 5.4.3) and in the presence (Sec. 5.4.4) of dissipation.

It is interesting to compare the time behavior of the concurrence with the half-system entanglement entropy (HSEE)

$$S_E(t) = -\operatorname{Tr}(\rho_A \log \rho_A), \tag{5.61}$$

where ρ_A is the reduced density matrix of the half system A in the bipartition $A|B$. Since the system is three-dimensional, and the TLS do not fall on a regular lattice, we bipartite the system in the following way. For each TLS, a bubble is constructed around it so that $N/2$ TLS fall inside and $N/2$ outside the bubble. The entanglement entropy relative to the bipartition is computed as in Eq. (5.61), and then averaged over all such bipartitions. We measure $S_E(t)$ both with and without the dissipator (see Sec. 5.4.3 and 5.4.4, respectively).

5.4.3 Unitary evolution of the TLS

This Section is entirely devoted to the study of the unitary time evolution of a system of N TLS governed by the Hamiltonian $H_{TLS} + H_{LS}$ of Eq. (5.55). As discussed in Sec. 5.3.4, this Hamiltonian is diagonal in the operators S_i^z, i.e. the values assumed by S_i^z are conserved quantities; therefore, adopting the terminology of MBL systems, we say that $H_{TLS} + H_{LS}$ is in the l-bit form, and S_i^z are local integrals of motion.

Studying the dynamics induced only by the Hamiltonian term of the GKSL equation (5.47) is equivalent to set $\epsilon = 0$ (see Eq. (5.57)), i.e. to assume that the timescales of dissipation are much longer than those of interactions: $1/Y_i^w \gg \hbar/J_{ij}^w$. In this limit, it is clear that a coherent many-body dynamics can take place before thermal equilibrium is reached. This situation corresponds to the bulk of the MBL phase depicted in the phase diagram of Fig. 5.4.

Thanks to the diagonal nature of the Hamiltonian (5.55) and to the choice of initial product states, few-sites observables are efficient to compute, as was recognized in previous studies [110, 111, 325]. We refer the interested reader to App. C.6 for more details on the computation. Here, we just mention that to compute the concurrence, which is a two-site observable, within the diagonal Hamiltonian (5.55) it is not necessary to perform the time evolution of the whole $2^N \times 2^N$ density matrix, but only to carry out $O(N)$ operations (see also Chap. 4 and App. B). Therefore, we could easily simulate systems of $N = 60$ TLS.

The results of the simulations for the unitary evolution are shown in Figs. 5.6a, 5.6b, and 5.7. One can see that the concurrence $C(t)$, defined in Eq. (5.60), raises linearly from the initial value 0 (the initial state is factorized) to a value independent of N (Fig. 5.6a), but slightly dependent on Δ_{typ} (Fig. 5.6b). It then falls off to a plateau via a power-law decay, whose exponent β_i remains finite in the thermodynamic limit (inset of Fig. 5.6a), and depends on Δ_{typ} (inset of Fig. 5.6b). Fig. 5.7a shows that the concurrence plateau decays exponentially with the system size: $C(\infty) \propto e^{-\alpha N}$. Finally, from Fig. 5.7b we see that the concurrence reaches its maximum on timescales

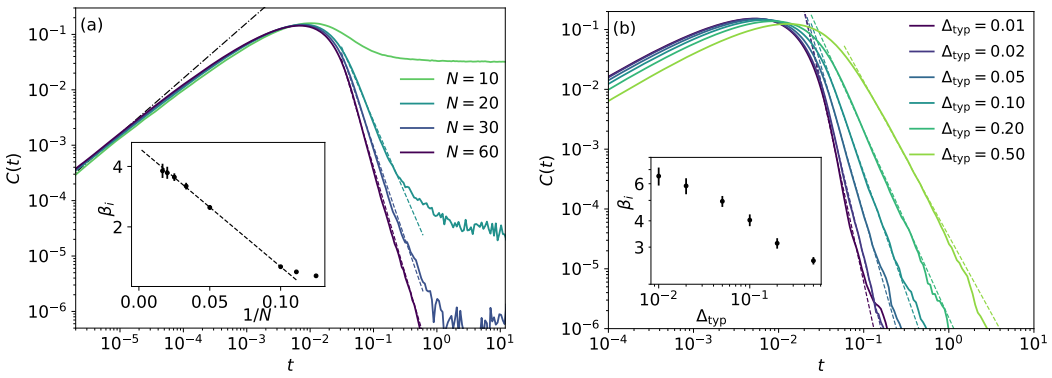

FIGURE 5.6: (a) Average concurrence within the unitary dynamics, $\epsilon = 0$ (solid lines). After a linear raise $C \sim t$ (black dashed-dotted line), the average concurrence decays with a power-law $C \sim t^{-\beta_i}$ (dashed lines), down to a value which is exponentially small in N. We set $\Delta_{typ} = 0.1$, $\eta = 10^5$; the results are averaged over 5000 disorder realizations. *Inset:* The exponent β_i depends on N and reaches a finite value in the thermodynamic limit. The errors are computed by using the statistical uncertainties of the concurrence values. Not all datasets were shown in the main figure to improve readability. (b) Dependence of the average concurrence decay exponent β_i on Δ_{typ} in the case of unitary evolution ($\epsilon = 0$). We set $N = 50$, $\eta = 10^5$ and averaged over 5000 disorder realization. We see that the smaller Δ_{typ}, the faster the decay, which remains however compatible with a power-law $C(t) \sim t^{-\beta_i}$ (dashed lines). This figure is taken from Ref. [2].

of order $\hbar/J_{ij}^w$. In conclusion, the concurrence time behavior can be schematized as

$$C(t) \sim \begin{cases} t & \text{if } t < t_1 \\ t^{-\beta_i} & \text{if } t_1 < t < t_2 \\ e^{-\alpha N} & \text{if } t > t_2, \end{cases} \tag{5.62}$$

where t_1 does not depend significantly on N, Δ_{typ} but depends parametrically on $\hbar/J_{ij}^w$, while t_2 grows with N and diverges in the thermodynamic limit.

The decay of the concurrence from its maximum is due to the fact that the interactions make the entanglement spread among many TLS, as illustrated in Fig. 5.8, while each TLS cannot be highly entangled with more than one other TLS because of the monogamy of the entanglement. The power-law decay of the concurrence from its maximum is in contrast to the behavior of ergodic systems, in which the concurrence vanishes exponentially fast [325]. The slowness of such decay is the fingerprint of the lack of thermalization and of the presence of many-body localization in the artificially isolated TLS system. In fact, the slow decay of correlation functions is known [110] to be a feature of MBL dynamics, and the concurrence (albeit not an operator nor a correlation function) follows the same behavior.

We stress again that $H_{TLS} + H_{LS}$, although completely expressed in terms of local integrals of motion, is different from the effective l-bit Hamiltonian of MBL systems, as already pointed out in Sec. 5.3.4. In particular, the TLS interactions in H_{LS} scale as a power law with distance. Following general arguments [110, 375], one would expect that for long-range interactions the correlation functions decay in time as stretched exponentials. We cannot exclude that a stretched-exponential behavior would be observed in TLS if one pushes the dynamics at larger times. In the present

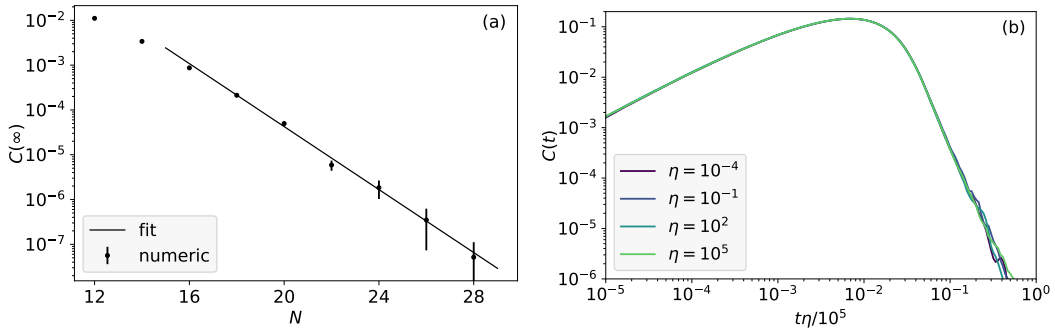

FIGURE 5.7: Results for the unitary dynamics, $\epsilon = 0$. (a) Plateau value of the average concurrence at long times (dots), with errors coming from statistical fluctuations. From a fit (solid line) we find that $C(\infty) \propto e^{-\alpha N}$ with $\alpha \approx 0.8$. This is considerably larger than the value given by the ETH prediction, i.e. a random state, which obeys $C \propto e^{-a2^N}$ with $a \approx 0.127$ (see App. C.7). Here $\eta = 10^5$, $\Delta_{typ} = 0.1$, and an average over 10000 disorder realizations was performed. (b) Average concurrence for different interaction strengths η. Rescaling the time as $t \to t\eta/10^5$ (we normalize to $\eta = 10^5$ to compare to the other plots) the curves collapse, showing that the value of η only shifts the timescale but does not modify the shape of the curve $C(t)$. Here $N = 50$, $\Delta_{typ} = 0.1$, and an average over 1000 disorder realizations was performed. This figure is taken from Ref. [2].

study, however, we are only interested in the TLS relaxation dynamics at intermediate timescales since, at long times, dissipation would always bring the system to a thermal state.

The results on the half-system entanglement entropy (HSEE) are shown in Fig. 5.8, compared with the behavior of $C(t)$. This comparison confirms, as anticipated, that the concurrence starts to decrease when the entanglement spreads and, thus, $S_E(t)$ starts to increase.

In addition, Fig. 5.8 shows that $S_E(t)$ grows slowly for a large time window. This slowness is known [129] to be the signature of localization, and shows that TLS remain coherent and non-ergodic during the time-evolution. According to the arguments in [106, 319, 375], we expect that for a long-range, $3d$ system as the TLS one entanglement would grow algebraically in time, $S_E(t) \sim t^\alpha$ with $\alpha \sim 1$. From our data, the entanglement growth is compatible with both a power-law with small exponent (~ 1), and a logarithmic growth. In the inset of Fig. 5.8, we see that the asymptotic value of HSEE, $S_E(\infty)$, is proportional to N, indicating a volume law.

5.4.4 Full evolution of the TLS

This Section is entirely devoted to the study of the time evolution of the TLS governed by the GKSL master equation (5.47). We set $T = 0$, but $\epsilon \neq 0$ (see Eq. (5.57)), i.e. the system is in the presence of dissipation and decoherence. Increasing ϵ, we increase the typical dissipation rate. For our particular choice of parameters (Sec. 5.4.1), when $\epsilon = 1$, dissipation ultimately becomes comparable with the timescale of the interactions.

To investigate the time evolution of the system, one has to integrate numerically the GKSL master equation for the TLS density matrix (see App. C.8 for more details). Because of the doubling of the Hilbert space dimension, we are forced to small system sizes, up to $N = 9$. In the following analysis, we varied both N (to perform a finite-size scaling) and ϵ.

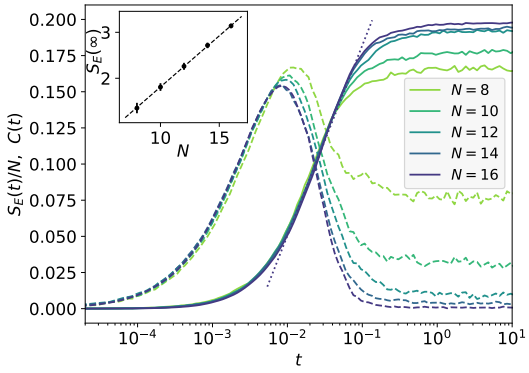

FIGURE 5.8: Unitary evolution: half-system entanglement entropy per unit volume $S_E(t)/N$, as defined in Eq. (5.61), for various system sizes (solid lines). We set $\Delta_{typ} = 0.1$, $\eta = 10^5$, and averaged over 1000 disorder realization. The average concurrences $C(t)$ (Eq. (5.60)) are shown as dashed lines for comparison. We see that the concurrence reaches a maximum at short times, as nearby TLS start to evolve coherently. Then, it starts to decay because the entanglement becomes many-body, as shown by the increase in the HSEE. In this regime, the growth of the HSEE is compatible both with a small power law $S_E(t) \sim t^{\alpha}$ with $\alpha \sim 1$, as well as $\log(t)$; the dotted line shows $\log(t)$ as a guide for the eye. *Inset:* The HSEE saturates to a volume law, as expected for an MBL system: the phase of each spin depends on all the others. The error bars are computed from the statistical fluctuations of the plateau values. This figure is taken from Ref. [2].

As can be seen from Fig. 5.9a, when ϵ is small enough the concurrence $C(t)$ reaches its maximum at the same time as with unitary dynamics ($\epsilon = 0$). Then, it decays from such peak and stabilizes around a finite value dependent on N (cf. Sec. 5.4.3), following the same behavior as in the case $\epsilon = 0$. Ultimately, the dissipation forces $C(t)$ to vanish; $C(t)$ departs from the $\epsilon = 0$ plateau, $C(\infty; \epsilon = 0)$, with a stretched-exponential functional form (Fig. 5.9b). We can ascribe this feature to the interaction between TLS and phonons: when $\epsilon \neq 0$, thanks to the dissipative terms in the GKSL equation (5.47), entanglement can spread among infinitely many phonons, preventing the concurrence from stabilizing around the plateau value.

Furthermore, Fig. 5.9a shows that, increasing the dissipation strength ($\epsilon = 1$), the concurrence maximum becomes smaller and is reached at earlier times. However, the decay from the maximum follows a power-law behavior as in the unitary case, albeit with a different exponent β_o, as reported in Fig. 5.10a. This feature is very important since it shows that the signatures of localization are visible also in the presence of dissipation, if the latter is not too large. The reason at its origin might be linked to the specific (in particular, on-site) form of the dissipation operators in the GKSL equation [335]. The power-law exponent β_o depends on ϵ and N, as shown in Fig. 5.10b, and remains finite in the thermodynamic limit. Due to the small sizes accessible when integrating the full GKSL equation, we expect the extrapolated thermodynamic value of β_o to be underestimated (see Fig. 5.10b, and the results on the unitary case $\epsilon = 0$).

Notice that the behavior of the concurrence is determined only by the ratio $\hbar Y_i^w / J_{ij}^w$. Remember that, in the unitary case, where the dissipation is absent, changing the typical strength of J_{ij}^w through the parameter η only shifts the timescale of $C(t)$, without modifying the shape of the curve (see Sec. 5.4.3, Fig. 5.7b). Hence, in this Section, we employ the artificial parameter ϵ to investigate the behavior of pairwise entanglement in the different regions of the phase diagram (Fig. 5.4) by (effectively) changing the ratio $\hbar Y_i^w / J_{ij}^w$.

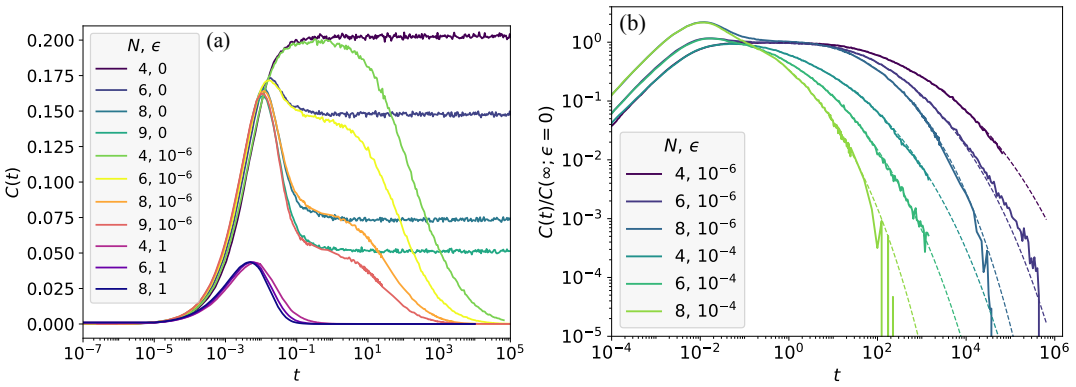

FIGURE 5.9: (a) $C(t)$, as defined in Eq. (5.60), for $\epsilon = 0, 10^{-6}, 1$, and different values of N. We see that the presence of dissipation in the GKSL master equation (5.47) decreases the concurrence maximum and moves it at earlier times. We set $\Delta_{typ} = 0.1$, $\eta = 10^5$, and averaged over at least 1000 disorder realizations. (b) Stretched-exponential fit of the concurrence for $\epsilon = 10^{-6}, 10^{-4}$, normalized to the plateau reached at $\epsilon = 0$: $C(t;\epsilon)/C(\infty;\epsilon = 0)$. Using as fitting function $\alpha \exp\{-(\frac{t+t_0}{\tau})^{\delta}\}$, we obtained $\delta \simeq 0.2$ and $\tau = O(1)$. The plot shows the results for $\Delta_{typ} = 0.1$, $\eta = 10^5$, averaged over at least 1000 disorder realizations. This figure is taken from Ref. [2].

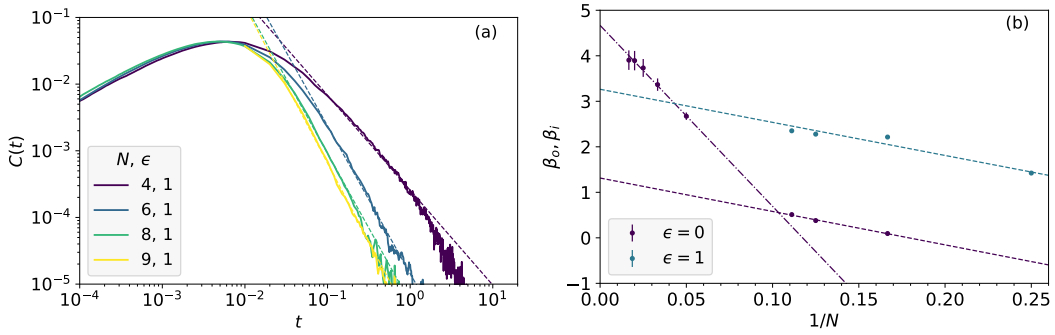

FIGURE 5.10: (a) Power-law fit of $C(t)$ at large times for $\epsilon = 1$. (b) Power-law exponents β_i ($\epsilon = 0$; data from Fig. 5.6a) and β_o ($\epsilon = 1$) as a function of $1/N$. We see that the concurrence decays faster as ϵ increases (dashed lines). However, our data can capture the behavior of $C(t)$ in the presence of dissipation only at small N, i.e. in the pre-asymptotic region. We expect the large N behavior to give a larger exponent β_o, as it happens for β_i (dashed-dotted line). We set $\Delta_{typ} = 0.1$, $\eta = 10^5$, and averaged over at least 5000 disorder realizations. The errors are computed by using the statistical uncertainties of the concurrence values. This figure is taken from Ref. [2].

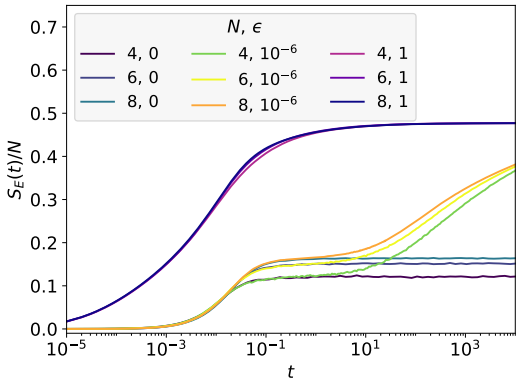

FIGURE 5.11: Half-system entanglement entropy $S_E(t)$, as defined in Sec. 5.4.2, per number of TLS for various N and ϵ. The plot shows the results for $\Delta_{typ} = 0.1$ and $\eta = 10^5$, averaged over at least 1000 disorder realizations. For $\epsilon = 10^{-6}$, we see that the entanglement spreading takes place in two steps: first, the TLS become entangled with other TLS and $S_E(t)/N$ reaches the plateau found in the case of unitary dynamics ($\epsilon = 0$); then, HSEE grows further due to the spread of the entanglement among TLS and phonons. For $\epsilon = 1$, $S_E(t)/N$ is almost independent of N, indicating a volume law. This figure is taken from Ref. [2].

Complementary to the concurrence is the HSEE $S_E(t)$, as defined in Sec. 5.4.2. Its behavior for various N and ϵ is shown in Fig. 5.11. As in the unitary case, HSEE starts to increase roughly when $C(t)$ reaches its maximum, i.e. when the TLS start to evolve coherently. It keeps increasing at larger times when entanglement spreads inside the system. From the data at $\epsilon = 10^{-6}$, it can be seen that the entanglement spreading takes place in two steps: first, the TLS become entangled one with another and $S_E(t)$ reaches the plateau found with unitary dynamics ($\epsilon = 0$); then, the HSEE increases further due to the dissipative terms in the Lindbladian (5.47). Indeed, for $\epsilon \neq 0$ the TLS entangle also with the thermal bath.

5.5 Conclusions and outlook

In this Chapter, we investigated the well-known Two-Level System (TLS) model for glasses at low temperatures. First, in the case of strongly-coupled TLS, we described how a polaron transformation can be performed, obtaining a new, weakly-coupled TLS model with renormalized parameters. Such transformation both sheds light on the separation of timescales between coherent quantum dynamics and dissipation, and paves the way for a non-perturbative analysis of the many-body relaxation of TLS (object of the forthcoming study [9]).

Then, assuming weak coupling, we studied the quantum dynamics of tunnelling TLS coupled to phonons. Within the framework of the GKSL master equation, we computed explicitly the phonon-mediated interactions among TLS and the dissipation rates. We found that, as a consequence of disorder, the Hamiltonian responsible for the unitary part of the TLS dynamics, and accounting for TLS-TLS interactions, is completely expressed in terms of local integrals of motion, and is thus many-body localized (MBL). Even though it differs from the effective l-bit Hamiltonian of standard MBL systems, in particular because the TLS-TLS interactions decay as a power law with distance, the TLS relaxation dynamics presents clear signatures of quantum MBL. Indeed, simulating the artificially isolated system with unitary dynamics governed by the TLS Hamiltonian, we found that the concurrence decays slowly in time as a power law, rather than exponentially fast as it would for an ergodic system.

We also observed that the entanglement entropy grows slowly, as in standard MBL systems.

This picture is broken by the presence of dissipation, induced by real processes of TLS and phonons, which destroy MBL and ultimately drive the system to a thermal state.

The competition between TLS-TLS interactions and dissipation determines the presence of two distinct regions in the dynamical phase diagram of the model: when interactions are comparable or stronger than dissipation, the system dynamics presents a transient *bona fide* MBL region; in the opposite case, the system quickly thermalizes. Considering the typical disorder distribution parameters encompassed in the literature, it seems that real glassy materials sit in the bulk of the transient MBL region of the phase diagram.

We explored numerically the dynamical phase diagram of the model, by tuning the interaction and dissipation strengths. We found that, in the MBL region of the phase diagram, even for dissipation strengths of the same order of magnitude of the interactions, the dynamics of the entanglement resembles the one in the absence of dissipation, showing clear signatures of localization: the concurrence decays as a power law as in the artificially isolated system.

These findings suggest that the signatures of MBL might be experimentally accessible in real glassy samples at ultra-low temperatures, for instance using ultra-fast laser probes. The dynamics we have depicted in this Chapter should be robust from material to material and against the uncertainty in the characterization of the disorder distributions.

6 Interface dynamics in the two-dimensional quantum Ising model

In this Chapter, I show how the dynamics of the two-dimensional Ising model can be solved in some sectors of physical interest. In Sec. 6.1 I introduce the model and show that, in the strong-coupling limit, the full Hamiltonian reduces to an effective "PXP" constrained Hamiltonian. Then, in Secs. 6.2 and 6.3 I show that, within certain sectors, the dynamical evolution is integrable if the coupling is infinite. In particular, in Sec. 6.3 I will show how to compute various quantities, and I will describe a connection to a relevant problem in contemporary mathematics. In Sec. 6.4 I will comment how integrability is broken when some of the assumptions are lifted, but also show that the timescales after which the breaking is manifest are very large. In Sec. 6.5 I will discuss at length the implications of having quenched disorder in the model: even if weak disorder breaks the integrability, and strong disorder is not able to form a stable localized phase, I will show that the dynamics undergoes a severe slowdown, and characterize it. Finally, in Sec. 6.6 I will draw the conclusions and hint at future developments. The Chapter is based on the publications [6, 8, 10].

As discussed in the Introduction, strongly interacting quantum many-body systems, evolving out of equilibrium, are generically expected to relax locally to thermodynamic equilibrium, after a short transient [376, 377]. In several cases, however, microscopic interactions support long-lived dynamical stages away from equilibrium. In the previous Chapters, we have focused on some systems that escape thermalization either by strong, quenched disorder (Chaps. 4 and 5) or by dynamical constraints (Chap. 3). Here, we move to formulate a general approach to analyze a wide class of non-ergodic, dynamical regimes of $2d$ quantum spin lattices.

For concreteness, we consider the quantum Ising model in two spatial dimensions, and inspect the non-equilibrium evolution of large domains (or bubbles) of negatively magnetized spins, initially prepared in a background of positively magnetized ones, as in Fig. 6.1a. We find that the limit of large Ising coupling $J \gg |h|, |g|$ (h and g are respectively the longitudinal and transverse fields) is amenable of several simplifications. In particular, for a large class of physically relevant initial states, characterized by the presence of a "smooth" interface, one can find a mapping to a one-dimensional lattice fermionic theory, which becomes integrable for $J \to \infty$. The integrability of this effective model is, of course, at the origin of ergodicity breaking: we will show, for example, that the corner of a large bubble melts and reconstructs itself periodically, with period $|g/h|$. This is to be expected, the model being integrable, and for the case of the corner we can point directly to the reason for this happening: the single-particle eigenstates of the dual fermionic theory are Wannier-Stark localized. More surprisingly, we find that even going away from the $J = \infty$ limit, in a perturbation theory in $g/J \ll 1$, the many-body eigenstates of the dual fermionic model are *Stark many-body localized* [378, 379], therefore reproducing

the whole MBL phenomenology, which gets uplifted back to the $2d$ quantum Ising model.

The phenomena investigated here have profound connections with important problems in contemporary physics and mathematics. First, they are the quantum counterpart of the dynamical nucleation of a region of true vacuum in a sea of false vacuum, which is a classic problem in statistical mechanics [380–382]. Most of the progress on the problem, however, has been achieved in the context of stochastic dynamics so far, since unitary quantum dynamics presents apparently insurmountable challenges. Undeniably, stochastic dynamics is often an adequate description of equilibrium condensed matter systems, such as magnets or crystal-liquid mixtures, due to the continuous influence of noisy, environmental degrees of freedom which act like a bath at a well-defined temperature. Nevertheless, there are situations in which one cannot rid of unitary quantum dynamical evolution of a pure initial state. For instance, this assumption is necessary in a cosmological setting: this was studied long ago by Kobzarev, Okun and Voloshin [383], and then by Coleman and Callan [384–386]; and it also found applications in inflationary models of the universe [387]. Furthermore, unitary evolution plays a crucial role in recent experiments with ultracold matter, as motivated above (see also Ref. [388] for a recent experiment in this direction). Finally, there are quantum optimization algorithms [240, 389, 390], which are designed to find the ground state of a classical Ising model (a computational NP-hard task), but can incur in several dynamical drawbacks associated to classical or quantum effects [238, 292, 391]. One can only expect that, in the near future, quantum simulators will allow finely controlled explorations of this physics using table-top experiments, allowing us to observe more counter-intuitive results of coherent quantum dynamics.

Second, our results show the presence of Hilbert space fragmentation in the $2d$ quantum Ising model: while this was already recognized in Refs. [392, 393], the dynamical implications of the shattering were left unaddressed. We show, instead, that analytical and numerical progress can be made on the problem, and we are able to predict the dynamical evolution of a large class of initial states. The timescales at which our analytical predictions start to break down are found to be exponentially large either in the linear size of the initial state, or in the coupling constant, thus making our description valid for most experimentally relevant situations.

Third, our mapping from the $2d$ Ising model to $1d$ confined fermions can also be interpreted as a toy model of duality between a theory of string (the domain wall) in 2+1 dimensions, and a theory of particles in one less dimension [394–396], which becomes integrable in the limit of infinite string tension. In our case, however, the confinement of the fermions is not due to their mutual interaction, but to an external potential.

Fourth, the dynamics at the corners of large bubbles in a $2d$ quantum ferromagnet turns out to be related to a measure concentration phenomenon for random Young diagrams, a well-known result to the mathematical community [397–400]. We will elaborate further on this point in Sec. 6.3.4, after having introduced the notation needed to make the connection precise, showing that a mapping to Young diagrams unveils connections with random integer partitions [400–402], determinantal point processes [403–405], and even Calabi-Yau manifolds [406, 407].

After having gone through all of the previous points, we will study also how the above picture gets modified if one instead starts from the two-dimensional quantum Ising model in presence of a random longitudinal field. The interest in the problem

stems from the fact that isolated quantum systems, out of equilibrium and in presence of disorder, can display a serious suppression of transport. Generically, they can pass from the usual diffusive dynamics at small disorder, to subdiffusive transport [408–411], and then finally to a localized regime (i.e. MBL), becoming effectively integrable systems.

Also for this latter lines of research, however, most of the results have been obtained in one spatial dimension. In dimensions two and higher, the existence of MBL beyond the original paper [46] and a few others [51, 308, 338, 412] is even more questionable. The main issue is that in $2d$ numerical results are limited to extremely small systems [345], and at the same time non-perturbative effects are thought to be stronger [112–114]. Some counterexamples are provided by two studies of dimer models in $2d$ [346, 413] which, because of the slow (though still exponential) growth of their Hilbert space dimension, can be studied up to 100 spins or so; and by some recent investigations on quasi-periodically-modulated $2d$ models [190–192]. Such studies show an MBL transition with the same confidence that it is seen in spin chains, giving hope that disorder can indeed localize in $2d$ following the same route that works in $1d$, at least for some particular microscopic Hamiltonians.

In the last part of this Chapter, we consider under the perspective of MBL the process of melting of a corner-shaped interface, separating a region of negatively magnetized spins from one of positively magnetized ones. This situation models an imperfect, two-dimensional quantum crystal. Also here, one can obtain an effective Hamiltonian, that is particularly suitable for interpreting the process in terms of the motion of the "crystal-liquid" interface. Such Hamiltonian is in the family of constrained PXP models [196–198], but with disordered terms. This difference is crucial: in the presence of disorder, in fact, PXP models have shown resilience towards localization already in $1d$ [199]. The explanation relies on the fact that the local disorder *before* the constraints are applied maps to *non-local* terms in the Hamiltonian, which escape in this way the usual arguments leading to localization in the perturbative limit. This is a first clue that makes us suspect that crystal melting cannot be stopped by disorder, no matter how strong the latter can be. We will exactly prove this working hypothesis: the dynamics of the crystal melting gets only slowed down—albeit quite dramatically—never stopping at any finite value of disorder. The fact that disorder in this case *helps* thermalization should not surprise: the integrability of the clean case is due to the free nature of the emergent excitations, therefore generic random terms in the Hamiltonian break the integrability, rather than constituting by themselves a source of MBL.

Because of the interplay of disorder and dynamical constraints, however, the delocalized nature of the emerging phase is rather peculiar. We find that, for any given system size, the eigenstate properties show some signs of localization, at least for disorder sufficiently large. However, the disorder strength for which localization is seen grows with the system size in a way which seems to indicate that no transition to MBL is present in the thermodynamic limit. Because of this, the dynamics is extremely slow: for example, the expected number of spin flips at time t grows like $\sim \log(gt)$, irrespective of the value of disorder. This is in contrast with other situations in which the delocalized side shows transport dictated by continuously changing exponents, that are functions of the disorder strength (see for example Refs. [133, 410, 411]).

6.1 Model

As anticipated in the Introduction, we are interested in the dynamics of the quantum Ising model on a two-dimensional square lattice. The Hamiltonian reads

$$H_{\rm Is} = -J \sum_{\langle ij \rangle} \sigma_i^z \sigma_j^z - g \sum_i \sigma_i^x - h \sum_i \sigma_i^z , \tag{6.1}$$

where $\sigma_i^{x,y,z}$ are Pauli matrices acting on a lattice site $i \in \mathbb{Z}^2$, $\langle ij \rangle$ indicates the restriction of the sum to nearest neighbors, g and h are the strength of the transverse and longitudinal magnetic fields, respectively, and $J > 0$ is the ferromagnetic coupling. We set $g > 0$, while we let h take both positive and negative values: the actual sign of h, indeed, will be relevant in Sec. 6.4.2. In Sec. 6.5, instead, we will allow the longitudinal field to take site-dependent values, and study the consequences of such quenched disorder on the dynamics.

In thermal equilibrium at temperature T, this model displays a quantum phase transition for $T = 0$ and $h = 0$, belonging to the universality class of the classical $3d$ Ising model: upon decreasing g below a critical value g_c, in fact, it passes from a quantum paramagnet to a quantum ferromagnet, characterized by two degenerate, magnetized ground states spontaneously breaking the $\mathbb{Z}_2$ symmetry. Upon increasing T, the ferromagnetic phase survives up to a finite critical temperature T_c (depending on g and J), since the energetic cost of creating domains with reversed magnetization increases upon increasing their perimeter (as entailed by Peierls' argument). At $g = 0$, the model becomes the $2d$ classical Ising model, therefore displaying the corresponding critical properties. These critical properties also characterize the transition occurring at the line of thermal critical points which joins the classical model at $g = 0$ to the quantum critical point at $T = 0$. The longitudinal field $h \neq 0$ breaks explicitly the $\mathbb{Z}_2$ symmetry of the two possible ground states, lifting their degeneracy. Accordingly, the model at $T = 0$ and $g < g_c$ undergoes a first-order quantum phase transition as h crosses 0. One expects that highly non-equilibrium false vacuum states exhibit a slow decay, through the nucleation of bubbles of characteristic size related to the inverse decay rate. With this background motivation in mind, we will be interested below in the fate of such bubbles, and more generally of interfaces, under the subsequent, coherent unitary evolution.

Studying the dynamics of $2d$ interacting models constitutes *a priori* a formidable task: numerical methods are limited to very small system sizes or very short times. In addition, analytical tools are restricted to near-equilibrium conditions or generally involve uncontrolled approximations, as dynamical mean-field theory [414] or kinetic equations [415].

Despite these shortcomings, insight can be obtained from suitable limits. While the extreme paramagnetic regime $J \ll |h|, g$ reduces to a set of weakly interacting "magnonic" excitations, the strong-coupling ferromagnetic regime $J \gg |h|, g$ retains great part of the interacting nature of the problem. It is the purpose of this Chapter to show that, in the strong-coupling limit, there exists a relevant class of highly excited non-equilibrium initial states, the dynamics of which is amenable of analytical treatment. In particular, in the next pages we show that the formal limit $J \to \infty$ of infinitely strong ferromagnetic coupling actually renders a highly non-trivial constrained dynamical problem, characterized by a fragmented Hilbert space.

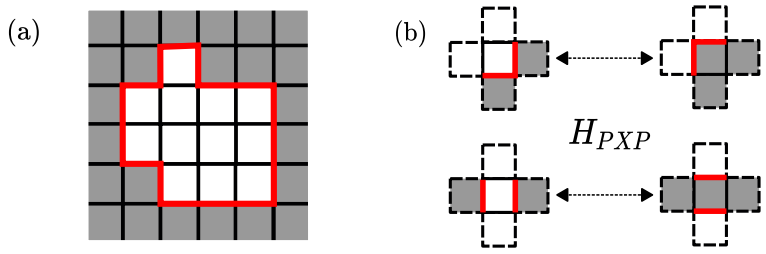

FIGURE 6.1: (a) Example of a "convex" (in the sense defined in Sec. 6.4.1) bubble of "up" spins ($\uparrow =$ □) in a sea of "down" spins ($\downarrow =$ ■). Here each spin is represented by the surrounding square plaquette in the dual lattice. The side of a plaquette separating neighbouring spins with the same or opposite orientation is marked in black or red, respectively, the latter corresponding to a portion of a domain wall. (b) Example of transitions allowed at the leading order in the coupling J, i.e. due to the term $\propto g$ in H_{PXP}, see Eq. (6.6). Flipping the central spin makes the part (highlighted in red) of the domain wall in the corresponding plaquette move as represented in the figure. The remaining possible moves (not displayed) are obtained by considering all the configurations of the central spin and its neighbours, with the constraint that two neighbours are up and two down. This figure is taken from Ref. [10].

6.1.1 Constrained dynamics in the strong-coupling limit

Starting from this Section, and throughout this Chapter, we will consider the strong-coupling limit, corresponding to $J \gg |h|, g$. In practice we start by formally taking $J = +\infty$, while later on in Sec. 6.4.2 we will relax this assumption. In this limit it is particularly convenient to study the problem in the basis of the Hilbert space provided by the eigenstates $\bigotimes_i |\uparrow/\downarrow\rangle_i$ of σ_i^z at each lattice site i, with $\sigma_i^z|\uparrow\rangle_i = |\uparrow\rangle_i$ and $\sigma_i^z|\downarrow\rangle_i = -|\downarrow\rangle_i$.

At the leading order in J, the model is actually diagonal (i.e., classical) in this basis and, up to a common constant, the energy of each of these eigenstates is given by $2J\ell$, where ℓ is the number of distinct pairs of neighbouring spins with opposite orientation. Accordingly, the Hilbert space $\mathcal{H}$ at infinite coupling is fragmented into dynamically independent sectors $\mathcal{H} = \bigoplus_\ell \mathcal{H}_\ell$, each sector being identified by ℓ [392]. Being $J = +\infty$, in fact, no transitions are actually allowed from a state in $\mathcal{H}_\ell$ to one in $\mathcal{H}_{\ell'}$, unless $\ell = \ell'$, since the energy difference between them would be infinite. Note that, equivalently, ℓ measures the total length of the domain walls which are present on the lattice, separating the regions with spins $\sigma_i^z = +1$ from those with $\sigma_i^z = -1$. Accordingly, in the limit $J \to \infty$, *dynamical constraints* emerge, in the form of a *perimeter constraint* on the bubbles of spins aligned along the same direction.

As a consequence of the perimeter constraint, the dynamics of the model can be effectively studied by focusing on each sector $\mathcal{H}_\ell$ separately, thereby reducing significantly the complexity of the problem. Let us start by determining the reduced Hamiltonian in $\mathcal{H}_\ell$ by elementary reasoning. Since the total domain wall length must be conserved, the only spins that can be flipped by the term $\propto g$ in Eq. (6.1) are those that just displace an existing domain wall. Considering the 16 possible configurations of the four spins Li/Ri/Ui/Di which are, respectively, left/right/above/below a site $i \in \mathbb{Z}^2$) and which can be up ($\uparrow$) or down ($\downarrow$), one easily gets convinced that the only allowed transitions are those generated by the following reduced Hamiltonian:

$$H_{\text{PXP}} = -h\sum_i \sigma_i^z - g\sum_i \big(P^{\uparrow}_{\text{L}i}P^{\uparrow}_{\text{D}i}\sigma_i^x P^{\downarrow}_{\text{R}i}P^{\downarrow}_{\text{U}i} + P^{\uparrow}_{\text{L}i}P^{\downarrow}_{\text{D}i}\sigma_i^x P^{\downarrow}_{\text{R}i}P^{\uparrow}_{\text{U}i} + P^{\downarrow}_{\text{L}i}P^{\downarrow}_{\text{D}i}\sigma_i^x P^{\uparrow}_{\text{R}i}P^{\uparrow}_{\text{U}i} + P^{\downarrow}_{\text{L}i}P^{\uparrow}_{\text{D}i}\sigma_i^x P^{\uparrow}_{\text{R}i}P^{\downarrow}_{\text{U}i} + P^{\uparrow}_{\text{L}i}P^{\downarrow}_{\text{D}i}\sigma_i^x P^{\uparrow}_{\text{R}i}P^{\downarrow}_{\text{U}i} + P^{\downarrow}_{\text{L}i}P^{\uparrow}_{\text{D}i}\sigma_i^x P^{\downarrow}_{\text{R}i}P^{\uparrow}_{\text{U}i}\big), \quad (6.2)$$

where we introduced the projectors

$$P_i^{\uparrow} := \frac{1+\sigma_i^z}{2} = |\uparrow\rangle\langle\uparrow|, \qquad \text{and} \qquad P_i^{\downarrow} := \frac{1-\sigma_i^z}{2} = |\downarrow\rangle\langle\downarrow|. \tag{6.3}$$

The term $\propto h$ in Eq. (6.1), being diagonal in σ_i^z, is instead unaffected. One can recognize that Eq. (6.2) has the structure of a so-called PXP Hamiltonian [416].

The elementary procedure outlined above can be viewed as the first step of a systematic elimination, from a Hamiltonian with large energy gaps, of highly non-resonant transitions. This is formally implemented by an order-by-order unitary transformation known as Schrieffer-Wolff transformation [417]. In Sec. 6.4.2 we will be concerned with the possible additional contributions to Eq. (6.2) due to higher-order corrections $O(J^{-1})$.

It is important to stress that the constrained Hamiltonian (6.2) is similar to the one describing strongly interacting Rydberg atom arrays [418, 419] in the regime of Rydberg blockade, given by

$$H^0_{\text{Ryd}} = \frac{\Delta}{2}\sum_i \sigma_i^z + \Omega \sum_i P^{\downarrow}_{\text{L}i} P^{\downarrow}_{\text{D}i} \sigma_i^x P^{\downarrow}_{\text{R}i} P^{\downarrow}_{\text{U}i}. \tag{6.4}$$

Here, each spin-1/2 describes a trapped neutral atom, which can be in either its ground state ($\downarrow$) or in a highly excited Rydberg state ($\uparrow$). The effective Hamiltonian that describes a lattice of such strongly interacting atoms reads [418]

$$H_{\text{Ryd}} = \Delta \sum_i n_i + \Omega \sum_i \sigma_i^x + \sum_{i,j} V_{ij} n_i n_j \tag{6.5}$$

where $n_i = (1+\sigma_i^z)/2$ counts the local number of atoms excited to the Rydberg state, and the interaction V_{ij} is very strong for neighboring sites and decays rapidly with the distance. The Rydberg-blockaded effective Hamiltonian (6.4) arises from setting $V_{ij} \to \infty$ for neighboring atoms $\langle i,j\rangle$ and $V_{ij} = 0$ otherwise. In this case, pairs of neighboring excited atoms are completely frozen, and an atom can flip only if all its four neighbors are in the ground state, which is expressed by the last term in Eq. (6.4). Our constrained Hamiltonian in Eq. (6.2), instead, arises from strong $\sigma_i^z\sigma_j^z$ rather than $n_i n_j$ interactions. This results in a different form of the constraint, which implements the local perimeter-conserving motion of domain walls.

It is interesting to note that the two constraints differ only by a strong longitudinal field term, which can be adjusted to transform one into the other. Specifically, identifying $V \equiv -4J$, it suffices to take a single-atom energy level detuning $\Delta \equiv 2J + h$ to obtain the Ising model (6.1) and hence, in the regime of Rydberg-blockade, the effective Hamiltonian Eq. (6.2)[1].

The Hamiltonian in Eq. (6.2) can be alternatively written via a shorthand notation which describes graphically the transitions induced on the domain wall (in red) possibly existing around the square plaquette surrouding a spin (see also Fig. 6.1):

$$H_{\text{PXP}} = -h\sum_i \sigma_i^z - g\sum_i \Big(|\ulcorner\rangle_{ii}\langle\lrcorner| + |\llcorner\rangle_{ii}\langle\urcorner| + |\!=\!\rangle_{ii}\langle\,\|\,\| + \text{h.c.}\Big). \tag{6.6}$$

Here, the action of the transitions due to the coupling g is apparent: they can either move a domain wall corner across the diagonal of a plaquette ($|\ulcorner\rangle_{ii}\langle\lrcorner| + |\llcorner\rangle_{ii}\langle\urcorner| +$

[1] We note, however, that this might be problematic at experimental level, as the Rydberg interactions are very sensitive to the precise position of the trapped atoms, resulting in unwanted noisy fluctuations of the longitudinal field.

$|\sqcup\rangle_{ii}\langle\sqcap| + |\sqcap\rangle_{ii}\langle\sqcup|$) or recombine two parallel segments of the domain wall across opposite sides of the square plaquette ($|\sqsupset\sqsubset\rangle_{ii}\langle\mathrm{I}\ \mathrm{I}| + |\mathrm{I}\ \mathrm{I}\rangle_{ii}\langle\sqsupset\sqsubset|$). The conservation of the domain wall length is thus guaranteed by construction.

6.1.2 Hilbert space fragmentation

The convenient notation of Eq. (6.6) makes it possible to analyze the fate of the dynamics of large portions of the $2d$ lattice in numerous cases. For instance, consider multiple non-neighboring spins oriented up, i.e. with $\sigma^z = +1$, embedded in a sea of oppositely aligned spins, with $\sigma^z = -1$. This configuration is fully frozen, as no allowed transition can shift any of the domain walls. Thus, all of these states are eigenstates of the constrained Hamiltonian (6.6). This simple example—easily generalizable to many others [392]—shows that individual sectors $\mathcal{H}_\ell$ are, in general, further heavily fragmentated. More formally, one can introduce the notion of *Krylov subspace* of a state $|\psi_0\rangle$: by definition, it is the subspace of $\mathcal{H}$ spanned by the set of vectors $\{|\psi_0\rangle, H|\psi_0\rangle, H^2|\psi_0\rangle, \dots\}$. With this definition, one recognizes that the Krylov sector of a state $|\psi\rangle \in \mathcal{H}_\ell$ may not coincide with the full $\mathcal{H}_\ell$, but instead represent a finer shattering. A detailed study of the Krylov sectors of the model under consideration was carried out in Ref. [393]; in this Chapter, instead, we will be concerned mainly with the *dynamical effects* of the fragmentation on some physically relevant states. This is exactly what we will start studying with the next Section.

6.2 Infinite coupling dynamics

In the previous Section we have argued that, in the limit of large J, the dynamics of the $2d$ quantum Ising model greatly simplifies because of the presence of emergent constraints. Here, we show that this simplification is really substantial in some particular cases, insofar it leads to simple *one-dimensional effective models*.

From Eq. (6.6), one can see that the first two transition matrix elements (namely, $|\sqcap\rangle_{ii}\langle\sqcup| + \text{h.c.}$ and $|\sqcup\rangle_{ii}\langle\sqcap| + \text{h.c.}$) correspond to the translation of a domain wall, while the last one (namely, $|\sqsupset\sqsubset\rangle_{ii}\langle\mathrm{I}\ \mathrm{I}| + \text{h.c.}$) cuts two domain walls and recombines them in the switched configuration. If the initial condition has a geometry that allows only one of the two types of transitions, then it is possible to have some analytical control on the dynamics. In particular, we will show in Sec. 6.2.1 that initial conditions consisting of a thin, pseudo-$1d$ domain only allow interface-recombining moves. This allows us to make a connection with $1d$ PXP and confining Ising models. In Sec. 6.2.2, instead, we show that if the $2d$ lattice is cut by a single, Lipschitz-continuous (the meaning of this will become clear later on) interface, then the interface dynamics can be studied by an effectively $1d$ model, which turns out to be a model of non-interacting fermions. This emergent integrability allows us to calculate the $2d$ evolution exactly, and to describe precisely how ergodicity is broken.

6.2.1 Strip-like configurations

In this Section we consider a particular type of initial configurations, that are essentially one dimensional. As it was already pointed out in Ref. [392], for this type of states, it is possible to make an explicit connection with $1d$ PXP models. We show here that, when the initial configuration $|\Psi_0\rangle$ has no overlap with scarred states, it is possible to compute the long-time magnetization of the bubble, and it can be expressed in terms of the golden ratio ϕ, as a consequence of the dimension of the Krylov sector of $|\Psi_0\rangle$.

As anticipated, let us consider a particularly simple initial condition for the dynamics of the $2d$ Ising model in the limit of infinite coupling: a linear strip of L "down" spins ($\downarrow$), surrounded by "up" spins ($\uparrow$). In the Krylov sector dynamically accessible from this configuration, in absence of longitudinal magnetic field, the PXP Hamiltonian (6.2) reduces to the one-dimensional PXP Hamiltonian familiar from tilted bosonic traps [196], one-dimensional Rydberg-blockaded arrays [32], or dimer models [420]. To see this, observe that no spin outside the strip can ever be flipped by H_{PXP}, so the only dynamical degrees of freedom are the spins initially set to be "down". This reduces the full, $2d$ dynamics to an effectively $1d$ dynamics. Let us mention in passing that, if instead a longitudinal magnetic field is turned on, a peculiar phase diagram is found for its ground state [32].

We label accessible basis states by the $1d$ configuration of the spins in the strip; the initial state is thus denoted $|\Psi_0\rangle \equiv |\downarrow\downarrow \dots \downarrow\rangle$. Assuming for the moment $h = 0$, the Hamiltonian (6.2) reduces to

$$H_{\text{PXP,1d}} = -g \sum_{j=2}^{L-1} P^{\downarrow}_{j-1} \sigma^x_j P^{\downarrow}_{j+1}, \tag{6.7}$$

as the spins above and below are fixed to be up. Because of the perimeter constraint, the first and last spin cannot be flipped.

Because of the constraints, not all $1d$ configurations are dynamically accessible. Denoting by l the number of dynamical spins reversed wrt. the initial configuration, the number of accessible basis states at fixed l satisfies the recursion relation (see also App. D.1)

$$C(L, l) = C(L-1, l) + C(L-2, l-1), \tag{6.8}$$

which has solution

$$C(L, l) = \binom{L-l-1}{l}, \tag{6.9}$$

once the initial condition $C(L, 0) = 1$ for all L is enforced. The maximum number of spins that can be flipped satisfying the perimeter constraint is

$$n_{\max} = \left\lceil \frac{L-2}{2} \right\rceil, \tag{6.10}$$

and the total number of accessible configurations is therefore the Fibonacci number

$$F_L = \sum_{l=0}^{l_{\max}} C(L, l). \tag{6.11}$$

It is worth recalling that the PXP Hamiltonian exhibits quantum many-body scars [416], i.e. particular eigenstates that violate the eigenstate thermalization hypothesis. The number of such eigenstates increases only algebraically with the system size, making them very rare in the many-body spectrum. However, they profoundly affect the dynamical properties of particular initial configurations such as the Néel state $|\mathbb{Z}_2\rangle = |\downarrow\uparrow\downarrow\uparrow \dots\rangle$, which exhibits remarkable long-lived revivals discovered in early experimental explorations [177]. While it has become clear that these non-thermal eigenstates slowly disappear in the large-size limit of the PXP model, their ultimate origin is still presently unclear, despite significant research efforts, and is the subject on an active ongoing debate [178]. On the other hand, our initial state $|\Psi_0\rangle$ is not significantly affected by quantum many-body scars [178, 416].

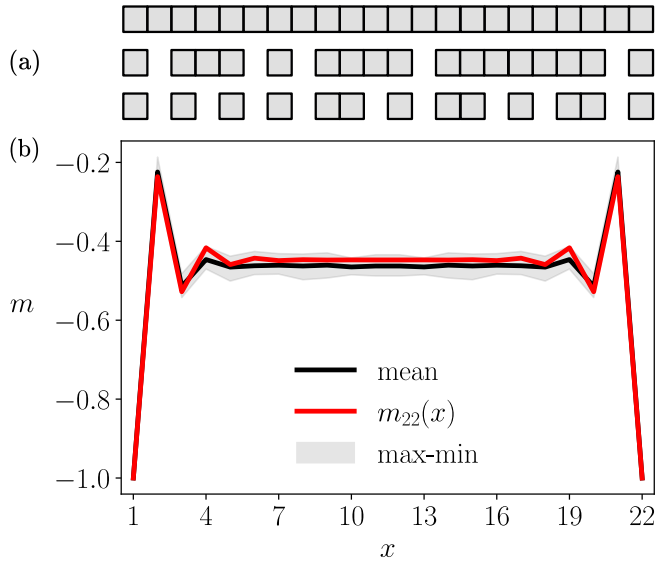

FIGURE 6.2: (a) Example of some strip configurations, with the initial state depicted in the top row, while a completely fragmented configuration is displayed in the bottom row. (b) Magnetization along the strip of panel (a) at equilibrium. The comparison between theoretical ($m_{22}(x)$, in red) and numerical results for the magnetization is reported. The plot shows the minimum and maximum magnetization for $5000 < t < 10000$ (shaded gray area) and the magnetization for $t = 10000$ (black). One can see a good agreement between numerical simulation and theoretical prediction, showing that the classical sampling performed is effective in describing the infinite-temperature magnetization. This figure is taken from Ref. [10].

Therefore, it is expected that the equilibrated magnetization profile along the chain at long times is compatible with an assumption of ergodicity, i.e. all allowed configurations will be occupied with uniform probability. Within this assumption, the long-time magnetization at position j along the strip is

$$\langle m_L(j)\rangle = 2\frac{F_{L-j}F_{j-1}}{F_L} - 1 \tag{6.12}$$

(see App. D.1 for the complete computation). The resulting profile is compared with numerical simulations in Fig. 6.2 for short strips, showing fairly good agreement with the assumption of ergodicity.

As a further step, one can compute the magnetization in the middle of the strip in the thermodinamic limit. Sending first $L \to \infty$, and then $j \to \infty$ in Eq. (6.12), one finds

$$\langle m_{\infty,\text{bulk}}\rangle = \frac{2}{(2\phi-1)\phi} - 1 = -\frac{1}{\sqrt{5}}. \tag{6.13}$$

Above, the properties of the Fibonacci numbers were used, and it was introduced the golden ratio ϕ. The value $\langle m_{\infty,\text{bulk}}\rangle$ is reached exponentially fast in the distance from the boundary, with a characteristic length $1/\log|\phi^{-1}-1|$. The complete derivation is reported in App. D.1.

We conclude this Section by noting that what we have done, essentially, was to compute local observables in the infinite-temperature ensemble, instead of computing the expectation values on $|\Psi_0(t)\rangle$. The two procedures are equivalent, since

the initial state $|\Psi_0\rangle$ lies in the middle of the spectrum (and thus is an infinite-temperature state)[2], and the $1d$ PXP model is ergodic [178, 416]. These facts also imply that any other classical initial configuration lying at the middle of the spectrum has the same properties at long times, provided that it does not overlap significantly with non-thermal energy eigenstates.

6.2.2 Smooth domain walls

In the previous Section we considered strip-like initial configuration, whose dynamics involved only the operators $|\sqsupset\rangle\langle| \; |$ + h.c. of Eq. (6.6), i.e. only domain-wall breaking transitions. We now turn to a different family of initial states, for which instead only the operators $|\llcorner\rangle\langle\urcorner|$ + h.c. or $|\ulcorner\rangle\langle\lrcorner|$ + h.c. are allowed, i.e. only domain-wall moving transitions.

Let us start by rotating, for later convenience, the square lattice by a $\pi/4$ angle with respect to the vertical and horizontal directions; in other words, orient the lattice so that its axes are along the NW-SE and SW-NE directions (as shown in Fig. 6.3). Then, let us consider an interface separating a domain of spins "up" ($\uparrow$) from one of spins "down" ($\downarrow$). We require that such interface vary only slowly, so that it can be thought of as the graph of a function (in the rotated setting). We make this statement more clear in Fig. 6.3: the interface should be described by a function $\mu : \mathbb{Z} \to \mathbb{Z}$ that is "Lipschitz-continuous", i.e.

$$|\mu(x) - \mu(y)| \leq |x - y|, \qquad \forall x, y \in \mathbb{Z}. \tag{6.14}$$

Initial states of this type, other than being rather generic in the context of interface dynamics, are interesting as they can be described by an equivalent one-dimensional system. The mapping simply consists in associating to each NW-SE segment an empty site on the $1d$ chain, and to each SW-NE a site occupied by a particle (see Fig. 6.3). Let us notice that such mapping is, basically, a differentiation procedure: one associates an empty (resp. occupied) site if the domain-wall derivative is negative (resp. positive). Consequently, the interface profile $\mu(x)$ can be obtained via "integration" of the density profile $n(x)$ on the chain:

$$\mu(x) = \sum_{y \leq x} n(y) + \text{const.} \tag{6.15}$$

The mapping described above works also in a classical setting, where a fluctuating interface induces on the $1d$ particles an effective dynamics, as the simple exclusion processes [422–424] (see also the discussion at the end of Sec. 6.3.1). In the quantum setting, one should also pay attention to what is the statistics of the particles. For the case under consideration—i.e. the $2d$ quantum Ising model—such particles should be hard-core bosons, as different sites commute, and there can be no more than one particle for each site. Applying a Jordan-Wigner transformation, the hard-core bosons can then be equivalently represented as fermions. From now on we will only restrict to this latter, more convenient representation.

Having set up the mapping for the accessible basis states, we can proceed to map the $2d$ PXP Hamiltonian to a $1d$ Hamiltonian on the chain. With a bit of reasoning one notices that to each spin flip in $2d$ there corresponds a fermion hop on the chain. At the same time, due to the longitudinal magnetic field, each spin flip in $2d$ contributes

[2] That $|\Psi_0\rangle$ lies in the middle of the spectrum follows from the fact that, first, it holds $\langle\Psi_0| H |\Psi_0\rangle = 0$; and second, that the spectrum is symmetric around zero ($H_{\text{PXP,1d}}$ commutes with the space reflection operator I, and anti-commutes with the spectral reflection operator $C = \prod_j \sigma_j^z$ [421]).

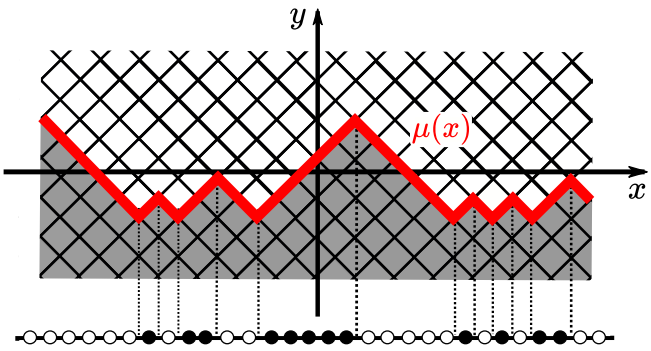

FIGURE 6.3: Graphical representation of the mapping from the $2d$ Lipschitz interface to the $1d$ fermionic chain. Moving from left to right, to each down-going line it corresponds an empty site on the chain, while an occupied site is associated to each up-going line. Notice that, in the projection process, the lattice spacing on the chain is reduced by a factor $\sqrt{2}$ compared to the original one on the $2d$ lattice. This figure is taken from Ref. [10].

with a $\pm 2h$ energy difference depending on the vertical direction of the domain-wall transition, and therefore every fermion hop must account for the same energy change. Thus, the fermionic Hamiltonian reads

$$H_{\mathrm{F}} = -g \sum_x \left(\psi_x^\dagger \psi_{x+1} + \mathrm{h.c.} \right) + 2h \sum_x x \, \psi_x^\dagger \psi_x, \tag{6.16}$$

up to che choice of the origin of x.

Equation (6.16) is the well-known Wannier-Stark Hamiltonian [425]. It is diagonalized by the unitary transformation

$$b_m = \sum_x J_{x-m}(\gamma) \, \psi_x \tag{6.17}$$

with $\gamma := g/h$ and $J_\nu(z)$ the Bessel function of the first kind, yielding

$$H_{\mathrm{F,diag}} = 2h \sum_{m \in \mathbb{Z}} m \, b_m^\dagger b_m. \tag{6.18}$$

The energy spectrum is thus given by a set of equally spaced levels $E_m = 2hm$, insensitive to g. We anticipate that this feature will be important in the later discussion about non-ergodicity in Secs. 6.4.2–6.4.3.

We are now able to give the general description of the dynamics of any "Lipschitz" initial state. The initial configuration is expressed as

$$|\Psi_0\rangle = \prod_k \psi_{x_k}^\dagger |0\rangle \tag{6.19}$$

on the chain, where the sequence $\{x_k\}_{k \in \mathbb{Z}}$ contains the sites occupied at $t = 0$. Time-evolving the operators b_m, one finds $b_m(t) = b_m(0) e^{-2iht m}$, and thus

$$\psi_x(t) = \sum_{m,y} J_{x-m}(\gamma) J_{y-m}(\gamma) e^{-2iht m} \psi_y(0). \tag{6.20}$$

For the average density it follows, using Wick contractions and the completeness relation of the Bessel functions (Eq. (D.62)),

$$\langle n(x,t)\rangle = \sum_{y,z}\sum_{k} J_{x_k-y}(\gamma)J_{x_k-z}(\gamma)J_{x-y}(\gamma)J_{x-z}(\gamma)e^{-iht(z-y)} \tag{6.21}$$

$$= \sum_{k} J^2_{x_k-x}(\omega_t), \tag{6.22}$$

where we defined the averages over the initial state

$$\langle A\rangle := \langle \Psi_0|\, A\, |\Psi_0\rangle \tag{6.23}$$

and

$$\omega_t := 2|\gamma \sin(ht)| = 2\left|\frac{g}{h}\sin(ht)\right|. \tag{6.24}$$

It is interesting to notice that, by time reversal symmetry, Eq. (6.22) can be also interpreted as the total probability of finding a single particle starting at x at time 0, in the subset $\{x_k\}$ at time t.

Equation (6.22) can also be rewritten in the continuum as

$$\langle n(x,t)\rangle = \int dy\, \rho(y) J^2_{y-x}(\omega_t), \tag{6.25}$$

having introduced the density

$$\rho(y) = \sum_k \delta(y - x_k). \tag{6.26}$$

The above expressions are valid in full generality, for any Lipschitz initial state on the lattice. When the continuum limit is considered (see Sec. 6.3.1 and App. D.3 for details), the comb-like function $\rho(y)$ in Eq. (6.26) is replaced with a smooth function, that is obtained by properly rescaling the coordinates with the lattice spacing.

Equations (6.22) and (6.24) entail that the dynamics on the chain is perfectly periodic, with period π/h: this is due to the *Bloch oscillations* on the chain [425], which localize each fermion near to its original position. Such perfect localization is a feature of the $J = +\infty$ limit, and of the presence of a nonzero longitudinal field h. If instead one takes $h \to 0$, one finds $\omega_t = 2|gt|$. Thus, the dynamics become in general ballistic, as the underlying fermionic excitations are free to move. In Secs. 6.4.2 and 6.4.3 we will investigate, on the other hand, to what extent the localization is preserved at finite but large J, and nonzero h.

Normally, the integral in Eq. (6.25) for $\langle n(x,t)\rangle$ cannot be computed in closed form, even if the expression is valid in full generality in the set of initial configurations we are considering, once the initial distribution $\rho(y)$ is specified. However, in some special cases it can be done. As an example, take $x_k = sk$ for some $s \in \mathbb{N}$, $s \geq 1$: thus, the initial state is a sequence of particles alternated by $s-1$ empty sites. One can compute the average profile $\mu(x,t)$ as follows: start from the average number density on the chain

$$\langle n(x,t)\rangle = \sum_k J^2_{sk-x}(\omega_t) = \frac{1}{s}\sum_{0\leq n<s} e^{2ixn\pi/s} J_0\left(2\omega_t \sin\frac{n\pi}{s}\right), \tag{6.27}$$

where the last step may be carried out using the integral representation of the Bessel functions (Eq. (D.55)). Notice that this equation, in the continuum limit (see App. D.3 for details), leads to $\langle n(x,t)\rangle = 1/s$: only the term $n = 0$ contributes for large x

because of the oscillating exponential. This is the expected result, as it corresponds to the average occupation along the chain in the initial condition. After a summation over space in Eq. (6.27), as prescribed by the mapping of Eq. (6.15), one is able to obtain the average shape of the interface. In the continuum limit this corresponds to $\langle \mu(x,t) \rangle = x(2/s - 1)$. In principle, also the fluctuations of the average shape can be computed with similar techniques, as we will do in the next section for a particular type of Lipschitz interface.

6.3 A particular initial condition: the infinite corner

In the previous Section we have studied two particular cases for which the dynamical constraints emerging at infinite J simplify so much the dynamics, that it can be described by an equivalent $1d$ model. In this Section we build on the case of Sec. 6.2.2, by considering a single interface shaped as in Fig. 6.4a: that is, an interface composed of two straight lines (parallel to the lattice directions) and a single, right-angled corner. This interface is "Lipschitz-continuous" in the sense of Eq. (6.14), so all the techniques of Sec. 6.2.2 can be applied.

The case of a corner-shaped interface is particularly instructive, because of several connections to other fields of physics and mathematics:

1. The evolution of a right-angled interface can be thought of as the quantum version of *corner growth models* commonly studied in classical, non-equilibrium statistical mechanics [405, 422, 426, 427]. Such models can be used to describe the process of erosion of crystals; thus our case here extends the melting phenomenon to *quantum* crystals [428, 429]. Indeed, while a straight interface (of the type considered in Sec. 6.2.2) can only fluctuate around its position at $t = 0$, the corner configuration can be eroded indefinitely (if no other localization mechanism is present, as we will discuss below). However, there is a caveat: for the model under consideration, the addition/removal of a block from the corner is always a *coherent* process, as if the removed blocks do not dephase in the liquid state before being reattached to the solid.

2. To every configuration that is dynamically connected to the corner there corresponds a *Young diagram*, as we detail in Sec. 6.3.4. We will show an interesting connection between two seemingly unrelated measures on such diagrams: the probability density of a quantum fluctuating interface, coming from the side of the $2d$ Ising model, and the Plancherel measure, commonly studied in representation theory [397–401, 406, 430].

3. Lastly, it is worth mentioning that the case of a corner the mapping to free fermions points to an explicit form of *holography*, where a two-dimensional quantum problem is mapped, in strong-coupling limit, to a free, simpler problem in one less spatial dimension. This is reminiscent of the AdS/CFT duality [394–396]: the interface in the Ising model is the string in two spatial dimensions (plus time), while the non-interacting fermions on the chain are the dual field theory. When the string tension J is large, the corresponding field theory is free. When the string tension decreases, the field theory becomes interacting and, in our case, non-integrable anymore. However, if one would like to discuss the melting of a bubble and not a simple corner, one should necessarily introduce a more complicated theory of fermions, possibly with many species. It worth noticing that going back further in time, one finds the conjecture that the $3d$ Ising model be dual to a weakly-coupled string theory [431, 432] (for a

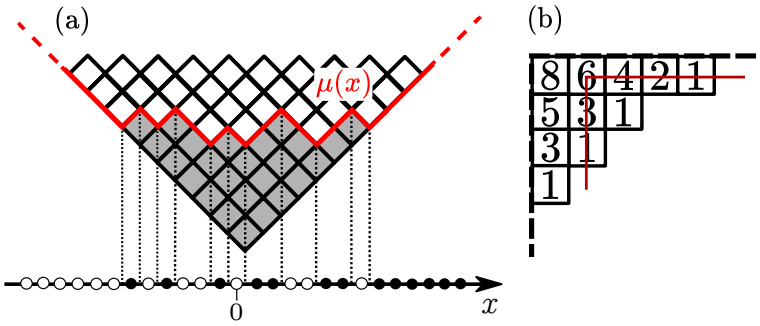

FIGURE 6.4: (a) Visual representation of the mapping introduced Sec. 6.2.2 applied to the corner configuration. The squares highlighted in gray correspond to the eroded area, that is forming a Young diagram. The interface $\mu(x)$ is displayed in red. (b) An example of Young diagram with the hook $\mathfrak{h}(\square)$ indicated for each element $\square$. The hook length formula prescribes that, for each box $\square$, its hook is obtained by summing the number of boxes below it and at its right, plus one. The red curve $\Omega(v)$, see Eq. (6.34), represents the shape to which the Young diagrams converge, in the Plancherel probability measure, in the limit of large N. This figure is taken from Ref. [10].

recent discussion see Ref. [433]), although that is supposed to hold only at the critical point.

As discussed in great details in Sec. 6.3.1, we will present the results for the dynamics taking as initial condition a perfect corner, corresponding to a domain wall configuration on the fermion chain. Let us underline that, for finite $h \neq 0$, this initial configuration is close to the ground state of the Krylov sector it belongs to. While in the limit $J = \infty$ this observation in marginal, as the system is integrable (thus any initial configuration leads to a non-ergodic behavior), it becomes relevant at finite J, where the behavior of states at the middle of the spectrum can be also qualitatively different from the ones at the edges.

6.3.1 Average of the interface and its continuum limit

Let us start by noticing that, in the language of Sec. 6.2.2, a corner-shaped initial state corresponds on the fermionic chain to a $1d$ domain-wall configuration:

$$|\Psi_0\rangle = \prod_{x>0} \psi_x^\dagger |0\rangle \,. \tag{6.28}$$

In the language of electronics, this would be called a "maximum voltage bias" Fermi sea (vacuum on the left, full on the right). Applying the same methods used previously (in particular Eq. (6.22)), one easily gets the form of the density profile on the chain:

$$\langle n(x,t)\rangle = \sum_{y<x} J_y^2(\omega_t) \,. \tag{6.29}$$

With a further summation over space (cf. Eq. (6.15)), one obtains the average interface profile:

$$\langle \mu(x,t)\rangle = 2\sum_{y\leq x}(x-y)J_y^2(\omega_t) - x. \tag{6.30}$$

The above expressions somewhat simplify in the continuum limit, which is valid in the regime in which the oscillation amplitude is much larger than the lattice spacing a. Thus, the correct prescription is to take both $a \to 0$ (so that one passes to the continuum) and $h \to 0$ (otherwise the dynamics is confined into a finite region

by Bloch oscillations). To do so, as we detail in App. D.3, it is sufficient to rescale $\gamma \to \gamma/a$ in Eqs. (6.29)–(6.30), where we recall $\gamma := g/h$. The resulting expression for $n(x,t)$ is

$$\langle n(ax,t)\rangle = \sum_{y<x} J_y^2\left(\frac{\omega_t}{a}\right). \tag{6.31}$$

The continuum limit leads to (see App. D.3 or Ref. [434])

$$\langle n(x,t)\rangle = \begin{cases} 0 & x \le -\omega_t \\ \frac{1}{2} + \frac{1}{\pi}\arcsin\frac{x}{\omega_t} & -\omega_t < x \le \omega_t \\ 1 & x > \omega_t. \end{cases} \tag{6.32}$$

Integrating wrt. x, one determines

$$\langle \mu(x,t)\rangle = \omega_t\,\Omega\left(\frac{x}{\omega_t}\right) \tag{6.33}$$

with

$$\Omega(v) = \begin{cases} |v| & |v| \ge 1, \\ \frac{2}{\pi}\left(\sqrt{1-v^2} + v\arcsin v\right) & |v| < 1. \end{cases} \tag{6.34}$$

The function $\Omega(v)$ first appeared in the context of random Young diagrams [397–399]; we will elaborate more on this point in Sec. 6.3.4. Here, instead, we flash out a connection with *classical* melting processes: the hard-core particles on the $1d$ chain, indeed, can be given a classical stochastic dynamics, as in the simple exclusion process (SEP) [405, 422, 423]. In the cases of the symmetric or totally asymmetric SEP (SSEP or TASEP, respectively), an analytic solution is possible [424, 435–437], and the long-time behaviour of the density of particles can be found. The scaling functions describing the erosion of the corner, however, turn out to be parabolas—a different functional form wrt. Ω of Eq. (6.34). This fact points at the conclusion that the concentration of measure in the thermodynamic limit is *not* a simply entropic phenomenon, but it really depends on the underlying microscopic dynamics. This will become evident from the discussion in Sec. 6.3.4.

6.3.2 Fluctuations of the interface

With techniques similar to those of the previous Section, the fluctuations of the interface can be obtained as well. While leaving the full computation to App. D.2, we report here the final result for the connected 2-point function:

$$\langle n(x,t)n(y,t)\rangle_C = \delta_{xy}\sum_{i>0} J_{i-x}^2(\omega_t) - \mathcal{B}(x,y;\omega_t)^2, \tag{6.35}$$

where we introduced the *Bessel kernel*

$$\mathcal{B}(x,y;\omega) := \omega\frac{J_{x-1}(\omega)J_y(\omega) - J_x(\omega)J_{y-1}(\omega)}{2(x-y)}. \tag{6.36}$$

Notice that, for $x = y$, Eq. (6.35) straightforwardly reduces to

$$\langle n(x,t)^2\rangle_C = \langle n(x,t)\rangle\left(1 - \langle n(x,t)\rangle\right), \tag{6.37}$$

a trivial statement for fermionic particles. Summing over x and y in Eq. (6.35)—thus applying the prescription of Eq. (6.15)—leads to the 2-point function of the interface

profile $\langle \mu(x,t)\mu(y,t)\rangle_C$.

It is instructive to discuss the continuum limit also for the fluctuations of the shape μ. As they involve the Bessel kernel Eq. (6.36), they are tightly linked to the universal fluctuations found in Laguerre and Jacobi ensembles of random matrices [438], and of random representations of the symmetric group [430]. In particular, the presence of the Bessel functions entails a *light-cone structure* for the correlations, see Fig. 6.5a: if either $|x| \gg \omega_t$ or $|y| \gg \omega_t$, then the correlations are exponentially suppressed (as follows from the large-index asymptotics of the Bessel function, Eq. (D.67)). If instead both $x, y \ll \omega_t$, then by virtue of the large-argument asymptotics of the Bessel functions (Eq. (D.68)), the kernel reduces to the *sine kernel*

$$\mathcal{S}(x,y) = \frac{\sin\left(\frac{\pi}{2}(x-y)\right)}{\pi(x-y)}. \tag{6.38}$$

The sine kernel is found in numerous contexts in physics and mathematics, among which gaussian ensembles of random matrices [439], and free fermion chains *without* a linear potential [440]. Notice that, in passing from the Bessel kernel to the sine kernel, the dependence on ω_t has dropped out, while it remains implicit in the maximum value attained by x or y (i.e. the border of the light cone).

Finally, a less trivial limit takes place in a region of order $\omega_t^{1/3}$ around the light cone, where by means of a uniform expansion (Eqs. (D.69)–(D.70)) the Bessel kernel reduces to the celebrated Airy kernel [441, 442]. Notwithstanding all of the connections, we stress that in this quantum setting the fluctuactions are given by the *square* of the Bessel kernel, see Eq. (6.35): thus, they are quantitatively different from the cited cases, which involve the kernels without the square.

6.3.3 Entanglement dynamics

Being the "holographic" description of the cornered interface in terms of an integrable $1d$ model (viz. free fermions), much more information besides averages and correlations can be extracted, using the vast amount of analytical techniques developed in recent years [16, 200, 443, 444]. For instance, one can compute the so-called *full counting statistics*, i.e. the probability distribution of the fermions, with the techniques of Ref. [445]. Or else, one can partition the lattice in two halves, by means of a "vertical" line (e.g. through the corner, corresponding to the time axis in Fig. 6.5a), and compute the entanglement growth accross the bipartition. The computation goes as detailed in Ref. [446]: from the eigenvalues $\zeta_l(t)$ of the correlation matrix $\mathcal{C}_{xy}(t) := \langle \psi_x^\dagger(t)\psi_y(t)\rangle$, the entanglement entropy is obtained as

$$S_{\text{ent}}(t) = -\sum_{l=0}^{\infty} \zeta_l \log \zeta_l + (1-\zeta_l)\log(1-\zeta_l). \tag{6.39}$$

The correlation matrix can be computed explicitly, using the same properties of the Bessel functions that are used for the average magnetization, obtaining

$$\mathcal{C}_{xy}(t) = e^{i\left(\frac{\pi}{2}+ht\right)(y-x)}\mathcal{B}(x,y;\omega_t), \tag{6.40}$$

$\mathcal{B}$ being the Bessel kernel of Eq. (6.36). If one computes the entanglement entropy between two subsystems A and B, the indices of the correlation matrix $\mathcal{C}_{xy}$ are such that $x, y \in A$ (or B equivalently). For a bipartition located in 0, one has $x, y > 0$. Let us notice that the phase factor in the last equation does not affect the entanglement entropy; in fact, it can be removed via a unitary transformation. It is therefore clear

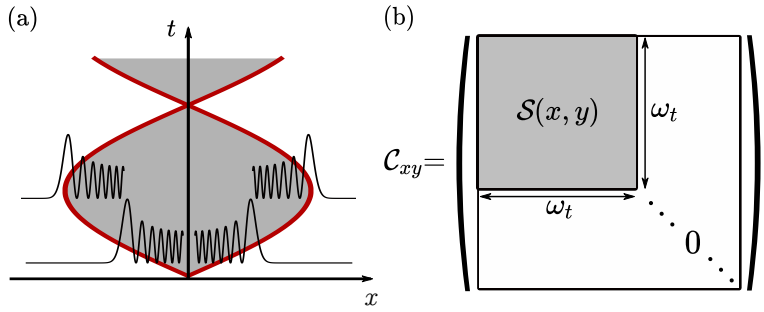

FIGURE 6.5: (a) Light-cone structure in the fluctuations, induced by the presence of the Bessel kernel. The red line represents the position of the light cone $x = |omega_t|$. Inside the light cone, the Bessel functions oscillate with a non-zero average value: it is in this region, in the continuum limit, that the Bessel kernel reduces to the sine kernel. Outside the light cone, instead, the Bessel functions decay exponentially, and in the continuum they can be approximated with zero. (b) Correlation matrix in the continuum limit. As discussed in the main text, in this regime $\mathcal{C}_{x,y}$ can be set to zero outside the light cone, while inside the light cone the Bessel kernel $\mathcal{B}(x,y;\omega_t)$ can be replaced by the sine kernel $\mathcal{S}(x,y)$. This figure is taken from Ref. [10].

that the correlation matrix (and therefore $S_{\text{ent}}(t)$) is periodic with period $T = |h|/\pi$, as the time dependence is only through ω_t.

Even if the eigenvalues of the correlation matrix of Eq. (6.40) cannot be obtained analytically to our knowledge, in the continuum limit some analytical progress can be made anyways [440, 447]. Let us introduce the entanglement Hamiltonian $\mathcal{H}$ such that

$$\rho_A = \mathcal{K}_A e^{-\mathcal{H}_A}, \tag{6.41}$$

being ρ_A the reduced density matrix of a subsystem A, and $\mathcal{K}_A$ a normalization constant. With this definition, one finds [447–449]

$$\mathcal{H}_A = \log\left[\frac{1-\mathcal{C}_A}{\mathcal{C}_A}\right]. \tag{6.42}$$

where $\mathcal{C}_A$ is here the correlation matrix restricted to positions within the considered subsystem A. This means that $\mathcal{H}_A$ and $\mathcal{C}_A$ are diagonal in the same basis, and the corresponding eigenvalues satisfy the relation in Eq. (6.42).

As discussed also in Sec. 6.3.2, the Bessel kernel reduces to the Sine kernel in the continuum limit inside the light cone. In this regime one can approximate the correlation matrix setting to zero the entries for $x, y \gtrsim \omega_t$, and therefore one is left with an effective matrix of size $\omega_t \times \omega_t$ (see Fig. 6.5b for a visual representation). Thanks to such approximation, one can obtain the eigenvalues ϵ_k of $\mathcal{H}$ as [440, 447]

$$\epsilon_k(t) = \pm\frac{\pi^2}{2\log\omega_t}(2k+1). \tag{6.43}$$

Denoting by ζ_k the eigenvalues of $\mathcal{C}$, one has from Eq. (6.42)

$$\zeta_k = \frac{1}{e^{\epsilon_k}+1}. \tag{6.44}$$

Notice, however, that the asymptotic value Eq. (6.43) needs very large ω_t to be accurate. For smaller values of ω_t, the eigenvalues vary as $1/(\log\omega_t + b_k)$ rather than $1/\log\omega_t$, where b_k are constants depending on the specific eigenvalue [447].

In this Section, we have shown how the mapping of the original $2d$ problem to a $1d$ chain is reflected also in the fact that the half-system entanglement entropy can be computed from the $1d$ setting. However, the computation was possible only because of a convenient choice of the bipartition (i.e. a vertical one): more general bipartitions of the $2d$ lattice would instead map non-locally on the chain. We believe that the possibility of computing the entanglement of the $2d$ system using the mapping is effective as long as the cut along which the entanglement is computed is parallel to the projection performed in the mapping itself.

As a final point of this Section, it is worth noticing that the above results, valid in general on the lattice for any value of the couplings g and h, reduce, in the limit $h \ll g$, to the outcomes gained using conformal field theory in curved space [450] or quantum generalized hydrodynamics (GHD) [451] for the entanglement entropy:

$$S(x,t) = \frac{1}{6}\log\left[\omega_t\left(1-\frac{x^2}{\omega_t^2}\right)^{3/2}\right] + c, \tag{6.45}$$

with $c \simeq 0.475$ and x being the position of the bipartition. The GHD formalism allows one to obtain results for the dynamics in one-dimensional integrable quantum systems directly in the continuum limit, even when the system is interacting; this justifies the necessity of taking the limit $h \ll g$ in our system to match the results.

6.3.4 Connection with the asymptotics of the Plancherel measure

As pointed out at the beginning of Sec. 6.3, the states in the Krylov sector connected to the infinite corner (e.g. the shaded state in Fig. 6.4a) are in one-to-one correspondence with *Young diagrams* (sometimes also called *Ferrers diagrams*). By definition, a Young diagram is a collection of boxes, arranged in left-justified rows, with the row lengths in non-increasing order [452]. Young diagrams are a graphical tool commonly used to represent integer partitions, to compute dimensions of group representations, and for many other mathematical purposes [452].

Let us introduce some notation, in order to clarify the discussion. A partition λ is a decomposition of the integer N as a sum of positive integers λ_k:

$$\lambda = (\lambda_1 \geq \lambda_2 \geq \cdots \geq \lambda_n \geq 0), \quad |\lambda| := \sum_{k=1}^{n} \lambda_k = N. \tag{6.46}$$

One may easily see that, representing each integer λ_k as a string of λ_k boxes $\square\square\cdots\square$, to each partition there corresponds a Young diagram, obtained stacking all the strings. It is a theorem that the irreducible representations of the symmetric group of degree N, S_N, are indexed by partitions of size $|\lambda| = N$. Moreover, the dimension of the representation corresponding to λ can be obtained via the *hook length formula*

$$\dim(\lambda) = \frac{|\lambda|!}{\prod_{\square\in\lambda} \mathfrak{h}(\square)} \tag{6.47}$$

$\mathfrak{h}(\square)$ being the so-called *hook* of the square $\square$ [452], see also Fig. 6.4b.

For our purposes, the most interesting interpretation of $\dim(\lambda)$ resides in the fact that it gives the number of ways to reach the diagram λ starting from the empty diagram, and adding one square at a time, in such a way that at each step one still has a partition [402]. In the mathematical literature, it is common to define the *Plancherel*

measure on the set of partitions as [397–400, 430]

$$\mu_{\mathrm{P}}(\lambda) := \frac{[\dim(\lambda)]^2}{|\lambda|!}, \tag{6.48}$$

It is proved that μ_{P} is a normalized measure, i.e. a probability.

Now, an important result of combinatorics is that the Plancherel measure μ_{P} *concentrates* at large N, that is to say it becomes a delta function on a particular set of diagrams [397–400, 430]. The diagrams belonging to this set all have roughly the same shape; more precisely, rescaling their sides by a factor $\sqrt{N}$, their shape becomes described by the function $\Omega(v)$ of Eq. (6.34). It is thus quite surprising to find that another, completely different growth process on the Young diagrams leads to the same rescaled shape induced by the quantum dynamics of the $2d$ Ising model.

While we could not devise a proof that would withstand the scrutiny of mathematical rigor, we understand the above correspondence in the following, intuitive way. Recalling that $\dim(\lambda)$ gives the number of paths that reach the diagram λ from the empty one, always remaining within the set of Young diagrams, we notice that the Plancherel measure μ_{P} is weighting each diagram with the *square* of the number of paths. On the other hand, one can consider the Green's function

$$G(\lambda', \lambda; E) = \langle \lambda' | \frac{1}{E - H} | \lambda \rangle \tag{6.49}$$

where λ and λ' are two Young diagrams. Performing the locator expansion of the resolvent [92, 94, 453, 454] (see also Sec. 6.5.2 below)

$$G(\lambda', \lambda; E) = \frac{\delta_{\lambda\lambda'}}{E - E_\lambda} + \frac{1}{E - E_\lambda} \sum_{p \in \mathrm{P}(\lambda, \lambda')} \prod_{k=1}^{|p|} \frac{g}{E - E_{p_k}}, \tag{6.50}$$

where $\mathrm{P}(\lambda, \lambda')$ denotes the set of paths from λ to λ'. In the spirit of the forward approximation (FA) [453, 454], one can approximate the sum in Eq. (6.50) by reducing $\mathrm{P}(\lambda, \lambda')$ to $\mathrm{SP}(\lambda, \lambda')$, i.e. the set of *shortest* paths from λ to λ'. This corresponds to work at lowest order in the hopping. With this assumption, the argument of the sum does not depend any more on the specific path, but only on its length $d(\lambda, \lambda')$, as all the diagrams with a fixed number of blocks have the same energy. This means that the sum gives the number of shortest paths from λ to λ' (for $\lambda \neq \lambda'$, otherwise it gives zero). Specifying the computation to the path from the empty diagram 0 to λ, one finds

$$G(\lambda, 0; E) = \frac{\dim(\lambda)}{E} \prod_{k=1}^{d(0,\lambda)} \frac{g}{E + hk} \tag{6.51}$$

$$= \frac{\dim(\lambda)}{E} \left(-\frac{g}{h}\right)^{d(0,\lambda)} \frac{\Gamma\left(1 + \frac{E}{h}\right)}{\Gamma\left(1 + \frac{E}{h} + d(0,\lambda)\right)} \tag{6.52}$$

since $E_0 = 0$. Taking the residue at $E = 0$, one gets the expression for the eigenfunction

$$\psi_{E=0}(\lambda) = \frac{\dim(\lambda)}{|\lambda|!} \left(\frac{g}{h}\right)^{|\lambda|}. \tag{6.53}$$

As a consequence of the equation above, the probability $|\psi(\lambda)|^2$ of being in the state $|\lambda\rangle$ is proportional to the square of the number of paths leading to it. This motivates the connection with the results on Plancherel measure concentration.

Before passing to the next Section, it is interesting to notice that the FA also gives the correct result for the decay of the eigenfunctions. To see that, one must plug in Eq. (6.53) the value of $\dim(\lambda)$, which clearly depends on the specific form of the diagram associated with the state $|\lambda\rangle$. Referring for details to Ref. [399], we just report that one can bound from above the maximal value and from below the typical value of $\dim(\lambda)$: in both cases, the leading term scales as $\sqrt{|\lambda|!}$. Using this result in Eq. (6.53), one gets that the eigenfunctions go to zero faster than exponentially, because of the overall factor $1/\sqrt{|\lambda|!}$. This estimate is in agreement with the exact result of Eq. (6.17), since the Bessel functions decay as the inverse factorial of the (large) index, cf. Eq. (D.67).

6.4 Mechanisms of integrability breaking

Let us summarize briefly what we have done until now. We started from the $2d$ Ising model in Sec. 6.1, and showed that in the infinite-coupling limit the Hilbert space shatters in many disconnected Krylov sectors. Then, we showed that some physically relevant Krylov sectors have an effective description in terms of $1d$ models, and are amenable of analytical treatment. In particular, the evolution of a class of interfaces described in Secs. 6.2.2–6.3 can be mapped to an integrable model, and we discussed in detail the exact solution of their dynamics. In this Section we discuss the phenomenology of interface dynamics beyond integrability, and explore the robustness of the qualitative features arising from the exact solutions.

We start in Sec. 6.4.1 by showing that interfaces that do not fulfil the Lipschitz criterion of Eq. (6.14) can potentially have a very different dynamical behaviour than the one described so far, because of the possibility of breaking into disconnected pieces. In particular, we will be concerned with the case in which an interface is *locally* Liphsitz, but at large scales it is not the graph of a function μ anymore. In Sec. 6.4.2 we consider instead another source of integrability breaking: the presence of a finite, albeit still large, coupling J. Specifically, we will discuss the $O(J^{-1})$ corrections to the infinite coupling Hamiltonian (6.2) and address the ergodicity of the model in this regime of broken integrability.

6.4.1 Finite bubbles

Throughout Secs. 6.2.2 to 6.3.4 we have always assumed the presence of a single interface, cutting the $2d$ lattice in two infinitely large domains. It is natural to question to what extent the presented results apply also to finite domains. The easiest and first case one should consider is that of a large bubble of "down" spins, surrounded by "up" spins (or vice-versa). Let us also introduce the notion of convexity on the lattice: we will say that a domain is convex if any line *parallel to the lattice axes* joining two points in the domain lies entirely in the domain itself. As already noted in Ref. [393], all convex bubbles are dynamically connected with the minimal rectangle (with sides parallel to the lattice axes) that contains them, i.e. they belong to the Krylov subspace generated by this rectangle. Moreover, because of the perimeter constraint, the domain-wall dynamics is always confined within such rectangle. Therefore, let us directly assume that at $t = 0$ the shape of the bubble is a rectangle; all the other cases follow from the understanding of this one.

We already have all the tools to describe the early-stage dynamics for such a rectangular bubble: the sides are immobile, since no spin can be flipped without modifying the perimeter, while the corners start to be eroded, as discussed in great

detail in Sec. 6.3. The dynamical evolution will however deviate from the one of an infinite, isolated corner as soon as two corners will start to "feel" the presence of one another. A lower bound for the timescale at which this happens can be estimated, in the fermionic language, by computing the probability of finding two fermions, each coming from an isolated corner, halfway on the flat interface.

Let us denote by L the length of the shortest side of the rectangular, finite bubble. There are now two possible cases. If the longitudinal field $h = 0$ (or, more generally, h is small enough for the Bloch oscillations to overcome the distance $L/2$) the excitations propagate ballistically on the chain with speed $2g$ (see Eq. (6.33)), and they meet at $L/2$ after a time

$$T_{\text{corner}}(h = 0) \sim \frac{L}{4g}. \tag{6.54}$$

If instead h is nonzero and large enough to confine the dynamics in a region *smaller* than $L/2$, one can estimate the probability of having a fermion at distance $x < 0$ from the corner (equivalently, a hole at distance $x > 0$) with $P(x,t) = 1 - n_x(t)$. On the maxima of the oscillations[3] where $\omega_{t^*} = 2\gamma$, i.e. when the eroded area has maximal expectation value, one finds $\langle n(x,t^*)\rangle = \sum_{y<x} J_y^2(2\gamma)$ (cf. Eq. (6.29)), and consequently

$$P\left(\frac{L}{2}, t^*\right) = \sum_{y \geq L/2} J_y^2\left(2\gamma\right). \tag{6.55}$$

Recalling that the Bessel functions of large order decay exponentially fast to zero, one can approximate (see also Eq. (D.67))

$$P\left(\frac{L}{2}, t^*\right) \approx J_{L/2}^2\left(2\gamma\right) \approx \frac{1}{\pi L}\left(\frac{2eg}{Lh}\right)^L. \tag{6.56}$$

Note that, as argued above, this estimate only makes sense in the localized regime $g/h \ll L/2$. From here, one can estimate the typical time a fermion needs to reach the midpoint of the side as the inverse of the probability:

$$T_{\text{corner}}(h \neq 0) \sim \frac{1}{g} e^{L\log L - L\log(2eg/h)}. \tag{6.57}$$

One can see that, in the case $h \neq 0$, a time more than exponentially large in the bubble size must pass, before integrability breaking starts to become manifest.

It is natural to wonder what happens to the bubble after this timescale. Based on elementary reasoning, one can argue that two kinds of processes may take place. On the one hand, excitations coming from one corner may start to affect the dynamics of adjacent corners, transferring energy between corners and deteriorating the perfect coherence of the single-corner oscillations. More dramatically, the interface may break by detaching isolated flipped spins via the interface-splitting transitions $|\overline{\square}\rangle\langle| \; \| + \text{h.c.}$ of Eq. (6.6). We note, however, that these detached pieces may truly evaporate away from the interface only via g^2/J processes, i.e. away from the $J = \infty$ limit consider here. We defer the detailed study of these difficult problems to the future.

We conclude this Section by noting that the case of two corners we have considered is applicable to any very large bubble, provided its boundaries are "smooth" enough—i.e., violations of the Lipshitz condition are very dilute. If instead one

[3] A very similar result is obtained if taking the average over a period, rather than the maximum of the oscillations.

starts with a rather corrugated interface, that is not the graph of a function $\mu(x)$ even at the local level, then we expect a complicated time evolution where all accessible configurations may be explored, and the single-interface description severely breaks down.

6.4.2 Finite coupling

We now relax the assumption that J be strictly infinite, allowing for the possibility of $J < +\infty$ but very large: $J \gg |h|, g$. A very large J is still imposing an *effective* dynamical constraint, that is valid up to a timescale exponentially long in J: this follows from the rigorous prethermalization bounds of Ref. [455]. Specifically, the perturbatively "dressed" version of the domain-wall length operator $D = \frac{1}{2}\sum_{\langle i,j\rangle}(1-\sigma_i^z\sigma_j^z)$, arising from the Schrieffer-Wolff transformation, is accurately conserved for a long time that scales (at least) exponentially:

$$T_{\text{preth}} \geq \frac{C}{g}\exp\left[\frac{cJ}{\max(g,|h|)}\right] \tag{6.58}$$

(here c and C are numerical constants independent of J, g, h). This is because the Schrieffer-Wolff effective Hamiltonian $H_{\text{eff}} = H_{\text{PXP}} + (1/J)(\cdots) + (1/J^2)(\cdots) + \cdots$, computed up to a suitable optimal perturbative order, commutes with D up to an exponentially small error [455]. Furthermore, the evolution of all local observables is well approximated by H_{eff} for $t \leq T_{\text{preth}}$ [455].

We have already obtained the zeroth-order effective Hamiltonian in Sec. 6.1.2. Computing higher order corrections to Eq. (6.2) becomes rapidly very complex, as the number of terms proliferate super-exponentially. In App. D.4.1 we sketch the computation that leads to the first-order corrections in $1/J$ of the Hamiltonian Eq. (6.2), while in App. D.4.2 we specify the computation to the dynamical sector of a smooth interface, of the type defined in Sec. 6.2.2: in such sector, the perturbative corrections take on a simpler and handy appearance. Using the fermionic representation, the resulting correction to the 0-th order fermionic Hamiltonian $H_F^{(0)} \equiv H_F$ of Eq. (6.16) are

$$H_{\text{eff}} = H_F^{(0)} + H_F^{(1)} + O\left(J^{-2}\right), \tag{6.59}$$

with

$$H_{\text{F}}^{(1)} = -\frac{g^2}{4J}\sum_x\left(\psi_x^\dagger\psi_{x+2} + \text{h.c.}\right) + \frac{g^2}{4J}\sum_x\left(2\psi_x^\dagger\psi_{x+1}^\dagger\psi_{x+1}\psi_{x+2} + \text{h.c.} - 3\psi_x^\dagger\psi_x\psi_{x+1}^\dagger\psi_{x+1}\right). \tag{6.60}$$

One may recognize that in $H_F^{(1)}$ there are next-nearest-neighbour hoppings, as well as density-density interactions. These terms are rather generic, and therefore it would be natural to expect that they break the integrability of the model, and make its dynamics thermalizing fast. Nonetheless, if h is large enough the perturbation is not able to restore ergodicity. In the next Section we describe this phenomenon in detail.

Let us briefly mention that, including the $O(J^{-1})$ corrections, a single flipped spin can spread in the $2d$ lattice with a hopping amplitude $\propto g^2/J$. This means that it is no longer possible to provide an effective $1d$ description for initial configurations of the strip-like form, discussed in Sec. 6.2.1 in the $J = \infty$ limit.

Before moving on, it is important to stress a fundamental issue with the Schrieffer-Wolff transformation. When $J < \infty$, taking initial product states of the form of classical configurations considered so far, the dynamics will exhibit nontrivial vacuum fluctuations even away from the location of domain walls, due to the perturbative dressing of the bare ferromagnetic state by virtual spin excitations. Formally, this arises from the application of the Schrieffer-Wolff unitary transformation $\exp(iS_1)$, cf. Eq. (D.38), to the fully polarized initial state. Thus, for such initial states, one should think of the ferromagnetic vacua (e.g. in the problems considered above, the two sides of an infinite interface or the inner and outer regions of a bubble) as *superpositions* of dilute spin flip excitations, of spatial density $\sim (g/J)^2$. Such excitations can be described as magnons, hopping on the $2d$ lattice with amplitude $\propto g^2/J$. In principle these dilute magnon gases contribute to the dynamics of the interface, but in the following we will ignore this occurrence, leaving it to future, more detailed studies. Formally, our choice consists in taking as initial state *the Schrieffer-Wolff transformed interface* rather than the bare classical interface.

6.4.3 Arguments in favour of Stark many-body localization

The goal of this section is to study the evolution induced by the Hamiltonian (6.59). The first term in Eq. (6.59) is the Hamiltonian H_F considered already in Secs. 6.2.2 and 6.3: it represents a chain of Stark-Wannier-localized, non-interacting fermions. The second term, viz. $H_F^{(1)}$ of Eq. (6.60), is a small perturbation containing both next-nearest-neighbour hoppings and two-body interactions. We see therefore that there is a competition between the localizing nature of $H_F^{(0)}$ and the interactions in $H_F^{(1)}$ that are generally expected to drive the system to a thermal phase. Previous works [378, 379, 456] have shown that, for interacting Hamiltonians very similar to Eq. (6.59), an extended non-thermal phase is present for sufficiently strong h, somewhat analogous to disorder-induced MBL—the phenomenon has indeed been dubbed *Stark MBL*.

To quantify the competition between interactions and the localizing linear potential, we developed an analytical argument á la Basko-Aleiner-Altshuler (BAA) [46] that goes as follows. Start from the integrable limit $J = +\infty$: the eigenfunctions are expressed in terms of the single-particle orbitals of Eq. (6.17), and are all localized. Their localization length ξ can be quantified by the participation ratio:

$$\xi^{-1} = \sum_x J_x^4(\gamma) = \frac{1}{\pi}\int_0^\pi d\theta\, J_0^2\left(\gamma\sqrt{2-2\cos\theta}\right), \tag{6.61}$$

where we remind $\gamma := g/h$. In App. D.5 we perform the asymptotic expansion of the above integral through the method of the Mellin transform, determining

$$\xi^{-1} = \frac{\log(\gamma C)}{\pi^2\gamma} + O\left(\frac{\log\gamma}{\gamma^3}\right), \tag{6.62}$$

where $C = 2^5\, e^{\gamma_E} \simeq 56$ and $\gamma_E = 0.5772\cdots$ is the Euler-Mascheroni constant. We now assume we can partition the system into boxes ("quantum dots") of size ξ, see Fig. 6.6. Within each of them, the number of states is clearly $N_\xi = 2^\xi$, whereas the maximum energy difference between two many-particle states is $\Delta_{\max} \approx |h|\xi^2$. To understand this latter statement, assume $h > 0$: then, the minimum energy is attained when no particle is present ($E_{\min} = 0$), while the maximum when all sites

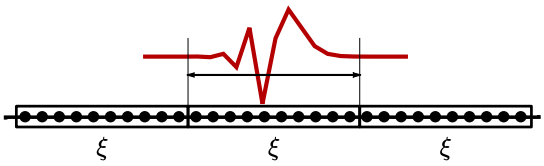

FIGURE 6.6: Graphical representation of a region of size ξ on the chain, corresponding to one localization length (a "quantum dot"). As described in the main text, focusing on one of such intervals, one can derive an estimate for the critical value of h, above which the system is not ergodic, even in presence of finite J. This figure is taken from Ref. [10].

are occupied (and thus $E_{\max} = \sum_{x=0}^{\xi} hx \approx h\xi^2$). With the same reasoning, for $h < 0$ one gets $\Delta_{\max} \approx |h|\xi^2$, thus confirming the claim.

Following BAA (and thus also building on Ref. [103]), we say that interactions should be unable to restore ergodicity (at least perturbatively) when their strength $\lambda \sim g^2/J$ is smaller than the average local level spacing:

$$\delta_\xi \approx \frac{\Delta_{\max}}{N_\xi} \approx \frac{|h|\xi^2}{2^\xi}, \tag{6.63}$$

i.e. when $\lambda < \delta_\xi$. This is equivalent to

$$\frac{g^2}{J} < \frac{|h|\,\xi^2}{2^\xi}, \tag{6.64}$$

which is always satisfied for $0 \leq |\gamma| \lesssim 1$, i.e. for $|h|$ large enough. It is interesting to notice that the regime of validity of the heuristic criterion (6.64) is only weakly dependent on J. In Fig. 6.7 we show, varying J and h, the regions of validity of the inequality (6.64); we can observe how, for fixed J, the criterion is satisfied for sufficiently large h. Moreover, for $J \gtrsim 1$, the relation (6.64) holds for $h \gtrsim 1$.

As a check for the above estimate, we performed numerical simulations, focusing in particular on the imbalance, a well-known witness of ergodicity breaking. Given a generic initial state $|\Psi_0\rangle$, the time-evolved imbalance for a system of length L is

$$I_L(t) = \sum_{x=-L/2+1}^{L/2} \frac{1}{L} \langle \Psi_0 |\, m(x,t) m(x,0) \,| \Psi_0 \rangle \,, \tag{6.65}$$

where we defined $m(x,t) := 2\,n(x,t) - 1$. Taking the infinite-size limit and averaging over time, one obtains

$$I = \lim_{L,T\to\infty} \frac{1}{T} \int_0^T dt\, I_L(t), \tag{6.66}$$

which is zero in generic thermalizing systems. Thus, a non-zero value of the imbalance is a sufficient condition for the system to be non-ergodic (even if it is not necessary). The infinite-time limit can be obtained also by using the diagonal ensemble: assuming $|\Psi_0\rangle = \prod_k \psi^\dagger_{x_k} |0\rangle$ as in Eq. (6.19), one finds

$$I = \lim_{L\to\infty} \frac{1}{L} \sum_{x=-L/2+1}^{L/2} \langle m(x,0) \rangle \sum_a \langle E_a | m(x,0) | E_a \rangle |\langle \Psi_0 | E_a \rangle|^2, \tag{6.67}$$

with the average $\langle \cdots \rangle$ defined in Eq. (6.23).

Such ergodicity test should in principle be verified for every initial configuration.

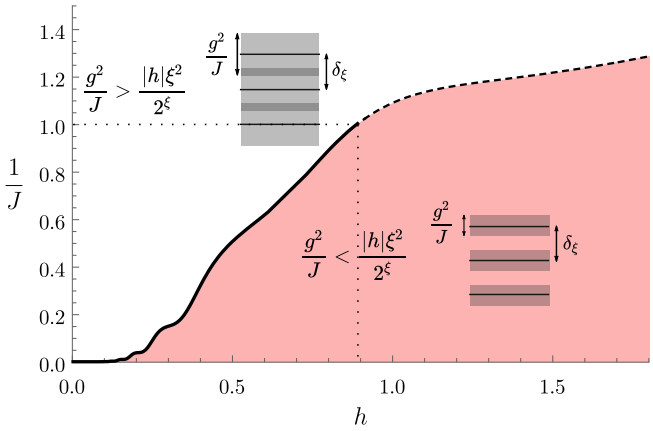

FIGURE 6.7: Region of validity of Eq. (6.64) (color), and region where delocalization is expected (white). The black curve is obtained by setting the two sides of Eq. (6.64) to be equal (here we set $g \equiv 1$). We also show, for the two regions, a sketchy comparison between the unperturbed level spacings (solid black line) and the strength of the interactions (shaded gray area). We can notice how, for fixed J, the condition is satisfied for h large enough. For $J \gtrsim 1$ (dashed line), the results are no more reliable as higher order corrections become dominant. This figure is taken from Ref. [10].

However, there are states $|\Psi_0\rangle$ that will trivially give a non-ergodic result $I > 0$. For example, states near the ground state will remain non-ergodic also in presence of the $1/J$ corrections, just because they lie at the edges of the spectrum: we checked numerically that this is the case, for instance, for the domain-wall state of Eq. (6.28). A non-trivial test is provided by generic states, that lie in the middle of the spectrum: for our purposes, the Néel state $|\mathbb{Z}_2\rangle = \prod_k \psi^\dagger_{2k} |0\rangle$, for which $\langle m(x,0)\rangle = (-1)^x$, will suffice.

In Fig. 6.8 we compare the numerical results for I at finite J, with the analytical prediction $\tilde{I}$ at $J = +\infty$: using the definition, Eq. (6.65),

$$\tilde{I}_\infty(t) = \lim_{L\to\infty} \sum_{x=-L/2+1}^{L/2} \frac{1}{L} \langle \mathbb{Z}_2 | \, m(x,t) m(x,0) \, | \mathbb{Z}_2 \rangle \tag{6.68}$$

$$= \lim_{L\to\infty} \frac{2}{L} \sum_{x=-L/2+1}^{L/2} (-1)^x \sum_{y=-\infty}^{\infty} J^2_{2y-x}(2\gamma \sin ht) \tag{6.69}$$

$$= J_0(4\gamma \sin ht). \tag{6.70}$$

In the long-time limit,

$$\tilde{I}_\infty = \lim_{T\to\infty} \frac{1}{T} \int_0^T dt \, J_0(4\gamma \sin ht) = J_0^2(2\gamma), \tag{6.71}$$

where the last step is a known property of the Bessel functions [457].

The curve $\tilde{I}_\infty$ is represented by the dashed lines in Figs. 6.8a and 6.8c. For finite values of J, instead, one is able to compute the imbalance only numerically and for L finite. Therefore, the $L \to \infty$ result has to be obtained via finite-size scaling, see Fig. 6.8b. As displayed there, the numerical values of the imbalance show a linear dependence on $1/L$, allowing for a good extrapolation at $L = \infty$ (see caption of Fig. 6.8b for more details). The final results are reported in Fig. 6.8c: while for $h \lesssim 1$ the imbalance is compatible with 0, differently from the integrable case, for $h > 1$ the results at finite J are perfectly compatible with the analytic prediction at $J = \infty$. This

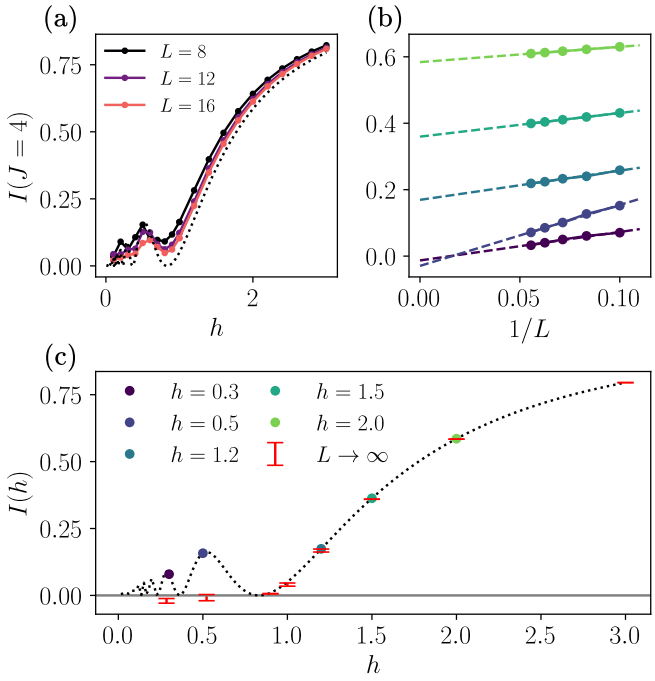

FIGURE 6.8: (a) Numerical values for the imbalance obtained in the diagonal ensemble at $J = 4$. To improve readability, only the data for $L = 8$, 12, 16 are reported. The dotted line represents the analytical result at $J = \infty$ and $L = \infty$ (see Eq. (6.71)). (b) Extrapolation to $L = \infty$ of the imbalance obtained numerically, and reported in panel (a). The extrapolation is performed using the ansatz $I(L) = I_\infty + A/L$. Different colors correspond to different values of h (see panel (c) for the legend). (c) The coloured dots are the values of h for which we reported the extrapolation in panel (b). The red error bars are the results of the extrapolation, with the error coming from the fit. The two points at smaller values of h are in correspondence of the local maxima of I_∞ at $J = \infty$ and are compatible with zero within the error bars. At larger values of h instead, the extrapolation gives values of the imbalance compatible with the result at $J = \infty$. This figure is taken from Ref. [10].

results are in agreement with the argument á la BAA that we discussed previously. Moreover, we performed also numerical simulations for the time evolution of the imbalance (that we are not reporting here), and we noticed that the relaxation time to the diagonal ensemble value depends on J (the larger J, the longer the time needed), whereas the asymptotic value does not, again in agreement with the argument á la BAA.

6.5 Melting in presence of quenched disorder

With this Section, we move to the case in which quenched disorder is added at the level of the original $2d$ Hamiltonian. That is to say, we start from the $2d$ Ising model in presence of a uniform transverse field g, and a random, on-site longitudinal field $h_i \in [-W/2, W/2]$:

$$H_{\text{Is,dis}} = -J \sum_{\langle ij \rangle} \sigma_i^z \sigma_j^z - g \sum_i \sigma_i^x - \sum_i h_i \sigma_i^z. \tag{6.72}$$

We will perform, for this disordered model, the same analysis of before, to explore to what extent the localization we have been discussing is resilient to the introduction of impurities. On the other hand, by making W very large, we will investigate

whether a different kind of localization takes place, on the lines of the standard MBL.

Throughout this Section, we will assume $J = +\infty$. While we could study also the effects of a finite J, we believe that such effects would just entail just a *quantitative* modification of the results presented, while leaving the physical picture unchanged. Therefore, in the following we will always neglect the $O(1/J)$ corrections, while leaving to Sec. 6.5.6 a brief informal discussion of their possible implications.

Because of the assumption of infinite coupling, the PXP-like Hamiltonian arising in each Krylov sector will be of the form (compare with Eq. (6.6))

$$H_{\text{PXP,dis}} = -\sum_i h_i \sigma_i^z - g \sum_i \Big(|\ulcorner\rangle_{ii}\langle\lrcorner| + |\llcorner\rangle_{ii}\langle\urcorner| + |\sqsupset\rangle_{ii}\langle\sqsubset| + \text{h.c.} \Big). \tag{6.73}$$

It is important to stress that, for PXP in $1d$, both the spectrum as a whole, and the dynamics at finite energy density, are ergodic (even if they can host scarred states). Such ergodicity is resistant also to the introduction of quenched disorder [199]: this is a consequence of the fact that the disorder maps, in an *unconstrained* basis of states, to generic, non-local interaction terms. This feature will be present also in the $2d$ model under consideration.

Now, in Sec. 6.5.1 we will discuss how the mapping of an interface changes to take into account the random, on-site potential. Then, in Sec. 6.5.2 we will provide an analytical argument supporting the absence of a truly localized phase, which is confirmed by the exact diagonalization results of Sec. 6.5.3. In Sec. 6.5.4 we will show how the dynamics of interfaces gets modified by the introduction of disorder, and in Sec. 6.5.5 we will compare such dynamics with similar classical models. Finally, in Sec. 6.5.6 we will discuss how our results change when taking a finite coupling.

6.5.1 Modifications in the holographic mapping

We are interested in the dynamics of melting generated by the Hamiltonian (6.72) (or equivalently Eq. (6.73)), starting from the corner initial condition. Thanks to the mapping described at lenght in Secs. 6.2.2–6.3, the quantum dynamics which makes the crystal wedge melt can be described equivalently by the hopping on the space of Young diagrams $\mathcal{D}$, see Fig. 6.9. The initial state, viz. the full wedge, is the empty Young diagram $\lambda = 0$. Then, the energy of a diagram $\lambda \in \mathcal{D}$ is given by the sum of the longitudinal fields on the "blocks" composing the diagram:

$$E_\lambda = \sum_{i \in \lambda} h_i. \tag{6.74}$$

The rate of hopping between two Young diagrams λ, λ' is g if they are connected by a single block addition or deletion (neighbouring diagrams), or zero otherwise. Therefore, the adjacency matrix of the Young lattice has non-zero elements only between the set of diagrams of size N, call it $\mathcal{D}_N$, and that of size $N-1$ ($\mathcal{D}_{N-1}$) or $N+1$ ($\mathcal{D}_{N+1}$); see Fig. 6.9b for a sketch.

In the end, one is left with a Hamiltonian operator, acting on the Hilbert space $\mathcal{H}_\mathcal{D}$ built on the set of diagrams $\mathcal{D}$, i.e. the Krylov subsector of the original Ising model that contains the infinite wedge:

$$H_\mathcal{D} = -g \sum_{\langle \lambda, \lambda' \rangle} |\lambda\rangle\langle\lambda'| - \sum_\lambda E_\lambda |\lambda\rangle\langle\lambda|. \tag{6.75}$$

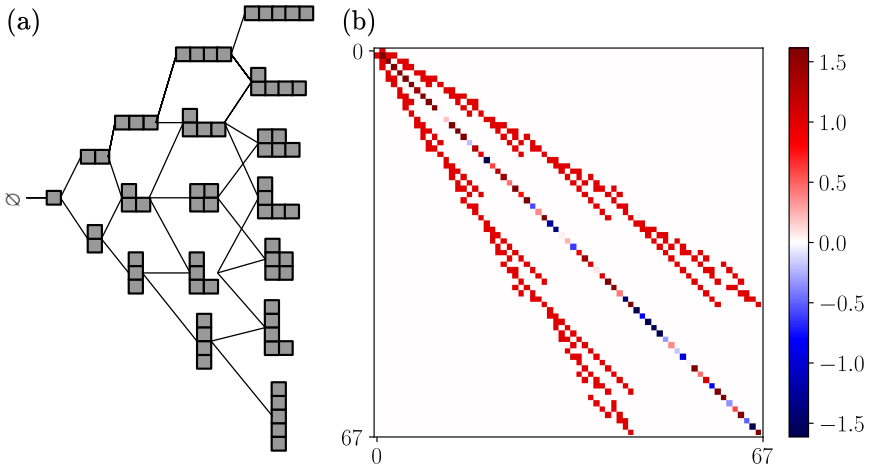

FIGURE 6.9: (a) Young lattice, i.e. the set of Young diagrams where two of them are connected if differing by a single box. In figure the lattice up to $N = 5$ is represented. (b) Matrix plot of the Hamiltonian Eq. (6.75) up to $N = 8$, corresponding to a Hilbert space of dimension 67. The off-diagonal elements correspond to the adjacency matrix of the Young lattice, and are all set to $-g \equiv 1$, while the diagonal part is determined by the disordered magnetic field as detailed in Sec. 6.3.4. This figure is taken from Ref. [8].

The net gain is that the dimension of $\mathcal{H}_{\mathcal{D}}$ is much smaller than that of the full Hilbert space of all the spins configurations $\{\sigma_i\}$ on the plane. Let us denote the dimension of the Hilbert subspace, made of diagrams composed of exactly N squares, as $d_N := \dim \mathcal{H}_{\mathcal{D}_N}$. It follows that, for the diagrams made up at most of N squares, one has to compute the cumulative $\bar{d}_N := \sum_{k=0}^{N} d_k$. Thus, from the Hardy-Ramanujan asymptotic formula for partitions, one finds $\bar{d}_N \simeq \exp(\pi\sqrt{2N/3})/\sqrt{8\pi^2 N}$: the mild, stretched-exponential growth of such numbers will enable us to reach system sizes of up to $N = 36$ spins. Notice that such dimensions correspond to a *vanishing entropy density* in the original model, since $s = \log(\bar{d}_N)/N \sim N^{-1/2}$. In other constrained models (including the $2d$ dimer models of Refs. [346, 413]) the growth of Krylov sectors is instead exponential, with a finite entropy density.

For what concerns the fermionic language, the hopping term becomes associated to simple nearest-neighbour hoppings on the chain like in the clean case. The energy $E_\lambda |\lambda\rangle \langle\lambda|$, on the other hand, has no simple interpretation as a local term. Instead, it is a generic operator which involves all the fermions, through their number operator n_x:

$$E_\lambda |\lambda\rangle\langle\lambda| \quad \longleftrightarrow \quad E(n_x, n_y, \dots) \tag{6.76}$$

where $x, y, \dots$ are the indices of the sites "touched" by the diagram λ. This non-locality of the disordered potential terms, already anticipated in the Introduction, is typycal of PXP models [199], and it comes from the interplay of dynamical constraints and local fluctuations in the potential energy. In one spatial dimension, it was proven to be the cause of the absence of a MBL phase [199]: indeed, the presence of non-local interactions on the chain makes the model evade all the arguments in favor of ergodicity breaking. We believe that the same happens in our $2d$ setting, since the perturbative arguments supporting MBL work equally in any dimension, while the non-perturbative effects that destabilize MBL are stronger. We see therefore that the presence of disorder is *assisting* the thermalization, since it breaks the integrability (in the sense of free fermions) of the model, while it is not able to make the model athermal by itself, due to its non-local nature.

We conclude this Section by remarking that the mapping of the $2d$ dynamics onto

a line of fermions is, also in presence of disorder, a form of holography. This surely deserves a better investigation, in view of the intense interest of the last years on such phenomena, especially in presence of quenched disorder [458, 459].

6.5.2 Perturbation theory estimates

It is becoming clear, as the discussion unfolds, that the melting of an infinite quantum crystal wedge does not undergo a localization phenomenon, even if it may be severely slowed down by disorder. Therefore, as a first thing we perform a perturbative estimate for the critical disorder strength W_c of a putative MBL transition, showing that such W_c flows to infinity as the thermodynamic limit is approached. To do so, we employ the so-called *forward approximation* (FA) [92, 94, 453, 454], which consists in calculating the Green's functions to lowest order in the hopping among localized orbitals. For the sake of being self-contained, we review briefly the main ideas of the FA, and then discuss the implications for our system.

Brief description of the forward approximation

In the FA, one starts from the locator expansion of the resolvent:

$$G(b,a;E) = \langle b| \frac{1}{E-H} |a\rangle \tag{6.77}$$

$$= \frac{\delta_{ab}}{E-E_a} + \frac{1}{E-E_a} \sum_{p\in \mathrm{P}(a,b)} \prod_{k=1}^{|p|} \frac{-g}{E-E_{p_k}} \tag{6.78}$$

where $\mathrm{P}(a,b)$ denotes the set of paths from a to b. Notice that in our case the labels $a, b, \dots$ will represent Young diagrams, and the graph will be defined by the adjacency matrix $\sum_{\langle\lambda,\lambda'\rangle} |\lambda\rangle\langle\lambda'|$ (see $H_{\mathcal{D}}$ in Eq. (6.75)). As customary, one can pass from the random walks $\mathrm{P}(a,b)$ to the self-avoiding walks $\mathrm{SAW}(a,b)$ at the cost of introducing a self energy term:

$$G(b,a;E) = G(a,a;E) \sum_{p\in \mathrm{SAW}(a,b)} \prod_{k=1}^{|p|} \frac{-g}{E-E_{p_k}-\Sigma_{p_k}^{\{p_0,p_1,\dots,p_{k-1}\}}(E)}, \tag{6.79}$$

where indeed $\Sigma_a^{\{b,c,\dots\}}(E)$ is the self-energy at site a obtained removing from the lattice the sites $b, c, \dots$. From the *exact* representation of Eq. (6.79) one can in principle obtain also the (many-body) amplitude $\Psi_\alpha(b)$ of the system to be found in configuration b, while being in the eigenstate α localized around configuration a:

$$\Psi_\alpha(b) = \frac{1}{\Psi_\alpha(a)} \lim_{E\to E_\alpha} (E-E_\alpha) G(b,a;E). \tag{6.80}$$

Notice that this reduces to δ_{ab} in the limit $g \to 0$. Finally, performing the approximation of summing only on the *shortest paths* (or *directed polymers*) $\mathrm{SP}(a,b)$ from a to b,

and thus working to lowest order in g, one finds

$$\Psi_\alpha(b) \approx \sum_{p\in \mathrm{SP}(a,b)} \prod_{k=1}^{|p|} \frac{-g}{E_a - E_{p_k}} \tag{6.81}$$

$$= \left(-\frac{g}{W}\right)^{d(a,b)} \sum_{p\in \mathrm{SP}(a,b)} \prod_{k=1}^{|p|} \frac{1}{E'_a - E'_{p_k}}. \tag{6.82}$$

Above, we have introduced the distance $d(a,b)$, and the rescaled diagonal elements of the Hamiltonian $E'_a := E_a/W$.

At this point, the criterion for localization is given by the requirement that, with probability 1 over the disorder realizations, the probability of finding a particle at distance $O(L)$ from the localization center of the state goes to zero for $L \gg 1$ [453, 454]. More formally, defining

$$\Psi_r := \max_{b:\, d(a,b)=r} |\Psi_\alpha(b)| \tag{6.83}$$

the system is considered to be localized if $Z_r := \frac{1}{r}\log|\Psi_r|$ satisfies

$$P\left(Z_r \leq -\frac{1}{\xi}\right) \longrightarrow 1 \qquad \text{for } r \to \infty \tag{6.84}$$

for some finite $\xi > 0$. The other way round, if the system is delocalized we expect

$$P\left(Z_r \geq -\epsilon\right) \longrightarrow 1 \qquad \text{for } r \to \infty \tag{6.85}$$

for any arbitrarily small $\epsilon > 0$. The critical value of the disorder can be estimated from the average value $\langle Z_\infty\rangle = \lim_{r\to\infty}\langle Z_r\rangle$ using the condition

$$\langle Z_\infty(W_c)\rangle = -\log|g|. \tag{6.86}$$

The possibility of passing from the statements in probability, Eqs. (6.84)–(6.85), to the one in terms of the average value, Eq. (6.86), is possible because of probability concentration as $r \to \infty$ [453].

Application to the melting process

The numerical results, obtained by using the empty diagram $\lambda = 0$ as starting point ("a" in the formulae above), are reported in Fig. 6.10. It is sufficient to plot a value of W only, in virtue of Eq. (6.82). As r is increased, $\langle Z_r\rangle$ diverges, being fitted reasonably well both by $\sim \sqrt{r}$ or $\log r$ (more on this below). This proves the absence of a finite critical value W_c, which instead can be present only if $\langle Z_r\rangle$ saturates to a finite constant.

We now explain why both the square-root and the logarithmic fits are reasonable for the data in Fig. 6.10 (larger system sizes are needed to discriminate between the two). Starting from the former, one can see that it traces back to the dimension of the Hilbert space as follows. In Eq. (6.82), the dominant contribution to the term $(E'_a - E'_{p_k})^{-1}$ is of order $\sim d_{|p_k|}$, being d_k the number of states at distance k from the initial configuration (cf. Sec. 6.3.4): indeed, one can take the average level spacing to be $\delta E'_{p_k} \approx 2k/d_{|p_k|}$, and take only the dominant (exponential) contribution. The initial configuration being empty, the diagrams at distance k are all made of k blocks, thus they belong to the subspace $\mathcal{H}_{\mathcal{D}_k} \subset \mathcal{H}_{\mathcal{D}}$. At this point, one can evaluate the

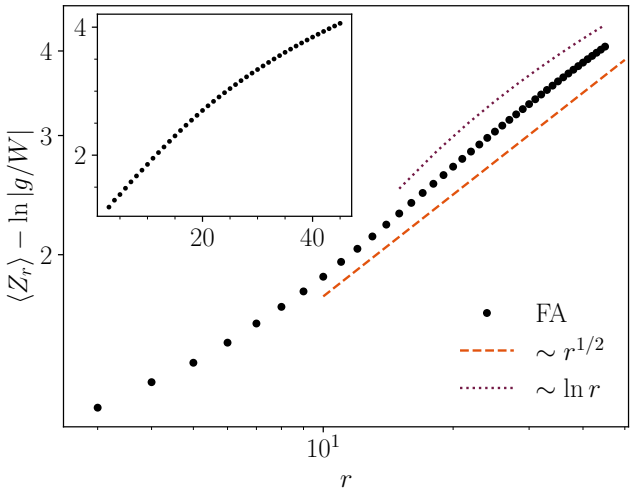

FIGURE 6.10: Plot of $\langle Z_r \rangle$ vs r as described in the main text: in the main panel it is shown in log-log scale, while in the inset in linear scale. The dots are the numerical results of the FA up to $r = 45$. Their growth should be compared either with a square-root (dashed orange line), or a logarithm (dotted purple line). Fitting a square-root behaviour compares reasonably well with the mean-field-like estimate of the main text: the fit (not shown) gives $Z_r \approx 0.57 r^{0.52}$, while the analytical prediction was $Z_r \approx \pi(2/3)^{3/2}\sqrt{r} \approx 1.71\sqrt{r}$. The numerical data was averaged over 3000 disorder realizations. This figure is taken from Ref. [8].

product over k in Eq. (6.82):

$$\prod_{k=1}^{r} \frac{1}{E'_a - E'_{p_k}} \sim \prod_{k=1}^{r} d_k \sim \exp\left[\sum_{k=1}^{r} \pi\sqrt{\frac{2k}{3}}\right] \sim \exp\left[\pi\left(\frac{2}{3}\right)^{3/2} r^{3/2}\right], \tag{6.87}$$

where there was used the Hardy-Ramanujan formula $\dim \mathcal{H}_{\mathcal{D}_k} = d_k \sim \exp\left(\pi\sqrt{2k/3}\right)$, and the asymptotic expansion of the harmonic numbers of order $1/2$[4]. Notice that one can set, according to the convention of Eq. (6.83), $|p| = r$ and $|p_k| = k$.

The further sum over the SP in Eq. (6.82) does not alter the behavior of the estimate for large $|p|$, as one can check by giving an upper bound to the number of SP: for example, one can bound it by making all diagrams of size k connected to all diagrams of size $k+1$, for all k. In this case, also the number of SP is $\prod_{k=1}^{r} d_k$, thus giving the same asymptotic behavior (see also the discussion below).

Putting the pieces together, one gets

$$Z_r = \frac{1}{r} \log|\Psi_r| \sim \sqrt{r}. \tag{6.88}$$

This estimate gives a good prediction for Z_r, as shown in Fig. 6.10, but it relies on the assumption that, at each step of the optimal path, it is feasible to remain as close as possible to the resonant energy. Therefore, we understand that this is a *optimistic* estimate for Z_r, yielding a scaling that we can consider to be a sort of upper bound for it.

[4] The summation can be performed using the Euler–Maclaurin formula. For the present case, it gives $\sum_{k=1}^{n} \sqrt{k} = \frac{2}{3}n^{3/2} + \frac{\sqrt{n}}{2} + \zeta\left(-\frac{1}{2}\right) + O(n^{-1/2})$, therefore yielding the leading contribution reported in Eq. (6.87).

The assumption of remaining on resonance at each step is not valid for general geometries: it is false, for instance, on the Bethe lattice—which usually constitutes a good approximation of many-body Fock spaces. On the other hand, it is surely valid in the case in which each configuration $\lambda \in \mathcal{D}_r$ is connected to any other configuration $\lambda' \in \mathcal{D}_{r+1}$, in a mean-field-like setting (this same mean-field approximation was used above to bound the number of SP). We argue that the Young lattice of Fig. 6.9, i.e. the graph obtained by joining two Young diagrams iff they differ by just one square, has indeed properties much closer to the mean-field case rather than to the Bethe lattice.

Let us consider the number of shortest paths connecting the empty diagram to a configuration made of r blocks, call it $\lambda \in \mathcal{D}_r$. For the Bethe lattice, by definition, the number of paths going between any two configurations is one, as there are no loops. On the other hand, considering the mean-field Young lattice in which any configuration in $\mathcal{D}_r$ is connected to any configuration in $\mathcal{D}_{r+1}$, we already showed that the number of shortest paths connecting the empty diagram with any diagram at level r is $\prod_{k=1}^{r} d_k \sim \exp(Cr^{3/2})$. For the true Young lattice, one can take advantage of the fact that the number of shortest paths leading to a Young diagram λ coincides with the so-called dimension $\dim(\lambda)$, computed according to the hook length formula [402]. Such number $\dim(\lambda)$ corresponds also to the dimension of the representation of the symmetric group identified by the diagram λ [452]. At this point, the typical dimension of a diagram λ made of r squares is found to be $\dim(\lambda) \sim \sqrt{r!}$ [399], so the typical number of SP will scale like $\sqrt{r!}$ as well. Therefore, even if the SP are less than in the mean-field case, they are more than exponentially many in the distance from the starting configuration. In conclusion, one obtains a growth

$$\langle Z_r \rangle \sim \log r. \tag{6.89}$$

The true behaviour of the curve in Fig. 6.10 will likely be something in between a square root and a logarithm. For the system sizes accessible to present-day computers, and given the slow growth of both curves, it is not possible to discern between the two hypotheses. Nevertheless, for our purposes the results shown are sufficient to claim that there is no finite-disorder localization transition, at least at the lowest order of perturbation theory.

6.5.3 Spectral statistics via exact diagonalization

In this Section, we support the conclusions found in perturbation theory by performing an extensive numerical study of the model through exact diagonalization. The numerics was performed by constructing explicitly the Hilbert space of the model, i.e. the Young lattice of Fig. 6.9a, with ad-hoc methods. An example of the Hamiltonian matrix, truncated to a finite N, is shown in Fig. 6.9b[5]. The code is made available on GitHub [460].

To distinguish between the MBL and ETH regimes of a system, one can consider various indicators, each with well-defined, and different behaviors in the two cases. Here, we consider mainly spectral indicators. Let us start from the results for the

[5]Another possible way of simulating the system is with the fermionic chain representation. However, we chose not to do so for two reasons. First, the Fock space of a chain of length L at half filling does not contain only the Young diagrams made at most of $L/2$ squares, but also Young diagrams with more squares: consider e.g. the state in which $L/2$ fermions are on the left half of the chain, and the right half is empty, that corresponds to a Young diagram made of $(L/2)^2$ squares. Second, and more importantly, the disorder maps to non-local interactions on the chain, which are more difficult to handle.

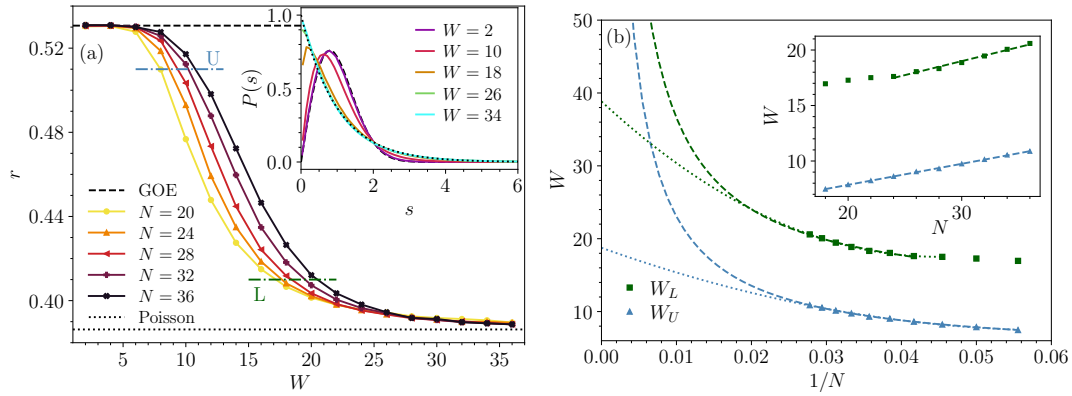

FIGURE 6.11: (a) r parameter as a function of the disorder strength W (in units of $-g \equiv 1$), and for increasing system sizes. The r value flows from the GOE prediction at small disorder, to the Poisson one at large disorder for any considered system size. However, no real sign of the build-up of a transition is found; rather, the crossover from GOE to Poisson simply seems to shift to larger values of W as the thermodynamic limit is approached. This feature is analyzed by means of the upper (U) and lower (L) cuts, represented by the dashed-dotted lines; see the main text for more details. The number of disorder realizations used ranges from 10000 (smallest system size) to 1700 (largest system size). (Inset) Histogram of the normalized level spacings s, for $N = 32$ and 3000 disorder realizations. Also here one can see flow from GOE (dashed black line) to Poisson (dotted black line). (b) Finite-size scaling analysis of the disorder strengths for which the r parameter becomes smaller than 0.51 (W_U) and 0.41 (W_L). In the inset, it is shown how they seem to diverge linearly with system size, but with two different slopes. In the main panel, two different possible fits are performed: a linear one $W = a + bN$ (dashed line), and one of the form $W = a' + b'/N + c'/N^2$ (dotted line). Further implications are discussed in the main text. This figure is taken from Ref. [8].

statistics of the energy levels E_n, summarized in Fig. 6.11. In the inset of Fig. 6.11a we show how, at finite system size N, there is a crossover from Wigner's surmise (viz. GOE, at small W) to the Poisson gap distribution (at large W) for the normalized level spacings $s_n = (E_{n+1} - E_n)/\langle E_{n+1} - E_n \rangle$, taken at the center of the spectrum. To argue that such crossover builds up into a sharp transition in the thermodynamic limit, one may look at the spectral gap ratio parameter

$$r = \left\langle \frac{\min(s_{n+1}, s_n)}{\max(s_{n+1}, s_n)} \right\rangle , \tag{6.90}$$

which needs not be normalized. In the main panel of Fig. 6.11a, one can see that the crossover from $r_{\text{GOE}} \simeq 0.5307$ to $r_{\text{Pois}} \simeq 0.3863$ gets slightly steeper as N increases, but it also moves to larger values of W. To perform a reliable finite-size scaling analysis, we decided to look at the disorder strengths W_U and W_L, for which the r parameter becomes smaller than 0.51 and 0.41, respectively[6]. Reliable estimates for W_U and W_L were obtained by fitting locally the values of $r(W)$ with a polynomial function, and solving for the intersection. In the inset of Fig. 6.11b, it is shown how the values found for W_U and W_L seem to diverge linearly with system size, but with two different slopes. In particular, the faster divergence of W_L indicates that no transition is being built up; instead, the crossover from GOE to Poisson seems to become smoother at larger system sizes. Notice that this last fact also prevents one to perform a scaling collapse of the data: it is impossible to accomodate the scalings of both $r > 0.51$ and $r < 0.41$ with only one function, since the two parts of the curve $r(W)$ are flowing towards larger values of W with different speeds. In addition to the previous observations, both W_U and W_L seem to represent *lower bounds* (see how the curves $r(W)$ change with system size in Fig. 6.11a) for the critical disorder strength W_c, at which a putative MBL transition may take place: therefore, we believe that such transition does *not* take place at all in the thermodynamic limit, being pushed to infinite disorder strength.

A more refined analysis is shown in the main panel of Fig. 6.11b. There, we try to extrapolate to $N = \infty$ with two different fits. The dashed line represents the same fit of the inset, i.e. a linear one: $W = a + bN$. The dotted line, instead, is a fit of the form $W = a' + b'/N + c'/N^2$, which extrapolates to a finite value at $N = \infty$. Nevertheless, one can notice that the values extrapolated from W_U and W_L are far apart, indicating that either the fitting region is severely pre-asymptotic, or there is no single transition point, but a slow crossover even in the thermodynamic limit. Moreover, one can recognize that, to truly distinguish between the two fitting functions, one would need to go to system sizes $N \gtrsim 60$ (at least for W_L, which is the most sensitive to delocalization). Such a system size corresponds to an Hilbert space dimension of more than $\sim 6 \times 10^6$, which is beyond reach for present-day computers and algorithms.

It is interesting to compare our Fig. 6.11 with the equivalents of Refs. [184, 461], where instead the data indicates the existence of a transition in the thermodynamic limit. The two plots are substantially different in the scaling as $N \to \infty$. In our case the curves $r(W)$ seem to emanate from a common asymptote as $W \to \infty$, and simply shift towards larger values of W as N is increased. On the contrary, in Refs. [184, 461] such curves become steeper already at small system sizes, and in particular the lower part of the curves *moves towards smaller values of* W. Therefore, in those works it was possible to analyze another reliable indicator of the MBL transition, namely

[6] The values of 0.51 and 0.41 are of no special importance; any other values near to $r_{\text{GOE}} \simeq 0.5307$ and $r_{\text{Pois}} \simeq 0.3863$ yield the same results.

W_*, the point at which the curves for N and $N+1$ intersect. Here, we could not extract a sensible W_* from the data of Fig. 6.11a being it ill-defined: the curves $r(W)$ are almost superposed at large W.

As a last thing, we remark that all the above results apply to the center of the spectrum, i.e. to *generic* states of the model under consideration. However, as stated before, we are interested in the dynamics *starting from a particular state*, i.e. the empty Young diagram. Such state has zero expected energy, but for the system under consideration there is no symmetry that forces the spectrum symmetric wrt. zero, thus making the corner an infinite-temperature state. We checked explicitly, however, that the corner state on average lies at the center of the spectrum, and that it has a vanishing probability of being very close to the ground state (or the most excited state).

6.5.4 Dynamics

In the previous Section, we have looked at spectral indicators of ergodicity, and the emerging picture is that there is no *bona fide* MBL phase in the thermodynamic limit for the model under consideration. The absence of a truly localized phase does not immediately imply that, even in the thermodynamic limit, the dynamics of the model should be the same of a standard, ergodic and diffusive system [408–410]. We will now show, in fact, that the $2d$ quantum Ising model induces on the "holographic" chain a peculiar type of dynamics. We will relate the properties on the chain to the ones in $2d$: in particular, the speed of the erosion of the corner will be mapped to the particle current on the chain. The entanglement entropy arising from a bipartition of the $1d$ chain, instead, will correspond again to the entanglement entropy of a bipartition of the $2d$ model. Finally, we present the numerical results both for transport and entanglement growth.

Transport on the chain

As a first step we find, in the ψ_x picture, the number of blocks a Young diagram is composed of. This is done by counting every fermion at distance x to the left from the domain wall, and every hole at distance x to the right, each weighted with the distance from the origin:

$$N = \sum_{x>0} x(1-n_x) + \sum_{x\leq 0} |x|\, n_x, \tag{6.91}$$

where $n_x = \psi_x^\dagger \psi_x$ is the fermion number at site x. Taking into account that the configurations are definitively $n_x \equiv 1$ as $x \to +\infty$, and $n_x \equiv -1$ as $x \to -\infty$, the sum converges. Then, let us take a derivative wrt. time in Eq. (6.91):

$$\dot{N}(t) = -\sum_x x\, \dot{n}_x(t). \tag{6.92}$$

Using the fermion number conservation $\dot{n}_x(t) + \partial_x J(x,t) = 0$, where ∂_x is the discrete space derivative, we can rewrite the total block number (after an integration by parts) as

$$N(t) = -\int_0^t dt' \sum_x J(x,t'). \tag{6.93}$$

This should be intended as an operator identity.

In the case of the clean crystal with $h_i \equiv 0$, we have shown before that in the limit $|x|, t \to \infty$ with $|x/gt|$ held finite, it holds

$$\langle n_x(t) \rangle \simeq \frac{1}{2} + \begin{cases} \frac{1}{\pi} \arcsin\left(\frac{x}{2|gt|}\right) & \text{if } |x| < 2|gt| \\ \frac{1}{2}\mathrm{sgn}(x) & \text{if } |x| > 2|gt|. \end{cases} \tag{6.94}$$

Using this result, in the continuum limit

$$\langle \dot{N}(t) \rangle \simeq 2g^2 t, \tag{6.95}$$

and it follows

$$\langle N(t) \rangle \simeq (gt)^2. \tag{6.96}$$

This power-law scaling can be traced back to the fact that for the ballistic propagation of free fermions

$$\langle J(x,t) \rangle \simeq \begin{cases} |g|/2 & \text{if } |x| < 2|gt| \\ 0 & \text{if } |x| > 2|gt|, \end{cases} \tag{6.97}$$

so

$$\langle N(t) \rangle \simeq 2g^2 \int_0^t dt'\, t' = (gt)^2. \tag{6.98}$$

Now consider, instead, the case of diffusive motion of the excitations in the fermionic chain. One has $J = -D\partial_x n_x$ for a diffusivity coefficient D, so

$$\int dx\, \langle J(x,t) \rangle = -D \langle n_{+\infty}(t) \rangle + D \langle n_{-\infty}(t) \rangle = -D \tag{6.99}$$

and

$$\langle N(t) \rangle \simeq Dt. \tag{6.100}$$

In a more general setting, the exponent of the growth of $\langle N(t) \rangle$ in the Young blocks is related to the nature of transport for the excitations of the ψ chain ($x(t)$ is the semiclassical trajectory of the excitation):

$$\langle N(t) \rangle \sim t^{2\beta} \quad \longleftrightarrow \quad x \sim t^{\beta}. \tag{6.101}$$

As just shown above, in the ballistic case $\beta = 1$ and in the diffusive case $\beta = 1/2$. In Refs. [409, 462, 463] it is discussed at length how the exponent β dictates the decay of the correlation functions of the current, of the number n, and the non-equilibrium steady state current J_{ness} in a driven set-up:

$\langle N(t) \rangle$	x^2	$\langle J(0,t)J(0,0) \rangle$	$\langle n_x(t) n_x(0) \rangle$	J_{ness}
$t^{2\beta}$	$t^{2\beta}$	$t^{-2+2\beta}$	$t^{-\beta}$	$L^{1-\frac{1}{\beta}}$

The extreme case in which $\beta \to 0$ is expected when entering a MBL phase: $\beta(W) \sim (W_c - W)^{\alpha}$, although the critical exponent α is currently unknown. In particular, for MBL systems it is possible to show that $N(t)$ saturate to a constant in the long-time limit [105–107]. As we will show numerically in Sec. 6.5.4, for the model under consideration $\beta \simeq 0$, but the absence of true MBL will manifest in the slow growth $\langle N(t) \rangle \sim \log|gt|$. This implies that the total current decays as $\sim 1/t$, which is indeed an extremely slow decay. We will comment in Sec. 6.5.5 how these features cannot be understood on the basis of simple semiclassical pictures, and instead are due to the quantum nature of the problem.

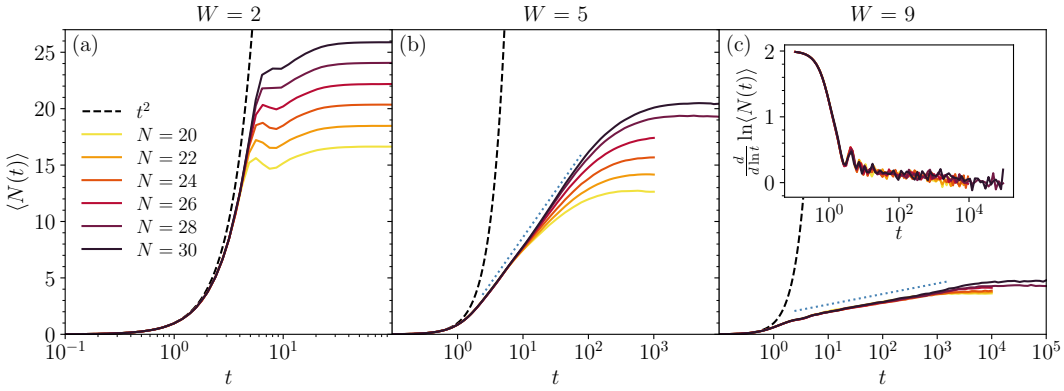

FIGURE 6.12: Time evolution generated by the Hamiltonian (6.2), starting from the corner state. The average number $\langle N(t)\rangle$ of fermions hops is plotted for various system sizes, and for three values of the disorder strength W (here we set $g \equiv 1$, fixing the energy scale). One can see that at small disorder (i.e. $W = 2$, panel (a)) the curves do not behave much differently from the prediction for $W = 0$, Eq. (6.96), increasing almost as g^2t^2 (dashed line) before saturating. Already at $W = 5$ (panel (b)), instead, the growth of $\langle N(t)\rangle$ has been severely hindered, insomuch that it is compatible with a logarithm (dotted blue line): $\langle N(t)\rangle \sim \eta_N \log t$. Finally, at $W = 9$ (panel (c)) the logarithmic behaviour of $\langle N(t)\rangle$ becomes manifest, as shown also by the inset: the logarithmic derivative keeps decreasing towards 0, indicating that $\langle N(t)\rangle$ must be slower than a power law. All the values of η_N, extracted from fits, are displayed in Fig. 6.13a. All the numerical data is averaged over at least 1600 disorder realizations. This figure is taken from Ref. [8].

Entanglement growth

For what concerns the entanglement growth, when the disorder is turned on ($W \neq 0$) the picture presented in Sec. 6.3.3 changes significantly. As anticipated above, indeed, the number of particles that hop across the bipartition is severely reduced from $\langle N(t)\rangle \sim (gt)^2$ to $\langle N(t)\rangle \sim \log|gt|$. Therefore, one should expect $S_E(t)$ to grow at most like $\sim \log|gt|$ as well. Below, we will show the exact growth of S_E obtained numerically, and comment it in detail.

Numerical results

Here we summarize the results of a numerical investigation for the dynamics generated by the Hamiltonian (6.2). Time evolution was performed through full (for $N \leq 26$) and sparse (for $N \geq 28$) matrix exponentiation with `SciPy`, having constructed the Hamiltonian matrix incorporating both the hopping and the on-site disorder as in Sec. 6.5.3. The code is made available on GitHub [460].

We start by showing in Fig. 6.12 the time evolution for the average number of fermions $\langle N(t)\rangle$ that have hopped. Equivalently, $\langle N(t)\rangle$ is the average number of squares the state is composed of, in the language of Young diagrams. One can see that the growth is ballistic—i.e. $\langle N(t)\rangle \sim (gt)^2$—both at short times for all disorder strengths, and at all times for small disorder: for this latter statement, see the case of $W = 2$ (in units of g) in Fig. 6.12a. Then, as the disorder is increased slightly, the growth of $\langle N(t)\rangle$ slows down considerably: it acquires a logarithmic behaviour that lasts for three decades already at $W = 5$ (Fig. 6.12b), and for four decades at $W = 9$ (Fig. 6.12c), for the largest system sizes considered, before saturating to a

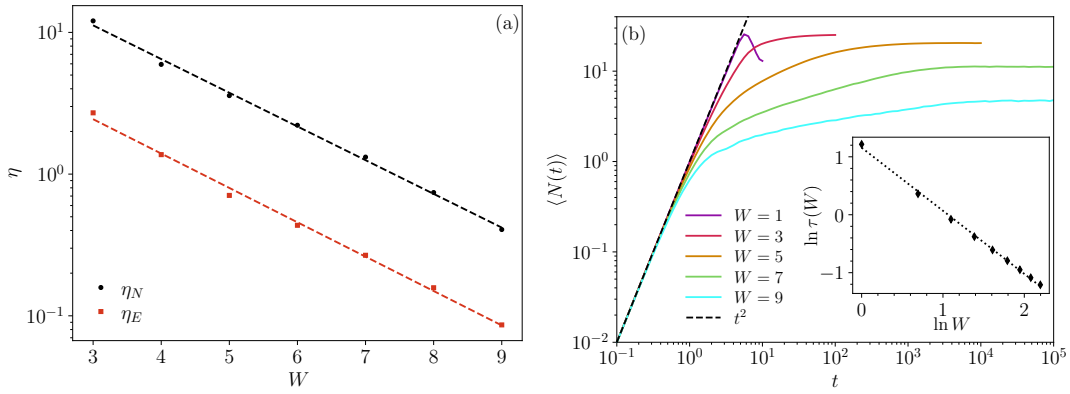

FIGURE 6.13: (a) For both the average number $\langle N(t)\rangle$ and the entanglement entropy $S_E(t)$ we performed logarithmic fits $\eta \log t + c$. Here, we display the dependence of the coefficients η_N and η_E on the disorder strength W. We find both of them compatible with an exponential decay $\eta = \eta_0 e^{-W/W_0}$, with $W_0 \simeq 1.8$ (the dashed lines show the fits). (b) Average number of fermion hops $\langle N(t)\rangle$, for various disorder strengths, with system size $N = 30$. The log-log scale makes manifest the behaviour $\langle N(t)\rangle \sim (gt)^2$ at small times ($g \equiv 1$ for numerical purposes), from which $\langle N(t)\rangle$ departs at the time $\tau(W)$. (Inset) Estimates of $\tau(W)$, using a threshold $\varepsilon = 0.05$ (see main text). The fit entails $\tau(W) \sim W^{-\gamma}$ with $\gamma = 1.0$. This figure is taken from Ref. [8].

finite-system value[7]. The growth of $\langle N(t)\rangle$ is more consistent with a logarithm than with a very small power law: in the inset of Fig. 6.12c we show how the logarithmic derivative $d \log \langle N(t)\rangle / d \log t$ keeps decreasing towards 0 also for the largest times reached—though some fluctuations are present. Large fluctuations are present also at the level of $\langle N(t)\rangle$: we found the fluctuation of $N(t)$ to be of the same order of magnitude of $\langle N(t)\rangle$ for the strongest disorders considered (i.e. $W \gtrsim 8$).

The remarkable feature of the results of Fig. 6.12 is that, for the same values of the disorder strength W, the spectral indicators predict the presence of a *thermal* phase, where it is natural to expect $\langle N(t)\rangle \sim t$ (i.e. diffusion), or at most $\langle N(t)\rangle \sim t^{2\beta}$, $\beta < 1/2$ (i.e. subdiffusion). We find, instead, a severe impediment to transport, that pushes down $\langle N(t)\rangle$ to a logarithm. In Fig. 6.13a we show the results of fits $\langle N(t)\rangle = \eta_N \log t + c_N$: we find the scaling $\eta_N(W) = \eta_{0,N} e^{-W/W_0}$ with $W_0 \simeq 1.8$.

In Fig. 6.13b we analyze instead the behavior of $N(t)$ at earlier times. To this end, we define the timescale $\tau(W)$ that quantifies when the curve $\langle N(t)\rangle$ departs from the ballistic growth g^2t^2, e.g. when $|\log \langle N(t)\rangle - 2 \log |gt|| > \varepsilon$ for some fixed threshold value ε. From the results of Fig. 6.12 we expect that $\tau(W)$ suffers of little finite-size effects. Moreover, it is natural to expect $\tau(W)$ to be a decreasing function of W, as for strong disorder, the departure from the ballistic motion is supposed to occur sooner. Also, one would guess $\tau(W) \to 0$ for $W \to \infty$, i.e. for every finite disorder strength there is a ballistic regime at small times. Indeed, one can see, in the inset of Fig. 6.13b, that $\tau(W) \sim W^{-1}$.

Let us finally move to the entanglement growth. In Fig. 6.14 we consider the entanglement entropy, relative to the bipartition along the bisectrix of the corner (and, consequently, that cuts the fermionic chain at the origin). Several comments are in order. First, despite the ballistic spreading of *particles*, at $W = 0$ the entanglement

[7] Due to the extremely slow dynamics, system sizes larger than $N = 30$ were not considered. We believe nonetheless that the system sizes analyzed in this Chapter represent good evidence supporting our claims.

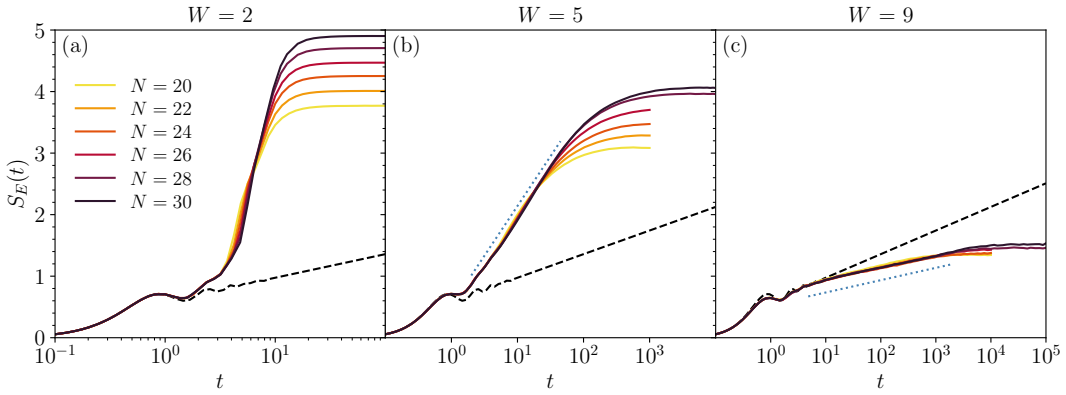

FIGURE 6.14: Time evolution of the half-system entanglement entropy S_E, for various system sizes, and three different disorder strengths. At small disorder ($W = 2$, panel (a)), the growth of entanglement is fast, probably a power law (even if larger system sizes are needed to extract a reliable scaling). Already at moderate disorder ($W = 5$, panel (b)), however, the growth of entanglement slows down to a logarithm (the dotted blue line serves as a guide to the eye), being impeded by a logarithmic transport (as described in the main text). When disorder is ramped up ($W = 9$, panel (c)), the logarithmic behaviour $S_E(t) \sim \eta_E \log t$ remains, but with a smaller coefficient η_E in front. The coefficients η_E extracted from fits are reported in Fig. 6.13a. This figure is taken from Ref. [8].

growth is only *logarithmic* in time (dashed black line in Fig. 6.14), because of integrability: this is traced back to excluded volume effects among the fermions. It should not worry, then, that $S_E(t)$ *grows faster if* $W > 0$, but small: indeed, a small amount of disorder helps the system in thermalizing, and the entanglement entropy raises linearly in time, essentially because of chaos propagation [464–466].

Second, in Fig. 6.13a we show the results of fits $S_E(t) = \eta_E \log t + c_E$, as was done for the number growth. We find the scaling $\eta_E(W) = \eta_{0,E} e^{-W/W_0}$ with the same $W_0 \simeq 1.8$. Such agreement does not come unexpected: if transport is blocked, and no long-range dephasing interactions are present (contrary to the l-bit model of MBL [105–107]), then entanglement cannot spread beyond the melted part of the corner. Indeed, for each particle that hops across the origin, the entanglement entropy between the left and right halves of the chain increases fast, well before the next hop, because of non-local interactions entailed by the disordered potential. But such non-local interactions act only on the melted part of the corner, and thus particle spreading functions as a bottleneck for the entanglement growth.

6.5.5 Comparison with classical corner growth models

The slow growth of the average number of squares in the Young diagrams $\langle N(t) \rangle$, observed in the quantum dynamics (Sec. 6.5.4), turns out to be anomalous also from the perspective of similar, classical models. We have already discussed in Sec. 6.3 the comparison with the simple exclusion processes: for instance, in absence of disorder the totally anti-symmetric simple exclusion process (TASEP) turns out to have ballistic dynamics too [436], but a different limiting shape for the eroded part. When disorder is added, instead, one might hope to reproduce the quantum dynamics with an exclusion process in which particles are subject to a strongly inhomogeneous waiting time before moving, according to some probability distribution. It turns out that, even when a fat-tailed probability distribution for the waiting times is chosen (notice that this also makes the process non-Markovian), the growth of the eroded corner is power-law [467], never attaining a logarithmic behavior as the

one observed in the quantum regime. In particular, a logarithmic growth can be obtained only if the waiting-time distribution behaves like $p(\tau) \sim \tau^{-1}$ for large τ, i.e. it is non-normalizable. This is an indication of the purely quantum nature of the problem we have discussed, that cannot be reproduced by classical means.

Another interesting question is about the comparison of the average limiting shapes, between classical and quantum melting processes. The clean case was already studied in Sec. 6.3.1; the disordered case is more intriguing, and difficult to analyze: we plan to discuss this issue in a future work.

6.5.6 Limits of validity of the approximations

So far, we have been discussing the dynamics of melting of a $2d$ disordered quantum crystal, by modelling it through the strong-coupling limit of the $2d$ quantum Ising model, in presence of a random longitudinal field. However, the coupling J was *effectively taken to be infinite* or, equivalently, the $O(1/J)$ corrections were considered always negligible. On the other hand, in the clean case the $O(1/J)$ corrections lead to interesting phenomena as Stark MBL. The rationale behind the choice of neglecting the corrections in this Section was the following: while in the clean system ($W = 0$) the introduction of interactions leads to integrability breaking, for $W \neq 0$ it would lead to just minor *quantitative* modifications in the dynamical behaviour. Looking at the precise form of the $O(1/J)$ corrections (Eq. (6.60)), one sees that they are (parametrically small) four-body interactions on the fermionic chain. Therefore, they become negligible in comparison with the strong, non-local interactions arising from the disorder. In particular, the sum appearing in Eq. (6.74) (and therefore in Eq. (6.76)) makes the disordered interactions of order $\sqrt{N}W$, when acting on Young diagrams of size N. Consequently, they become stronger as time passes by, and the Hilbert space of larger Young diagrams is explored, making the $O(1/J)$ corrections even less relevant.

Of course, we expect the picture presented to break down at small values of J: there, also the mapping to fermions ceases to be valid, since it becomes possible for any $2d$ spin to flip with non-vanishing probability, and the interface is no more well defined. How the dynamics changes in such limit is however a very interesting question, that we hope may be the object of future studies.

6.6 Conclusions and outlook

In this Chapter we have shown, how to describe the dynamics of interfaces in the two-dimensional quantum Ising model, in the strong-coupling limit. As a first step, we discussed the *infinite*-coupling limit ($J = \infty$), focusing both on the equilibrium properties of $1d$ linear domains embedded in the $2d$ lattice, and of interfaces described by Lipschitz functions. In the first case, we have shown that, for such initial conditions, the model reduces to a PXP Hamiltonian, for which one can compute the equilibrium magnetization (if the initial state has negligible overlap with quantum many-body scars). In the second case, the interest for such configurations is twofold: on the one hand, they effectively describe smooth interfaces and, on the other hand, given the impossibility of breaking the domain wall ensured by the Lipschitz condition, an effective $1d$ description can be provided, which is amenable of exact solution.

Then, we moved to the case of an interface shaped like an infinite corner. After having discussed the properties of the average limiting shape, both on the lattice and

in the continuum, we characterized the growth of the entanglement entropy after a quench, and unveiled a deep connection between the dynamics of the quantum problem and the asymptotics of the Plancherel measure on Young diagrams. We finally relaxed the assumption of having an infinite Ising coupling, and made use of a Schrieffer-Wolff transformation to obtain the $O(1/J)$ corrections. The first-order corrections break the integrability of the model at $J = \infty$ but, remarkably, ergodicity is not restored. In fact, the presence of the longitudinal magnetic field causes the emergence of Stark many-body localization, that we characterized both numerically, computing the imbalance, and analytically, giving an argument for its validity.

To support our results, it is fundamental to discuss the timescales entering the problem in generic conditions. In particular, we identified in T_{preth} the *prethermal* timescale, after which the description in terms of Schrieffer-Wolff expansion is no longer valid: it turned out to be (at least) exponentially long in J. Moreover, the possibility of utilizing a $1d$ chain to describe interfaces in $2d$ is well grounded as long as the effects of a finite bubble size are negligible. We estimated the timescale T_{corner} below which this is a reliable assumption, and it turned out to be more than exponentially long in the linear size of the domain. Both of these timescales ensure that the results presented are not valid strictly only in the infinite coupling or infinite size limits, but they represent a good description also for finite coupling and finite sizes, up to very large times.

An intriguing question is about the dynamical effects arising at times larger than T_{preth} and T_{corner}. While we leave this problem to future work, we can argue that the description given here is no longer valid, as the interface-splitting moves start playing a major role, and even the conservation of the interface length is no longer strict. As a consequence, the possibility of employing a $1d$ chain to describe the dynamics of a *generic* $2d$ domain will likely become impossible. However, for some initial configurations or at least in some regimes, we expect that it will still be possible to give a description in terms of a $1d$ effective problem. We aim at attacking this problem in future works.

Let us remark that, in the general case, the full $2d$ nature of the problem will emerge in the long-time limit, or for generic couplings. In these regimes no $1d$ description will be reliable and new techniques will be needed. Ultimately, we expect that a complete solution of the $2d$ quantum Ising model is at least as hard as the solution of the $3d$ classical Ising model.

Finally, in this Chapter we addressed the spectral and dynamical properties of the disordered version of the problem. We used as initial configuration the infinite, corner-shaped interface: while this same problem turned out to display ergodicity breaking in absence of disorder, we presented both analytical and numerical evidence supporting the *absence* of a many-body localized phase when disorder is added. We established, through an analytical argument based on the forward approximation, and numerical results for spectral properties, that the model is ergodic for any finite W in the thermodynamic limit. However, we also showed that the dynamics turns out to be extremely slow: we found through an extensive numerical analysis that the growth of the average number of melted squares, $\langle N(t) \rangle$, passes from ballistic to logarithmic in time already for small disorder, and we characterized the crossover between these two regimes with various indicators. Also the entanglement entropy $S_E(t)$ shows a similar behavior, that traces back to the growth of $\langle N(t) \rangle$.

While the results showed in this Chapter support the common belief that MBL does not survive in dimensions higher than one, we presented strong evidence for

the onset of slow dynamics, namely slower than subdiffusive. Surprisingly, such behavior is already present at small disorder strength, when the system, at finite size, is fully ergodic according to the spectral indicators. An explanation of this slow, logarithmic dynamics in terms of the phenomenology of avalanches [112–114] would be desirable, but we did not address it in this first work.

7 Optimal control of a spin qubit for quantum sensing

In this Chapter, I demonstrate how to solve the control problem of a single-qubit sensor of magnetic fields. After having introduced the context, in Sec. 7.1 I describe how to model the qubit sensor. Then, in Sec. 7.2 I show how to find, with both analytical and numerical techniques, the optimal control protocol. In Sec. 7.3 I compare the results with real experimental data, showing good agreement. Finally, in Sec. 7.4 I discuss the implications of the results and suggest future applications. The Chapter is based on the publications [5, 7].

The aim of this Chapter is to show how techniques coming from the physics of spin glasses, and disordered systems more in general, can be fruitfully applied to the control problem of a single-qubit quantum sensor. In order to understand the relevance of the problem, and to motivate the study, let us start with a very brief introduction of quantum optimal control and quantum sensing.

Optimal control (OC) theory began to be formulated in the 1950s as an extension of the calculus of variations, with the aim of developing tools for the control of dynamical systems. More precisely, when a system is used to to perform some task, one would like to boost its performance—as measured by some figure of merit—, and OC theory sets the framework for this optimization. So far, OC methods have been applied to many different problems, ranging from engineering, to computer science, economics, and so on. OC methods have been fruitful also in fundamental science applications. For instance, starting from the 1980s, the technological capability to manipulate individual quantum objects as electrons, photons or atoms has been steadily increasing, and OC methods have been a fundamental player in this [468–471]. Such methods are needed, to begin with, in quantum state preparation, the first step necessary in any quantum technology application, as one wants to initialize the system in some well-defined state, possibly in the shortest time. Then, OC strategies can be helpful also in the engineering of better quantum gates (so that both the time needed and the losses are minimized) [472–475], or even in devising better quantum algorithms [476, 477].

One of the quantum technology applications in which OC theory plays a central role is quantum sensing [40]: by definition, it is the use of quantum mechanics in a fundamental way to design better sensor of physical properties. By "fundamental" we mean that properties unique to the quantum world as coherence, superposition, discreteness of the spectrum or entanglement are pivotal in the design itself of the sensor. That small quantum systems can be good candidates for sensors is already understood from the fact that they are very sensitive to external influences: this is a remarkable intuition, since it turns one of the main weaknesses of quantum devices into their strength. However, even if quantum sensing devices can in principle attain precision, accuracy, and repeatability reaching fundamental limits [478], their extreme sensitivity to external perturbations also causes them to couple with detrimental noise sources, that induce decoherence and therefore limit the interaction

time with the target signal. It is in this respect that OC comes into play, providing effective strategies that can both increase the sensitivity and decrease the influence of the noise.

In this Chapter, we introduce a method to find OC protocols for alternating current (AC) quantum sensing in the presence of dephasing noise. Such optimization problem is in general a complex classical problem. Our method, that draws an analogy between pulsed dynamical decoupling (DD) protocols [479–483] and spin glass systems [68], maximizes the phase acquired by the quantum sensor due to the target AC field while minimizing the noise detrimental effect. The OC strategy yields an improved sensitivity, and this is experimentally demonstrated using a spin-qubit magnetometer based on a Nitrogen-Vacancy (NV) center in diamond [28, 31, 484–488].

The study of optimization problems in statistical physics is a large field of research in disordered systems, with far-reaching connections from the physics of spin glasses [206, 209] and other frustrated, classical and quantum models [208, 210, 211, 241, 292, 489, 490] (see also Chap. 2). For our particular case, we find that the problem of optimizing the control protocol for our quantum sensor is homologous to that of finding the ground state of a classical Ising spin Hamiltonian. The control π-pulse times correspond to the locations in the chain of the domain walls. The couplings between the spins are of both signs, and this is customary in optimization problems: their antiferromagnetic nature captures the frustration between the different terms in the Hamiltonian, which then *prima facie* is that of a spin-glass model [491]—which does not mean that there is a *spin-glass phase* at low temperature. Indeed, we find that, by trading the Ising $\mathbb{Z}_2$ spins for the continuous spins of a spherical model (SM) [80, 81], one gets rid of frustration altogether, and there are little signs of competing equilibria at low temperature, typical of replica-symmetry-broken phases [68]. Since the ground state of the spherical model can be found analytically if the spectra of the signal and of the noise are known, we obtain from this both a *lower bound* for the sensitivity[1], and a quasi-optimal controlled pulsed field. The quasi-optimal sequence can be further fed to a simulated annealing (SA) algorithm [65, 66, 492, 493], in order to find the optimal one. Such annealed sequences show, in agreement with the experiments, very good sensitivities (only about 20% higher than the bound). To show the unparalleled performance of the algorithm, we also run it on a Raspberry Pi microcomputer, where it takes milliseconds to find the optimal solutions.

7.1 Optimized dynamical decoupling for sensing

We consider a single spin-qubit sensor of time-varying magnetic fields, in the presence of dephasing noise. This quantum sensing task can be described as a compromise between spin phase accumulation due to the external target field to be measured $b(t) \equiv bf(t)$, and refocusing of the non-Markovian noise, obtained via dynamical decoupling (DD) protocols [479–483]. As in the Hahn's echo [494–496], a DD sequence is implemented by applying sets of n π-pulses that act as time reversal for the phase acquired by the qubit during its free evolution, and can be described by a modulation function $y\colon [0,T] \ni t \mapsto \{-1,1\}$ (see Fig. 7.1b). The DD sequence is embedded within a Ramsey interferometer, hence the qubit coherence is mapped

[1] The lower bound is *not* related to the Cramér-Rao bound, since the latter is used to define the sensitivity itself (see App. E.1).

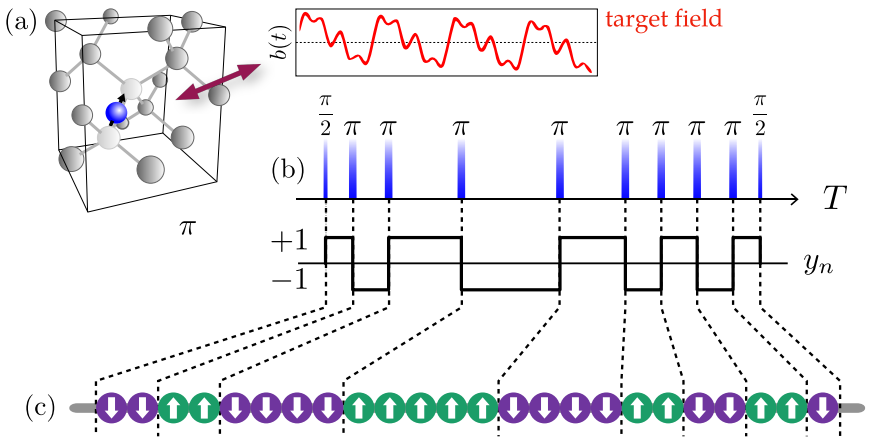

FIGURE 7.1: (a) A single spin sensor is used to detect an AC target magnetic field $b(t)$. (b) An OC field applied to the spin sensor increases its coherence, hence improving its sensitivity. (c) The difficult problem of finding an OC sequence can be mapped into a problem of finding the ground state of a virtual spin chain. This figure is taken from Ref. [5].

onto the probability of the qubit to populate the excited state $|1\rangle$:

$$P(T,b) = \mathrm{Tr}\,(\rho|1\rangle\langle 1|) = \frac{1}{2}\left(1 + e^{-\chi(T)}\cos\varphi(T,b)\right). \tag{7.1}$$

Here, φ is the phase acquired by the qubit during the sensing time T:

$$\varphi(T,b) = b\gamma\int_0^T dt\, f(t)\, y(t), \tag{7.2}$$

with γ the coupling to the field (e.g., the electronic gyromagnetic ratio of the spin sensor). The noise-induced decoherence function

$$\chi(T) \equiv \frac{1}{\pi}\int \frac{d\omega}{\omega^2}\, S(\omega)|Y(T,\omega)|^2 \tag{7.3}$$

is the convolution between the noise spectral density (NSD) $S(\omega)$ and the filter function $Y(T,\omega) = i\omega\int_0^T dt\, e^{-i\omega t}y(t)$. Note that we neglect the effect of the target field on the noise source [497].

Dynamical decoupling is a very versatile control technique, with a virtually infinite space of degrees of freedom spanned by all the possible distributions of π pulses, even at finite sensing time T. One of the most common DD sequences is the Carr-Purcell (CP) sequence [495, 496], formed by a set of equidistant pulses. Non-equidistant sequences have been proposed and experimentally tested, e.g. in Refs. [482, 498, 499]. Each of these sequences has internal degrees of freedom, that can be tuned to increase the sensing capabilities for specific target fields. However, as the complexity of the target field increases, increases also the difficulty to find a pulse sequence that successfully filters out the noise components, while still maintaining the sensitivity to the target field.

A possible approach is to use an optimization algorithm to find a sequence that optimizes a desired figure of merit, for example the sensitivity, i.e. the smallest detectable signal. This concept was proposed and demonstrated experimentally for an NV center used as a quantum magnetometer [500]. The sensitivity, which can be

expressed as (see App. E.1 for a derivation)

$$\eta = \frac{e^{\chi(T)}}{|\varphi(T)/b|}\sqrt{T}, \tag{7.4}$$

encompasses both the effect of the detrimental noise, and the effect of the target AC field. Despite the achieved improvements [500], the computational complexity of the optimization problem limited its applicability.

In our approach, instead, the cost function η is redefined to mimic the Hamiltonian of a classical Ising spin system. In this way, the continuous optimization problem for the minimization of the sensitivity of a NV-center magnetometer is reinterpreted as a discrete energy minimization problem. Specifically, we define the new cost function to be the (dimensionless) logarithmic sensitivity

$$\epsilon = \log\left(\eta\gamma\sqrt{T}\right) = \chi(T) - \log\left|\frac{\varphi(T)}{T\gamma b}\right|, \tag{7.5}$$

and we will show in Sec. 7.2 that upon time discretization ϵ will become the Ising Hamiltonian, albeit with sign-alternating, long-range interactions and a peculiar logarithmic field-spin coupling. Before doing that, however, we show how the problem can be tackled with continuous time, and by means of a reasonable approximation.

7.2 A variational approach

Our task is to find the optimal function $y(t)$ which minimizes the sensitivity η—or the logarithmin sensitivity ϵ. First of all, we rewrite ϵ as

$$\epsilon[y] = \frac{1}{2}\int_{[0,T]^2} dtdt'\; y(t)J(t,t')y(t') - \log\left|\int_0^T dt\, h(t)y(t)\right|, \tag{7.6}$$

with

$$J(t,t') = \frac{2}{\pi}\int d\omega\, \cos(\omega(t'-t))S(\omega). \tag{7.7}$$

Notice that J is a positive operator even though $J(t',t)$ can take up any values in $\mathbb{R}$, and we have the constraint $y(t)^2 = 1$ for all t. We can impose the constraint via a Lagrange multiplier function $\lambda(t)$:

$$F[y,\lambda] = \epsilon[y] + \frac{1}{2}\int_0^T dt\,\lambda(t)\left(y(t)^2 - 1\right). \tag{7.8}$$

We need to find the stationary point of $F[y]$ w.r.t. $y(t)$ and $\lambda(t)$. Formally, the saddle point equations are

$$0 = \frac{\delta F}{\delta y(t)} = \int_0^T dt'\left[J(t,t') + \lambda(t)\delta(t-t')\right]y(t') - \frac{h(t)}{\int_0^T dt\, h(t')y(t')}, \tag{7.9}$$

$$0 = \frac{\delta F}{\delta \lambda(t)} = y^2(t) - 1\,. \tag{7.10}$$

One can see that the extreme w.r.t. λ simply gives the constraint. The formal solution of the above equations is

$$y(t) = \frac{1}{D}\int_0^T dt' \left(\frac{1}{J+\lambda}\right)_{t,t'} h(t'), \tag{7.11}$$

where λ stands for the diagonal operator $\lambda(t)\delta(t-t')$, and

$$D = \int_0^T dt\, h(t)\, y(t) = \frac{1}{D}\int_0^T dtdt'\, h(t) \left(\frac{1}{J+\lambda}\right)_{t,t'} h(t')$$
$$\implies D = \left(\int_0^T dtdt'\, h(t) \left(\frac{1}{J+\lambda}\right)_{t,t'} h(t')\right)^{1/2}. \tag{7.12}$$

By plugging Eq. (7.11) in Eq. (7.8), one can express the cost function at the saddle as

$$\begin{aligned} F &= \frac{1}{2}\int_{[0,T]^2} dtdt'\, y(t)\, J(t,t')\, y(t') - \log\left|\int_0^T dt\, h(t)y(t)\right| + \frac{1}{2}\int_0^T dt\, \lambda(t)\left(y(t)^2-1\right) \\ &= \frac{1}{2D^2}\int_{[0,T]^2} dtdt'\, h(t)\left(\frac{1}{J+\lambda}\right)_{t,t'} h(t') - \log\left|\frac{1}{D}\int_0^T dt\, h(t)\left(\frac{1}{J+\lambda}\right)_{t,t'} h(t')\right| \\ &\quad - \frac{1}{2}\int_0^T dt\, \lambda(t) \\ &= \frac{1}{2} - \log|D| - \frac{1}{2}\int_0^T dt\, \lambda(t). \end{aligned} \tag{7.13}$$

The last expression is a function of $\lambda(t)$ only and one can, in principle, find the saddle point of it and substitute it in (7.11) to obtain the optimum DD sequence.

Short of solving exactly the model in Eq. (7.8), we can get good results to guide the experiment by simplifying the space in which we are searching for the minimum. We can do this in two ways: either we keep $y(t)$ defined on $\mathbb{R}$ (i.e. we keep the time continuum) and we give more structure to $\lambda(t)$, or we discretize time and enforce the constraint $y(t)^2 = 1$ exactly (therefore getting rid of λ). These two approaches will be implemented in the following.

7.2.1 Spherical approximation

In order to make progress, we substitute for the moment the constraint $y(t)^2 = 1$, for all t, with the constraint

$$\frac{1}{T}\int_0^T dt\, y^2(t) = 1. \tag{7.14}$$

This is equivalent to finding the stationary point of $F[y,\lambda]$, Eq. (7.8), in the subspace in which $\lambda(t) \equiv \lambda$. We call the resulting approximation *spherical model* (SM) since the constraint in Eq. (7.14), after discretization of time in N different, equally spaced values $t_i = i\Delta t$, puts the variable $y(t)$ on a sphere of radius $N = T/\Delta t$. The SM in the continuum limit, obtained by substituting $\lambda(t) \to \lambda$ in Eq. (7.13), provides one theoretical lower bound for the sensitivity: this simply follows from the fact that we are minimizing ϵ w.r.t. $y(t)$ over a *larger* space of functions.

Spherical models are often good mean field models of spin glasses and of their dynamics [80, 81, 501], and this case will prove to be of similar nature despite the unusual logarithmic field coupling term. By setting $\lambda(t) \to \lambda$ we have the function

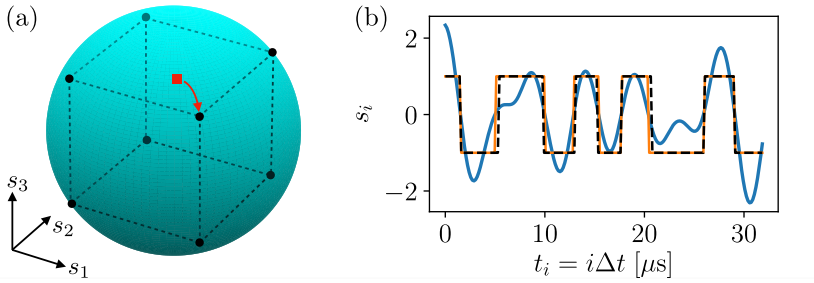

FIGURE 7.2: (a) The solution of the spherical model (red square) is, in general, not a point on the hypercube (black dots), but it can be projected (arrow) onto the latter, giving a good value for the sensitivity. (b) Comparison between solutions for 200 spins ($T = 32$ μs, $\Delta t = 0.16\mu$s): The continuous spins $s_i \in \mathbb{R}$ (blue line) can be converted into Ising spins $s_i = \pm 1$ (necessary for π-pulses) by using the sign function (orange line). The sensitivity can be improved further with a few iterations of SA to get a close-by sequence (dashed black). In this example, the trichromatic target signal and the noise are equal to the ones used in the experiment (see text). This figure is taken from Ref. [5].

of the single parameter

$$\epsilon_{\text{SM}}(\lambda) = -\frac{1}{2}\log\left|\int_0^T dtdt'\, h(t)\left(\frac{1}{J+\lambda}\right)_{t,t'} h(t')\right| + \frac{1}{2} - \frac{T}{2}\lambda, \tag{7.15}$$

where $J + \lambda$ is the operator with integral kernel $J(t', t) + \lambda\delta(t' - t)$. Maximizing w.r.t. $\lambda \in \mathbb{R}$, one finds a lower bound on the sensitivity: $\eta > \eta_{\text{SM}} = e^{\epsilon_{\text{SM}}}/\gamma\sqrt{T}$. In principle the bound is not sharp, however it provides a quick and accurate measure of the goodness of our results. Moreover, we have found by experience that it is *in practice* pretty close to being sharp and that it can hardly be improved analytically by adding more freedom to the function $\lambda(t)$ beyond the constant $\lambda(t) = \lambda$. For example the test function $\lambda(t) = \lambda_1\chi_{[0,T/2]}(t) + \lambda_2\chi_{[T/2,T]}(t)$ ($\chi_{[a,b]}$ is the characteristic function of the interval $[a, b]$), giving a two-parameters space (λ_1, λ_2) for minimization, gives at most a few percent increase on the bound on η. We therefore use it *as if it were sharp*.

One can, in fact, define for any DD sequence the dimensionless quantity $\eta_{\text{SM}}/\eta < 1$. We will see in the next section how different approximate solutions give different values of this quantity. Moreover, we will see how the solution of the SM, although not *per se* a DD sequence, can function as a starting point for finding an optimal DD sequence.

7.2.2 Time discretization and Simulated Annealing

Let us focus now on the second method: time discretization. We discretize the sensing time T into small time intervals Δt, to obtain a sequence of times $t_i = i\Delta t$ with $i \in 1, ..., N = T/\Delta t$. The interval Δt is the smallest time we allow the π-pulses of the DD sequence to be separated by. Apart from the physical limit given by the experimental apparatus, which gives a possible Δt to choose, one does not expect to need in the optimal solution π-pulses separated by much less than the minimum period of $b(t)$, if it exists (the spectrum of $b(t)$ can extend up to infinite frequency).

As introduced before, the modulation function at each of these times is $y(t_i) = \pm 1$, which dictates the sign of the phase acquired by the spin qubit during the time

interval $[t_i - \Delta t, t_i]$. We can therefore write the modulation function as

$$y(t) = \sum_{i=1}^{N=T/\Delta t} s_i \chi_{[(i-1)\Delta t, i\Delta t]}(t), \tag{7.16}$$

where $s_i = \pm 1$, and as before $\chi_{[a,b]}$ is the characteristic function of an interval $[a,b]$. Writing the modulation function in this way allows us to recast Eqs. (7.2) and (7.3) respectively as

$$\varphi(T) = T\gamma b \sum_{i=1}^{N} h_i s_i, \tag{7.17}$$

$$\chi(T) = \frac{1}{2} \sum_{i,j=1}^{N} J_{ij} s_i s_j \tag{7.18}$$

where

$$h_i = \frac{1}{T} \int_{(i-1)\Delta t}^{i\Delta t} dt\, f(t) \tag{7.19}$$

represents the interaction with a normalized target AC field, and

$$J_{ij} \equiv \frac{4}{\pi} \int d\omega \frac{[1 - \cos(\omega \Delta t)]}{\omega^2} \cos(\omega(j-i)\Delta t) S(\omega) \tag{7.20}$$

represents the interaction with the detrimental noise. We can now express the new cost function as

$$\epsilon = \frac{1}{2} \sum_{i,j=1}^{N} J_{ij} s_i s_j - \log \left| \sum_{i=1}^{N} h_i s_i \right|, \tag{7.21}$$

that closely resembles the Hamiltonian of the Ising spin glass problem for a set of N spins s_i. The ground state for this Hamiltonian can be used to obtain a modulation function, therefore a DD sequence, that minimizes the sensitivity η.

At first sight, minimizing ϵ in Eq. (7.21) on the hypercube $\{s_i\} \in \{-1,1\}^N$ can be in general a difficult problem, since the couplings J_{ij} can be of both signs. Therefore, one is tempted to use a simulated annealing (SA) minimization algorithm [65, 66, 492] to find the minimum of the energy ϵ. However, the performance of SA is strongly affected by the starting configuration both in the final value and, at least as importantly, in the time to reach it. With this in mind we turn to the SM solved in the previous section but with our discretized time, in terms of which the spherical constraint reads $\sum_{i=1}^{N} y_i^2 = N$. In the discretized form, the solution of the SM is (see Eq. (7.11))

$$y_j = \frac{1}{D} \sum_{k=1}^{N} \frac{e^{i\frac{2\pi j}{N}k}}{\sqrt{N}} \frac{\tilde{h}_k}{\tilde{J}_k + \lambda}. \tag{7.22}$$

Above, we introduced the Fourier transform of the signal term $\tilde{h}_k = \frac{1}{\sqrt{N}} \sum_j e^{-i\frac{2\pi k}{N}j} h_j$, and of the noise term $\tilde{J}_k = \frac{1}{\sqrt{N}} \sum_j e^{-i\frac{2\pi k}{N}j} J_{i,i-j}$: indeed, since $\lambda(t)$ is constant and J_{ij} depends only on the difference $i-j$, the matrix $J + \lambda$ is diagonal in Fourier space[2]. The value of λ is chosen to enforce the spherical constraint, and $D = \left(\sum_{k'} |\tilde{h}_{k'}|^2 / (\tilde{J}_{k'} + \lambda) \right)^{1/2}$.

[2]Strictly speaking, the noise term is represented by a Toeplitz matrix J_{ij}, which is diagonalized by the discrete Fourier transform only in the limit $N \to \infty$. However, already at finite N plane waves constitute a reasonable approximation for the eigenvectors. For numerical purposes, any diagonalization routine will suffice.

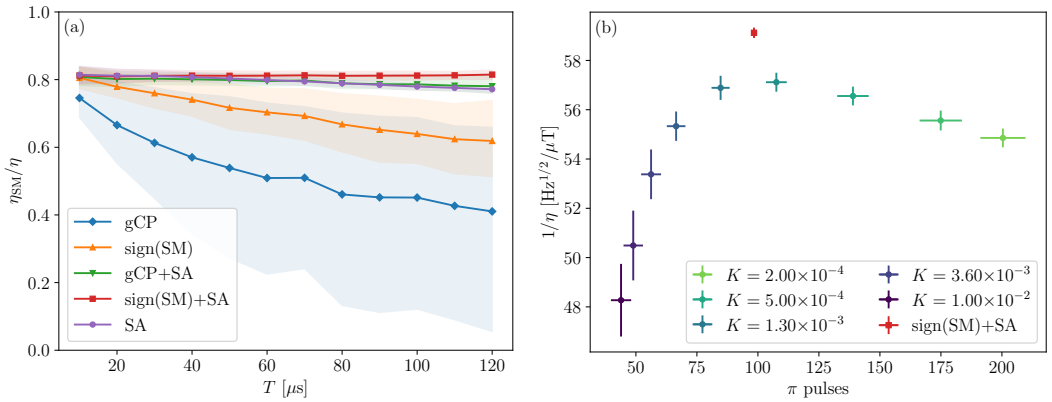

FIGURE 7.3: (a) Comparison of performances for the DD sequences discussed in the main text: generalized Carr-Purcell (gCP), spherical model projected with the sign function onto the hypercube (sign(SM)), simulated annealing (SA), and SA optimization starting from gCP and sign(SM). One can see that the best results are obtained for the SA optimization guided by the SM solution. The data refer to the ensemble of random test signals described in the main text: the dots are the average values, and the shaded area represents the 20–80 percentile of the distribution of results. The discretization interval is $\Delta t = 0.1$ μs. (b) Single instance of a random signal, corresponding to $T = 100$ μs. It is shown the comparison of the unbiased SA, i.e. starting from infinite temperature (purple to green circles), and SA guided by the SM solution (red square). The unbiased SA needs a ferromagnetic term $\propto K$—to be optimized over—in order to keep under control the number of π pulses (see Eq. (7.23)). From this plot, one learns that first, the optimal solution represents also the best trade-off between number of π pulses and sensitivity, and second, that the SA optimization guided from the SM performs better, and with less fluctuations. Here, each unbiased SA procedure uses 10^5 Monte Carlo steps and a power-law temperature ramp, while only 10^3 steps are needed for the SA from the SM solution. The dots represents the averages, and the error bars the standard deviations of the distributions. This figure is taken from Ref. [5].

One can notice that in Fourier space the optimal solution is aligned with the field, and orthogonal to the noise.

An example solution is shown in Fig. 7.2. The values of y_i do not form a sequence of ± 1, but the solution is reasonably close to the minimum of the original functional Eq. (7.21) over the hypercube $\{-1,1\}^N$. We can now use the solution in Eq. (7.22) as a starting point to find the optimal sequence $s_i \in \{-1,1\}$. To do so, we first define $s_i = \text{sign}(y_i) \in \{-1,1\}$ and then run few steps of SA *moving only the domain walls*, i.e. flipping only spins which are on a sign change: $s_i = -s_{i+1}$. The π-pulse sequence is, as before, the sequence of times where the spins change sign (the position of the domain walls in the spin chain).

We test our procedure on an ensemble of test cases constructed as follows. The signal is a superposition $f(t) = \sum_{n=1}^{N_{\text{freq}}} A_n \cos(\omega_n t + \phi_n)$: we fix $N_{\text{freq}} = 7$ and extract uniformly random frequencies in the interval $[0,1]$ MHz, uniformly random phases ϕ_n, and uniformly random amplitudes A_n s.t. $\sum_{n=1}^{N_{\text{freq}}} A_n = 1$. The noise spectrum is instead a gaussian centered at 0.4316 MHz, and with standard deviation 0.016 MHz: thus, it is close to (but a little bit stronger w.r.t.) the experimentally relevant situation discussed in the next session.

First, we use a generalized Carr-Purcell (gCP) protocol in which the DD sequence is identified by the times at which the signal $f(t)$ changes sign, i.e. its zeros. This procedure is simple but not very effective: on average, it returns between 2/3 and

1/3 of the maximum inverse sensitivity, monotonically decreasing with the time of the sampling (see Fig. 7.3a). Second, we use the solution of the SM, viz. $s_i = \text{sign}(y_i)$, as DD sequence: this gives a better solution, but still not optimal. The best results are obtained by running a fixed number of steps of SA starting from the SM DD sequence $\text{sign}(y_i)$. As it is seen in Fig. 7.3a, this last strategy gives solution close to the upper bound given by the SM itself (before projecting on the hypercube).

Finally, we compare our results with an unbiased SA optimization, starting at infinite temperature from a uniformly random sequence of $s_i = \pm 1$. In this case, to reduce the number of π pulses it is necessary to introduce by hand a ferromagnetic coupling term in the Hamiltonian:

$$\epsilon \to \epsilon - K \sum_{i=1}^{N-1} s_i s_{i+1} \tag{7.23}$$

with $K > 0$ to be tuned. One can see in Fig. 7.3b that still the best sensitivity is obtained with the combination of the SM solution and SA optimization. Additionally, from Fig. 7.3b one can also understand that the optimal solution represents the best trade-off between number of π pulses (which the experimenter would like to maintain low) and sensitivity.

To conclude, we stress that our optimization procedure is very fast, if compared to standard, general-purpose routines. In particular, we were able to run our codes on a Raspberry Pi microcomputer, where the single instance takes ~ 0.5 s for the unbiased SA algorithm, and ~ 0.02 s for the solution of the SM and subsequent annealing (using $N = 500$ spins). This fact opens the door to the miniaturization of the control electronics, in view of possible technological applications of quantum sensing.

7.3 Comparison with experiments

In this Section, we will show how the optimized DD sequences perform in real-life experiments. The experiments were performed in the "Diamond Quantum Nanoengineering" group at the European Laboratory for Non-Linear Spectroscopy (LENS), Florence, by Nicole Fabbri and Santiago Hernández-Gómez.

7.3.1 An application to magnetic field sensing

While our method is general and applicable to any spin-qubit sensor, we exemplify it through experiments with a single NV center in bulk diamond with naturally abundant ^{13}C nuclear spins, at room temperature. The ground state electron spin of the NV center can be initialized and measured by exploiting spin-dependent fluorescence, and can be coherently manipulated by microwaves [488]. We consider the two ground-state spin levels, $m_S = 0$ and $m_S = +1$, to form the computational basis of the qubit sensor $\{|0\rangle, |1\rangle\}$. The main source of noise for the NV spin qubit derives from the collective effect of ^{13}C impurities randomly oriented in the diamond lattice.

In the presence of a relatively high bias field ($\gtrsim 150$ G), the collective effect of the nuclear spin bath on the NV spin is effectively described as a classical stochastic field, with gaussian noise spectral density (NSD) centered at the ^{13}C Larmor frequency ν_L [502, 503]. We preliminarily characterize the NSD of the NV spin sensor as in Ref. [503]. The direct coupling between the target field and the nuclear spins is negligible due to the small nuclear magnetic moment [497], and the indirect coupling via the NV electronic spin is also negligible due to the presence of the strong

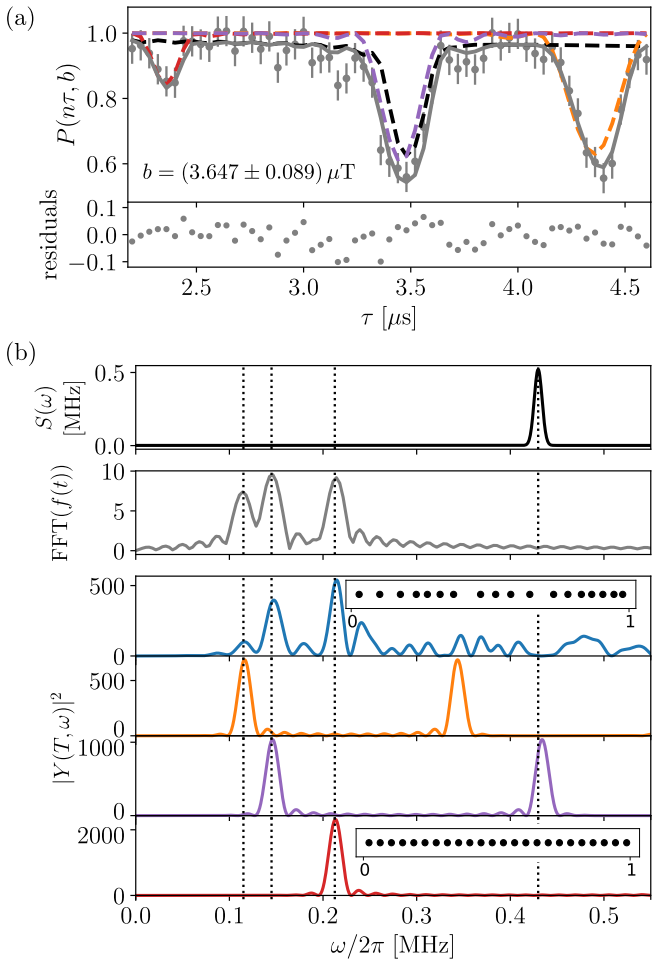

FIGURE 7.4: (a) Dynamics of the NV spin qubit under a DD sequence with $n = 16$ equidistant pulses (CP) for a trichromatic signal (see text). The NV spin coherence is mapped onto the probability of the NV spin to be in the state $|1\rangle$), $P(n\tau, b)$. Gray bullets: experimental data. Black dashed line: simulated spin coherence in the presence of noise, without any external target signals. Orange, red, and purple dashed lines: simulated spin coherence in the presence of monochromatic target fields with ω_1, ω_2, and ω_3, respectively, with no noise. Gray solid line: simulated data combining all of the above using Eq. (7.1). Residuals between gray experimental data and gray solid line are shown in the bottom plot. (b) NSD given by the nuclear spin environment of the NV sensor (black line); fast Fourier transform (FFT) of the target signal $f(t)$ (gray line). Vertical dotted lines: frequency components of the target signal, and center of the NSD. Orange, purple, and red lines: filter function for a CP sequence with $T = \frac{n}{2\nu_i}$, for $i = -1, 0$, and $+1$, respectively. Blue line: filter function of the optimized sequence. Inset: examples of time distribution of π pulses. This figure is taken from Ref. [5].

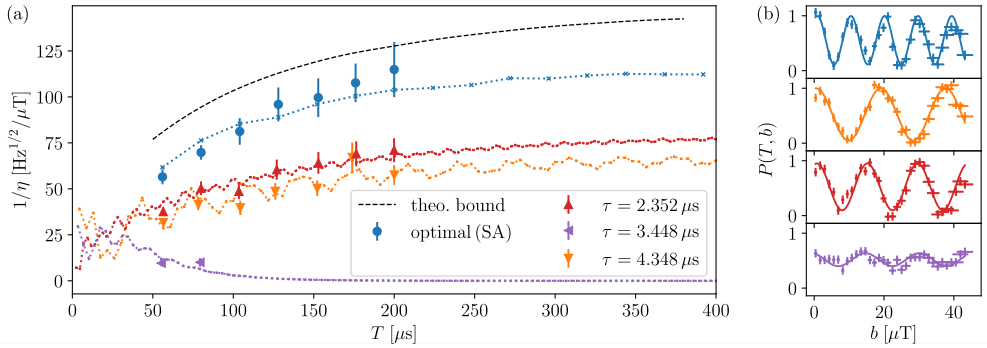

FIGURE 7.5: (a) Experimental values of the inverse sensitivity for the optimized sequences (blue circles), and for the CP sequences (orange, red, and purple triangles). The predicted values of $1/\eta$ are represented by dotted lines. Black dashed line: theoretical upper bound of $1/\eta$, obtained from the solution of the spherical model in the continuum limit. (b) $P(T, b)$ as a function of the amplitude of b, at $T \simeq 152$ μs. Same color code as in (a). Lines are a cosine fit (see text). This figure is taken from Ref. [5].

bias field [503]. Therefore, the NV spin dynamics is well described by Eq. (7.1). For the experiments we present throughout this Chapter we used a bias magnetic field of 403.2(2) G, for which the NSD is $S(\omega) = S_0 + A\exp(-(\omega-\omega_L)^2/(2\sigma^2))$, with $S_0 = 0.00119(9)$ MHz,$\omega_L/2\pi \equiv \nu_L = 0.4316(2)$ MHz, $A = 0.52(4)$ MHz, and $\sigma/2\pi = 0.0042(2)$.

As a test case for our OC method versus standard control, we consider a three-chromatic target signal, with $f(t) = \sum_{i=-1}^{+1} A_i \cos(2\pi\nu_i t)$, where $\nu_i = \{0.1150, 0.2125, 0.1450\}$ MHz are the frequency components, and $A_i = \{0.288, 0.335, 0.377\}$ are the relative amplitudes, respectively for $i = -1, 0, +1$.

In Fig. 7.4a we show the NV spin coherence $P(n\tau, b)$ under Carr-Purcell (CP)-type DD control, formed by n pulses with uniform interpulse spacing $\tau = T/n$, as a function of τ. The value of b at the position of the NV defect inside the diamond is obtained from minimizing the squared residuals between experiment (gray bullets) and simulation (gray line), for which b is the only free parameter.

The CP pulse sequence acts as a quasi-monochromatic filter centered at $1/\tau$, so that a single component of $b(t)$ can be sensed in each experimental realization. As a consequence, $P(n\tau, b)$ in Fig. 7.4a shows collapses occurring at $\tau \sim 1/2\nu_i$. Notice that the collapse corresponding to the frequency component ν_{+1} ($\tau \simeq 3.448$ μs) cannot be resolved from noise since the first harmonic of the filter function roughly coincides with the NSD peak ($\nu_{+1} \simeq \nu_L/3$) (see 7.4b). To detect the three components of the target signal and filter out the NSD, we need an optimized sequence. We thus apply the optimization algorithm detailed before to solve this experimental sensing problem.

In order to confirm the theoretical prediction on how the optimized DD sequence can outperform the standard control in terms of sensitivity, we performed measurements of the sensitivity itself. Specifically we used three different CP sequences, each with time between pulses $\tau = \frac{1}{2\nu_i}$, for $i = -1, 0, +1$. Having a previous knowledge of the NSD allows us to predict the sensitivity of the the spin sensor using Eqs. (7.3), (7.2), and (7.4), for any given DD sequence, and for any target AC signal $b(t)$. In Fig. 7.5a we show the estimated values for the inverse of the sensitivity as a function of the sensing time $T = n\tau$. Since $\tau = \frac{1}{2\nu_i}$ is fixed for each of the CP sequences, the variation of T corresponds to a variation of the number of pulses n. Notice how for $\tau = \frac{1}{2\nu_{+1}}$, the inverse of the sensitivity rapidly goes to zero. The estimated inverse

sensitivity for the optimized sequences is also shown in Fig. 7.5a. The inverse sensitivity increases as a function of T, although we expect it to decrease at longer times due to decoherence.

In the experiment, we measure $P(T, b)$ as a function of the field amplitude b at a fixed sensing time. An example of this kind of measurements is shown in Fig. 7.5b. From the analysis of the oscillation of $P(n\tau, b)$, we can directly fit the values of χ and φ/b (see Eqs. (7.1) and (7.2)), and therefore we can obtain the values of η using Eq. (7.4). The sensitivity measured experimentally shows an excellent agreement with the expected simulated values (see Fig. 7.5a). See the Supplementary Information of Ref. [5] for two additional test cases: one for a monochromatic target signal such that the fifth harmonic of the NSD coincides with the frequency of the target signal; and one for a target signal with seven frequency components, all close to the NSD peak. These two cases confirm the results of the experiments shown here.

7.3.2 An application to biological signals sensing

As an exemplary case, we consider the electromagnetic signal generated by a microtubole. Microtuboles are cytoskeletal polymers, whose excitation is supposed to be a fundamental process of life in multicellular systems [504]. They exhibit a rather complex spectra, with many peaks in the range of tens of MHz [505]. We consider here a signal with five frequency components $\omega_i/2\pi = \{9.5, 15, 18, 25, 31\}$ MHz. The time dependence and normalized spectrum of such a signal are shown in Figs. 7.6a and 7.6b (blue line), respectively. We also consider that the NV spin qubit sensor is subject to noise dominated by a $1/f$ contribution [506, 507], with functional form A/f^{α} (with fixed $\alpha = 1$ and variable amplitude A), plus the intrinsic Gaussian noise of the diamond device given by the ^{13}C spin bath [503]. The noise spectral density $S(\omega)$ is represented by the orange line in Fig. 7.6b, for a magnetic bias field of $B = 40$ mT. Note that this value is incidental, since the bias field can be tuned within a wide range $B \geq 15$ mT [502, 503].

We now aim at identifying the pulsed control field that drives the dynamics of the spin qubit sensor in a way that optimizes its sensitivity to the given signal in the presence of such a noise.

An intuitive solution that maximizes the phase φ acquired by the sensor due to the coupling to the signal, corresponds to flipping the spin sensor at each zero crossing of the signal (see blue dots in Fig. 7.6a). Note, however, that these solutions (that we denote as 'generalized Carr-Purcell (gCP)' solutions) depend only on the signal spectral content, and do not take into account the presence of noise, which significantly affects sensitivity instead. The inverse of sensitivity (expressed in $\mathrm{Hz}^{1/2}/\mu\mathrm{T}$) under this kind of control field is reported in Fig. 7.6c (see crosses), as a function of the sensor interrogation time T, for different amplitudes of the $1/f$ noise. As the noise amplitude increases, the sensitivity rapidly degrades.

By applying the optimization algorithm described in Sec. 7.2.2, we take into account both the signal and the noise effect. For the optimization, we use a time base $\Delta t = 10$ ns, which sets the minimum distance between the control pulses. Note that this parameter establishes an upper bound for the detectable target signal frequency (in the present case, $\nu_{max} = 1/2\Delta t \sim 50$ MHz). With this method, we find optimal pulsed control fields that improve sensitivity to the target signal up to a factor of 3.3×10^3. The sensitivity of the optimized sequences in shown in Fig. 7.6c (see dots). The optimal sequences perform well for arbitrarily strong noise, whose amplitude we vary over two orders of magnitude ($A = 10^{-2} - 1$). The sensitivity of the optimal sequences monotonically improves with the interrogation time reaching around

30 nT/Hz$^{1/2}$ at time 30μs, where the gCP sequences already falls down even in the presence of weak noise.

A bound of the achievable sensitivity can be obtained from the solution of the spherical model in the continuum limit ($N \to \infty$) (dashed black line in Fig. 7.6c). The optimized control sequence is up to 4.5 times closer to this bound than the gCP sequence.

7.4 Conclusions and outlook

We have shown that the problem of finding an optimal solution to the control of a single spin for quantum sensing can be solved by, first, finding the ground state of a solvable spherical model of classical spins and, second, using this as a starting point for a simulated annealing algorithm. In this way, this optimization algorithm is able to find a control sequence that shows a significant improvement of the sensitivity with respect to standard control sequences. In addition, from the spherical model we found a theoretical bound on the sensitivity. Although the spherical model can be mapped to a control sequence that gives relatively good results, using the simulated annealing algorithm is necessary to improve even further the sensitivity, approaching 80–85% of the bound. Our experimental results confirm the theoretical predictions, hence validating our algorithm as an optimization protocol applicable to single spin sensors.

The proposed algorithm can solve the problem of finding the optimal DD sequence of a given signal $b(t)$ in a few *milliseconds* on a Raspberry Pi, which opens the door to the miniaturization of the control electronics, using for example low-power processors. Fast optimization would also enable the implementation of adaptive protocols for sensing and spectroscopy.

Of course, several possible routes are left open for future studies. First of all, the phase diagram of the optimization problem could be studied in more detail (e.g. on the lines of Ref. [491]), also with the perspective of using *more than one qubit* as sensor—and thus increasing the complexity of the spin-glass-like Hamiltonian. Second, on a practical level, the performance of our optimization scheme could be compared with the plethora of existing, general-purpose algorithm for quantum optimal control, maybe showing that some degree of customization helps substantially the solution of the optimization problem. Third, as suggested above, one could embed the fast optimization in a larger scheme, with the idea of setting up an adaptive protocol, that can learn in real time the field that is measured. Finally, so far we restricted the optimization procedure to bang-bang protocols, i.e. only π pulses were used. One could instead think of more general transformations on the Bloch sphere, that may boost the sensitivity, as suggested by the higher sensitivity of the spherical model *before* the projection on ± 1 values.

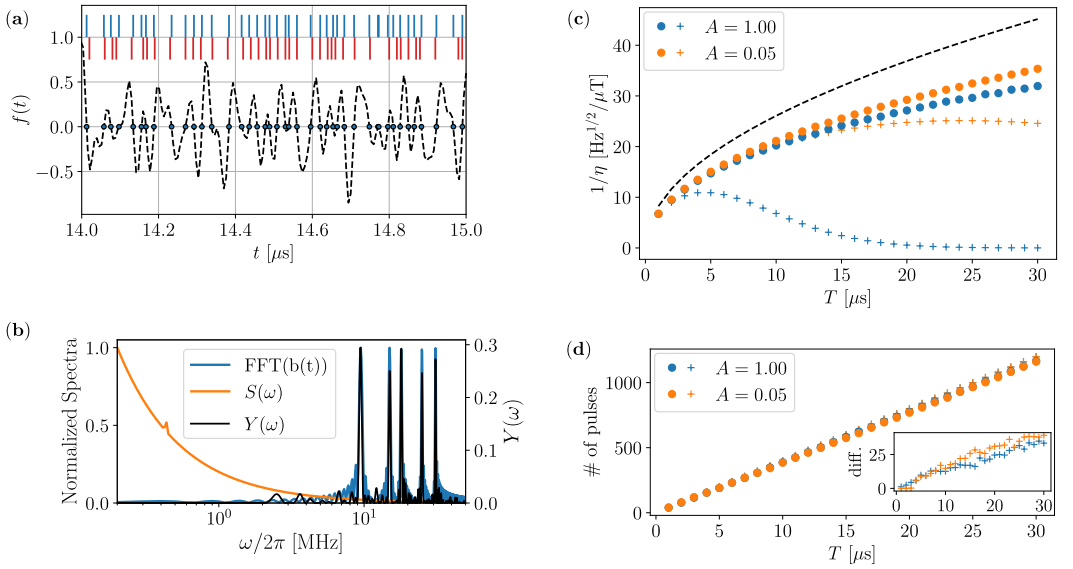

FIGURE 7.6: (a) Normalized temporal dependence of the considered AC target field (dashed black line). Blue dots pick out the zero crossings of the signal, which determine the time distribution of the π pulses for the generalized Carr-Purcell (gCP) sequence, indicated on the top as vertical blue lines. In contrast, the vertical red lines represent the time distribution of the π pulses for the gCP sequence. (b) Blue line: Normalized spectrum of the AC target field. Orange line: spectral density $S(\omega)$ of the noise, which entails a dominant contribution A/f^{α}, with $\alpha = 1$ and $A = 1$, and a Gaussian peak due to the nuclear spin bath inherent in the diamond device (centered around $\sim$ 430 kHz in the presence of a bias magnetic field of 40 mT). Black line: Filter function of the optimized control field that drives the diamond spin qubit dynamics. The filter function is the Fourier transform of the Ising chain distribution. (c) Inverse sensitivity to the AC target signal for different control sequences. Crosses: inverse sensitivity of the sensor when its dynamics is driven by the gCP control solution (the spin qubit sensor is flipped for each zero crossing of the signal). Note that the gCP sequences are noise-independent, but $1/\eta$ does depend on the noise spectral density. Bullets: inverse sensitivity of the sensor under optimized control sequences, which take into account noise. The color code of dots and crosses refers to different values of the noise amplitude A, as reported in the label. Black dashed line: theoretical upper bound obtained from the solution of the spherical model in the continuum limit. (d) Number of pulses for the gCP (crosses) and for the optimized control (bullets) sequences. Inset: difference between the number of pulses for the gCP solution and for the optimal solution. This figure is taken from Ref. [7].

A Addendum to Chapter 2

In this Appendix, I give additional details on the perceptron model. In Sec. A.1 I show how to derive the saddle-point free energy with a standard replica computation. In Sec. A.2 I show how to parametrize the overlap matrix at the saddle via a RSB ansatz. In Sec. A.3 replica symmetry is assumed, and the free energy used in the main text is derived. In Sec. A.4 I show how to set up a small-disorder perturbative expansion. In Sec. A.5 I present a variational computation that shows how the classical critical exponents are modified by quantum fluctuations.

A.1 Replicated and disorder-averaged free energy

In this Section we show the details of the computation that leads to the replicated and disorder-averaged partition function in Eqs. (2.10)–(2.11). This is a standard replica symmetry breaking (RSB) computation; it was originally performed in Ref. [224] in a classical setting, and then extended to the quantum case in Ref. [244].

Let us start by implementing the spherical constraint through a Lagrange multiplier:

$$Z = \oint D\vec{X} \exp\left\{-\frac{1}{\hbar}\int_0^{\beta\hbar} dt \left[\frac{m}{2}\dot{\vec{X}}^2(t) + \sum_{\mu=1}^{M} v(h^\mu(\vec{X}))\right]\right\} \delta\left[\vec{X}^2 - N\right] \tag{A.1}$$

$$= \oint D\vec{X} D\lambda \exp\left\{-\frac{1}{\hbar}\int_0^{\beta\hbar} dt \left[\frac{m}{2}\dot{\vec{X}}^2(t) + \sum_{\mu=1}^{M} v(h^\mu(\vec{X}))\right]\right. \tag{A.2}$$

$$\left. + \frac{im}{2\hbar}\int_0^{\beta\hbar} dt\, \lambda(t)(\vec{X}^2(t) - N)\right\}, \tag{A.3}$$

where the symbol $\oint$ reminds that $\vec{X}(0) = \vec{X}(\beta\hbar)$. Then introduce replicas $\vec{X}_a$, with $a = 1, 2, \ldots, n$:

$$Z^n = \oint \left[\prod_{a=1}^{n} D\vec{X}_a D\lambda_a\right] \exp\left\{-\frac{1}{\hbar}\sum_{a=1}^{n}\int_0^{\beta\hbar} dt \left[\frac{m}{2}\dot{\vec{X}}_a^2(t) + \sum_{\mu=1}^{M} v(h^\mu(\vec{X}_a))\right]\right.$$

$$\left. + \frac{im}{2\hbar}\sum_a \int_0^{\beta\hbar} dt\, \lambda_a(t)(\vec{X}_a^2(t) - N)\right\} \tag{A.4}$$

It is convenient to introduce the auxiliary processes (the same of Eq. (2.8))

$$r_a^\mu(t) := \frac{\vec{X}_a(t)\cdot\vec{\xi}^\mu}{\sqrt{N}} : \tag{A.5}$$

they are scalar quantities of $O(1)$, incorporating the quantum fluctuations at large N, and physically they represent the typical overlap of the particle with an obstacle.

The processes $r_a^\mu(t)$ can be inserted in the path integral through the identity

$$1 = \oint \left[\prod_{\mu=1}^{M} Dr_a^\mu\right] \delta\left[r_a^\mu(t) - \frac{\vec{X}_a(t)\cdot\vec{\xi}^\mu}{\sqrt{N}}\right] \tag{A.6}$$

$$= \oint \left[\prod_{\mu=1}^{M} Dr_a^\mu D\hat{r}_a^\mu\right] e^{i\sum_\mu \int_0^{\beta\hbar} \frac{dt}{\beta\hbar}\, \hat{r}_a^\mu(t) r_a^\mu(t) - i\sum_\mu \int_0^{\beta\hbar} \frac{dt}{\beta\hbar}\, \hat{r}_a^\mu(t) \frac{\vec{X}_a(t)\cdot\vec{\xi}^\mu}{\sqrt{N}}}. \tag{A.7}$$

It follows, for the replicated and disorder-averaged partition function:

$$\overline{Z^n} = \oint \left[\prod_{a=1}^{n} D\vec{X}_a D\lambda_a \prod_{\mu=1}^{M} Dr_a^\mu D\hat{r}_a^\mu\right] e^{i\sum_{a,\mu}\int_0^{\beta\hbar}\frac{dt}{\beta\hbar}\,\hat{r}_a^\mu(t) r_a^\mu(t)}$$
$$\times \overline{e^{-i\sum_{a,\mu}\int_0^{\beta\hbar}\frac{dt}{\beta\hbar}\,\hat{r}_a^\mu(t)\frac{\vec{X}_a(t)\cdot\vec{\xi}^\mu}{\sqrt{N}}}} e^{-\frac{1}{\hbar}\sum_{a=1}^{n}\int_0^{\beta\hbar} dt\left[\frac{m}{2}\dot{\vec{X}}_a^2(t) + \sum_{\mu=1}^{M} v(r_a^\mu - \sigma)\right] + \frac{im}{2\hbar}\int_0^{\beta\hbar} dt\,\lambda_a(t)(\vec{X}_a^2(t) - N)}. \tag{A.8}$$

The only term involved in the average over disorder is

$$\overline{e^{-i\sum_{a,\mu}\int_0^{\beta\hbar}\frac{dt}{\beta\hbar}\,\hat{r}_a^\mu(t)\frac{\vec{X}_a(t)\cdot\vec{\xi}^\mu}{\sqrt{N}}}} = \int_{-\infty}^{+\infty}\left[\prod_{\mu=1}^{M}\prod_{i=1}^{N}\frac{d\xi_i^\mu}{\sqrt{2\pi}}\right] e^{-\frac{1}{2}\sum_{\mu,i}(\xi_i^\mu)^2 - i\sum_{a,\mu,i}\int_0^{\beta\hbar}\frac{dt}{\beta\hbar}\,\hat{r}_a^\mu(t)\frac{X_{a,i}(t)\xi_i^\mu}{\sqrt{N}}} \tag{A.9}$$

$$= e^{-\frac{1}{2}\sum_{a,b,\mu}\iint_0^{\beta\hbar}\frac{dt}{\beta\hbar}\frac{ds}{\beta\hbar}\,\hat{r}_a^\mu(t)\frac{\vec{X}_a(t)\cdot\vec{X}_b(s)}{N}\hat{r}_b^\mu(s)}. \tag{A.10}$$

At this point, the particle position $\vec{X}_a(t)$ appears in the exponent only quadratically. Therefore, one can change variables from $\vec{X}_a(t)$ to the overlap (the same of Eq. (2.9))

$$Q_{ab}(t,s) := \frac{\vec{X}_a(t)\cdot\vec{X}_b(s)}{N}, \tag{A.11}$$

which is a standard quantity in RSB computations, measuring the similarity between two replicas. Moreover, integrating by parts the kinetic term, and redefining $\lambda_a \to i\lambda_a$, one gets to

$$\overline{Z^n} \overset{N\to\infty}{\propto} \oint \left[\prod_{a=1}^{n} D\lambda_a \prod_{b\geq a} DQ_{ab}\right] [\det Q(t,s)]^{\frac{N}{2}}\, e^{\frac{Nm}{2\hbar}\sum_a \int_0^{\beta\hbar} dt\,[\partial_s^2 Q_{aa}(t,s)|_{s=t} - \lambda_a(t)(Q_{aa}(t,t)-1)]}$$
$$\times \left\{\oint\left[\prod_{a=1}^{n} Dr_a D\hat{r}_a\right] e^{i\sum_a\int_0^{\beta\hbar}\frac{dt}{\beta\hbar}\,\hat{r}_a(t)r_a(t) - \frac{1}{2}\sum_{a,b}\iint_0^{\beta\hbar}\frac{dt}{\beta\hbar}\frac{ds}{\beta\hbar}\hat{r}_a(t)Q_{ab}(t,s)\hat{r}_b(s) - \frac{1}{\hbar}\sum_a\int_0^{\beta\hbar} dt\, v(r_a-\sigma)}\right\}^M, \tag{A.12}$$

where the determinant $[\det Q(t,s)]^{N/2}$ is the Jacobian of the transformation $\vec{X}_a(t) \to Q_{ab}(t,s)$ (see also Ref. [244]). The integral in the curly brackets can be performed with the rules of Gaussian integration, finding

$$\oint\left[\prod_{a=1}^{n} Dr_a D\hat{r}_a\right] e^{i\sum_a\int_0^{\beta\hbar}\frac{dt}{\beta\hbar}\,\hat{r}_a(t)r_a(t) - \frac{1}{2}\sum_{a,b}\iint_0^{\beta\hbar}\frac{dt}{\beta\hbar}\frac{ds}{\beta\hbar}\hat{r}_a(t)Q_{ab}(t,s)\hat{r}_b(s) - \frac{1}{\hbar}\sum_a\int_0^{\beta\hbar} dt\, v(r_a-\sigma)}$$
$$= \frac{1}{\sqrt{\det Q}}\oint\left[\prod_{a=1}^{n} Dr_a\right] e^{-\frac{1}{2}\sum_{a,b}\iint_0^{\beta\hbar}\frac{dt}{\beta\hbar}\frac{ds}{\beta\hbar} r_a(t)Q_{ab}^{-1}(t,s)r_b(s) - \frac{1}{\hbar}\sum_a\int_0^{\beta\hbar} dt\, v(r_a-\sigma)} \tag{A.13}$$

$$=: \left\langle e^{-\frac{1}{\hbar}\sum_a\int_0^{\beta\hbar} dt\, v(r_a-\sigma)}\right\rangle_Q. \tag{A.14}$$

Finally,

$$\overline{Z^n} = \oint \left[\prod_{a=1}^{n} D\lambda_a \prod_{b\geq a} DQ_{ab}\right] \exp\left\{N\mathcal{A}(Q_{ab},\lambda_a)\right\} \tag{A.15}$$

where

$$\begin{aligned}\mathcal{A} = &\frac{1}{2}\log\det Q(t,s) + \frac{\beta m}{2}\sum_a \int_0^{\beta\hbar}\frac{dt}{\beta\hbar}\,\partial_s^2 Q_{aa}(t,s)\Big|_{s=t} \\ &- \frac{\beta m}{2}\sum_a \int_0^{\beta\hbar}\frac{dt}{\beta\hbar}\,\lambda_a(t)[Q_{aa}(t,t)-1] + \alpha\log\left\langle e^{-\beta\sum_a\int_0^{\beta\hbar}\frac{dt}{\beta\hbar}\,v(r_a-\sigma)}\right\rangle_Q,\end{aligned} \tag{A.16}$$

that are respectively Eqs. (2.10) and (2.11).

A.2 Replica-symmetry-breaking ansatz for the overlap matrix

To carry on with the computations, it is necessary to specify what is the form of the overlap matrix at the saddle point $Q_{ab}^{\mathrm{sp}}(t,s)$. Recalling the definition of the overlap from Eqs. (2.9) or (A.11), one notices that

- $Q_{ab}(t,s)$ periodic both in t and s with period $\beta\hbar$;
- $Q_{aa}(t,t) = 1$ due to the spherical constraint;
- from the very definition, $Q_{ab}(t,s) = Q_{ba}(s,t)$;
- being the computation at equilibrium, time-translational invariance holds: $Q_{ab}(t,s) \equiv Q_{ab}(t-s)$;
- because of time-reversal symmetry, $Q_{ab}(t-s) \equiv Q_{ab}(s-t)$;
- when $a \neq b$ it holds

$$NQ_{a\neq b}^{\mathrm{sp}}(t,s) = \overline{\left\langle \vec{X}_a(t)\cdot\vec{X}_b(s)\right\rangle} = \overline{\left\langle \vec{X}_a(t)\right\rangle\cdot\left\langle\vec{X}_b(s)\right\rangle} = \overline{\left\langle\vec{X}_a\right\rangle\cdot\left\langle\vec{X}_b\right\rangle}. \tag{A.17}$$

  In fact, fixing the realization of the disorder, replicas are decoupled, thermal averages factorizes and $\langle\vec{X}_a(t)\rangle$ is stationary.

In view of the above, the following ansatz is very reasonable [234, 244]:

$$Q_{ab}^{\mathrm{sp}}(t,s) = q_d(t-s)\delta_{ab} + Q_{ab}^{*} \tag{A.18}$$

where q_d is some function, and Q_{ab}^{*} is a static, hierarchical matrix. Thus, the replica symmetry acts non-trivially only on the zero Matsubara mode, and Q_{ab}^{*} is the quantum analog of the classical order parameter in mean-field spin glasses.

A.3 Replica-symmetric free energy

In this Section, it is shown how to pass from the general expression for the saddle-point action, that can be found in Eqs. (2.11) or (A.16), to the RS free energy Eq. (2.20).

To begin with, consider the first term on the r.h.s., i.e. the determinant of the RS overlap at the saddle (introduced in Eq. (2.14)):

$$\det Q^{\mathrm{RS}}_{ab}(t,s) = \det\left[q_d(t-s)\delta_{ab} + q(1-\delta_{ab})\right], \tag{A.19}$$

The determinant takes two independent contributions: that from the time indices, and that from the replica indices, the two sharing only the zero Matsubara mode. Therefore,

$$\begin{aligned}\log\det\left[q_d(t-s)\delta_{ab} + q(1-\delta_{ab})\right] = \sum_{k\neq 0}\log\tilde{q}_d(\omega_k) \\ + \log\det\left[\tilde{q}_d(\omega_0)\delta_{ab} + q(1-\delta_{ab})\right]\end{aligned} \tag{A.20}$$

using the Fourier transform convention of Eqs. (2.16)–(2.17). The second term of the r.h.s. above can be computed by means of Sherman-Morrison formula:

$$\det(\mathbb{1} + \mathbf{u}\mathbf{v}^T) = 1 + \mathbf{v}^T\mathbf{u}, \qquad \text{with } \mathbf{u},\mathbf{v} \text{ vectors.} \tag{A.21}$$

Thus, defining $\mathbf{e}^T = (1,1,\dots,1)$, it holds

$$\det\left(\tilde{q}_d(\omega_0)\delta_{ab} + q(1-\delta_{ab})\right) = \det\left((\tilde{q}_d(\omega_0)-q)\mathbb{1} + q\,\mathbf{e}\mathbf{e}^T\right) \tag{A.22}$$

$$= (\tilde{q}_d(\omega_0)-q)^n \det\left(\mathbb{1} + \frac{q}{\tilde{q}_d(\omega_0)-q}\mathbf{e}\mathbf{e}^T\right) \tag{A.23}$$

$$= (\tilde{q}_d(\omega_0)-q)^n\left(1 + \frac{nq}{\tilde{q}_d(\omega_0)-q}\right) \tag{A.24}$$

$$= (\tilde{q}_d(\omega_0)-q)^{n-1}\left(\tilde{q}_d(\omega_0) + (n-1)q\right). \tag{A.25}$$

In conclusion, only the $O(n)$ contribution to the action is needed (this works as long as the saddles do not coalesce), so that

$$\log\det Q^{\mathrm{RS}} = \text{const.} + n\sum_{k\in\mathbb{Z}}\log\tilde{G}(\omega_k) + \frac{nq}{\tilde{G}(\omega_0)} + O(n^2) \tag{A.26}$$

using the autocorrelation function G defined in Eq. (2.15).

Moving on to the second term of $\mathcal{A}$, it is simply

$$\frac{\beta m}{2}\sum_a\int_0^{\beta\hbar}\frac{dt}{\beta\hbar}\,\partial_s^2 Q_{aa}(t,s)\Big|_{s=t} = -\frac{n\beta m}{2}\sum_{k\in\mathbb{Z}}\omega_k^2\tilde{G}(\omega_k). \tag{A.27}$$

Also the third term is quite immediate:

$$\frac{\beta m}{2}\sum_a\int_0^{\beta\hbar}\frac{dt}{\beta\hbar}\,\lambda_a(t)[Q_{aa}(t,t)-1] = \frac{n\beta m\lambda}{2}\left[\sum_{k\in\mathbb{Z}}\tilde{G}(\omega_k) - (1-q)\right], \tag{A.28}$$

and the spherical constraint becomes time-independent because $Q_{aa}(t,t)$ is.

To conclude, the last term on the r.h.s. of Eq. (A.16) needs some manipulations. The main point is to invert the matrix Q by means of another form of Sherman-Morrison formula: for an invertible matrix A and vectors $\mathbf{u}$,$\mathbf{v}$,

$$\left(A + \mathbf{u}\mathbf{v}^T\right)^{-1} = A^{-1} - \frac{A^{-1}\mathbf{u}\mathbf{v}^T A^{-1}}{1 + \mathbf{v}^T A^{-1}\mathbf{u}}. \tag{A.29}$$

It is sufficient to apply this formula to the zero Matsubara mode:

$$\tilde{Q}^{-1}_{ab}(\omega_0) = \left[\tilde{G}(\omega_0)\delta_{ab} + q\right]^{-1} \tag{A.30}$$

$$= \frac{\delta_{ab}}{\tilde{G}(\omega_0)} - \frac{q\tilde{G}^{-2}(\omega_0)}{1 + nq\tilde{G}^{-1}(\omega_0)}; \tag{A.31}$$

and reintroducing all the other modes:

$$\tilde{Q}^{-1}_{ab}(\omega_k) = \frac{\delta_{ab}}{\tilde{G}(\omega_k)} - \frac{\delta_{k0}}{\tilde{G}(\omega_0)}\frac{q}{\tilde{G}(\omega_0) + nq}. \tag{A.32}$$

The quantity above goes in the exponent; therefore it is possible to put it in a more convenient form by writing

$$\left\langle e^{-\beta\sum_a \int_0^{\beta\hbar} \frac{dt}{\beta\hbar}\, v(r_a - \sigma)} \right\rangle_Q = \gamma_q \star \left\langle e^{-\beta\sum_a \int_0^{\beta\hbar} \frac{dt}{\beta\hbar}\, v(r_a + h)} \right\rangle_G^n (-\sigma) \tag{A.33}$$

where $\langle\cdots\rangle_G$ are the averages defined in Eq. (2.18), γ_q is the Gaussian kernel of Eq. (2.19) and $\star$ indicates the convolution over h. In words, the combination of q and $\tilde{G}(\omega_0)$ in a fraction in the exponent has been traded for two separate integrations, one over all the frequencies $\tilde{G}(\omega_k)$ and the other over h.

Taking finally the limit $n \to 0$, and retaining only the $O(n)$ contributions, one finds

$$\gamma_q \star \left\langle e^{-\beta\sum_a \int_0^{\beta\hbar} \frac{dt}{\beta\hbar}\, v(r_a + h)} \right\rangle_G^n (-\sigma) = n\alpha\gamma_q \star \log \left\langle e^{-\beta \int_0^{\beta\hbar} \frac{dt}{\beta\hbar}\, v(r(t) + h)} \right\rangle_r (-\sigma) + O(n^2). \tag{A.34}$$

having used

$$\begin{aligned} \log\left[\gamma_q \star f^n\right] = \log\left[\gamma_q \star e^{n\log f}\right] &= \log\left[\gamma_q \star (1 + n\log f) + O(n^2)\right] \\ &= n\gamma_q \star \log f + O(n^2). \end{aligned} \tag{A.35}$$

Putting together all the pieces above, one gets to Eq. (2.20).

A.4 Perturbation theory at zero temperature

In this Section, we show how to obtain Eq. (2.29) from the self-consistency equations (2.22)–(2.24). Let us start from Eq. (2.24), rewritten here for readability:

$$q = \alpha\gamma_q \star \langle r_0\rangle_v^2. \tag{A.36}$$

Since there is already an α in front, everything can be computed at order α^0; in particular, the autocorrelation G reduces to

$$G_n^{-1} = \beta m\omega_n^2 + \beta\mu. \tag{A.37}$$

Therefore, the only thing to be computed is the average $\langle r_0\rangle_v$, that is the average position in the ground state of a harmonic oscillator restricted to the half line $r > 0$:

$$\langle r_0\rangle_v = \int_0^\infty dr\, |\psi_0(r)|^2\, r = \sqrt{\frac{4\hbar}{\pi m\Omega}}, \tag{A.38}$$

where $\Omega = \sqrt{\mu/m}$ and having used

$$\psi_0(r) = \left(\frac{m^3\Omega^3}{\pi\hbar^3}\right)^{1/4} r \exp\left\{-\frac{m\Omega}{2\hbar}r^2\right\}. \tag{A.39}$$

The only thing left to do is to fix μ from the spherical constraint, Eq. (2.23):

$$1 = \sum_{n\in\mathbb{Z}} G_n = \sum_{n\in\mathbb{Z}} \frac{1}{\beta\mu + \beta m\omega_n^2}. \tag{A.40}$$

Using the identity

$$\sum_{n\in\mathbb{Z}} \frac{1}{A^2+n^2} = \frac{\pi}{A}\coth(\pi A), \tag{A.41}$$

one gets to

$$\sqrt{\frac{m}{\mu}}\coth\left(\frac{\beta\hbar}{2}\sqrt{\frac{\mu}{m}}\right) = \frac{2}{m\hbar}, \tag{A.42}$$

which is solved by

$$\mu = \frac{m^3\hbar^2}{4} \tag{A.43}$$

in the limit $\beta \to \infty$. Finally,

$$q = \frac{8}{\pi m^2} + O(\alpha^2), \tag{A.44}$$

which is Eq. (2.29).

A.5 Quadratic approximation for the propagator

In this Section, we show the details of the approximate computation leading to the exponent $\kappa = 3/2$. The starting point is the approximation of Eq. (2.32), reported here for readability:

$$G_n^{-1} = \frac{\beta m}{1-q}\left(\omega_n^2 + \frac{\hbar^2}{4m^2}\right). \tag{A.45}$$

Such approximation is completely uncontrolled, since it is neglecting the long-time structure of the propagator. However, the spherical constraint Eq. (2.23) is automatically satisfied up to exponentially small corrections, and the values of m and q can be fixed by Eqs. (2.22) and (2.24). Notice that there is an equation of the form (2.22) for every $n \in \mathbb{Z}$, yielding a deeply overcomplete set of constraints for the ansatz, but let us restrict to the $n = 0$ case only.

It is convenient to set

$$x := \frac{r}{\sqrt{1-q}}, \qquad H := \frac{h}{\sqrt{1-q}}, \tag{A.46}$$

so that Eq. (2.24) becomes

$$\frac{q}{(1-q)^{3/2}} = \alpha \int \frac{dH}{\sqrt{2\pi q}} e^{-\frac{(1-q)H^2}{2q}} \left\langle \psi_0^{(H)} \middle| x \middle| \psi_0^{(H)} \right\rangle^2. \tag{A.47}$$

The reduced Schrödinger problem to solve is

$$-\frac{1}{2}\frac{d\psi_k^{(H)}}{dx^2}+\frac{1}{8}x^2\psi_k^{(H)}=E_k^{(H)}\psi_k^{(H)},\quad \psi_k^{(H)}(H)=0. \tag{A.48}$$

Self-consistently it will become clear that only the ground-state contribution matters; indeed, it was already argued that the model becomes temperature-independent as $q\to 1$. With this in mind, one can employ the one-parameter variational wavefunction for the ground state

$$\psi^{(H)}(x;L)=\frac{1}{\sqrt{Z}}(x-H)\theta(x-H)e^{-x^2/4L^2}, \tag{A.49}$$

with an appropriate normalization Z, for which the energy reads

$$E^{(H)}(L)=\frac{1+L^4}{8L^2}\frac{\phi(H/\sqrt{2}L)(H^2+3L^2)-2HL}{\phi(H/\sqrt{2}L)(H^2+L^2)-2HL}. \tag{A.50}$$

Above, we introduced the function

$$\phi(y):=\sqrt{2\pi}\,e^{y^2}\,\mathrm{Erfc}\,(y), \tag{A.51}$$

where Erfc is the complementary error function. The equation $dE^{(H)}/dL=0$ can be solved using suitable asymptotic expansions. Remembering that $q\to 1$, it follows $H\to\infty$, and the relevant region is $H\gg L$. Performing the explicit computation, one fixes L as a function of the other parameters, and then finds

$$\left\langle\psi_0^{(H)}\middle|\,x\,\middle|\psi_0^{(H)}\right\rangle\simeq H+3^{2/3}H^{-1/3}+O(H^{-5/3}). \tag{A.52}$$

By inserting this expansion in Eq. (A.47), one arrives at

$$q=\alpha\left[(1-q)\xi\left(\frac{q}{1-q}\right)+\frac{q}{2}\right] \tag{A.53}$$

with

$$\xi(\lambda):=\int_0^\infty\frac{dH}{\sqrt{2\pi\lambda}}\,e^{-H^2/2\lambda}\left[\frac{(6H)^{2/3}}{2^{1/3}}+\cdots\right]=\frac{3^{2/3}\Gamma(5/6)}{\sqrt{\pi}2^{1/3}}\lambda^{1/3}+\cdots. \tag{A.54}$$

Eq. (A.53) can now be solved for q, yielding $\kappa=3/2$:

$$q=1-\frac{\sqrt{2}\,\pi^{3/4}(2-\alpha)^{3/2}}{24\,\Gamma(5/6)^{3/2}}. \tag{A.55}$$

The same scaling has been observed by solving the Schrödinger equation (A.48) numerically, discretizing the x-axis and employing imaginary-time evolution to find the ground state.

Knowing q as a function of α, one can now check the consistency of the procedure by inspecting Eq. (2.22) for $n=0$. Handling with care the self-energy, such equation can be put in the form

$$m=\beta\gamma_{q/(1-q)}\star\left\langle\psi_0^{(H)}\middle|\,x^2\,\middle|\psi_0^{(H)}\right\rangle_{\mathrm{conn}}. \tag{A.56}$$

It is straightforward to determine

$$\left\langle \psi_0^{(H)} \middle| x^2 \middle| \psi_0^{(H)} \right\rangle_{\text{conn}} = 3^{1/3} H^{-2/3} \theta(H) + \cdots , \tag{A.57}$$

so that finally

$$m = \beta \frac{3^{1/3}\Gamma(1/6)}{2^{5/6}} \left(\frac{1-q}{q} \right)^{1/3} . \tag{A.58}$$

Thus one can see that, as $q \to 1$, $\beta/m \to \infty$ and the approximation of taking only the ground state becomes more and more reliable.

B Addendum to Chapter 4

In this Appendix, I give more details on the techiques used to study the heterogeneity of entanglement in MBL systems. In Sec. B.1 I show how the l-bit model can be used to access different parts of the spectrum. In Sec. B.2 I show what are the effects of considering finite systems, and finite samples of the disorder distributions. In Sec. B.3 I show some preliminary results concerning the heterogeneity of entanglement in the delocalized phase. In Sec. B.4 I show how to perform some analytical estimates, that help understanding the numerical results. In Sec. B.5 I show that the correlation functions used in the main text are self-averaging, thus well-suited to study the disordered systems under consideration.

B.1 Energy of the initial states

In the l-bit model, given a disorder realization $\{J_{ij}\}$, we sample the local magnetization configurations $\{m_i\} = \{\langle\sigma_i^z\rangle\}$ with probability $\propto e^{-E/T}$, T being a fictitious temperature to be gradually lowered. Since $m_i \in [-1,1]$ are continuous variables, the annealing procedure has easy access to states down to the edge of the spectrum. From $\{m_i\}$, we fix the coefficients of the initial states of the dynamics (see Eq. (4.2)) as $A_i = \sqrt{(1+m_i)/2}$, and $B_i = e^{i\phi_i}\sqrt{(1-m_i)/2}$. This choice guarantees that $\langle\psi_0|H_{l\text{-bit}}|\psi_0\rangle = E$, i.e. the quantum initial state has an energy expectation value equal to the desired one.

For what concerns our choice of the energy scale in Eq. (4.3), the reasoning goes as follows. The l-bit Hamiltonian (4.1) can be interpreted as a *classical* spin glass, if one substitutes $\sigma_i^z \longrightarrow s_i = \pm 1$. Then, one can compute the (annealed) density of states of the model, finding that with high probability the ground state is at

$$E = -N\sqrt{\frac{h^2}{4} + \frac{4J_0^2}{e^{2/\kappa}-1}}, \tag{B.1}$$

see also Ref. [508]. Changing the spins to *continuous* variables $\sigma_i^z \longrightarrow m_i \in [-1,1]$ will just modify the prefactors of h^2 and $J_0^2/(e^{2/\kappa}-1)$, without changing much the scale. For this reason, we have chosen to put in Eq. (4.3) simply the sum of the variances of h_i and $\sum_j J_{ij}$. The ground state will not be exactly at $\varepsilon = -1$, but close to it.

B.2 Finite-size and finite-sample effects

B.2.1 Relaxation times within the XXZ model

In view of the strong finite-size effects in the results for the XXZ model shown in Fig. 4.2a, let us better analyze the probability distribution function (pdf) of τ_i.

In Fig. B.1 we show the distribution of the local relaxation times of the concurrence, computed within the XXZ model. The tail of the distribution is cut away according to the following procedure. We observe that in some instances the nearest-neighbor concurrence $C_{i,i+1}(t)$ becomes numerically indistinguishable from 0 at a time t^*, and then stays equal to 0 definitively. We perform an evolution lasting only a finite time $t_{\rm fin}$, so for the finite size we consider there will be many sites and realizations with $t^* > t_{\rm fin}$. This is the reason why the full distributions in Figs. B.1 and 4.2a show such a huge peak at large times: it is formed by the contributions of $C_{i,i+1}(t)$ which have not vanished on the finite-time window $t_{\rm fin}$ of our evolution, for the finite system size we consider.

In order to get rid of this peak, we choose a certain truncation time $t_{\rm tr} \leq t_{\rm fin}$, and select only the sites and the realizations for which $t^* < t_{\rm tr}$. As we can see in Fig. B.1 the huge peak disappears and there is a large-time tail which depends on the chosen value of $t_{\rm tr}$. The small-time structure is, on the opposite, quite independent of the truncation, so we expect that it has a physical meaning. There is a peak around $\log \tau_i \simeq -1$, which resembles the one appearing in the l-bit distributions; however, another peak is present around $\log \tau_i \simeq 1$. The two-peak structure has no equal in the l-bit model results; we argue that this might be due to the n-body interactions with $n \geq 3$ missing in the l-bit model.

B.2.2 Relaxation times within the *l*-bit model

Figure B.2a shows the pdf's of $\log_{10}(\tau_i)$, obtained within the l-bit model for different values of L, at $\kappa = 1$, $\varepsilon = 0$. We see that, when $L \leq 20$, the probability distribution presents a peak at $\tau_i = O(t_{\rm fin})$, where $t_{\rm fin}$ is the final time used in the numerical simulations for the time evolution. This is the same effect observed in Fig. 4.2a. In particular, we see that the shape of the pdf's at $L = 10, 15, 20$ strongly resembles the behavior observed in the XXZ model, confirming that those results are strongly affected by finite-size effects.

In Figs. B.2b–B.2c we reproduce the pdf's at $L = 16$, $\varepsilon = 0$, and different values of κ an $t_{\rm fin}$. In the presence of finite-size effects we do not observe the decay of the pdf that is found in larger system sizes. We observe instead a peak in the distribution at $\tau_i = t_{\rm fin}$.

B.3 Heterogeneity in the ergodic regime

We now present some qualitative results on entanglement heterogeneity in the ergodic regime. As shown in Fig. B.3, broad distributions of the relaxation times appear for the XXZ model, Eq. (4.4), also in the ergodic regime, and become broader as the disorder W increases and the MBL-ergodicity transition is approached. Such distributions present a clear peak at small values of τ_i, which decreases when disorder increases and the transition to the MBL phase is approached. This peak corresponds to realizations of the on-site concurrence that vanish very fast in time, corresponding to situations in which entanglement spreads quickly in the system. The number of such ergodic sites diminishes as the localization transition is approached, as it is quantified by the decrease in the peak height.

Notice that in the thermal phase the distributions do not show the spurious peak for large τ_i, which in contrast appears in the MBL phase due to those realizations in which some $C_i(t)$ are still nonzero for $t = t_{\rm fin}$ (contrast Fig. B.3 with Fig. 4.2a).

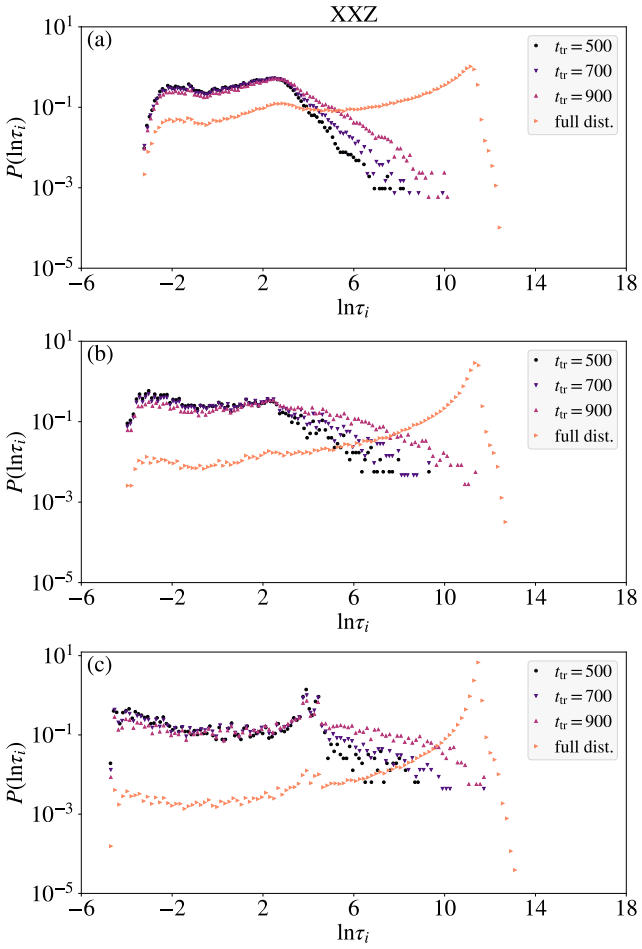

FIGURE B.1: Results for the XXZ model. We show the pdf's of log τ_i, truncated as described in the text. The simulations were performed with a chain of length $L = 16$, final time $t_{\text{fin}} = 1000$, and disorder strength $W = 9$ (panel (a)), $W = 15$ (panel (b)), $W = 25$ (panel (c)). We compare the truncated distributions with the corresponding full distribution. Data from at least 8000 disorder realizations.

B.4 Analytical estimates of local timescales

Let us focus on the l-bit model and on the computation of typical relaxation-time scale of the "one-site concurrence" Eq. (4.8). The concurrence is a complicated non-linear function of the two-site reduced density matrix $\rho_{i,j}$, therefore it is really hard to make analytical predictions for it. However, one can hope to get a rough estimate of its behavior by considering instead the correlation function $\langle \sigma_i^x(t)\sigma_j^x(t)\rangle$. This type of correlation functions were already considered in previous works (see e.g. Ref. [110]), and are easy to access. Choosing $i = 0$ and $j = 1$ without loss of generality, it explicitly reads

$$\langle \sigma_0^x(t)\sigma_1^x(t)\rangle = \sum_{s_0,s_1=\pm 1} (\rho_{0,0})_{s_0,-s_0}(\rho_{0,1})_{s_1,-s_1} e^{-2ih_1 s_0 t - 2ih_2 s_1 t + 8iJ_{01}s_0 s_1 t} \times \prod_{j\neq 0,1} \left[e^{-4iJ_{0j}s_0 t - 4iJ_{1j}s_1 t} \cos^2\frac{\theta_j}{2} + e^{4iJ_{0j}s_0 t + 4iJ_{1j}s_1 t} \sin^2\frac{\theta_j}{2} \right], \quad \text{(B.2)}$$

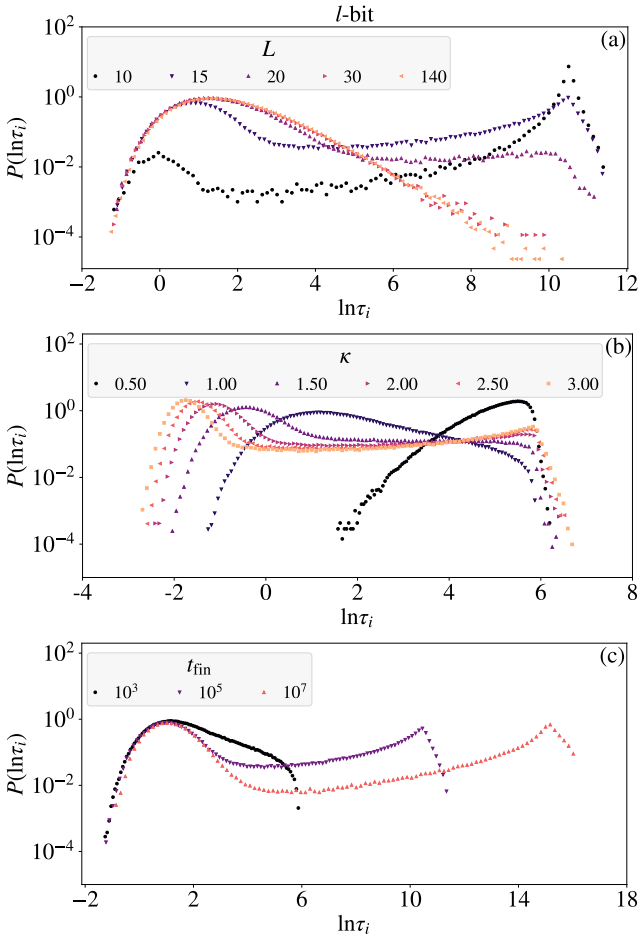

FIGURE B.2: Pdf's of $\log_{10}(\tau_i)$, obtained within the l-bit model. (a) Results for $\kappa = 1$, $\varepsilon = 0$, and different values of L. We see that, when the system size is too small, the pdf's present a spurious peak at large values of τ_i. Indeed, entanglement cannot spread over many sites, and the concurrence of some strongly interacting couples remains finite even at infinite times ($C_i(\infty) = O(2^{-L})$). We collected data from 20 initial states for, at least, 300 disorder realizations. (b) Results for $L = 16$, $\varepsilon = 0$, and different values of κ. Data collected from 21000 disorder realizations. (c) Results for $L = 16$, $\kappa = 1$, $\varepsilon = 0$, and different values of the final time of the time evolution, t_{fin}. Data collected from 21000 disorder realizations.

where $\rho_{0,0}$ and $\rho_{0,1}$ are the initial density matrices of sites 0 and 1, and θ_j is the azimuthal angle on the Bloch sphere for the initial state of site j. We take a further step, and also simplify $\theta_j \equiv \pi/2$, i.e. we choose a particular initial condition at infinite temperature. As a result, we find that $\langle \sigma_0^x(t)\sigma_1^x(t)\rangle$ is an oscillating function, modulated by envelopes of the form

$$A_{\pm}(t) := \prod_{j\neq 0,1} \left|\cos\left(4J_{0j}t \pm 4J_{1j}t\right)\right|. \tag{B.3}$$

It is clear that, if we want to understand the leading-order behaviour in time, we can reduce to study the simpler function

$$A(t) := \prod_{j\neq 0} \left|\cos\left(J_{0j}t\right)\right| \tag{B.4}$$

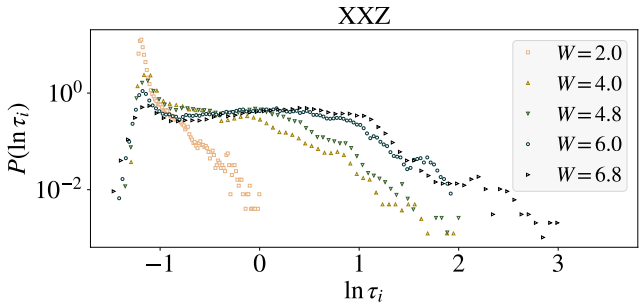

FIGURE B.3: Distributions of the relaxation times in the XXZ model in Eq. (4.4) for different values of W in the ergodic phase. The peak corresponding to ergodic realizations of the on-site concurrence is very evident and decreases as the disorder increases and the transition to MBL regime is approached. Numerical parameters: $J = 2$, $V = 1$ (transition to MBL for $W \simeq 10$), $L = 18$, at least 300 disorder realizations for each curve.

where, we recall, J_{0j} are Gaussian variables of zero average and standard deviation $w_j := J_0 e^{-|j|/\kappa}$.

We can estimate the *typical* value of $A(t)$ by means of $\mathrm{typ}[A(t)] := \exp \overline{\log A(t)}$ (we need to average the *logarithm* of A because, with hindsight, there is a power-law tail in the relaxation-time distribution). Since

$$\overline{\log A(t)} = \sum_j \int dJ_{0j} \frac{e^{-J_{0j}^2/2w_j^2}}{\sqrt{2\pi w_j^2}} \log\left|\cos(J_{0j}t)\right|, \tag{B.5}$$

we just need to compute the integral

$$\begin{aligned}
&\int dJ_{0j} \frac{e^{-J_{0j}^2/2w_j^2}}{\sqrt{2\pi w_j^2}} \log\left|\cos(J_{0j}t)\right| \\
&= \int dJ_{0j} \frac{e^{-J_{0j}^2/2w_j^2}}{\sqrt{2\pi w_j^2}} \left[\log\left|1+e^{2iJ_{0j}t}\right| - \log 2\right] \\
&= \int dJ_{0j} \frac{e^{-J_{0j}^2/2w_j^2}}{\sqrt{2\pi w_j^2}} \sum_{n\geq 1} \frac{(-1)^{n+1}}{n} e^{2inJ_{0j}t} - \log 2 \\
&= \sum_{n\geq 1} \frac{(-1)^{n+1}}{n} e^{-2n^2 w_j^2 t^2} - \log 2.
\end{aligned} \tag{B.6}$$

Let us first focus on the asymptotic value in time of $\mathrm{typ}[A(t)]$. Substituting Eq. (B.6) in Eq. (B.5), for finite system size L, and applying the dominated convergence theorem when performing the limit $t \to \infty$, one can show that $\mathrm{typ}[A(\infty)] := \lim_{t\to\infty} \exp \overline{\log A(t)} \simeq 2^{-L}$. This result is also related to the asymptotic value of the concurrence $\mathrm{typ}[C_i(\infty)]$ being exponentially small in the system size, as discussed in Sec. 4.2.

Now, we focus on finite time t, and we consider $L \gg 1$ so that $\mathrm{typ}[A(\infty)] \simeq 0$. We further proceed by approximating

$$\sum_{n\geq 1} \frac{(-1)^{n+1}}{n} e^{-2n^2 w_j^2 t^2} \approx \begin{cases} 0 & w_j^2 t^2 \gtrsim 1 \\ \log 2 & w_j^2 t^2 \lesssim 1, \end{cases} \tag{B.7}$$

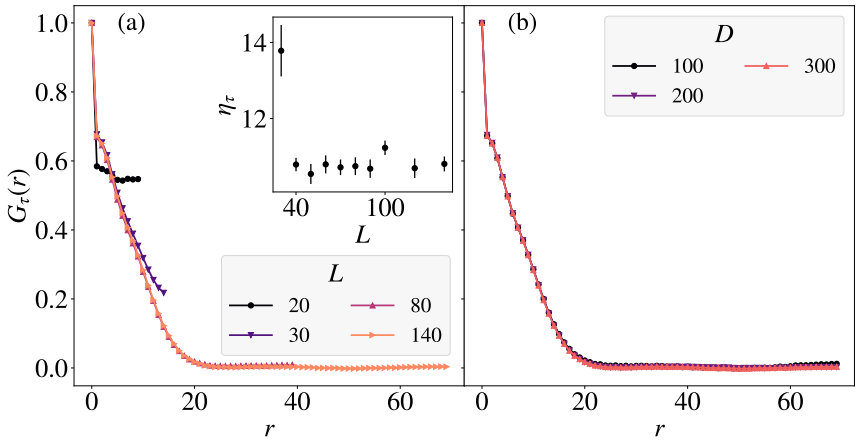

FIGURE B.4: $G_\tau(r)$ defined in Eq. (4.11). Results for the l-bit model for: (a) $\kappa = 1$, $\varepsilon = 0$, and various system sizes L, averaged over $D = 300$ disorder realizations and 20 initial states; (b) $\kappa = 1$, $\varepsilon = 0$, $L = 140$, averaged over a different number of disorder realizations D, and 20 initial states. We see that $G_\tau(r)$ converges quickly to its thermodynamic value (panel (a)), and is almost independent of the number of disorder realizations (panel (b)). (Inset of (a)) The dynamical correlation length η_τ from stretched exponential fits of $G_\tau(r)$ reported in (a) as a function of the system size L. We see that η_τ is almost independent of the system size for $L \geq 40$. The error bars are given by the fit errors.

which implies

$$\sum_j \left\{ \sum_{n\geq 1} \frac{(-1)^{n+1}}{n} e^{-2n^2 w_j^2 t^2} - \log 2 \right\} \approx -N(t) \log 2 \tag{B.8}$$

with $N(t)$ given by

$$N(t) = \#\{j \mid w_j^2 t^2 > 1\} = \begin{cases} 2\kappa \log(J_0 t) & t > 1/J_0 \\ 0 & t < 1/J_0. \end{cases} \tag{B.9}$$

Finally, we find

$$\mathrm{typ}[A(t)] = \begin{cases} (J_0 t)^{-\kappa \log 4} & t > 1/J_0 \\ 1 & t < 1/J_0. \end{cases} \tag{B.10}$$

Substituting this typical value in the definition of τ_i, Eq. (4.9), one gets

$$\mathrm{typ}[\tau] = J_0^{-1} \exp\left(\frac{\int_0^\infty dt\ \mathrm{typ}[A(t)]\ \log(J_0 t)}{\int_0^\infty dt\ \mathrm{typ}[A(t)]} \right) \tag{B.11}$$

$$= (eJ_0)^{-1} \exp\left\{ \frac{1}{\kappa \log 4 - 1} \right\}. \tag{B.12}$$

B.5 Self-averaging property of the correlation function

As anticipated in Chap. 4, the correlation function $G_\tau(r)$ Eq. (4.11) is a self-averaging quantity, as depicted in Fig. B.4. It is indeed only slightly sensitive to finite-size

effects (see Fig. B.4a), and to disorder fluctuations (see Fig. B.4b). As a consequence, the dynamical correlation length η_τ is almost independent of the system size as well (see inset of (a)).

C Addendum to Chapter 5

In this Appendix, I detail all the calculations for the two-level system (TLS) model of glasses. In Sec. C.1 I show how to derive from first principles the form of the dipole tensor, that couples TLS to phonons. In Sec. C.2 I present the computation of the interactions J_{ij}, in Sec. C.3 of the Debye-Waller factor, and in Sec. C.4 of the decay rate through Fermi's golden rule. In Sec. C.6 I show how the few-site observables are efficient to compute for the artificially isolated, interacting TLS model. In Sec. C.7 I show what is the expected concurrence for a fully thermal state. In Sec. C.8 I show how the master equation was integrated numerically.

C.1 Estimate of the dipole tensor

In Table 5.1 all the parameters entering the Hamiltonian (5.1) were fixed, except for the precise form of the elastic dipole tensors D_i^{ab}. As anticipated in Sec. 5.1, one can choose D_i^{ab} in different ways. According to point 1, one can set

$$\mathsf{D}_i^{ab} = O^T \begin{pmatrix} x & 0 & 0 \\ 0 & y & 0 \\ 0 & 0 & z \end{pmatrix} O \tag{C.1}$$

where O is a Haar-random orthogonal matrix and x, y, z are i.i.d. random variables with average 0 and standard deviation 1.

According to Ref. [365] (i.e. point 2 of Sec. 5.1), instead, D_i^{ab} should be the *difference* between two random dipoles, one for each well of the TLS:

$$\mathsf{D}_i = \frac{1}{2}\left(\mathsf{D}_i^{(l)} - \mathsf{D}_i^{(r)}\right). \tag{C.2}$$

Both $\mathsf{D}_i^{(l)}$ and $\mathsf{D}_i^{(r)}$ are assumed to be vector dipoles oriented in two random directions:

$$\mathsf{D}_i^{(l,r)} = \delta \left[O^{(l,r)}\right]^T \begin{pmatrix} 0 & 0 & 0 \\ 0 & 0 & 0 \\ 0 & 0 & 1 \end{pmatrix} O^{(l,r)} \tag{C.3}$$

where $O^{(l)}$,$O^{(r)}$ are two Haar-random orthogonal matrices, and δ is a dimensionless number that needs to be fixed to match experiments and simulations. The authors of Ref. [365] argue that

$$[\gamma \mathsf{D}_i]_{max} \approx 8 \left(\frac{2\pi^2}{9}\right)^{2/3} \frac{\rho v^2}{q_D^3} \tag{C.4}$$

where v is the average over polarizations of the sound velocity, Eq. (5.18), and similarly γ is the average of Eq. (5.19). With D_i of the form specified above, one finds that

$$[\mathsf{D}_i]_{max} = \max \left(\frac{\mathrm{Tr}(\mathsf{D}_i^2)}{3}\right)^{1/2} = \frac{\delta}{\sqrt{6}}. \tag{C.5}$$

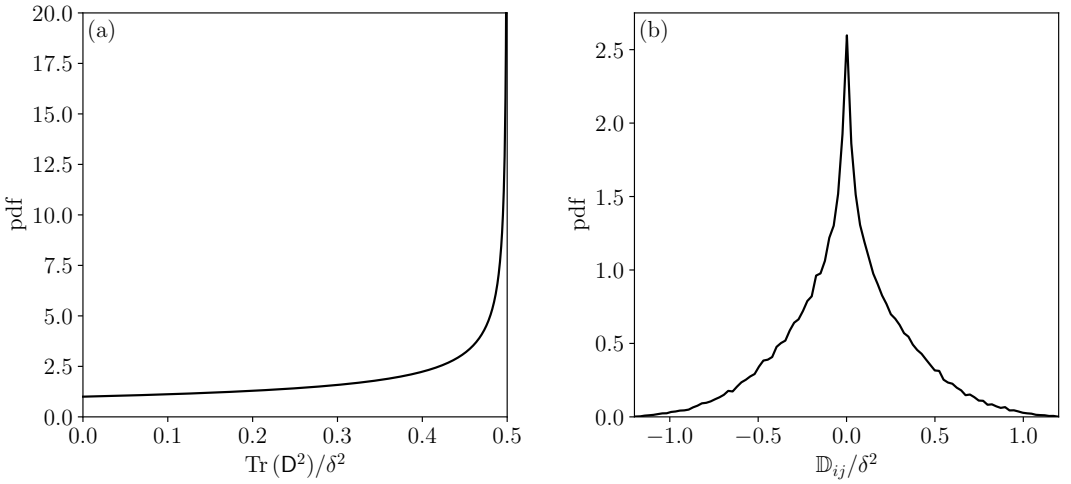

FIGURE C.1: (a) The distribution of $x := \mathrm{Tr}(\mathsf{D}^2)/\delta^2$ is simply given by $p(x) = (1-2x)^{-1/2}$ (see also Ref. [365]). The values of δ for some typical glass formers are given in Eq. (C.6). (b) Distribution of $\mathbb{D}_{ij}/\delta^2$, where $\mathbb{D}_{ij}$ is defined in Eq. (C.19). The distribution is sampled using D_i^{ab} of the form specified in Eqs. (C.2)–(C.3), i.e. using point 2 in Sec. 5.1. To a good approximation, one can assume $\mathbb{D}_{ij}/\delta^2$ to come from a compact distribution over $[-1,1]$.

Therefore, fixing γ from Table 5.1, one finds respectively

$$\delta_{\mathrm{SiO_2}} \approx 8.5, \qquad \delta_{\mathrm{BK7}} \approx 9.4 \qquad \text{and} \qquad \delta_{\mathrm{PMMA}} \approx 6.4. \tag{C.6}$$

One can see that the dimensionless number δ is silently boosting the coupling of TLS and phonons. Since in particular the dipole tensor appears also in rapidly varying functions (e.g. for the Debye-Waller factor), a δ different from 1 can change noticeably the physics.

C.2 Computation of the interaction strength

We want to determine explicitly J_{ij} from Eq. (5.15):

$$J_{ij} = \sum_{\mathbf{q}s} \frac{\gamma_s^2}{2\omega_{\mathbf{q}s}^2} \Xi_{i\mathbf{q}s} \Xi_{j\mathbf{q}s}^* \tag{C.7}$$

$$= \frac{1}{8\rho} \sum_s \gamma_s^2 \int \frac{d^3q}{(2\pi)^3} \frac{q^2}{\omega_{\mathbf{q}s}^2} \mathsf{D}_i^{ab} \mathsf{D}_j^{cd} \left(\hat{q}^a \hat{e}_{\mathbf{q}s}^b + \hat{q}^b \hat{e}_{\mathbf{q}s}^a\right)\left(\hat{q}^c \hat{e}_{\mathbf{q}s}^d + \hat{q}^d \hat{e}_{\mathbf{q}s}^c\right) e^{i\mathbf{q}\cdot(\mathbf{r}_i - \mathbf{r}_j)}. \tag{C.8}$$

To begin with, define some quantities that will help in computing the angular integrals:

$$I^{abcd}(\zeta) := \frac{1}{4\pi} \int d\Omega\, \hat{q}^a \hat{q}^b \hat{q}^c \hat{q}^d e^{i\zeta\cos\theta}, \qquad I^{ab}(\zeta) := \frac{1}{4\pi} \int d\Omega\, \hat{q}^a \hat{q}^b e^{i\zeta\cos\theta}. \tag{C.9}$$

Explicitly, they read

$$
\begin{aligned}
I^{xxyy}(\zeta) &= \frac{1}{3} I^{xxxx}(\zeta) = -\frac{3\zeta\cos\zeta + (\zeta^2-3)\sin\zeta}{\zeta^5}, \\
I^{xxzz}(\zeta) &= -\frac{\zeta(\zeta^2-12)\cos\zeta - (5\zeta^2-12)\sin\zeta}{\zeta^5}, \\
I^{zzzz}(\zeta) &= \frac{4\zeta(\zeta^2-6)\cos\zeta + (\zeta^4-12\zeta^2+24)\sin\zeta}{\zeta^5}, \\
I^{xx}(\zeta) &= \frac{-\zeta\cos\zeta + \sin\zeta}{\zeta^3}, \\
I^{zz}(\zeta) &= \frac{2\zeta\cos\zeta + (\zeta^2-2)\sin\zeta}{\zeta^3}.
\end{aligned}
\tag{C.10}
$$

Similar ones are obtained by exchanging x and y and permuting indices; all the others are zero. One can parametrize them as

$$
I^{abcd}(\zeta) = \frac{1}{\zeta^5}\sum_{l=0}^{4} C_l^{abcd}\,\zeta^l\, s_l(\zeta), \qquad I^{ab}(\zeta) = \frac{1}{\zeta^3}\sum_{l=0}^{2} C_l^{ab}\,\zeta^l\, s_l(\zeta) \tag{C.11}
$$

where

$$
s_l(\zeta) := \begin{cases} \sin\zeta & l \text{ even} \\ \cos\zeta & l \text{ odd.} \end{cases} \tag{C.12}
$$

Now, remember that for the longitudinal mode $\hat{\mathbf{e}}_{\mathbf{q}L} = \hat{\mathbf{q}}$. Thus, the longitudinal (L) contribution to J_{ij} is

$$
\begin{aligned}
\left[J_{ij}\right]_L &= \frac{\gamma_L^2}{2\rho v_L^2}\mathsf{D}_i^{ab}\mathsf{D}_j^{cd}\int\frac{d^3q}{(2\pi)^3}\hat{q}^a\hat{q}^b\hat{q}^c\hat{q}^d e^{i\mathbf{q}\cdot(\mathbf{r}_i-\mathbf{r}_j)} && \text{(C.13)} \\
&= \frac{\gamma_L^2}{4\pi^2\rho v_L^2 r_{ij}^3}\mathsf{D}_i^{ab}\mathsf{D}_j^{cd}\int_0^\infty d\zeta\,\zeta^2 I_{abcd}(\zeta) && \text{(C.14)} \\
&= \frac{\gamma_L^2}{4\pi^2\rho v_L^2 r_{ij}^3}\sum_{l=0}^{4}(C_l^{abcd}\mathsf{D}_i^{ab}\mathsf{D}_j^{cd})\int_0^\infty d\zeta\,\zeta^{l-3}s_l(\zeta) && \text{(C.15)}
\end{aligned}
$$

where the z axis is set along $(\mathbf{r}_i - \mathbf{r}_j)$, and $\zeta := qr_{ij}$. The ζ integrals can be easily computed: the IR divergences of $l = 0$ and $l = 1$ cancel out since $C_0^{abcd} \equiv -C_1^{abcd}$ (see Eq. (C.10)), and

$$
\left[J_{ij}\right]_L = \frac{\gamma_L^2}{4\pi^2\rho v_L^2 r_{ij}^3}\left(\frac{\pi}{4}C_0^{abcd} + \frac{\pi}{2}C_2^{abcd}\right)\mathsf{D}_i^{ab}\mathsf{D}_j^{cd} \tag{C.16}
$$

For the transverse (T) contribution the computation is very similar; one needs just to use $\sum_{s\ \text{trans.}}\hat{e}^a_{\mathbf{q}s}\hat{e}^b_{\mathbf{q}s} = \delta^{ab} - \hat{q}^a\hat{q}^b$, substitute v_L with v_T, and handle the I^{ab} functions as done with the I^{abcd}. The final result is

$$
\left[J_{ij}\right]_T = \frac{\gamma_T^2}{4\pi^2\rho v_T^2 r_{ij}^3}\left(\frac{\pi}{2}C_0^{ac}\delta^{bd} - \frac{\pi}{4}C_0^{abcd} - \frac{\pi}{2}C_2^{abcd}\right)\mathsf{D}_i^{ab}\mathsf{D}_j^{cd} \tag{C.17}
$$

All in all, the interaction generated by the shift of the phonon vacuum is

$$J_{ij} = \frac{\gamma^2 \mathbb{D}_{ij}}{16\pi\rho v^2 r_{ij}^3}, \tag{C.18}$$

having defined

$$\mathbb{D}_{ij} := \frac{v^2}{\gamma^2}\left[\frac{2\gamma_T^2}{v_T^2}C_0^{ac}\delta^{bd} + \left(C_0^{abcd} + 2C_2^{abcd}\right)\left(\frac{\gamma_L^2}{v_L^2} - \frac{\gamma_T^2}{v_T^2}\right)\right]. \tag{C.19}$$

This is exactly what anticipated in Eq. (5.17). In Fig. C.1b the distribution of $\mathbb{D}_{ij}$ is reported for the case of SiO_2.

C.3 Computation of the Debye-Waller factor

The goal of this Appendix is to compute explicitly the Debye-Waller factor of Eq. (5.26):

$$\frac{\Gamma_i^2}{2} = \sum_{\mathbf{q}s}\frac{\gamma_s^2}{\hbar\omega_{\mathbf{q}s}^3}\Xi_{i\mathbf{q}s}\Xi_{i\mathbf{q}s}^*\coth\left(\frac{\beta\hbar\omega_{\mathbf{q}s}}{2}\right) \tag{C.20}$$

$$= \frac{1}{4\rho\hbar}\sum_s \gamma_s^2\int\frac{d^3q}{(2\pi)^3}\frac{q^2}{\omega_{\mathbf{q}s}^3}\mathsf{D}_i^{ab}\mathsf{D}_i^{cd}\left(\hat{q}^a\hat{e}_{\mathbf{q}s}^b + \hat{q}^b\hat{e}_{\mathbf{q}s}^a\right)\left(\hat{q}^c\hat{e}_{\mathbf{q}s}^d + \hat{q}^d\hat{e}_{\mathbf{q}s}^c\right)\coth\left(\frac{\beta\hbar\omega_{\mathbf{q}s}}{2}\right). \tag{C.21}$$

C.3.1 Considering sound polarization differences

As for the computation of J_{ij}, it is convenient to consider separately the longitudinal (L) and transverse (T) contributions. The former is the easier to compute:

$$\left[\frac{\Gamma_i^2}{2}\right]_L = \frac{\gamma_L^2}{\rho\hbar}\int\frac{d^3q}{(2\pi)^3}\frac{q^2}{v_L^3q^3}\mathsf{D}_i^{ab}\mathsf{D}_i^{cd}\hat{q}^a\hat{q}^b\hat{q}^c\hat{q}^d\coth\left(\frac{\beta\hbar v_L q}{2}\right). \tag{C.22}$$

One is led to consider

$$\frac{1}{4\pi}\int d\Omega\,\hat{q}^a\hat{q}^b\hat{q}^c\hat{q}^d\mathsf{D}_i^{ab}\mathsf{D}_i^{cd} = \frac{1}{15}(\delta^{ab}\delta^{cd} + \delta^{ac}\delta^{bd} + \delta^{ad}\delta^{bc})\mathsf{D}_i^{ab}\mathsf{D}_i^{cd} \tag{C.23}$$

$$= \frac{1}{15}\left[2\,\mathrm{Tr}(\mathsf{D}_i^2) + (\mathrm{Tr}\,\mathsf{D}_i)^2\right] \tag{C.24}$$

$$=: \frac{1}{15}\langle\langle\mathsf{D}_i^2\rangle\rangle_L, \tag{C.25}$$

so that

$$\left[\frac{\Gamma_i^2}{2}\right]_L = \frac{\gamma_L^2}{30\pi^2\rho\hbar v_L^3}\langle\langle\mathsf{D}_i^2\rangle\rangle_L\int_0^{q_D}dq\,q\coth\left(\frac{\beta\hbar v_L q}{2}\right) \tag{C.26}$$

where q_D is the Debye wavevector. In terms of a real-space UV cutoff a, $q_D = \sqrt[3]{6\pi^2}/a$. The previous is a well-known, condensed-matter-textbook integral, that is usually considered in the two regimes of low and high temperature [425]. In the end one finds

$$\left[\frac{\Gamma_i^2}{2}\right]_L = \frac{\gamma_L^2 q_D^2}{30\pi^2\rho\hbar v_L^3}\langle\langle D_i^2\rangle\rangle_L\,\mathcal{F}\left(\frac{\hbar v_L q_D}{2k_BT}\right) \tag{C.27}$$

with

$$\mathcal{F}(w) := \int_0^1 d\zeta\, \zeta \coth(\zeta w) \tag{C.28}$$

$$= -\frac{1}{2w^2}\mathrm{Li}_2(e^{-2w}) + \frac{1}{w}\log(1-e^{-2w}) + \frac{\pi^2}{12w^2} + \frac{1}{2}. \tag{C.29}$$

A more manageable expression can be found by using the asymptotic expansion

$$\mathcal{F}(w) = \begin{cases} 1/w + O(w) & w \ll 1 \\ 1/2 + O(e^{-w}) & w \gg 1. \end{cases} \tag{C.30}$$

Considering that $w = \beta\hbar v q_D/2 = T_D/2T$, the high and low temperature regimes are defined with respect to $T_D/2$.

For the transverse contribution, the polarization sums yield

$$\sum_{s\ transv.} \left(\hat{q}^a \hat{e}^b_{\mathbf{q}s} + \hat{q}^b \hat{e}^a_{\mathbf{q}s}\right)\left(\hat{q}^c \hat{e}^d_{\mathbf{q}s} + \hat{q}^d \hat{e}^c_{\mathbf{q}s}\right)$$

$$= \delta^{ac}\hat{q}^b\hat{q}^d + \delta^{ad}\hat{q}^b\hat{q}^c + \delta^{bc}\hat{q}^a\hat{q}^d + \delta^{bd}\hat{q}^a\hat{q}^c - 4\hat{q}^a\hat{q}^b\hat{q}^c\hat{q}^d. \tag{C.31}$$

Since

$$\frac{1}{4\pi}\int d\Omega\, \hat{q}^a\hat{q}^b = \frac{1}{3}\delta^{ab}, \tag{C.32}$$

it is convenient to define

$$\langle\langle \mathsf{D}_i^2\rangle\rangle_T := 5\,\mathrm{Tr}(\mathsf{D}_i^2) - \langle\langle \mathsf{D}_i^2\rangle\rangle_L = 3\,\mathrm{Tr}(\mathsf{D}_i^2) - (\mathrm{Tr}\,\mathsf{D}_i)^2. \tag{C.33}$$

Therefore one finds, with a calculation similar to before,

$$\left[\frac{\Gamma_i^2}{2}\right]_T = \frac{\gamma_T^2 q_D^2}{30\pi^2\rho\hbar v_T^3}\langle\langle \mathsf{D}_i^2\rangle\rangle_T\, \mathcal{F}\left(\frac{\hbar v_T q_D^2}{2k_B T}\right). \tag{C.34}$$

Putting the results together:

$$\frac{\Gamma_i^2}{2} = \frac{q_D^2}{30\pi^2\rho\hbar}\left[\frac{\gamma_L^2\langle\langle \mathsf{D}_i^2\rangle\rangle_L}{v_L^3}\mathcal{F}\left(\frac{\hbar v_L q_D}{2k_B T}\right) + \frac{\gamma_T^2\langle\langle \mathsf{D}_i^2\rangle\rangle_T}{v_T^3}\mathcal{F}\left(\frac{\hbar v_T q_D}{2k_B T}\right)\right]. \tag{C.35}$$

In the limit of small temperature, one can approximate $\mathcal{F} \approx 1/2$ and find

$$\frac{\Gamma_i^2}{2} = \frac{q_D^2}{60\pi^2\rho\hbar}\left[\frac{\gamma_L^2\langle\langle \mathsf{D}_i^2\rangle\rangle_L}{v_L^3} + \frac{\gamma_T^2\langle\langle \mathsf{D}_i^2\rangle\rangle_T}{v_T^3}\right] + O(e^{-T_D/2T}). \tag{C.36}$$

C.3.2 Disregarding sound polarization

Now the same computation of the previous section is performed, but employing from the beginning an isotropic Debye model. The correct sound velocity to employ is v from Eq. (5.18); and having a look at Eq. (C.35) one can also see that the correct average γ to use is the one of Eq. (5.19). Then, we have only one angular average:

$$\frac{1}{4\pi}\sum_s \int d\Omega\, e^{ab}_{\mathbf{q}s} e^{cd}_{\mathbf{q}s} \mathsf{D}_i^{ab}\mathsf{D}_i^{cd} = \frac{1}{3}\mathrm{Tr}(\mathsf{D}_i^2). \tag{C.37}$$

Therefore, one finds

$$\frac{\Gamma_i^2}{2} = \frac{\gamma^2 \operatorname{Tr}(\mathsf{D}_i^2)}{6\pi^2\rho\hbar v^3} \int_0^{q_D} dq\, q \coth\left(\frac{\beta\hbar v q}{2}\right) \tag{C.38}$$

$$= \frac{\gamma^2 q_D^2 \operatorname{Tr}(\mathsf{D}_i^2)}{6\pi^2\rho\hbar v^3} \mathcal{F}\left(\frac{\hbar v q_D}{2k_B T}\right), \tag{C.39}$$

where $\mathcal{F}$ was defined in Eq. (C.28). In the limit of small temperature:

$$\frac{\Gamma_i^2}{2} = \frac{\gamma^2 q_D^2 \operatorname{Tr}(\mathsf{D}_i^2)}{12\pi^2\rho\hbar v^3} + O\left(e^{-T_D/2T}\right). \tag{C.40}$$

Notice that this equation is also obtained from Eq. (C.36) by putting $v_L = v_T = v$ and $\gamma_L = \gamma_T = \gamma$. We can rewrite the previous expression as

$$\frac{\Gamma_i^2}{2} = \frac{E_D^2}{4E_i^2} + O\left(e^{-T_D/2T}\right). \tag{C.41}$$

where E_D is the Debye energy and

$$E_i := \sqrt{\frac{3\pi^2\hbar^3\rho v^5}{\gamma^2 \operatorname{Tr}(\mathsf{D}_i^2)}}, \tag{C.42}$$

which is the same of Eq. (5.29). The value of Γ_i^2 depends on the random variable $\operatorname{Tr}(\mathsf{D}_i^2)$, whose distribution is shown in Fig. C.1b.

C.4 Fermi's Golden Rule

Here we estimate the rate of decay of a TLS into phonons, namely Y_i of Eq. (5.37):

$$Y_i = \sum_f \frac{2\pi}{\hbar} \left| \langle f, \downarrow | \,\overline{\Delta}_i \sigma_i^- e^{i\Gamma_{i,0}\tilde{b}_i^\dagger} e^{-i\Gamma_{i,0}\tilde{b}_i} \,|0, \uparrow\rangle \right|^2 \rho_f(2\varepsilon_i). \tag{C.43}$$

Let us separate the contributions $Y_i^{(n)}$ coming from final states with a fixed number n of phonons. Therefore, one has to sum over all the n-phonon configurations allowed by energy conservation:

$$\frac{1}{V^n}\sum_f = \frac{1}{n!}\sum_{s_1\cdots s_n} \int_{BZ} \frac{d^3q_1}{(2\pi)^3} \cdots \frac{d^3q_n}{(2\pi)^3} \delta\left(2\varepsilon_i - \sum_k \hbar\omega_{\mathbf{q}_k s_k}\right) \tag{C.44}$$

with $n!$ because there are n indistinguishable bosons in the final state. The matrix element is formed by two pieces:

$$\left| \langle\downarrow| \,\overline{\Delta}_i \sigma_i^- \,|\uparrow\rangle \right|^2 = \overline{\Delta}_i^2. \tag{C.45}$$

coming from the TLS, and

$$\left| \langle \mathbf{q}_1 s_1, \cdots, \mathbf{q}_n s_n | \, e^{i\Gamma_{i,0}\tilde{b}_i^\dagger} \,|0\rangle \right|^2 = \prod_{k=1}^{n} \left[\frac{2\gamma_{s_k}^2}{\hbar\omega_{\mathbf{q}_k s_k}^3} |\Xi_{i\mathbf{q}_k s_k}|^2 \right] \tag{C.46}$$

coming from the phonons. Notice that the case in which $q_k = q_{k'}$ for some $k \neq k'$ can be disregarded, being subleading. All in all, one finds

$$\Upsilon_i^{(n)} = \frac{2\pi V^n}{\hbar n!} \sum_{s_1 \cdots s_n} \int_{BZ} \frac{d^3q_1}{(2\pi)^3} \cdots \frac{d^3q_n}{(2\pi)^3} \, \overline{\Delta}_i^2 \prod_{k=1}^{n} \left[\frac{2\gamma_{s_k}^2}{\hbar \omega_{\mathbf{q}_k s_k}^3} |\Xi_{i\mathbf{q}^s}|^2 \right] \delta\left(2\varepsilon_i - \sum_k \hbar\omega_{\mathbf{q}^s} \right) \tag{C.47}$$

The δ-function can now be exponentiated via Laplace transform:

$$\widetilde{\Upsilon}_i^{(n)}(\lambda) = \int_0^\infty d\varepsilon \, e^{-2\lambda\varepsilon} \, \Upsilon_i^{(n)}(2\varepsilon). \tag{C.48}$$

In this way, all the q integrals are factorized, and similar to the ones already computed for the Debye-Waller factor. In particular, using an isotropic Debye model:

$$\begin{aligned} \frac{2\gamma^2}{\hbar\rho} \sum_s \int_{BZ} \frac{d^3q}{(2\pi)^3} \frac{q^2}{\omega_{\mathbf{q}^s}^3} e^{-\lambda\hbar\omega_{\mathbf{q}^s}} \mathsf{D}_i^{ab} \mathsf{D}_i^{cd} e_{\mathbf{q}^s}^{ab} e_{\mathbf{q}^s}^{cd} &= \frac{\gamma^2 \operatorname{Tr}(\mathsf{D}_i^2)}{3\pi^2\hbar\rho v^3} \int_0^\infty dq \, q \, e^{-\eta q - \lambda\hbar v q} \\ &= \frac{\gamma^2 \operatorname{Tr}(\mathsf{D}_i^2)}{3\pi^2\hbar\rho v^3} \frac{1}{(\eta + \lambda\hbar v)^2} \end{aligned} \tag{C.49}$$

having employed an exponential cutoff $\eta \approx 1/q_D$. Thus, the Laplace-transformed rate reads

$$\widetilde{\Upsilon}_i^{(n)}(\lambda) = \frac{2\pi\overline{\Delta}_i^2}{\hbar n!} \left[\frac{\gamma^2 \operatorname{Tr}(\mathsf{D}_i^2)}{3\pi^2\hbar\rho v^3} \frac{1}{(\eta + \lambda\hbar v)^2} \right]^n, \tag{C.50}$$

and now the inverse Laplace transform is immediate:

$$\int_{-i\infty}^{+i\infty} \frac{d\lambda}{2\pi i} \frac{e^{2\lambda\varepsilon}}{(\eta + \lambda\hbar v)^{2n}} = \frac{(2\varepsilon)^{2n-1} e^{-2\eta\varepsilon/\hbar v}}{(\hbar v)^{2n}(2n-1)!}. \tag{C.51}$$

In conclusion:

$$\Upsilon_i^{(n)} = \frac{\pi\overline{\Delta}_i^2 e^{-2\eta\varepsilon/\hbar v}}{\hbar\varepsilon n!(2n-1)!} \left[\frac{\gamma^2\varepsilon^2 \operatorname{Tr}(\mathsf{D}_i^2)}{3\pi^2\hbar^3\rho v^5} \right]^n. \tag{C.52}$$

At this point, all the n-phonon contributions can be resummed. The resulting series is of the form

$$\sum_{n\geq 1} \frac{w^n}{n!(2n-1)!} = w \, {}_0F_2\left(; \frac{3}{2}, 2; \frac{w}{4} \right), \tag{C.53}$$

where ${}_0F_2$ is a generalized hypergeometric function. It is enough to know its asymptotics:

$$w \, {}_0F_2\left(; \frac{3}{2}, 2; \frac{w}{4} \right) = \begin{cases} w + \dfrac{w^2}{12} + O(w^3) & w \ll 1 \\ \exp\left(\dfrac{3w^{1/3}}{4^{1/3}} \right) \left[\dfrac{w^{1/6}}{2^{1/3}\sqrt{3\pi}} + O(w^{-1/6}) \right] & w \gg 1. \end{cases} \tag{C.54}$$

Therefore, in general it holds

$$\Upsilon_i = \sum_{n\geq 1} \Upsilon_i^{(n)} = \frac{\pi\overline{\Delta}_i^2 \varepsilon_i e^{-2\eta\varepsilon_i/\hbar v}}{\hbar E_i^2} \, {}_0F_2\left(; \frac{3}{2}, 2; \frac{\varepsilon_i^2}{4E_i^2} \right) \tag{C.55}$$

with E_i defined in Eq. (5.29).

C.5 Computations for the master equation

We want to compute explicitly Γ^{ω}_{ij} defined in Eq. (5.50), that we reproduce here:

$$\Gamma^{\omega}_{ij} := \frac{1}{\hbar^2}\int_0^{\infty} dt'\, e^{i\omega t'}\ \mathrm{Tr}_B\left[\rho_B^T\, \hat{\mathcal{E}}_i^{\dagger}(t)\, \hat{\mathcal{E}}_j(t-t')\right] \tag{C.56}$$

As a first thing, we need to time-evolve the operators $\mathcal{E}_i$ in the interaction picture. Using Eqs. (5.12) and (5.49), one determines

$$\begin{aligned}\hat{\mathcal{E}}_i(t) &= e^{iH_{ph}t/\hbar}\mathcal{E}_i e^{-iH_{ph}t/\hbar}\\ &= \sum_{\mathbf{q}s}\left(\gamma_{is}\Xi_{i\mathbf{q}s}\sqrt{\frac{\hbar}{2\omega_{\mathbf{q}s}}}e^{-i\omega_{\mathbf{q}s}t}b_{\mathbf{q}s} + \text{h.c.}\right).\end{aligned} \tag{C.57}$$

Thus, it follows

$$\begin{aligned}\hbar^2\Gamma^{\omega}_{ij} = \int_0^{\infty} dt'\, e^{i\omega t'}\ \mathrm{Tr}_B\Bigg\{\rho_B^T\sum_{\mathbf{q}s}\sum_{\mathbf{q}'s'}\left(\gamma_{is}\Xi_{i\mathbf{q}s}\sqrt{\frac{\hbar}{2\omega_{\mathbf{q}s}}}e^{-i\omega_{\mathbf{q}s}t}b_{\mathbf{q}s} + \text{h.c.}\right)\\ \times\left(\gamma_{js'}\Xi_{j\mathbf{q}'s'}\sqrt{\frac{\hbar}{2\omega_{\mathbf{q}'s'}}}e^{-i\omega_{\mathbf{q}'s'}(t-t')}b_{\mathbf{q}'s'} + \text{h.c.}\right)\Bigg\}.\end{aligned} \tag{C.58}$$

Collecting terms:

$$\begin{aligned}\hbar^2\Gamma^{\omega}_{ij} = \int_0^{\infty} dt'\, e^{i\omega t'}\sum_{\mathbf{q}s}\frac{\hbar}{2\omega_{\mathbf{q}s}}\Big\{\gamma_{is}\gamma_{js}\Xi_{i\mathbf{q}s}\Xi^*_{j\mathbf{q}s}\, e^{-i\omega_{\mathbf{q}s}t'}\ \mathrm{Tr}_B\left[\rho_B^T b_{\mathbf{q}s}b^{\dagger}_{\mathbf{q}s}\right]\\ +\gamma_{is}\gamma_{js}\Xi^*_{i\mathbf{q}s}\Xi_{j\mathbf{q}s}\, e^{i\omega_{\mathbf{q}s}t'}\ \mathrm{Tr}_B\left[\rho_B^T b^{\dagger}_{\mathbf{q}s}b_{\mathbf{q}s}\right]\Big\},\end{aligned} \tag{C.59}$$

and introducing f_T, i.e. the Bose-Einstein distribution function at temperature T:

$$\begin{aligned}\hbar^2\Gamma^{\omega}_{ij} = \int_0^{\infty} dt'\, e^{i\omega t'}\sum_{\mathbf{q}s}\frac{\hbar}{2\omega_{\mathbf{q}s}}\Big\{\gamma_{is}\gamma_{js}\Xi_{i\mathbf{q}s}\Xi^*_{j\mathbf{q}s}\, e^{-i\omega_{\mathbf{q}s}t'}\ \left(f_T(\hbar\omega_{\mathbf{q}s})+1\right)\\ +\gamma_{is}\gamma_{js}\Xi^*_{i\mathbf{q}s}\Xi_{j\mathbf{q}s}\, e^{i\omega_{\mathbf{q}s}t'}\ f_T(\hbar\omega_{\mathbf{q}s})\Big\}.\end{aligned} \tag{C.60}$$

We perform the time integral using the identity

$$\int_0^{\infty} dt\, e^{i\zeta t} = i\ \mathrm{PV}\,\frac{1}{\zeta} + \pi\delta(\zeta). \tag{C.61}$$

Plugging in the explicit expression of $\Xi_{i\mathbf{q}s}$ from Eq. (5.12), one arrives at

$$\begin{aligned}\Gamma^{\omega}_{ij} = -\frac{1}{2\rho}\sum_{abcd}D_i^{ab}D_j^{cd}\sum_s\gamma_{is}\gamma_{js}\int\frac{d^3q}{(2\pi)^3}\frac{q^2}{\hbar\omega_{\mathbf{q}s}}e^{ab}_{\mathbf{q}s}e^{cd}_{\mathbf{q}s}\\ \times\Bigg[\left(f_T(\hbar\omega_{\mathbf{q}s})+1\right)\left(i\,\mathrm{PV}\,\frac{1}{\omega-\omega_{\mathbf{q}s}}+\pi\delta(\omega-\omega_{\mathbf{q}s})\right)e^{i\mathbf{q}\cdot(\mathbf{r}_i-\mathbf{r}_j)}\\ +\ f_T(\hbar\omega_{\mathbf{q}s})\left(i\,\mathrm{PV}\,\frac{1}{\omega+\omega_{\mathbf{q}s}}+\pi\delta(\omega+\omega_{\mathbf{q}s})\right)e^{-i\mathbf{q}\cdot(\mathbf{r}_i-\mathbf{r}_j)}\Bigg].\end{aligned} \tag{C.62}$$

From this integral, one can obtain J^w_{ij} and Y^w_i by essentially taking the imaginary and real parts, respectively. The resulting expressions are very similar to the ones we already dealt with in Secs. C.2 and C.3, respectively, therefore we will not repeat the computation, which is practically identical. In the end, one finds the expressions reported in Eqs. (5.54) and (5.53).

C.6 Two-site observables within the diagonal unitary evolution

In this Section, we show how to compute with $O(N)$ steps the two-site density matrix ρ_{ij}, and therefore any two-site observable, for the Hamiltonian (5.55). Call the initial density matrix

$$\rho_0 = \bigotimes_{i=1}^{N} \rho_{0,i} = \bigotimes_{i=1}^{N} \sum_{s_i,s_i'} \rho_{0,i}^{s_i s_i'} \left|s_i\right\rangle \left\langle s_i'\right|, \tag{C.63}$$

and recall that the Hamiltonian (5.55) reads explicitly

$$H_{TLS} + H_{LS} = -\frac{1}{2}\sum_i \hbar\nu_i S_i^z + \sum_{ij} J_{ij} S_i^z S_j^z. \tag{C.64}$$

Time evolving the density matrix according to the von Neumann equation and rearranging the sum, one finds

$$\rho(t) = \sum_{s,s'} \prod_i \rho_{0,i}^{s_i s_i'} \left|s\right\rangle \left\langle s'\right| e^{-i(H[s]-H[s'])t/\hbar} \tag{C.65}$$

with $H[s] = -\frac{1}{2}\sum_i \hbar\nu_i s_i + \sum_{ij} J_{ij} s_i s_j$, where $s_i = \pm 1$ is the projection of the spin-1/2 on the z axis. Without loss of generality, we can trace out all the spins but the first two. The matrix elements of the two-site reduced density matrix read

$$\begin{aligned}
\left\langle s_1 s_2\right| \rho_{12}(t) \left|s_1' s_2'\right\rangle &= \left\langle s_1 s_2\right| \mathrm{Tr}_{3\cdots N}\, \rho(t) \left|s_1' s_2'\right\rangle \\
&= \sum_{s_3\cdots s_N} \rho_{0,1}^{s_1,s_1'} \rho_{0,2}^{s_2,s_2'} \rho_{0,3}^{s_3,s_3} \cdots \rho_{0,N}^{s_N,s_N} e^{-i(H[s_1 s_2 s_3\cdots s_N]-H[s_1' s_2' s_3\cdots s_N])t/\hbar} \\
&= \rho_{0,1}^{s_1,s_1'} \rho_{0,2}^{s_2,s_2'} e^{-i\Delta H_{12}[s]t/\hbar} \prod_{j=3}^{N} \left[\rho_{0,j}^{\uparrow,\uparrow} e^{-i\Delta H_{12j}[s]t/\hbar} + \rho_{0,j}^{\downarrow,\downarrow} e^{i\Delta H_{12j}[s]t/\hbar}\right],
\end{aligned} \tag{C.66}$$

having defined

$$\begin{aligned}
\Delta H_{12}[s] &:= 2J_{12}(s_1 s_2 - s_1' s_2') - \frac{\hbar\nu_1}{2}(s_1 - s_1') - \frac{\hbar\nu_2}{2}(s_2 - s_2'), \\
\Delta H_{12j}[s] &:= 2J_{1j}(s_1 - s_1') + 2J_{2j}(s_2 - s_2').
\end{aligned} \tag{C.67}$$

From the knowledge of ρ_{ij}, the concurrence follows by using Eq. (5.59).

Notice that an analogue procedure gives the k-site reduced density matrix with $O(k^2 N)$ steps. Thus, this computation allows to access few-sites observables for large system sizes.

C.7 Concurrence in a random state

Let us consider a system of N spin-1/2. A random, uniformly distributed state is $|\psi\rangle = U|\psi_0\rangle$, U being a Haar-random unitary, and $|\psi_0\rangle$ a reference state. Equivalently, a random state is $|\psi\rangle = \sum_{\{s\}} A_{\{s\}} |\{s\}\rangle$, with the coefficients $A_{\{s\}}$ being uniformly distributed over $\mathbb{C}P^{M-1}$, with $M = 2^N$.

The concurrence of two spins, say sites 1 and 2 wlog., follows from the knowledge of the square roots of the eigenvalues of the matrix $R_{12} = \rho_{12}(\sigma_y \otimes \sigma_y)\rho_{12}^*(\sigma_y \otimes \sigma_y)$. The exact determination of such eigenvalues has evaded our analytical attempts, but we can give an heuristic argument that captures the scaling with N. Consider, instead of the square roots of the eigenvalues of R_{12}, directly the eigenvalues λ_a of ρ_{12}. Classical works [509, 510] give us their probability density function:

$$p(\lambda_1, \lambda_2, \lambda_3, \lambda_4) \propto \delta\Big(1 - \sum_{a=1}^{4} \lambda_a\Big) \prod_{a=1}^{4} \lambda_a^{M-4} \prod_{a<b} (\lambda_a - \lambda_b)^2 \tag{C.68}$$

with the constraint $\lambda_a > 0$, $a = 1, \ldots, 4$. With hindsight, we perform the change of variables

$$\rho_{12} \equiv \frac{1}{4}\mathrm{Id} + \frac{1}{4\sqrt{M-4}}\tau_{12}, \qquad \lambda_a \equiv \frac{1}{4} + \frac{\mu_a}{4\sqrt{M-4}}, \tag{C.69}$$

so that

$$\begin{aligned} p(\mu_1, \mu_2, \mu_3, \mu_4) &\propto \delta\Big(\sum_{a=1}^{4} \mu_a\Big) \prod_{a=1}^{4} \left(1 + \frac{\mu_a}{\sqrt{M-4}}\right)^{M-4} \prod_{a<b} (\mu_a - \mu_b)^2 \\ &\propto \delta\Big(\sum_{a=1}^{4} \mu_a\Big) \exp\left[-\frac{1}{2}\sum_a \mu_a^2 + O\left(\frac{1}{\sqrt{M-4}}\right)\right] \prod_{a<b} (\mu_a - \mu_b)^2. \end{aligned} \tag{C.70}$$

We see that, at this order, we can let μ_a range from $-\infty$ to $+\infty$ if N is big enough.

At this point we note that not only the eigenvalues of τ_{12}, but every entry of the matrix is at most of order 1 because of our rescaling. This enables us to expand

$$\begin{aligned} \sqrt{R_{12}} &= \left[\frac{1}{16}\mathrm{Id} + \frac{1}{16\sqrt{M-4}}\left[\tau_{12} + (\sigma_y \otimes \sigma_y)\tau_{12}^*(\sigma_y \otimes \sigma_y)\right] + O\left(\frac{1}{M}\right)\right]^{1/2} \\ &= \frac{1}{4}\mathrm{Id} + \frac{1}{8\sqrt{M-4}}\left[\tau_{12} + (\sigma_y \otimes \sigma_y)\tau_{12}^*(\sigma_y \otimes \sigma_y)\right] + O\left(\frac{1}{M}\right) \end{aligned} \tag{C.71}$$

The matrix $\frac{1}{2}[\tau_{12} + (\sigma_y \otimes \sigma_y)\tau_{12}^*(\sigma_y \otimes \sigma_y)]$ is traceless and very roughly its eigenvalues will have a joint probability density function very similar to that of τ_{12}. For this reason, we can approximate the average concurrence with

$$\langle C \rangle \approx \int d\vec{\mu}\, p(\vec{\mu})\, \max\left\{0, \frac{2\mu_1 - 1}{4\sqrt{M-4}} - \frac{1}{2}\right\}, \tag{C.72}$$

where we have used the δ-function constraint and called μ_1 the largest eigenvalue.

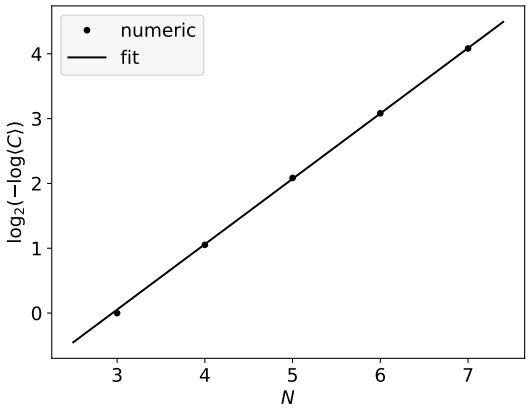

FIGURE C.2: The average concurrence in a random state follows the scaling $\langle C\rangle \sim e^{-a2^{bN}}$. The dots show the concurrence averaged over 10^7 randomly generated states, and over every couple of spins for each state. A linear fit is shown for comparison: $b = 1.0$, but $a = 0.13$, differing from $a = 1/2$ found analytically (Eq. (C.74)).

Integrating only on μ_1, and forgetting the presence of μ_2, μ_3, μ_4 (otherwise the integration becomes rather cumbersome), we find

$$\langle C\rangle \approx \frac{e^{-(M+\sqrt{M-4})/2}}{2\sqrt{2\pi}(M-4)^{3/2}}, \tag{C.73}$$

from which

$$\log_2\big(-\log\langle C\rangle\big) \approx \log(a) + bN + \cdots \tag{C.74}$$

with $a = 1/2$ and $b = 1$. As can be seen from Figure C.2, this scaling is correct, but the numerical factor a is different.

C.8 Integration of the GKSL master equation

The density matrix of the system can be parametrized as

$$\rho(t) = \sum_{\mu_1\cdots\mu_N} C_{\mu_1\cdots\mu_N}(t) S_1^{\mu_1}\otimes\cdots\otimes S_N^{\mu_N}, \tag{C.75}$$

where $S_i^{\mu_i} \in \{\mathrm{Id}_i, S_i^+, S_i^-, S_i^z\}$. Writing explicitly the GKSL equation (see Eqs. (5.47) and (5.55) in the main text), we get

$$\begin{aligned}\partial_t\rho(t) = -\frac{i}{\hbar}\Big[-\sum_i \frac{\hbar\nu_i}{2}S_i^z + \sum_{ij} J_{ij}S_i^zS_j^z,\ \rho(t)\Big] \\ + \sum_i \Upsilon_i f_T(\hbar\nu_i)\left[S_i^+\rho(t)S_i^- + S_i^-\rho(t)S_i^+ - 4\rho(t)\right] \\ + \sum_i \Upsilon_i\left[S_i^+\rho(t)S_i^- + \{\rho(t), S_i^z\} - 2\rho(t)\right].\end{aligned} \tag{C.76}$$

In the absence of the interactions (i.e. ignoring the term $\sum_{ij} J_{ij}S_i^zS_j^z$), the evolution can be easily computed, and the density matrix evolves as

$$\partial_t C_{\mu_1\cdots\mu_N} = \Big[\sum_i \lambda_i^{\mu_i}\Big] C_{\mu_1\cdots\mu_N} + \sum_i 4\Upsilon_i\,\delta^{\mu_i z} C_{\mu_1\cdots 0_i\cdots\mu_N}, \tag{C.77}$$

where the $\delta^{\mu_i z}$ are Kronecker deltas, the $\lambda_i^{\mu_i}$'s are given by

$$\lambda_i^z = -4Y_i(1+2f_T), \qquad \lambda_i^{\pm} = \frac{1}{2}\lambda_i^z \pm i\nu_i, \tag{C.78}$$

and $\lambda_i^0 = 0$. When interactions are suppressed, the TLSs evolve independently one from the other and any factorized initial state will remain such at all times. One has

$$\rho(t) = \bigotimes_{i=1}^{N} \sum_{\mu_i} P_i^{\mu_i}(t) S_i^{\mu_i} \implies C_{\mu_1 \cdots \mu_N}(t) = P_1^{\mu_1}(t) \cdots P_N^{\mu_N}(t) \quad \forall t. \tag{C.79}$$

The interactions among TLSs make the evolution more complicated. Computing the commutator

$$\begin{aligned}\left[S_i^z S_j^z, S_i^{\mu_i} S_j^{\mu_j}\right] &= S_i^z S_i^{\mu_i}\left[S_j^z, S_j^{\mu_j}\right] + \left[S_i^z, S_i^{\mu_i}\right] S_j^{\mu_j} S_j^z \\ &= 2\sum_{\mu_i'\mu_j'} \big[(\delta^{\mu_i 0}\delta^{\mu_i' z} + \delta^{\mu_i z}\delta^{\mu_i' 0} + \delta^{\mu_i +}\delta^{\mu_i' +} - \delta^{\mu_i -}\delta^{\mu_i' -})(\delta^{\mu_j +}\delta^{\mu_j' +} - \delta^{\mu_j -}\delta^{\mu_j' -}) \\ &+ (\delta^{\mu_j 0}\delta^{\mu_j' z} + \delta^{\mu_j z}\delta^{\mu_j' 0} - \delta^{\mu_j +}\delta^{\mu_j' +} + \delta^{\mu_j -}\delta^{\mu_j' -})(\delta^{\mu_i +}\delta^{\mu_i' +} - \delta^{\mu_i -}\delta^{\mu_i' -})\big] S_i^{\mu_i'} S_j^{\mu_j'},\end{aligned} \tag{C.80}$$

and defining

$$\zeta^{\mu\mu'} := \delta^{\mu 0}\delta^{\mu' 3} + \delta^{\mu 3}\delta^{\mu' 0}, \qquad \kappa^{\mu\mu'} := 2\delta^{\mu +}\delta^{\mu' +} - 2\delta^{\mu -}\delta^{\mu' -}, \tag{C.81}$$

one arrives at

$$\sum_{i\neq j} J_{ij}\left[S_i^z S_j^z, S_i^{\mu_i} S_j^{\mu_j}\right] = 2\sum_{i<j} J_{ij} \sum_{\mu_i'\mu_j'} \left[\zeta^{\mu_i\mu_i'}\kappa^{\mu_j\mu_j'} + (i \leftrightarrow j)\right] S_i^{\mu_i'} S_j^{\mu_j'}. \tag{C.82}$$

The full evolution of the density matrix is given by

$$\begin{aligned}\partial_t C_{\mu_1\cdots\mu_N} = &\sum_i \lambda_i^{\mu_i} C_{\mu_1\cdots\mu_N} + \sum_i 4Y_i\, \delta^{\mu_i z} C_{\mu_1\cdots 0_i\cdots\mu_N} \\ &- \frac{2i}{\hbar}\sum_{i<j} J_{ij} \sum_{\mu_i'\mu_j'} \left(\zeta^{\mu_i\mu_i'}\kappa^{\mu_j\mu_j'} + \kappa^{\mu_i\mu_i'}\zeta^{\mu_j\mu_j'}\right) C_{\mu_1\cdots\mu_i'\cdots\mu_j'\cdots\mu_N}.\end{aligned} \tag{C.83}$$

This is a systems of 4^N partial differential equations. We solved it by matrix exponentiation, using the library for linear algebra with sparse matrices contained in `SciPy`.

D Addendum to Chapter 6

In this Appendix, I report all the computations left aside in the study of the two-dimensional Ising model at strong coupling. In Sec. D.1 I show how the magnetization for the 1d "embedded" configurations can be obtained analytically. In Sec. D.2 I show how to compute the two-site correlations for the 1d effective model of interfaces. In Sec. D.3 I detail the correct prescription for taking the continuum limit. In Sec. D.4 I show the full computation for the corrections in $1/J$. In Sec. D.5 I show how to obtain the localization length for the Stark-localized model. In Sec. D.6 I group all the useful properties of the Bessel functions.

D.1 Magnetization in the linear strip

We give here a more detailed analysis of the results for the dynamics of a linear strip of spins, treated in Sec. 6.2.1. As pointed out in Eq. (6.8), the number of configurations for a strip of spins of length L with l flipped spins is

$$C(L,l) = C(L-1,l) + C(L-2,l-1). \tag{D.1}$$

Such recursion relation is obtained by summing the number of configurations in which the $L-1$-th spin is not flipped, which is $C(L-1,l)$, and the number in which it is flipped, given by $C(L-2,l-1)$. The initial condition is clearly $C(L,0) = 1$, as there is only one configuration without any spin flip. The recursion relation has solution

$$C(L,l) = \binom{L-l-1}{l}. \tag{D.2}$$

In order to obtain the total number of possible configurations, one needs also to know the maximum number of spins that can be flipped, without violating the perimeter constraint. Obviously, the first and last spin cannot flip, and therefore we are left with $L-2$ "active" spins. If $L-2$ is even, one can flip at most $(L-2)/2$ spins, whereas if $L-2$ is odd, one can flip $(L-1)/2$ spins. Therefore

$$n_{max} = \left\lceil \frac{L-2}{2} \right\rceil, \tag{D.3}$$

as reported in Eq. (6.10) in the main text.

The magnetization profile is found using the following argument: consider the j-th spin of a chain of length L. The number of configurations having the j-th spin that is "up" are given by the total number of allowed configurations for the two sub-chains split by the j-th spin, that is $F_{L-j}F_{j-1}$ configurations. Of course, in the remaining $F_L - F_{L-j}F_{j-1}$ cases the j-th spin is "down", and thus the magnetization at site j is

$$\langle m_L(j)\rangle = \frac{-(F_L - F_{L-j}F_{j-1}) + F_{L-j}F_{j-1}}{F_L} = 2\frac{F_{L-j}F_{j-1}}{F_L} - 1, \tag{D.4}$$

as written in the main text, Eq. (6.12). Using the properties of Fibonacci numbers, one gets, for $L \to \infty$

$$\langle m_\infty(j)\rangle = \frac{2}{(2\phi-1)\phi} - 1 + \frac{2}{(\phi-1)(2\phi-1)}\left(\frac{1}{\phi}-1\right)^j, \tag{D.5}$$

ϕ being the golden ratio. In the limit $j \to \infty$, one finds the magnetization at center of the strip to be

$$\lim_{j\to\infty} m_\infty(j) = \frac{2}{(2\phi-1)\phi} - 1 = -\frac{1}{\sqrt{5}}. \tag{D.6}$$

D.2 Two-point functions

In order to obtain the fluctuations of the limiting shape μ of the Young's diagrams, one needs the two-point function of the number operator n, see also Eq. (6.15). For simplicity, we report here the computation done at equal times, but the same procedure can be extended also for different times. Let us start by computing

$$\langle\Psi_0|\, n(x,t)n(y,t)\,|\Psi_0\rangle = \langle\Psi_0|\, \psi_x^\dagger(t)\psi_x(t)\psi_y^\dagger(t)\psi_y(t)\,|\Psi_0\rangle\,. \tag{D.7}$$

Also in this case, one can expand the initial state and use the time evolution of the fermionic operators. The expectation value one gets, using Wick contractions, is

$$\langle 0|\, \psi_\infty \dots \psi_1\, \psi_j^\dagger \psi_i \psi_l^\dagger \psi_k\, \psi_1^\dagger \dots \psi_\infty^\dagger\,|0\rangle = -\delta^+_{jk}\delta^+_{il} + \delta_{jk}\delta^+_{il} + \delta^+_{ij}\delta^+_{kl}, \tag{D.8}$$

being, by definition,

$$\delta^+_{ab} := \begin{cases} 1 & \text{if } a = b > 0 \\ 0 & \text{otherwise.} \end{cases} \tag{D.9}$$

After some straightforward steps one arrives at

$$\begin{aligned}\langle\Psi_0|\, n(x,t)n(y,t)\,|\Psi_0\rangle = &\left(\sum_{i>0} J^2_{i-x}(\omega_t)\right)\left(\sum_{i>0} J^2_{i-y}(\omega_t)\right) \\ &- \left(\sum_{i>0} J_{i-x}(\omega_t)J_{i-y}(\omega_t)\right)^2 + \delta_{x,y}\left(\sum_{i>0} J_{i-x}(\omega_t)J_{i-y}(\omega_t)\right),\end{aligned} \tag{D.10}$$

being $\omega_t = 2|\gamma \sin(ht)|$, as in the main text. Therefore, the connected 2-point function is

$$\langle\Psi_0|\, n(x,t)n(y,t)\,|\Psi_0\rangle_C = \delta_{xy}\left(\sum_{i>0} J^2_{i-x}(\omega_t)\right) - \left(\sum_{i>0} J_{i-x}(\omega_t)J_{i-y}(\omega_t)\right)^2. \tag{D.11}$$

Using Eq. (D.64), one arrives at (see also Ref. [511])

$$\begin{aligned}\langle\Psi_0|\, n(x,t)n(y,t)\,|\Psi_0\rangle_C = &\,\delta_{xy}\left(\sum_{i>0} J^2_{i-x}(\omega_t)\right) \\ &- \left(\frac{\omega_t[J_x(\omega_t)J_{y-1}(\omega_t) - J_{x-1}(\omega_t)J_y(\omega_t)]}{2(y-x)}\right)^2.\end{aligned} \tag{D.12}$$

The fluctuations of the number operator of the fermions along the chain is readily obtained from Eq. (D.10) by setting $x = y$:

$$\delta n(x,t) = \langle \Psi_0 | \, n(x,t)^2 \, | \Psi_0 \rangle_C = \sum_{i>0} J_{i-x}^2(\omega_t) \left(1 - \sum_{i>0} J_{i-x}^2(\omega_t) \right). \tag{D.13}$$

At this point, summing over space as it was done before, one arrives at the correlation function for the shape operator

$$\langle \Psi_0 | \, \mu(x',t)\mu(y',t) \, | \Psi_0 \rangle_C = - \sum_{x \le x'} \sum_{y \le y'} \left(\frac{\omega_t \left[J_x(\omega_t) J_{y-1}(\omega_t) - J_y(\omega_t) J_{x-1}(\omega_t) \right]}{x-y} \right)^2 + 4 \sum_{x \le x'} \sum_{y \le y'} \delta_{xy} \left(\sum_{i>0} J_{i-x}^2(\omega_t) \right). \tag{D.14}$$

With the same procedure one can compute the expectation value of the current operator, defined as:

$$j(x,t) \equiv i(\psi_x^\dagger(t)\psi_{x+1}(t) - \psi_{x+1}^\dagger(t)\psi_x(t)). \tag{D.15}$$

Using this definition, one obtains

$$\langle \Psi_0 | \, j(x,t) \, | \Psi_0 \rangle = \gamma \sin 2ht \left[J_x^2 \left(2\gamma \sin ht \right) - J_{x+1} \left(2\gamma \sin ht \right) J_{x-1} \left(2\gamma \sin ht \right) \right]. \tag{D.16}$$

At $x = 0$ it reduces to

$$\langle \Psi_0 | \, j(0,t) \, | \Psi_0 \rangle = \gamma \sin 2ht \left[J_0^2 \left(2\gamma \sin ht \right) + J_1^2 \left(2\gamma \sin ht \right) \right]. \tag{D.17}$$

Also the current-current correlator can be computed with the same tools: we report here the result for $x = 0$, which is given by

$$\langle \Psi_0 | \, j(0,t) j(0,0) \, | \Psi_0 \rangle = J_1^2 \left(2\gamma \sin ht \right) - J_0^2 \left(2\gamma \sin ht \right). \tag{D.18}$$

D.3 Continuum limit of the interface

We now explore how to modify the lattice spacing a in the fermionic model, in order to obtain a non-trivial continuum limit as $a \to 0$. We start from the results obtained in the case $a = 1$, that simply translate in the case of generic a: for instance,

$$m(ax,t) = 2 \sum_{y<x} J_y^2 \left(\omega_t \right) + \text{const.}, \tag{D.19}$$

and consequently

$$\mu(ax,t) = 2a \sum_{y \le x} (x-y) \, J_y^2 \left(\omega_t \right) - xa. \tag{D.20}$$

This is what one would expect since, without appropriately rescaling the fields, the change of lattice spacing simply consists in zooming in ($a > 1$) or zooming out ($a < 1$). In order to get something non-trivial, also the fields g and h should be rescaled. A simple way to find the correct rescaling is to focus on $\mu(0,t)$, and find under which conditions the limit $a \to 0$ gives a non trivial result. The behaviour of $\mu(0,t)$ suggests that the proper rescaling is $\gamma \to \gamma/a$; indeed one has, according to

Eq. (D.20),

$$\lim_{a\to 0}\mu(0,t)=\lim_{a\to 0}\omega_t\left[\frac{\omega_t}{a}J_0^2\left(\frac{\omega_t}{a}\right)-J_0\left(\frac{\omega_t}{a}\right)J_1\left(\frac{\omega_t}{a}\right)+\frac{\omega_t}{a}J_1^2\left(\frac{\omega_t}{a}\right)\right]=\frac{2}{\pi}\omega_t. \quad \text{(D.21)}$$

This result is meaningful, as it corresponds to effectively diminishing the value of h with respect to g, viz. making it easier for fermions to move. In conclusion, the correct rescaling is the one obtained by including the factor $1/a$ also in front of the linear potential in the Hamiltonian Eq. (6.16). This can be understood also because the electric potential must be taken proportional to the physical position in the continuum: if $V(x)=-Ex=-Eja$, then $h\propto a$.

Having found the appropriate rescaling for a non-trivial limit $a\to 0$, one can ask what happens to the average fermion density and to the whole shape of the domain wall in such limit. Consider then

$$\mu(ax,t)=2a\sum_{x\le z}(z-x)\,J_x^2\left(\frac{\omega_t}{a}\right)-za: \quad \text{(D.22)}$$

since the shape is symmetric under $z\to -z$, one can restrict for simplicity to the case $z\ge 0$. Let us define $\xi:=za$ and $\eta:=xa$: in the limit $a\to 0$, ξ and η will be kept fixed, and it is $\mu(\xi)$ that will be evaluated. Write

$$\mu(\xi)=2\left(\sum_{x\le 0}+\sum_{0<x\le z}\right)(\xi-ax)\,J_x^2\left(\frac{\omega_t}{a}\right)-\xi: \quad \text{(D.23)}$$

the first sum is easily computed, and it gives

$$\begin{aligned}2\sum_{x\le 0}(\xi-ax)J_x^2(\omega_t/a)&=\xi\left[1+J_0\left(\frac{\omega_t}{a}\right)\right]\\&+\omega_t\left[\frac{\omega_t}{a}J_0^2\left(\frac{\omega_t}{a}\right)-J_0\left(\frac{\omega_t}{a}\right)J_1\left(\frac{\omega_t}{a}\right)+\frac{\omega_t}{a}J_1^2\left(\frac{\omega_t}{a}\right)\right]\overset{a\to 0}{\longrightarrow}\ \xi+\frac{2}{\pi}\omega_t. \quad \text{(D.24)}\end{aligned}$$

In order to compute the other sum, notice that, in order to have ξ finite, z needs to be very large in the limit $a\ll 1$. Therefore the sum can be approximated with an integral as

$$2\sum_{0<x\le z}(\xi-ax)J_x^2\left(\frac{\omega_t}{a}\right)\ \longrightarrow 2\int_0^\xi\frac{d\eta}{a}(\xi-\eta)J_{\eta/a}^2\left(\frac{\omega_t}{a}\right) \quad \text{(D.25)}$$

In the limit $a\to 0$, one may further approximate the Bessel function with an asymptotic expansions. In particular, if $\eta>\omega_t$, the Bessel function decays exponentially as $a\to 0$, and one can safely neglect its contribution to the integral. This means that, if $\xi>\omega_t$, the integral can be restricted from 0 to ω_t. If instead $\eta/a<2\omega_t/a$, one should use the expansion Eq. (D.70); in the limit $a\to 0$, one can safely approximate the fast oscillating squared cosine by its average value $1/2$, and obtain

$$2\int_0^\xi\frac{d\eta}{a}(\xi-\eta)J_{\eta/a}^2\left(\frac{\omega_t}{a}\right)\simeq\int_0^\xi d\eta\,\frac{\xi-\eta}{\pi\gamma\sqrt{1-\left(\frac{\eta}{\omega_t}\right)^2}} \quad \text{(D.26)}$$

$$=\frac{2\xi}{\pi}\arcsin\frac{\xi}{\omega_t}+\frac{2\omega_t}{\pi}\left(\sqrt{1-\frac{\xi^2}{\omega_t^2}}-1\right) \quad \text{(D.27)}$$

Putting all the pieces together:

$$\mu(\xi,t)=\begin{cases}\dfrac{2\xi}{\pi}\arcsin\dfrac{\xi}{\omega_t}+\dfrac{2\omega_t}{\pi}\sqrt{1-\dfrac{\xi^2}{\omega_t^2}} & \text{if } 0\leq|\xi|\leq\omega_t\\ \xi & \text{if } |\xi|>\omega_t.\end{cases} \tag{D.28}$$

One arrives then at the expression reported in the main text, Eqs. (6.33) and (6.34).

An equivalent derivation of the above result can be obtained passing through the continuum limit of the number density. Following Ref. [434], one has

$$\Phi'_x(v)\equiv[\langle n(x+1,t)\rangle-\langle n(x,t)\rangle]_{x/\omega_t=v}=J_x^2\left(\frac{x}{v}\right). \tag{D.29}$$

Since we are in absence of longitudinal field, excitations propagate ballistically in the system, and thus the continuum limit is achieved by treating v as a continuous variable (corresponding to the scaling limit x, $\omega_t\to\infty$ with x/ω_t finite). In order to obtain the scaling form of the magnetization profile, one has to integrate back Eq. (D.29) over space and this is done more easily using the asymptotic forms of the Bessel functions. One has to distinguish the cases $|v|\geq 1$ and $|v|<1$: the former case gives 0 or 1 (according to the sign of v), whereas the latter yields

$$\Phi(v)=\omega_t\lim_{x\to\infty}\int dv\,\Phi'_x(v)\simeq\int\frac{1}{\pi\sqrt{1-v^2}}dv=\frac{1}{\pi}\arcsin v \tag{D.30}$$

A further integration gives the continuum limit of the limiting shape.

Let us mention also that the continuum limit of Eq. (6.27) can be computed, and one gets $\langle n(x,t)\rangle=1/s$, as only the first term in the sum of Eq. (6.27) contributes when the lattice spacing is sent to zero; this translates into $\langle\mu(x,t)\rangle=x(2/s-1)$.

D.4 Second order Schrieffer-Wolff and integrability breaking

In this section, we perform a Schrieffer-Wolff transformation [417] to get a renormalized Hamiltonian, describing the effective degrees of freedom in each sector $\mathcal{H}_\ell$ when $g,h\ll J<+\infty$. We remind that the Schrieffer-Wolff transformation consists in a renormalization procedure that progressively eliminates, order by order in perturbation theory, all the block-off-diagonal Hamiltonian matrix elements, i.e. the ones coupling different sectors $\mathcal{H}_\ell$ and $\mathcal{H}_{\ell'}$ with $\ell\neq\ell'$. Mathematically, it is a unitary rotation $U=e^S$, with $S=S_1+S_2+\cdots$, that gives

$$e^S H e^{-S}=H_0+H_1+H_2+\cdots \tag{D.31}$$

where S_n and H_n are of order n in the perturbative coupling. Moreover, performing the expansion up to a finite n yields a rotated Hamiltonian in which the block-off-diagonal terms are of order $n+1$ or higher.

We will follow a recent derivation of the transformation, given in Refs. [170, 455], that gives directly the correct result at any desired order.

D.4.1 First order corrections: PXP Hamiltonian

Let us start by separating the original $2d$ Ising Hamiltonian, Eq. (6.1), as follows:

$$H = H_{\rm Is} = \Big(-J \sum_{\langle i,j \rangle} \sigma_i^z \sigma_j^z \Big) + \Big(-g \sum_i \sigma_i^x - h \sum_i \sigma_i^z \Big) \equiv H_0 + V_1. \tag{D.32}$$

Let us also set $h = 0$ for the moment. Then, the Schrieffer-Wolff transformation amounts to the following iterative algorithm (starting from $n = 1$):

1. Split $V_n \equiv H_n + R_n$, where H_n contains only the block-diagonal terms and R_n only the block-off-diagonal ones.
2. Determine S_n from the equation
$$\big[S_n, H_0\big] + R_n = 0. \tag{D.33}$$
3. Set
$$V_{n+1} = \sum_{(k_1,\dots,k_p)\in[n+1]'} \frac{1}{p!} [S_{k_1}, [S_{k_2}, \dots, [S_{k_p}, H_0] \dots]] + \sum_{(k_1,\dots,k_p)\in[n]} \frac{1}{p!} [S_{k_1}, [S_{k_2}, \dots, [S_{k_p}, V] \dots]] \tag{D.34}$$
where the summations run over the set $[m]$ of the ordered partitions $(k_1, \dots, k_p)$ of an integer m, and $[m]'$ excludes the partition $(k_1 = m)$ with $p = 1$.

Let us apply the algorithm described above to our case, up to order $n = 2$. First of all, we identify in V_1 the block-diagonal terms:

$$\begin{aligned} H_1 = -g \sum_i \big(& P^{\uparrow}_{{\rm L}i} P^{\uparrow}_{{\rm D}i} \sigma^x_i P^{\downarrow}_{{\rm R}i} P^{\downarrow}_{{\rm U}i} + P^{\uparrow}_{{\rm L}i} P^{\downarrow}_{{\rm D}i} \sigma^x_i P^{\downarrow}_{{\rm R}i} P^{\uparrow}_{{\rm U}i} + P^{\downarrow}_{{\rm L}i} P^{\downarrow}_{{\rm D}i} \sigma^x_i P^{\uparrow}_{{\rm R}i} P^{\uparrow}_{{\rm U}i} \\ & + P^{\downarrow}_{{\rm L}i} P^{\uparrow}_{{\rm D}i} \sigma^x_i P^{\uparrow}_{{\rm R}i} P^{\downarrow}_{{\rm U}i} + P^{\uparrow}_{{\rm L}i} P^{\downarrow}_{{\rm D}i} \sigma^x_i P^{\uparrow}_{{\rm R}i} P^{\downarrow}_{{\rm U}i} + P^{\downarrow}_{{\rm L}i} P^{\uparrow}_{{\rm D}i} \sigma^x_i P^{\downarrow}_{{\rm R}i} P^{\uparrow}_{{\rm U}i} \big). \end{aligned} \tag{D.35}$$

and the block-off-diagonal terms:

$$\begin{aligned} R_1 = -g \sum_i \big(& P^{\downarrow}_{{\rm L}i} P^{\downarrow}_{{\rm D}i} \sigma^x_i P^{\downarrow}_{{\rm R}i} P^{\downarrow}_{{\rm U}i} + P^{\downarrow}_{{\rm L}i} P^{\downarrow}_{{\rm D}i} \sigma^x_i P^{\downarrow}_{{\rm R}i} P^{\uparrow}_{{\rm U}i} + P^{\downarrow}_{{\rm L}i} P^{\downarrow}_{{\rm D}i} \sigma^x_i P^{\uparrow}_{{\rm R}i} P^{\downarrow}_{{\rm U}i} \\ & + P^{\downarrow}_{{\rm L}i} P^{\uparrow}_{{\rm D}i} \sigma^x_i P^{\downarrow}_{{\rm R}i} P^{\downarrow}_{{\rm U}i} + P^{\downarrow}_{{\rm L}i} P^{\uparrow}_{{\rm D}i} \sigma^x_i P^{\uparrow}_{{\rm R}i} P^{\uparrow}_{{\rm U}i} + P^{\uparrow}_{{\rm L}i} P^{\downarrow}_{{\rm D}i} \sigma^x_i P^{\downarrow}_{{\rm R}i} P^{\downarrow}_{{\rm U}i} + P^{\uparrow}_{{\rm L}i} P^{\downarrow}_{{\rm D}i} \sigma^x_i P^{\uparrow}_{{\rm R}i} P^{\uparrow}_{{\rm U}i} \\ & + P^{\uparrow}_{{\rm L}i} P^{\uparrow}_{{\rm D}i} \sigma^x_i P^{\downarrow}_{{\rm R}i} P^{\uparrow}_{{\rm U}i} + P^{\uparrow}_{{\rm L}i} P^{\uparrow}_{{\rm D}i} \sigma^x_i P^{\uparrow}_{{\rm R}i} P^{\downarrow}_{{\rm U}i} + P^{\uparrow}_{{\rm L}i} P^{\uparrow}_{{\rm D}i} \sigma^x_i P^{\uparrow}_{{\rm R}i} P^{\uparrow}_{{\rm U}i} \big). \end{aligned} \tag{D.36}$$

In the previous equations, $P^{\uparrow}_i = (1 + \sigma^z_i)/2$, $P^{\downarrow}_i = (1 - \sigma^z_i)/2$, and ${\rm L}i/{\rm R}i/{\rm U}i/{\rm D}i$ stands for the left/right/above/below neighbour of site i, as in the main text. One easily gets convinced that the terms in H_1 couple states within each $\mathcal{H}_\ell$, since they conserve the number of domain walls; contrarily, each term in R_1 changes their number.

Then, we need to solve Eq. (D.33), specified for S_1:

$$\big[S_1, H_0\big] + R_1 = 0. \tag{D.37}$$

A bit of reasoning leads to the conclusion that one can compensate each term in R_1, of the form $P_{{\rm L}i} P_{{\rm D}i} \sigma^x_i P_{{\rm R}i} P_{{\rm U}i}$, with a term in S_1 of the form $P_{{\rm L}i} P_{{\rm D}i} \sigma^y_i P_{{\rm R}i} P_{{\rm U}i}$. Fixing the

correct signs, one finds

$$S_1 = -\frac{ig}{4J}\sum_i \Big(\frac{1}{2}P^{\downarrow}_{\mathrm{L}i}P^{\downarrow}_{\mathrm{D}i}\sigma^y_i P^{\downarrow}_{\mathrm{R}i}P^{\downarrow}_{\mathrm{U}i} + P^{\downarrow}_{\mathrm{L}i}P^{\downarrow}_{\mathrm{D}i}\sigma^y_i P^{\downarrow}_{\mathrm{R}i}P^{\uparrow}_{\mathrm{U}i} + P^{\downarrow}_{\mathrm{L}i}P^{\downarrow}_{\mathrm{D}i}\sigma^y_i P^{\uparrow}_{\mathrm{R}i}P^{\downarrow}_{\mathrm{U}i}$$
$$+ P^{\downarrow}_{\mathrm{L}i}P^{\uparrow}_{\mathrm{D}i}\sigma^y_i P^{\downarrow}_{\mathrm{R}i}P^{\downarrow}_{\mathrm{U}i} - P^{\downarrow}_{\mathrm{L}i}P^{\uparrow}_{\mathrm{D}i}\sigma^y_i P^{\uparrow}_{\mathrm{R}i}P^{\uparrow}_{\mathrm{U}i} + P^{\uparrow}_{\mathrm{L}i}P^{\downarrow}_{\mathrm{D}i}\sigma^y_i P^{\downarrow}_{\mathrm{R}i}P^{\downarrow}_{\mathrm{U}i} - P^{\uparrow}_{\mathrm{L}i}P^{\downarrow}_{\mathrm{D}i}\sigma^y_i P^{\uparrow}_{\mathrm{R}i}P^{\uparrow}_{\mathrm{U}i}$$
$$- P^{\uparrow}_{\mathrm{L}i}P^{\uparrow}_{\mathrm{D}i}\sigma^y_i P^{\downarrow}_{\mathrm{R}i}P^{\uparrow}_{\mathrm{U}i} - P^{\uparrow}_{\mathrm{L}i}P^{\uparrow}_{\mathrm{D}i}\sigma^y_i P^{\uparrow}_{\mathrm{R}i}P^{\downarrow}_{\mathrm{U}i} - \frac{1}{2}P^{\uparrow}_{\mathrm{L}i}P^{\uparrow}_{\mathrm{D}i}\sigma^y_i P^{\uparrow}_{\mathrm{R}i}P^{\uparrow}_{\mathrm{U}i}\Big). \quad \text{(D.38)}$$

Finally, applying Eq. (D.34) for $n = 2$ yields

$$V_2 = \frac{1}{2}[S_1,[S_1,H_0]] + [S_1,V_1] = -\frac{1}{2}[S_1,R_1] + [S_1,V_1]. \quad \text{(D.39)}$$

The expression above generates a plethora of terms; however, we are interested *only in the block-diagonal part* of V_2, namely H_2: indeed, the block-off-diagonal part R_2 can be removed by going to the next order in the perturbative construction. For now, we will compute only the terms in Eq. (D.39) that are *diagonal* in σ^z (thus leaving out terms involving σ^x and σ^y that are still block-diagonal). It is easy to spot them, since they come from commuting σ^x_i in R_1,V_1 with σ^y_i in S_1, while leaving the projectors untouched (and therefore the 4 projectors around i have to be the same both in R_1,V_1 and S_1). With a bit of patience, one may work out all the details, to find

$$[H_2]_{\mathrm{diag}} = \frac{g^2}{4J}\sum_i \Big(\frac{1}{2}P^{\downarrow}_{\mathrm{L}i}P^{\downarrow}_{\mathrm{D}i}\sigma^z_i P^{\downarrow}_{\mathrm{R}i}P^{\downarrow}_{\mathrm{U}i} + P^{\downarrow}_{\mathrm{L}i}P^{\downarrow}_{\mathrm{D}i}\sigma^z_i P^{\downarrow}_{\mathrm{R}i}P^{\uparrow}_{\mathrm{U}i} + P^{\downarrow}_{\mathrm{L}i}P^{\downarrow}_{\mathrm{D}i}\sigma^z_i P^{\uparrow}_{\mathrm{R}i}P^{\downarrow}_{\mathrm{U}i}$$
$$+ P^{\downarrow}_{\mathrm{L}i}P^{\uparrow}_{\mathrm{D}i}\sigma^z_i P^{\downarrow}_{\mathrm{R}i}P^{\downarrow}_{\mathrm{U}i} - P^{\downarrow}_{\mathrm{L}i}P^{\uparrow}_{\mathrm{D}i}\sigma^z_i P^{\uparrow}_{\mathrm{R}i}P^{\uparrow}_{\mathrm{U}i} + P^{\uparrow}_{\mathrm{L}i}P^{\downarrow}_{\mathrm{D}i}\sigma^z_i P^{\downarrow}_{\mathrm{R}i}P^{\downarrow}_{\mathrm{U}i} - P^{\uparrow}_{\mathrm{L}i}P^{\downarrow}_{\mathrm{D}i}\sigma^z_i P^{\uparrow}_{\mathrm{R}i}P^{\uparrow}_{\mathrm{U}i}$$
$$- P^{\uparrow}_{\mathrm{L}i}P^{\uparrow}_{\mathrm{D}i}\sigma^z_i P^{\downarrow}_{\mathrm{R}i}P^{\uparrow}_{\mathrm{U}i} - P^{\uparrow}_{\mathrm{L}i}P^{\uparrow}_{\mathrm{D}i}\sigma^z_i P^{\uparrow}_{\mathrm{R}i}P^{\downarrow}_{\mathrm{U}i} - \frac{1}{2}P^{\uparrow}_{\mathrm{L}i}P^{\uparrow}_{\mathrm{D}i}\sigma^z_i P^{\uparrow}_{\mathrm{R}i}P^{\uparrow}_{\mathrm{U}i}\Big). \quad \text{(D.40)}$$

D.4.2 First order corrections: corner Hamiltonian

Now we specify the results of the previous section to the sector within $\mathcal{H}_\ell$ that is dynamically connected to the corner considered in the main text, i.e. we restrict our attention to the Young diagrams subspace $\mathcal{H}_{\mathrm{Y}}$. In the previous section we have already determined the diagonal part of the second order correction H_2, see Eq. (D.40). We just need to determine the off-diagonal (but block-diagonal) part. With a bit of reasoning, one may get convinced that the only allowed moves in 2nd order perturbation theory, that bring a state out of $\mathcal{H}_{\mathrm{Y}}$ and then back in, are the ones in Fig. D.1. Correspondingly, the Schrieffer-Wolff Hamiltonian reads

$$H_{2,\mathrm{Y}} = [H_2]_{\mathrm{diag}} - \frac{g^2}{4J}\sum_i \Big[P^{\uparrow}_{\mathrm{L}i}P^{\uparrow}_{\mathrm{LU}i}P^{\uparrow}_{\mathrm{UU}i}\big(\sigma^+_i\sigma^+_{\mathrm{U}i} + \sigma^-_i\sigma^-_{\mathrm{U}i}\big)P^{\downarrow}_{\mathrm{R}i}P^{\downarrow}_{\mathrm{RU}i}P^{\downarrow}_{\mathrm{D}i}$$
$$+ P^{\uparrow}_{\mathrm{L}i}P^{\uparrow}_{\mathrm{U}i}P^{\uparrow}_{\mathrm{RU}i}\big(\sigma^+_i\sigma^+_{\mathrm{R}i} + \sigma^-_i\sigma^-_{\mathrm{R}i}\big)P^{\downarrow}_{\mathrm{D}i}P^{\downarrow}_{\mathrm{RD}i}P^{\downarrow}_{\mathrm{RR}i}\Big]. \quad \text{(D.41)}$$

The factor in front of the sum is fixed by a careful use of Eq. (D.39).

Now that we have the Hamiltonian in $2d$, we can express it in the $1d$ language of fermions. Before, however, it is convenient to expand all the projectors $P^{\uparrow,\downarrow}$ in terms

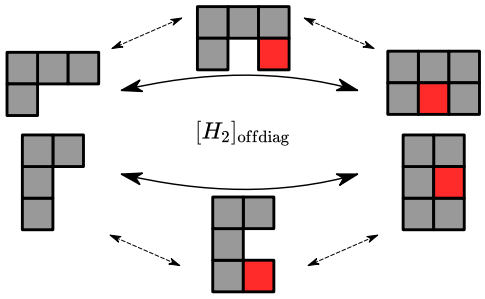

FIGURE D.1: Graphical representation of the off-diagonal part of $H_{2,Y}$, corresponding to a next-to-nearest neighbors hopping (see Eq. (D.40)), constrained to Young diagrams configurations.

of σ^z: one finds

$$[H_2]_{\text{diag}} = -\frac{5g^2}{64J}\sum_i \left(\sigma^z_{Li}\sigma^z_i + \sigma^z_i\sigma^z_{Ri} + \sigma^z_i\sigma^z_{Ui} + \sigma^z_{Di}\sigma^z_i\right) + \frac{3g^2}{64J}\sum_i \left(\sigma^z_{Li}\sigma^z_{Di}\sigma^z_i\sigma^z_{Ri} + \sigma^z_{Li}\sigma^z_{Di}\sigma^z_i\sigma^z_{Ui} + \sigma^z_{Di}\sigma^z_i\sigma^z_{Ri}\sigma^z_{Ui} + \sigma^z_{Li}\sigma^z_i\sigma^z_{Ri}\sigma^z_{Ui}\right). \quad \text{(D.42)}$$

The term with only two Pauli matrices gives a constant contribution on the Young diagram states, since it counts the number of horizontal and vertical frustrated bonds (it is a Lamb shift constant in the whole sector $\mathcal{H}_\ell$). The term with four spins instead can be represented, up to a term constant in the subspace $\mathcal{H}_Y$, by an operator that counts the number of corners in each diagram. Therefore, in the hard-core boson language one finds the Hamiltonian

$$H_{2,B} = -\frac{g^2}{4J}\sum_x \left(S^+_x S^-_{x+2} + S^-_x S^+_{x+2} + 3S^3_x S^3_{x+1}\right). \quad \text{(D.43)}$$

By means of a Jordan-Wigner transformation, one gets a fermionized version of the latter (see also Eq. (6.16)):

$$H_{2,F} = -\frac{g^2}{4J}\sum_x \left(\psi^\dagger_x e^{-i\pi n_{x+1}}\psi_{x+2} + \text{h.c.} + 3n_x n_{x+1}\right) \quad \text{(D.44)}$$

$$= -\frac{g^2}{4J}\sum_x \left(\psi^\dagger_x\psi_{x+2} + \text{h.c.}\right) + \frac{g^2}{4J}\sum_x \left(2\psi^\dagger_x\psi^\dagger_{x+1}\psi_{x+1}\psi_{x+2} + \text{h.c.} - 3\psi^\dagger_x\psi_x\psi^\dagger_{x+1}\psi_{x+1}\right), \quad \text{(D.45)}$$

where the first term is a correction to the kinetic energy and the second a four-fermions interaction.

D.5 Participation ratio and localization length

In this section we compute the (inverse) participation ratio, from which one can easily derive the localization length of the eigenfunctions. By definition

$$\text{IPR} = \sum_k J^4_k(\gamma) = \frac{1}{\pi}\int_0^\pi d\theta J^2_0(\gamma\sqrt{2-2\cos\theta}), \quad \text{(D.46)}$$

where we used both the Neumann's addition theorem to write the sum as an integral and the explicit form of the eigenfunctions. With a change of variables, the integral can be cast in the form

$$\text{IPR} = \frac{2}{\pi}\int_0^1 dx \frac{J_0^2(2\gamma x)}{\sqrt{1-x^2}} = {}_2F_3\left(\frac{1}{2},\frac{1}{2};1,1,1;-4\gamma^2\right). \tag{D.47}$$

At this stage one can take the asymptotic expansion of the hypergeometric function, and for large γ the (non-oscillating part of the) IPR is

$$\text{IPR} = \frac{2\gamma_E + 5\log 4 + \log\gamma^2}{2\pi^2\gamma} + \frac{3-\gamma_E-\log(32\gamma)}{64\pi\gamma^3} + O\left(\frac{1}{\gamma^5}\right) \tag{D.48}$$

being γ_E the Euler constant. Since the localization length of the eigenfunctions is roughly $\xi \approx 1/\text{IPR}$,

$$\xi \sim \frac{2\pi^2\gamma}{2\gamma_E + 5\log 4 + \log\gamma^2}. \tag{D.49}$$

Alternatively, one can also determine the asymptotic expansion for the IPR directly from the integral, using the Mellin transform. In particular, it holds

$$\int_0^\infty f_1(x)f_2(x)dx = \frac{1}{2\pi i}\int_{c-i\infty}^{c+i\infty}\tilde{f}_1(1-s)\tilde{f}_2(s)ds, \tag{D.50}$$

being, in our case, $f_1(x) = \frac{1}{\sqrt{1-x^2}}$ (for $x < 1$, $f_1(x) \equiv 0$ otherwise) and $f_2(x) = J_0^2(2\gamma x)$. One gets then

$$\tilde{f}_1(s) = \frac{\sqrt{\pi}}{2}\frac{\Gamma\left(\frac{s}{2}\right)}{\Gamma\left(\frac{1+s}{2}\right)}, \qquad \tilde{f}_2(s) = \frac{1}{(2\gamma)^s}\frac{\Gamma\left(\frac{1-s}{2}\right)\Gamma\left(\frac{s}{2}\right)}{2\sqrt{\pi}\Gamma\left(1-\frac{s}{2}\right)^2}. \tag{D.51}$$

Therefore, we obtain the alternative form

$$\text{IPR} = \frac{1}{2\pi i}\int_{c-i\infty}^{c+i\infty} ds \frac{1}{2\pi}\frac{1}{(2\gamma)^s}\frac{\Gamma\left(\frac{1-s}{2}\right)^2\Gamma\left(\frac{s}{2}\right)}{\Gamma\left(1-\frac{s}{2}\right)^3} \equiv \frac{1}{2\pi i}\int_{c-i\infty}^{c+i\infty} ds\, \mathcal{F}(s). \tag{D.52}$$

The poles structure of the Γ-function sets $c \in (0,1)$. To compute the integral, one can move the Bromwich path towards increasing values of $\text{Re}(s)$; this way one has to go around the poles of the integrand, which are double poles located on the odd integer numbers, and use the residue theorem to compute their contribution to the integral. As an example, we report the residue at $s = 1$, for other values of s the computation is analogous. By definition one has

$$\text{Res}\left[\mathcal{F}(s), s=1\right] = \frac{d}{ds}\left[(s-1)^2\frac{1}{2\pi}\frac{1}{(2\gamma)^s}\frac{\Gamma\left(\frac{1-s}{2}\right)^2\Gamma\left(\frac{s}{2}\right)}{\Gamma\left(1-\frac{s}{2}\right)^3}\right]\Bigg|_{s=1}. \tag{D.53}$$

Expanding around $s = 1$ one has $(s-1)^2\Gamma\left(\frac{1-s}{2}\right) = 4(1+\gamma_E(s-1)) + O(s-1)^2$, from which it follows

$$\text{Res}\left[\mathcal{F}(s), s=1\right] = -\frac{2\gamma_E + 5\log 4 + \log\gamma^2}{2\pi^2\gamma} \tag{D.54}$$

Applying the residue theorem, one obtains a $2\pi i$ factor that cancels the one in front

of Eq. (D.52) and a minus sign given by the index of the contour, which is clockwise, obtaining the first term of Eq. (D.48). The other terms are obtained with the residues of the other poles. In general, from the dependence $1/\gamma^s$ in the integral, one can see that the residue of the pole at $s = 2n + 1$ gives the order $1/\gamma^{2n+1}$ of the asymptotic expansion. In this way, one obtains the same result as in Eq. (D.48) from the asymptotic expansion of the hypergeometric function. Notice that the residues of the poles give only the power series contribution to the whole integral. There is a bounded oscillating term missing, that comes from the remaining part of integral on the Bromwich path.

D.6 Useful properties of the Bessel functions

We collect here a series of useful properties of Bessel functions that are widely used in the main text, giving also a sketch of their proof. Many of these properties can be found in [457, 512]. One of the equivalent definitions for the Bessel function of the first kind is in terms of the integral:

$$J_n(\gamma) = \frac{1}{2\pi}\int_{-\pi}^{\pi} d\tau\, e^{i(n\tau - \gamma\sin\tau)}. \tag{D.55}$$

From this definition it follows immediately that

$$\sum_{n=-\infty}^{\infty} J_n(x) = 1 \tag{D.56}$$

and, for $n \in \mathbb{Z}$

$$J_{-n}(\gamma) = (-1)^n J_n(\gamma). \tag{D.57}$$

Using again the definition, we can compute

$$\sum_{n=-\infty}^{\infty} J_{x-n}(\gamma)J_{y-n}(\gamma)e^{-2ithn}$$

$$= \sum_{n=-\infty}^{\infty} \frac{1}{(2\pi)^2}\int_{-\pi}^{\pi} d\tau\, d\tau'\, e^{i((x-n)\tau-\gamma\sin\tau)}e^{i((y-n)\tau'-\gamma\sin\tau')}e^{-2ithn} \tag{D.58}$$

$$= \frac{e^{-2iyht}}{2\pi}\int_{-\pi}^{\pi} d\tau\, e^{i[(x-y)\tau-\gamma(\sin\tau-\sin(\tau+2ht))]} \tag{D.59}$$

$$= \frac{e^{-i(x+y)ht}}{2\pi}\int_{-\pi}^{\pi} d\tau\, e^{i[(x-y)\tau+2\gamma\sin ht\cos\tau]} \tag{D.60}$$

$$= e^{-i(x+y)ht}\, i^{x-y}\, J_{x-y}(2\gamma\sin(ht)) \tag{D.61}$$

where we used $\sum_{n=-\infty}^{\infty} e^{inx} = 2\pi\delta(x + 2k\pi)$. Setting $t = 0$ we obtain the completeness relation

$$\sum_{n=-\infty}^{\infty} J_{n-m}(\gamma)J_{n-k}(\gamma) = \delta_{mk}, \tag{D.62}$$

that also leads immediately to

$$\sum_{n=-\infty}^{\infty} J_n^2(\gamma) = 1. \tag{D.63}$$

If the sums of the previous equation is restricted to positive integer values, using telescopic sums one obtains

$$\sum_{j=1}^{\infty} J_{j+m}(\gamma)J_{j+n}(\gamma) = \frac{\gamma[J_m(\gamma)J_{n+1}(\gamma) - J_{m+1}(\gamma)J_n(\gamma)]}{2(m-n)}, \tag{D.64}$$

that reduces to

$$\sum_{j=0}^{\infty} J_{j+n}^2(\gamma) = \frac{\gamma}{2}\left[J_n(\gamma)\partial_n J_{n-1}(\gamma) - J_{n-1}(\gamma)\partial_n J_n(\gamma)\right] \tag{D.65}$$

when the limit $m \to n$ is taken. Using the same procedure as in Eq. (D.58) we can compute also

$$\sum_{k\in\mathbb{Z}} J_{mk-x}^2(\gamma) = \frac{1}{m}\sum_{0\le n<m} e^{2ixn\pi/m} J_0\left(2\gamma \sin\frac{n\pi}{m}\right). \tag{D.66}$$

Another very useful tool is the asymptotic expansion of the Bessel functions for large order and argument. For fixed γ and $x \to \infty$

$$J_x(\gamma) \sim \frac{1}{\sqrt{2\pi x}}\left(\frac{e\gamma}{2x}\right)^x, \tag{D.67}$$

i.e. the Bessel functions decay more than exponentially fast for $x \gg \gamma$. Instead, in the limit $\gamma \to \infty$ with fixed x we have, at leading order

$$J_x(\gamma) \sim \sqrt{\frac{2}{\pi\gamma}}\cos\left(\gamma - \frac{\pi}{2}x - \frac{\pi}{4}\right) \tag{D.68}$$

If both the order and the argument of the Bessel function diverge, the asymptotic expansion is different if the argument is larger than the order or vice versa: at leading order

$$J_x(x\,\mathrm{sech}\,\alpha) \sim \frac{e^{x(\tanh\alpha-\alpha)}}{\sqrt{2\pi x\tanh\alpha}}, \qquad \mathrm{sech}\,\alpha < 1, \tag{D.69}$$

$$J_x(x\sec\beta) \sim \sqrt{\frac{2}{\pi x\tan\beta}}\cos\left(x(\tan\beta-\beta) - \frac{\pi}{4}\right), \qquad \sec\beta > 1, \tag{D.70}$$

from which we notice the strong similarity between Eqs. (D.67)–(D.69) and Eqs. (D.68)–(D.70).

E Addendum to Chapter 7

In this Appendix, I give some additional details for the optimal control problem of the spin qubit. In Sec. E.1 I report the derivation of the sensitivity, while in Sec. E.2 the experimental platform is described in detail. In Sec. E.3 I report some additional test cases that validate our procedure.

E.1 Definition of the sensitivity

The sensitivity η introduced in Eq. (7.4) represents the minimum detectable signal for unit time in our experimental platform. To justify this statement, here we sketch a brief derivation using both a direct approach, and a more formal one through the Fisher information.

First, let us define η as the signal strength yielding a signal-to-noise ratio SRN $=$ 1 for a total experiment time of 1 s. Following Ref. [40], the SNR for N independent experiments can be defined as

$$\text{SNR} = \frac{\delta P(T,b)}{\sigma_N}, \tag{E.1}$$

where σ_N encompasses all the sources of error, and $\delta P(T,b)$ is the spin population difference between the cases with and without target signal: $\delta P(T,b) = P(T,b) - P(T,0)$. Now, the error can be shown to be of the form $\sigma_N \approx C^{-1}/\sqrt{N}$, with a dimensionless constant $C = O(1)$ depending on the experimental platform [40]. Also, using Eq. (7.1), and assuming slope detection, one easily gets to

$$\delta P(T,b) \approx e^{-\chi(T)} \left| \sin\left(\varphi(T,b)\right) \frac{\partial \varphi(T,b)}{\partial b} b \right| = e^{-\chi(T)} |\varphi(T,b)|. \tag{E.2}$$

Thus, imposing SNR $\equiv 1$ one finds

$$1 = e^{-\chi(T)} |\varphi(T,b)| \frac{1}{C\sqrt{N}} \tag{E.3}$$

and finally, using that one performs N experiments in 1 s in total,

$$\eta = \frac{e^{\chi(T)}}{|\varphi(T)/b|} \sqrt{T}, \tag{E.4}$$

with T being the time for a single experiment, and C set to unity. This is exactly Eq. (7.4).

As anticipated above, the sensitivity can be defined also through the Fisher information and the Cramér-Rao bound. Specifically, we define η to be the minimum signal that can be distinguished from 0 in a total time of 1 s. Assuming that our

estimator of the magnetic field b is unbiased, from the Cramér-Rao bound it must be

$$\Delta b \geq \frac{1}{\sqrt{F_N}}, \tag{E.5}$$

where F_N is the Fisher information associated with N measurements of the magnetic field strength b from an estimator x [500, 513]:

$$F_N = \sum_x \frac{1}{p_N(x|b)} \left(\frac{\partial p_N(x|b)}{\partial b} \right)^2. \tag{E.6}$$

In our case, since we detect the $|\pm\rangle$ states in a Ramsey interferometry experiment, it holds $p(\pm|b) = \mathrm{Tr}(\rho\,|\pm\rangle\,\langle\pm|)$ with

$$\rho = \begin{pmatrix} 1/2 & e^{-\chi(T)-i\varphi(T,b)/2}/2 \\ e^{-\chi(T)+i\varphi(T,b)/2}/2 & 1/2 \end{pmatrix}, \tag{E.7}$$

and thus

$$F = \frac{8\varphi^2(T,b)}{b^2} \frac{e^{-2\chi(T)} \sin^2 \varphi(T,b)}{1 - e^{-2\chi(T)} \cos^2 \varphi(T,b)}. \tag{E.8}$$

Assuming slope detection, and for N repeated measurements,

$$F_N = N \frac{8\varphi^2(T,b) e^{-2\chi(T)}}{b^2}, \tag{E.9}$$

since the Fisher information is additive for independent trials. At this point, recalling that the N experiments have to be done in a total time of 1 s, and using the Cramér-Rao bound Eq. (E.5), one easily gets to Eq. (E.4), that is Eq. (7.4).

E.2 Details on the experimental platform

The ground state of an NV center is a spin triplet $S = 1$, naturally suited for sensing magnetic fields via Zeeman effect. The NV electronic spin presents extremely long coherence times, of the order of milliseconds at room temperature [487], due to the protective environment provided by the diamond itself. The $S = 1$ electronic spin can be initialized into the $m_S = 0$ state by addressing the NV center with green light (532 nm). This is due to an excitation–decay process involving radiative (637 nm) and non-radiative decay routes, occurring with a probability that depends on the spin projection m_S. This same mechanism implies that the red photoluminescence intensity of the $m_S = 0$ state is higher than the one of $m_S = \pm 1$, hence enabling to optically readout the state of the system. In addition, the internal structure of the NV center removes the degeneracy between the $m_S = \pm 1$ states and the $m_S = 0$ state, imposing a zero-field-splitting of $D_g \simeq 2.87$ GHz. An external bias field, aligned with the spin quantization axis, removes the degeneracy between the $m_S = \pm 1$ states, allowing to individually address the $m_S = 0 \leftrightarrow m_S = +1$ transition using on-resonance microwave radiation. By using microwave pulses with a appropriate duration, amplitude and phase, it is possible to apply any kind of gate to the single two level system. Therefore, the two level system formed by the $m_S = 0$ ($|0\rangle$) and $m_S = +1$ ($|1\rangle$) states fulfills the requirements to be used as a qubit based magnetometer.

E.2.1 Characterization of the amplitude of the target signal

The target signal is delivered via a signal radio-frequency (RF) generator connected to the same wire, placed close to the diamond, that delivers the MW control field. We can control the amplitude of the target field by changing the output amplitude of the RF generator. However, the absolute value of the amplitude of the target field b has to be characterized in order to take into account the attenuation of the circuit, the emission efficacy of the wire (which depends on the RF frequency) and the distance between the wire and the NV defect. To achieve such characterization, as explained in Chap. 7, we measure the spin dynamics for a CP sequence as a function of the sequence interpulse time, and we compare with the simulation to minimize the residuals using b as the only free parameter. By performing this measurements for different values of the RF generator output amplitude a_{RF}, we can extract a relation between a_{RF} (in [Vpp]) and the amplitude of the target magnetic field b (in [T]).

E.3 Additional test cases

In order to reinforce our results, we repeated the analysis presented in Chap. 7.3 for two different target signals. A monochromatic target signal that coincides with one of the NSD harmonics, and a 7-chromatic target signal that accentuates the difference between the generalized CP and the optimal solution.

E.3.1 Monochromatic target signal

If we want to detect a monochromatic target signal $b(t)$, in most cases a Carr-Purcell CP sequence of equidistant pulses is the best way to increase the sensor's response to that target signal and filter out the noise. This is due to the quasi-monochromatic filter function associated with a CP sequence. Assuming that τ is the time between pulses, the filter function shows a peak centered at $\omega/2\pi = \frac{1}{2\tau}$. However, the filter function is not exactly monochromatic, it shows harmonics at $\omega/2\pi = \frac{1}{2(2\ell+1)\tau}$, with $\ell \in \{1, 2, ...\}$. Therefore, if the frequency associated with $b(t)$ is close to $\omega_{\mathrm{L}}/(2\ell+1)$, then a CP sequence will amplify the effect of both, the target signal and the noise, leading to not-optimal sensitivities.

Here we used the optimization algorithm described in Sec. 7.2.2 in order to obtain optimal sequences for this problem. In particular, we explored the case of a monochromatic signal with frequency $\nu_{\mathrm{mono}} = 39.29$ kHz, which is close enough to $\nu_{\mathrm{L}}/11$ so that the 5-th harmonic of the CP sequence coincides with the noise components. We used the same NSD $S(\omega)$ as in the three-chromatic case. The experimental values of $1/\eta$ are obtained from the measurement of $P(T, b)$ as a function of b. The results of $P(T, b)$ for one value of the sensing time T are shown in Fig. E.1a. The predicted values of the inverse sensitivity, together with their experimental values are shown in Fig. E.1b. Similarly to the case detailed in 7.3.1, the optimal sequences improve the sensitivity of the quantum sensor, resulting in some cases to an inverse sensitivity that is close to a twice the one from the CP sequence. In the monochromatic case explored here, the sensitivity gets worse when increasing the sensing time beyond 100 μs. Instead the optimal solutions are able to improve the sensitivity even for times $T > 300$ μs. For $T \simeq 100$ μs, and longer sensing times, the optimized sequences achieve higher values of $1/\eta$ than the maximum value achieved by a CP sequence.

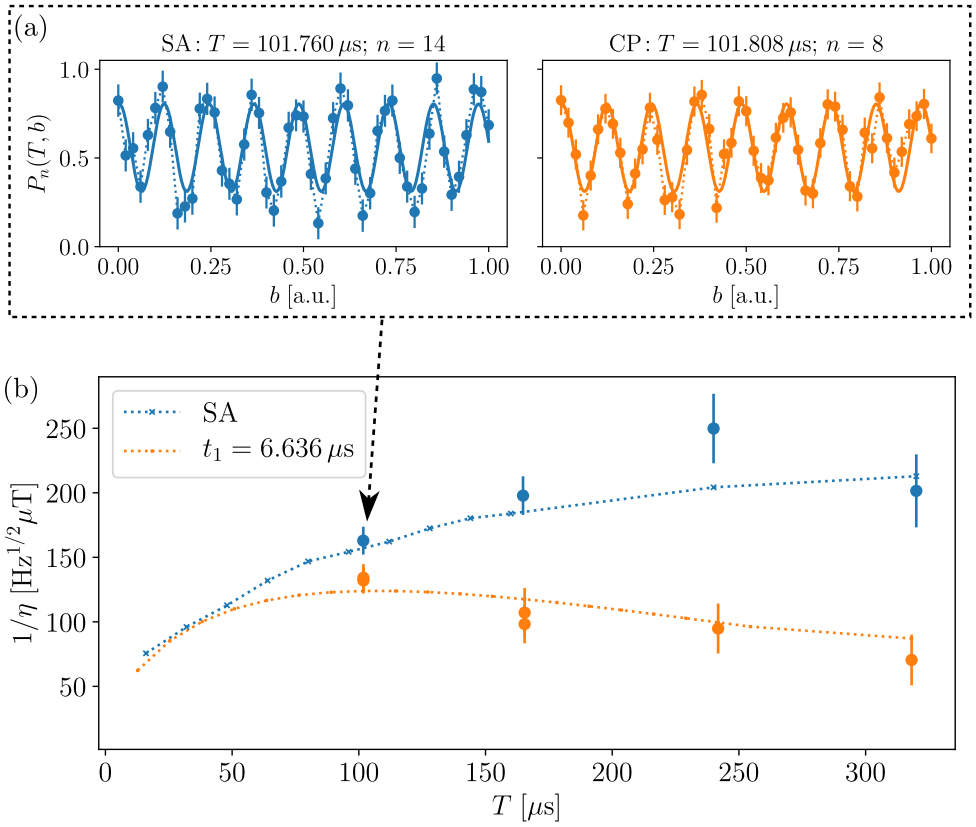

FIGURE E.1: Results for the case of a monochromatic target signal. (a) Probability to remain in the state $|1\rangle$ as a function of b, for fixed sensing times T for an optimal DD sequence (blue), and for a CP sequence (orange). The values of the sensing time and of the number of pulses for both sequences are shown as titles of the plots. A cosine function is fitted (solid lines) to the experimental data (bullets with errorbars) in order to obtain $1/\eta$. (b) Inverse sensitivity as a function of the sensing time T. Blue data corresponds to the optimized sequences obtained with simulated annealing (SA). Orange data corresponds to the CP sequences with $\tau = 12.726\,\mu$s. We found a good agreement between the predicted values (dotted lines) and the experimental values (bullets with errorbars). This figure is taken from Ref. [5].

(a)

i	A_i	ν_i [MHz]	c_i
0	0.213919	0.420068	2.248311
1	0.130194	0.564180	0.451269
2	0.141141	0.226517	2.531370
3	0.031116	0.900518	2.715790
4	0.050013	0.756436	0.265970
5	0.320765	0.286164	5.786594
6	0.112853	0.366105	1.622823

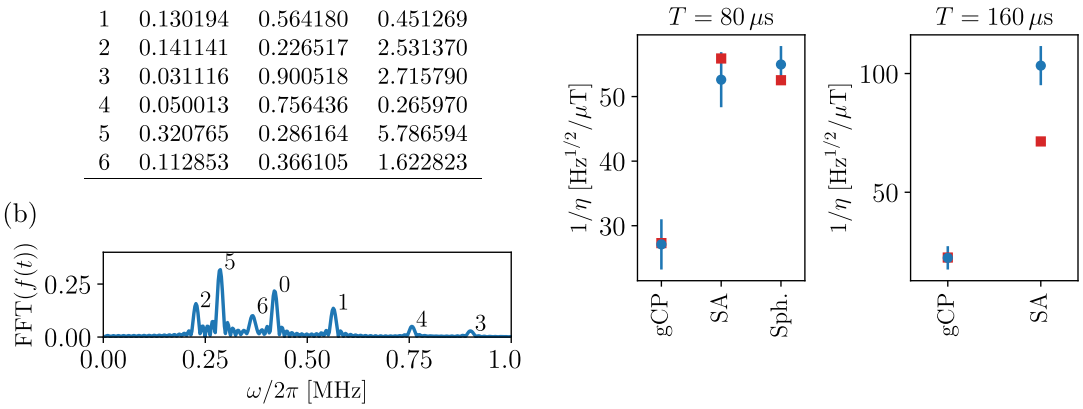

FIGURE E.2: Results for the case of a target signal with seven frequency components. (a) Table to indicate the amplitude, frequency and phase of each component of the target signal $f(t) = \sum_{i=0}^{6} A_i \cos(2\pi\nu_i t + c_i)$. (b) Fast Fourier transform (FFT) of the target signal. (c) Inverse sensitivity for $T = 80$ μs and 160 μs. The predicted values (squares) and the experimental values (bullets with errorbars) show that the sequences obtained from the spherical solution (Sph.) or from the simulated annealing solution (SA) result in an improved sensitivity with respect to the generalized CP (gCP) sequences. This figure is taken from Ref. [5].

E.3.2 7-chromatic target signal

We have explored the case of a target signal with 7 frequency components, as specified in Figs. E.2a–E.2b. As in Chap. 7, we used the optimization algorithm either to find the approximated spherical solution, or the solution using simulated annealing (SA) in order to minimize the sensitivity. The predicted values of the inverse sensitivity, together with their experimental values are shown in Fig. E.2c. Similarly to the previous test cases, the optimal sequences improve the sensitivity of our quantum sensor. In this case, the sensitivity obtained with the optimal solutions almost $1/2$, and $1/3$ with respect to the generalized CP (gCP) sequence for $T = 80$ μs, and $T = 160$ μs, respectively.

Bibliography

[1] C. Artiaco, F. Balducci, G. Parisi, and A. Scardicchio, "Quantum jamming: Critical properties of a quantum mechanical perceptron", Phys. Rev. A **103**, L040203 (2021).

[2] C. Artiaco, F. Balducci, and A. Scardicchio, "Signatures of many-body localization in the dynamics of two-level systems in glasses", Phys. Rev. B **103**, 214205 (2021).

[3] C. Arezzo, F. Balducci, R. Piergallini, A. Scardicchio, and C. Vanoni, "Localization in the Discrete Non-linear Schrödinger Equation and Geometric Properties of the Microcanonical Surface", J. Stat. Phys. **186**, 24 (2022).

[4] C. Artiaco, F. Balducci, M. Heyl, A. Russomanno, and A. Scardicchio, "Spatiotemporal heterogeneity of entanglement in many-body localized systems", Phys. Rev. B **105**, 184202 (2022).

[5] S. Hernández-Gómez, F. Balducci, G. Fasiolo, P. Cappellaro, N. Fabbri, and A. Scardicchio, "Optimal control of a quantum sensor: A fast algorithm based on an analytic solution", arXiv:2112.14998 (2021).

[6] F. Balducci, A. Gambassi, A. Lerose, A. Scardicchio, and C. Vanoni, "Localization and melting of interfaces in the two-dimensional quantum ising model", Phys. Rev. Lett. **129**, 120601 (2022).

[7] S. Hernández-Gómez, F. Balducci, P. Cappellaro, A. Scardicchio, and N. Fabbri, "Optimal quantum control of a spin qubit in diamond for biosensing", in Proceedings of the 2022 IEEE International Workshop on Metrology for Industry 4.0 & IoT (2022), pp. 115–120.

[8] F. Balducci, A. Scardicchio, and C. Vanoni, "Slow melting of a disordered quantum crystal", arXiv:2207.11246 (2022).

[9] C. Artiaco and F. Balducci, "Slow thermalization of strongly-coupled two-level systems in glasses", (to be published).

[10] F. Balducci, A. Gambassi, A. Lerose, A. Scardicchio, and C. Vanoni, "Interface dynamics in the two-dimensional quantum Ising model", (to be published).

[11] E. Fermi, "Dimostrazione che in generale un sistema meccanico normale è quasi-ergodico", Il Nuovo Cimento **25**, 267–269 (1923).

[12] G. D. Birkhoff, "Proof of the Ergodic Theorem", Proc. Natl. Acad. Sci. USA **17**, 656–660 (1931).

[13] J. von Neumann, "Proof of the Quasi-Ergodic Hypothesis", Proc. Natl. Acad. Sci. USA **18**, 70–82 (1932).

[14] E. Fermi, J. Pasta, and S. Ulam, "Studies of Nonlinear Problems", Los Alamos Natl. Lab. Rep. No. LA-1940 (1955).

[15] A. Das, "Integrable Models" (World Scientific, Singapore, 1989).

[16] V. E. Korepin, N. M. Bogoliubov, and A. G. Izergin, "Quantum Inverse Scattering Method and Correlation Functions" (Cambridge University Press, 1993).

[17] O. Babelon, D. Bernard, and M. Talon, "Introduction to Classical Integrable Systems" (Cambridge University Press, 2003).

[18] A. N. Kolmogorov, "On the Conservation of Conditionally Periodic Motions under Small Perturbation of the Hamiltonian (*in Russian*)", Dokl. Akad. Nauk SSR **98** (1954).

[19] J. Moser, "On invariant curves of area-preserving mappings of an annulus", Nachr. Akad. Wiss. Göttingen Math.-Phys. Kl. **2**, 1–20 (1962).

[20] V. I. Arnol'd, "Proof of a Theorem of A. N. Kolmogorov on the Invariance of Quasi-Periodic Motions Under Small Perturbations of the Hamiltonian", Russ. Math. Surv. **18**, 9–36 (1963).

[21] P. Castiglione, M. Falcioni, A. Lesne, and A. Vulpiani, "Chaos and Coarse Graining in Statistical Mechanics" (Cambridge University Press, 2008).

[22] A. J. Lichtenberg and M. A. Lieberman, "Regular and chaotic dynamics", Vol. 38 (Springer, New York, 2013).

[23] M. V. Berry and M. Tabor, "Level Clustering in the Regular Spectrum", Proc. R. Soc. London A **356**, 375–394 (1977).

[24] J. M. Deutsch, "Quantum statistical mechanics in a closed system", Phys. Rev. A **43**, 2046–2049 (1991).

[25] M. Srednicki, "Chaos and quantum thermalization", Phys. Rev. E **50**, 888–901 (1994).

[26] L. D'Alessio, Y. Kafri, A. Polkovnikov, and M. Rigol, "From quantum chaos and eigenstate thermalization to statistical mechanics and thermodynamics", Adv. Phys. **65**, 239–362 (2016).

[27] D. Leibfried, R. Blatt, C. Monroe, and D. Wineland, "Quantum dynamics of single trapped ions", Rev. Mod. Phys. **75**, 281–324 (2003).

[28] F. Jelezko and J. Wrachtrup, "Single defect centres in diamond: A review", Phys. Status Solidi **203**, 3207–3225 (2006).

[29] I. Bloch, J. Dalibard, and W. Zwerger, "Many-body physics with ultracold gases", Rev. Mod. Phys. **80**, 885–964 (2008).

[30] M. Devoret, B. Huard, R. Schoelkopf, and L. F. Cugliandolo, eds., "Quantum Machines: Measurement and Control of Engineered Quantum Systems: Lecture Notes of the Les Houches Summer School: Volume 96, July 2011" (Oxford University Press, 2014).

[31] R. Schirhagl, K. Chang, M. Loretz, and C. L. Degen, "Nitrogen-Vacancy Centers in Diamond: Nanoscale Sensors for Physics and Biology", Annu. Rev. Phys. Chem. **65**, 83–105 (2014).

[32] H. Bernien et al., "Probing many-body dynamics on a 51-atom quantum simulator", Nature **551**, 579–584 (2017).

[33] A. Browaeys and T. Lahaye, "Many-body physics with individually controlled Rydberg atoms", Nature Physics **16**, 132–142 (2020).

[34] J. P. Dowling and G. J. Milburn, "Quantum technology: the second quantum revolution", Philos. Trans. R. Soc. A **361**, 1655–1674 (2003).

[35] J. Preskill, "Quantum Computing in the NISQ era and beyond", Quantum **2**, 79 (2018).

[36] M. A. Nielsen and I. L. Chuang, "Quantum Computation and Quantum Information" (Cambridge University Press, 2010).

[37] H. Häffner, C. Roos, and R. Blatt, "Quantum computing with trapped ions", Phys. Rep. **469**, 155–203 (2008).

[38] C. D. Bruzewicz, J. Chiaverini, R. McConnell, and J. M. Sage, "Trapped-ion quantum computing: Progress and challenges", Appl. Phys. Rev. **6**, 021314 (2019).

[39] P. Jurcevic et al., "Demonstration of quantum volume 64 on a superconducting quantum computing system", Quantum Sci. Tech. **6**, 025020 (2021).

[40] C. L. Degen, F. Reinhard, and P. Cappellaro, "Quantum sensing", Rev. Mod. Phys. **89**, 035002 (2017).

[41] I. Buluta and F. Nori, "Quantum Simulators", Science **326**, 108–111 (2009).

[42] R. Blatt and C. F. Roos, "Quantum simulations with trapped ions", Nat. Phys. **8**, 277–284 (2012).

[43] I. M. Georgescu, S. Ashhab, and F. Nori, "Quantum simulation", Rev. Mod. Phys. **86**, 153–185 (2014).

[44] A. J. Daley, I. Bloch, C. Kokail, S. Flannigan, N. Pearson, M. Troyer, and P. Zoller, "Practical quantum advantage in quantum simulation", Nature **607**, 667–676 (2022).

[45] I. V. Gornyi, A. D. Mirlin, and D. G. Polyakov, "Interacting Electrons in Disordered Wires: Anderson Localization and Low-T Transport", Phys. Rev. Lett. **95**, 206603 (2005).

[46] D. M. Basko, I. L. Aleiner, and B. L. Altshuler, "Metal–insulator transition in a weakly interacting many-electron system with localized single-particle states", Ann. Phys. (Amsterdam) **321**, 1126 (2006).

[47] V. Oganesyan and D. A. Huse, "Localization of interacting fermions at high temperature", Phys. Rev. B **75**, 155111 (2007).

[48] M. Žnidarič, T. Prosen, and P. Prelovšek, "Many-body localization in the Heisenberg XXZ magnet in a random field", Phys. Rev. B **77**, 064426 (2008).

[49] A. Pal and D. A. Huse, "Many-body localization phase transition", Phys. Rev. B **82**, 174411 (2010).

[50] D. A. Abanin, E. Altman, I. Bloch, and M. Serbyn, "Colloquium: Many-body localization, thermalization, and entanglement", Rev. Mod. Phys. **91**, 021001 (2019).

[51] S. Gopalakrishnan and S. Parameswaran, "Dynamics and transport at the threshold of many-body localization", Phys. Rep. **862**, 1–62 (2020).

[52] W. Götze, "Aspects of Structural Glass Transitions", in *Liquids, Freezing and the Glass Transition*, edited by J. Hansen, D. Levesque, and J. Zinn-Justin (North-Holland, 1991) Chap. 5, pp. 287–504.

[53] L. Berthier and G. Biroli, "Theoretical perspective on the glass transition and amorphous materials", Rev. Mod. Phys. **83**, 587 (2011).

[54] K. Binder and W. Kob, "Glassy Materials and Disordered Solids" (World Scientific, 2011).

[55] G. Biroli and J.-P. Bouchaud, "The Random First-Order Transition Theory of Glasses: A Critical Assessment", in *Structural Glasses and Supercooled Liquids* (John Wiley & Sons, Ltd, 2012) Chap. 2, pp. 31–113.

[56] A. Cavagna, "Supercooled liquids for pedestrians", Phys. Rep. **476**, 51–124 (2009).

[57] G. Biroli and J. P. Garrahan, "Perspective: The glass transition", J. Chem. Phys. **138**, 12A301 (2013).

[58] B. Ruzicka et al., "Evidence of anomalous dispersion of the generalized sound velocity in glasses", Phys. Rev. B **69**, 100201 (2004).

[59] S. F. Edwards and P. W. Anderson, "Theory of spin glasses", J. Phys. F **5**, 965–974 (1975).

[60] G. Parisi, "Infinite Number of Order Parameters for Spin-Glasses", Phys. Rev. Lett. **43**, 1754–1756 (1979).

[61] G. Parisi, "A sequence of approximated solutions to the S-K model for spin glasses", J. Phys. A **13**, L115–L121 (1980).

[62] G. Parisi, "The order parameter for spin glasses: a function on the interval 0-1", J. Phys. A **13**, 1101–1112 (1980).

[63] G. Parisi, "Order Parameter for Spin-Glasses", Phys. Rev. Lett. **50**, 1946–1948 (1983).

[64] D. Sherrington and S. Kirkpatrick, "Solvable Model of a Spin-Glass", Phys. Rev. Lett. **35**, 1792–1796 (1975).

[65] S. Kirkpatrick, C. D. Gelatt, and M. P. Vecchi, "Optimization by Simulated Annealing", Science **220**, 671–680 (1983).

[66] S. Kirkpatrick, "Optimization by simulated annealing: Quantitative studies", J. Stat. Phys. **34**, 975–986 (1984).

[67] M. Goldstein, "Viscous Liquids and the Glass Transition: A Potential Energy Barrier Picture", J. Chem. Phys. **51**, 3728–3739 (1969).

[68] M. Mézard, G. Parisi, and M. A. Virasoro, "Spin Glass Theory and Beyond" (World Scientific, 1987).

[69] T. R. Kirkpatrick and D. Thirumalai, "Dynamics of the Structural Glass Transition and the p-Spin—Interaction Spin-Glass Model", Phys. Rev. Lett. **58**, 2091–2094 (1987).

[70] T. R. Kirkpatrick and D. Thirumalai, "p-spin-interaction spin-glass models: Connections with the structural glass problem", Phys. Rev. B **36**, 5388–5397 (1987).

[71] T. R. Kirkpatrick and P. G. Wolynes, "Connections between some kinetic and equilibrium theories of the glass transition", Phys. Rev. A **35**, 3072–3080 (1987).

[72] T. R. Kirkpatrick, D. Thirumalai, and P. G. Wolynes, "Scaling concepts for the dynamics of viscous liquids near an ideal glassy state", Phys. Rev. A **40**, 1045–1054 (1989).

[73] T. R. Kirkpatrick and D. Thirumalai, "Random solutions from a regular density functional Hamiltonian: a static and dynamical theory for the structural glass transition", J. Phys. A **22**, L149–L155 (1989).

[74] P. Charbonneau, E. I. Corwin, G. Parisi, and F. Zamponi, "Universal Microstructure and Mechanical Stability of Jammed Packings", Phys. Rev. Lett. **109**, 205501 (2012).

[75] P. Charbonneau, E. I. Corwin, G. Parisi, and F. Zamponi, "Jamming Criticality Revealed by Removing Localized Buckling Excitations", Phys. Rev. Lett. **114**, 125504 (2015).

[76] J. Kurchan, G. Parisi, and F. Zamponi, "Exact theory of dense amorphous hard spheres in high dimension I. The free energy", J. Stat. Mech. Theory Exp. **2012**, P10012 (2012).

[77] J. Kurchan, G. Parisi, P. Urbani, and F. Zamponi, "Exact Theory of Dense Amorphous Hard Spheres in High Dimension. II. The High Density Regime and the Gardner Transition", J. Phys. Chem. B **117**, 12979–12994 (2013).

[78] P. Charbonneau, J. Kurchan, G. Parisi, P. Urbani, and F. Zamponi, "Exact theory of dense amorphous hard spheres in high dimension. III. The full replica symmetry breaking solution", J. Stat. Mech. Theory Exp. **2014**, P10009 (2014).

[79] G. Parisi, P. Urbani, and F. Zamponi, "Theory of Simple Glasses: Exact Solutions in Infinite Dimensions" (Cambridge University Press, 2020).

[80] J. M. Kosterlitz, D. J. Thouless, and R. C. Jones, "Spherical Model of a Spin-Glass", Phys. Rev. Lett. **36**, 1217–1220 (1976).

[81] J. Kosterlitz, D. Thouless, and R. C. Jones, "Spherical model of a spin glass", Physica B+C **86-88**, 859–860 (1977).

[82] P. G. Kevrekidis, "The Discrete Nonlinear Schrödinger Equation" (Springer, Berlin, 2009).

[83] L. Berthier, G. Biroli, J.-P. Bouchaud, L. Cipelletti, and W. van Saarloos, "Dynamical Heterogeneities in Glasses, Colloids, and Granular Media", Vol. 150 (Oxford University Press, Oxford, 2011).

[84] L. Berthier, "Dynamic Heterogeneity in Amorphous Materials", Physics **4**, 42 (2011).

[85] R. C. Zeller and R. O. Pohl, "Thermal Conductivity and Specific Heat of Noncrystalline Solids", Phys. Rev. B **4**, 2029–2041 (1971).

[86] P. W. Anderson, B. I. Halperin, and C. M. Varma, "Anomalous Low-temperature Thermal Properties of Glasses and Spin Glasses", Philos. Mag. **25**, 1–9 (1972).

[87] W. Phillips, "Tunneling states in amorphous solids", J. Low Temp. Phys. **7**, 351–360 (1972).

[88] W. A. Phillips, "Two-level states in glasses", Rep. Progr. Phys. **50**, 1657–1708 (1987).

[89] S. Hunklinger and A. Raychaudhuri, "Thermal and Elastic Anomalies in Glasses at Low Temperatures", in *Progress in Low Temperature Physics*, Vol. 9, edited by D. Brewer (Elsevier, 1986), pp. 265–344.

[90] P. Esquinazi, "Tunneling Systems in Amorphous and Crystalline Solids" (Springer Science, 2013).

[91] M. A. Ramos, "Low-Temperature Thermal and Vibrational Properties of Disordered Solids: A Half-Century of Universal "Anomalies" of Glasses" (World Scientific, Europe, 2022).

[92] P. W. Anderson, "Absence of diffusion in certain random lattices", Phys. Rev. **109**, 1492 (1958).

[93] D. J. Thouless, "A relation between the density of states and range of localization for one dimensional random systems", J. Phys. C **5**, 77–81 (1972).

[94] R. Abou-Chacra, D. J. Thouless, and P. W. Anderson, "A selfconsistent theory of localization", J. Phys. C **6**, 1734–1752 (1973).

[95] E. Abrahams, P. W. Anderson, D. C. Licciardello, and T. V. Ramakrishnan, "Scaling Theory of Localization: Absence of Quantum Diffusion in Two Dimensions", Phys. Rev. Lett. **42**, 673–676 (1979).

[96] F. Evers and A. D. Mirlin, "Anderson transitions", Rev. Mod. Phys. **80**, 1355–1417 (2008).

[97] E. Abrahams, ed., "50 Years of Anderson Localization" (World Scientific, 2010).

[98] D. S. Wiersma, P. Bartolini, A. Lagendijk, and R. Righini, "Localization of light in a disordered medium", Nature **390**, 671–673 (1997).

[99] M. Störzer, P. Gross, C. M. Aegerter, and G. Maret, "Observation of the Critical Regime Near Anderson Localization of Light", Phys. Rev. Lett. **96**, 063904 (2006).

[100] J. Billy et al., "Direct observation of Anderson localization of matter waves in a controlled disorder", Nature **453**, 891–894 (2008).

[101] G. Roati et al., "Anderson localization of a non-interacting Bose–Einstein condensate", Nature **453**, 895–898 (2008).

[102] L. Fleishman and P. W. Anderson, "Interactions and the Anderson transition", Phys. Rev. B **21**, 2366–2377 (1980).

[103] B. L. Altshuler, Y. Gefen, A. Kamenev, and L. S. Levitov, "Quasiparticle Lifetime in a Finite System: A Nonperturbative Approach", Phys. Rev. Lett. **78**, 2803–2806 (1997).

[104] H. Bethe, "Zur Theorie der Metalle", Z. Phys. **71**, 205–226 (1931).

[105] M. Serbyn, Z. Papić, and D. A. Abanin, "Local Conservation Laws and the Structure of the Many-Body Localized States", Phys. Rev. Lett. **111**, 127201 (2013).

[106] D. A. Huse, R. Nandkishore, and V. Oganesyan, "Phenomenology of fully many-body-localized systems", Phys. Rev. B **90**, 174202 (2014).

[107] V. Ros, M. Müller, and A. Scardicchio, "Integrals of motion in the many-body localized phase", Nucl. Phys. **B891**, 420–465 (2015).

[108] J. Z. Imbrie, "On Many-Body Localization for Quantum Spin Chains", J. Stat. Phys. **163**, 998–1048 (2016).

[109] J. Z. Imbrie, "Diagonalization and Many-Body Localization for a Disordered Quantum Spin Chain", Phys. Rev. Lett. **117**, 027201 (2016).

[110] M. Serbyn, Z. Papić, and D. A. Abanin, "Quantum quenches in the many-body localized phase", Phys. Rev. B **90**, 174302 (2014).

[111] M. Žnidarič, "Entanglement in a dephasing model and many-body localization", Phys. Rev. B **97**, 214202 (2018).

[112] W. De Roeck and F. Huveneers, "Stability and instability towards delocalization in many-body localization systems", Phys. Rev. B **95**, 155129 (2017).

[113] W. De Roeck and J. Z. Imbrie, "Many-body localization: stability and instability", Philos. Trans. R. Soc. A **375**, 20160422 (2017).

[114] T. Thiery, F. Huveneers, M. Müller, and W. De Roeck, "Many-Body Delocalization as a Quantum Avalanche", Phys. Rev. Lett. **121**, 140601 (2018).

[115] J. Šuntajs, J. Bonča, T. Prosen, and L. Vidmar, "Quantum chaos challenges many-body localization", Phys. Rev. E **102**, 062144 (2020).

[116] P. J. D. Crowley and A. Chandran, "A constructive theory of the numerically accessible many-body localized to thermal crossover", arXiv:2012.14393 (2020).

[117] D. Sels and A. Polkovnikov, "Dynamical obstruction to localization in a disordered spin chain", Phys. Rev. E **104**, 054105 (2021).

[118] D. Sels and A. Polkovnikov, "Thermalization of dilute impurities in one dimensional spin chains", arXiv:2105.09348 (2021).

[119] D. Sels, "Markovian baths and quantum avalanches", arXiv:2108.10796 (2021).

[120] A. Morningstar, L. Colmenarez, V. Khemani, D. J. Luitz, and D. A. Huse, "Avalanches and many-body resonances in many-body localized systems", Phys. Rev. B **105**, 174205 (2022).

[121] R. Vosk and E. Altman, "Many-Body Localization in One Dimension as a Dynamical Renormalization Group Fixed Point", Phys. Rev. Lett. **110**, 067204 (2013).

[122] A. C. Potter, R. Vasseur, and S. A. Parameswaran, "Universal Properties of Many-Body Delocalization Transitions", Phys. Rev. X **5**, 031033 (2015).

[123] L. Zhang, B. Zhao, T. Devakul, and D. A. Huse, "Many-body localization phase transition: A simplified strong-randomness approximate renormalization group", Phys. Rev. B **93**, 224201 (2016).

[124] T. Thiery, M. Müller, and W. De Roeck, "A microscopically motivated renormalization scheme for the MBL/ETH transition", arXiv:1711.09880 (2017).

[125] A. Goremykina, R. Vasseur, and M. Serbyn, "Analytically Solvable Renormalization Group for the Many-Body Localization Transition", Phys. Rev. Lett. **122**, 040601 (2019).

[126] P. T. Dumitrescu, A. Goremykina, S. A. Parameswaran, M. Serbyn, and R. Vasseur, "Kosterlitz-Thouless scaling at many-body localization phase transitions", Phys. Rev. B **99**, 094205 (2019).

[127] A. Morningstar and D. A. Huse, "Renormalization-group study of the many-body localization transition in one dimension", Phys. Rev. B **99**, 224205 (2019).

[128] A. Morningstar, D. A. Huse, and J. Z. Imbrie, "Many-body localization near the critical point", Phys. Rev. B **102**, 125134 (2020).

[129] J. H. Bardarson, F. Pollmann, and J. E. Moore, "Unbounded Growth of Entanglement in Models of Many-Body Localization", Phys. Rev. Lett. **109**, 017202 (2012).

[130] A. D. Luca and A. Scardicchio, "Ergodicity breaking in a model showing many-body localization", Europhys. Lett. **101**, 37003 (2013).

[131] D. J. Luitz, N. Laflorencie, and F. Alet, "Many-body localization edge in the random-field Heisenberg chain", Phys. Rev. B **91**, 081103(R) (2015).

[132] P. Prelovšek, O. S. Barišić, and M. Žnidarič, "Absence of full many-body localization in the disordered Hubbard chain", Phys. Rev. B **94**, 241104 (2016).

[133] R. K. Panda, A. Scardicchio, M. Schulz, S. R. Taylor, and M. Žnidarič, "Can we study the many-body localisation transition?", Europhys. Lett. **128**, 67003 (2020).

[134] D. Abanin et al., "Distinguishing localization from chaos: Challenges in finite-size systems", Ann. Phys. (Amsterdam) **427**, 168415 (2021).

[135] P. Sierant and J. Zakrzewski, "Challenges to observation of many-body localization", Phys. Rev. B **105**, 224203 (2022).

[136] M. Schreiber et al., "Observation of many-body localization of interacting fermions in a quasirandom optical lattice", Science **349**, 842–845 (2015).

[137] J. Smith et al., "Many-body localization in a quantum simulator with programmable random disorder", Nat. Phys. **12**, 907–911 (2016).

[138] P. Bordia, H. P. Lüschen, S. S. Hodgman, M. Schreiber, I. Bloch, and U. Schneider, "Coupling identical one-dimensional many-body localized systems", Phys. Rev. Lett. **116**, 140401 (2016).

[139] H. P. Lüschen, P. Bordia, S. Scherg, F. Alet, E. Altman, U. Schneider, and I. Bloch, "Observation of Slow Dynamics near the Many-Body Localization Transition in One-Dimensional Quasiperiodic Systems", Phys. Rev. Lett. **119**, 260401 (2017).

[140] T. Kohlert, S. Scherg, X. Li, H. P. Lüschen, S. Das Sarma, I. Bloch, and M. Aidelsburger, "Observation of Many-Body Localization in a One-Dimensional System with a Single-Particle Mobility Edge", Phys. Rev. Lett. **122**, 170403 (2019).

[141] A. Lukin et al., "Probing entanglement in a many-body localized system", Science **364**, 256–260 (2019).

[142] M. Rispoli, A. Lukin, R. Schittko, S. Kim, M. E. Tai, J. Léonard, and M. Greiner, "Quantum critical behaviour at the many-body localization transition", Nature **573**, 385–389 (2019).

[143] G. Carleo, F. Becca, M. Schirò, and M. Fabrizio, "Localization and Glassy Dynamics Of Many-Body Quantum Systems", Sci. Rep. **2**, 243 (2012).

[144] Z. Papić, E. M. Stoudenmire, and D. A. Abanin, "Many-body localization in disorder-free systems: The importance of finite-size constraints", Ann. Phys. (Amsterdam) **362**, 714–725 (2015).

[145] M. Schiulaz, A. Silva, and M. Müller, "Dynamics in many-body localized quantum systems without disorder", Phys. Rev. B **91**, 184202 (2015).

[146] N. Y. Yao, C. R. Laumann, J. I. Cirac, M. D. Lukin, and J. E. Moore, "Quasi-Many-Body Localization in Translation-Invariant Systems", Phys. Rev. Lett. **117**, 240601 (2016).

[147] A. Smith, J. Knolle, D. L. Kovrizhin, and R. Moessner, "Disorder-Free Localization", Phys. Rev. Lett. **118**, 266601 (2017).

[148] A. A. Michailidis, M. Žnidarič, M. Medvedyeva, D. A. Abanin, T. Prosen, and Z. Papić, "Slow dynamics in translation-invariant quantum lattice models", Phys. Rev. B **97**, 104307 (2018).

[149] M. Brenes, M. Dalmonte, M. Heyl, and A. Scardicchio, "Many-Body Localization Dynamics from Gauge Invariance", Phys. Rev. Lett. **120**, 030601 (2018).

[150] P. Karpov, R. Verdel, Y.-P. Huang, M. Schmitt, and M. Heyl, "Disorder-Free Localization in an Interacting 2D Lattice Gauge Theory", Phys. Rev. Lett. **126**, 130401 (2021).

[151] O. Hart, S. Gopalakrishnan, and C. Castelnovo, "Logarithmic Entanglement Growth from Disorder-Free Localization in the Two-Leg Compass Ladder", Phys. Rev. Lett. **126**, 227202 (2021).

[152] C. Chamon, "Quantum glassiness in strongly correlated clean systems: an example of topological overprotection", Phys. Rev. Lett. **94**, 040402 (2005).

[153] Z. Lan, M. van Horssen, S. Powell, and J. P. Garrahan, "Quantum Slow Relaxation and Metastability due to Dynamical Constraints", Phys. Rev. Lett. **121**, 040603 (2018).

[154] R. M. Nandkishore and M. Hermele, "Fractons", Annu. Rev. Condens. Matter Phys. **10**, 295–313 (2019).

[155] M. Pretko, X. Chen, and Y. You, "Fracton phases of matter", Intl. J. Mod. Phys. A **35**, 2030003 (2020).

[156] F. M. Surace, P. P. Mazza, G. Giudici, A. Lerose, A. Gambassi, and M. Dalmonte, "Lattice Gauge Theories and String Dynamics in Rydberg Atom Quantum Simulators", Phys. Rev. X **10**, 021041 (2020).

[157] N. Pancotti, G. Giudice, J. I. Cirac, J. P. Garrahan, and M. C. Bañuls, "Quantum East Model: Localization, Nonthermal Eigenstates, and Slow Dynamics", Phys. Rev. X **10**, 021051 (2020).

[158] N. D. Oppong, G. Pasqualetti, O. Bettermann, P. Zechmann, M. Knap, I. Bloch, and S. Fölling, "Probing transport and slow relaxation in the mass-imbalanced Fermi-Hubbard model", arXiv:2011.12411 (2020).

[159] M. Kastner, "Diverging Equilibration Times in Long-Range Quantum Spin Models", Phys. Rev. Lett. **106**, 130601 (2011).

[160] T. Mori, "Prethermalization in the transverse-field Ising chain with long-range interactions", J. Phys. A **52**, 054001 (2019).

[161] F. Liu, R. Lundgren, P. Titum, G. Pagano, J. Zhang, C. Monroe, and A. V. Gorshkov, "Confined Quasiparticle Dynamics in Long-Range Interacting Quantum Spin Chains", Phys. Rev. Lett. **122**, 150601 (2019).

[162] A. Lerose and S. Pappalardi, "Origin of the slow growth of entanglement entropy in long-range interacting spin systems", Phys. Rev. Research **2**, 012041 (2020).

[163] N. Defenu, "Metastability and discrete spectrum of long-range systems", Proc. Natl. Acad. Sci. USA **118**, e2101785118 (2021).

[164] M. Kormos, M. Collura, G. Takács, and P. Calabrese, "Real time confinement following a quantum quench to a non-integrable model", Nat. Phys. **13**, 246–249 (2017).

[165] C.-J. Lin and O. I. Motrunich, "Quasiparticle explanation of the weak-thermalization regime under quench in a nonintegrable quantum spin chain", Phys. Rev. A **95**, 023621 (2017).

[166] A. J. A. James, R. M. Konik, and N. J. Robinson, "Nonthermal States Arising from Confinement in One and Two Dimensions", Phys. Rev. Lett. **122**, 130603 (2019).

[167] J. Park, Y. Kuno, and I. Ichinose, "Glassy dynamics from quark confinement: Atomic quantum simulation of the gauge-Higgs model on a lattice", Phys. Rev. A **100**, 013629 (2019).

[168] N. J. Robinson, A. J. A. James, and R. M. Konik, "Signatures of rare states and thermalization in a theory with confinement", Phys. Rev. B **99**, 195108 (2019).

[169] P. P. Mazza, G. Perfetto, A. Lerose, M. Collura, and A. Gambassi, "Suppression of transport in nondisordered quantum spin chains due to confined excitations", Phys. Rev. B **99**, 180302(R) (2019).

[170] A. Lerose, F. M. Surace, P. P. Mazza, G. Perfetto, M. Collura, and A. Gambassi, "Quasilocalized dynamics from confinement of quantum excitations", Phys. Rev. B **102**, 041118 (2020).

[171] R. Verdel, F. Liu, S. Whitsitt, A. V. Gorshkov, and M. Heyl, "Real-time dynamics of string breaking in quantum spin chains", Phys. Rev. B **102**, 014308 (2020).

[172] S. Pai and M. Pretko, "Fractons from confinement in one dimension", Phys. Rev. Research **2**, 013094 (2020).

[173] T. Chanda, J. Zakrzewski, M. Lewenstein, and L. Tagliacozzo, "Confinement and Lack of Thermalization after Quenches in the Bosonic Schwinger Model", Phys. Rev. Lett. **124**, 180602 (2020).

[174] G. Magnifico, M. Dalmonte, P. Facchi, S. Pascazio, F. V. Pepe, and E. Ercolessi, "Real Time Dynamics and Confinement in the $\mathbb{Z}_n$ Schwinger-Weyl lattice model for 1+1 QED", Quantum **4**, 281 (2020).

[175] P. Sala, T. Rakovszky, R. Verresen, M. Knap, and F. Pollmann, "Ergodicity Breaking Arising from Hilbert Space Fragmentation in Dipole-Conserving Hamiltonians", Phys. Rev. X **10**, 011047 (2020).

[176] V. Khemani, M. Hermele, and R. Nandkishore, "Localization from Hilbert space shattering: From theory to physical realizations", Phys. Rev. B **101**, 174204 (2020).

[177] C. J. Turner, A. A. Michailidis, D. A. Abanin, M. Serbyn, and Z. Papić, "Weak ergodicity breaking from quantum many-body scars", Nat. Phys. **14**, 745–749 (2018).

[178] M. Serbyn, D. A. Abanin, and Z. Papić, "Quantum Many-Body Scars and Weak Breaking of Ergodicity", Nat. Phys. **17**, 675–685 (2021).

[179] A. Lazarides, A. Das, and R. Moessner, "Fate of Many-Body Localization Under Periodic Driving", Phys. Rev. Lett. **115**, 030402 (2015).

[180] P. Ponte, A. Chandran, Z. Papić, and D. A. Abanin, "Periodically driven ergodic and many-body localized quantum systems", Ann. Phys. (Amsterdam) **353**, 196–204 (2015).

[181] D. A. Abanin, W. De Roeck, and F. Huveneers, "Theory of many-body localization in periodically driven systems", Ann. Phys. (Amsterdam) **372**, 1–11 (2016).

[182] L. Zhang, V. Khemani, and D. A. Huse, "A Floquet model for the many-body localization transition", Phys. Rev. B **94**, 224202 (2016).

[183] E. Bairey, G. Refael, and N. H. Lindner, "Driving induced many-body localization", Phys. Rev. B **96**, 020201 (2017).

[184] P. Sierant, M. Lewenstein, A. Scardicchio, and J. Zakrzewski, "Stability of many-body localization in Kicked Ising model", arXiv:2203.15697 (2022).

[185] S. Iyer, V. Oganesyan, G. Refael, and D. A. Huse, "Many-body localization in a quasiperiodic system", Phys. Rev. B **87**, 134202 (2013).

[186] V. Khemani, D. N. Sheng, and D. A. Huse, "Two Universality Classes for the Many-Body Localization Transition", Phys. Rev. Lett. **119**, 075702 (2017).

[187] F. Setiawan, D.-L. Deng, and J. H. Pixley, "Transport properties across the many-body localization transition in quasiperiodic and random systems", Phys. Rev. B **96**, 104205 (2017).

[188] S.-X. Zhang and H. Yao, "Universal Properties of Many-Body Localization Transitions in Quasiperiodic Systems", Phys. Rev. Lett. **121**, 206601 (2018).

[189] E. V. H. Doggen and A. D. Mirlin, "Many-body delocalization dynamics in long Aubry-André quasiperiodic chains", Phys. Rev. B **100**, 104203 (2019).

[190] U. Agrawal, R. Vasseur, and S. Gopalakrishnan, "A note on the quasiperiodic many-body localization transition in dimension $d > 1$", arXiv:2204.03665 (2022).

[191] A. Štrkalj, E. V. H. Doggen, and C. Castelnovo, "Coexistence of localization and transport in many-body two-dimensional Aubry-André models", arXiv: 2204.05198 (2022).

[192] P. J. D. Crowley and A. Chandran, "Mean field theory of failed thermalizing avalanches", arXiv:2204.09688 (2022).

[193] A. C. Potter and R. Vasseur, "Symmetry constraints on many-body localization", Phys. Rev. B **94**, 224206 (2016).

[194] I. V. Protopopov, W. W. Ho, and D. A. Abanin, "Effect of SU(2) symmetry on many-body localization and thermalization", Phys. Rev. B **96**, 041122 (2017).

[195] I. V. Protopopov, R. K. Panda, T. Parolini, A. Scardicchio, E. Demler, and D. A. Abanin, "Non-Abelian Symmetries and Disorder: A Broad Nonergodic Regime and Anomalous Thermalization", Phys. Rev. X **10**, 011025 (2020).

[196] P. Fendley, K. Sengupta, and S. Sachdev, "Competing density-wave orders in a one-dimensional hard-boson model", Phys. Rev. B **69**, 075106 (2004).

[197] I. Lesanovsky, "Liquid Ground State, Gap, and Excited States of a Strongly Correlated Spin Chain", Phys. Rev. Lett. **108**, 105301 (2012).

[198] F. M. Surace, M. Votto, E. G. Lazo, A. Silva, M. Dalmonte, and G. Giudici, "Exact many-body scars and their stability in constrained quantum chains", Phys. Rev. B **103**, 104302 (2021).

[199] P. Sierant, E. G. Lazo, M. Dalmonte, A. Scardicchio, and J. Zakrzewski, "Constraint-Induced Delocalization", Phys. Rev. Lett. **127**, 126603 (2021).

[200] T. Giamarchi, "Quantum Physics in One Dimension" (Oxford University Press, 2003).

[201] U. Schollwöck, "The density-matrix renormalization group in the age of matrix product states", Ann. Phys. (Amsterdam) **326**, 96–192 (2011).

[202] S. A. Cook, "The Complexity of Theorem-Proving Procedures", in Proceedings of the Third Annual ACM Symposium on Theory of Computing, STOC '71 (1971), pp. 151–158.

[203] L. A. Levin, "Universal Sequential Search Problems", Probl. Peredachi Inf. **9**, 115–116 (1973).

[204] M. Mezard and A. Montanari, "Information, Physics, and Computation" (Oxford University Press, 2009).

[205] S. Kirkpatrick and B. Selman, "Critical Behavior in the Satisfiability of Random Boolean Expressions", Science **264**, 1297–1301 (1994).

[206] R. Monasson, R. Zecchina, S. Kirkpatrick, B. Selman, and L. Troyansky, "Determining computational complexity from characteristic 'phase transitions'", Nature **400**, 133 (1999).

[207] A. K. Hartmann and M. Weigt, "Phase Transitions in Combinatorial Optimization Problems" (Whiley-VCH, Weinheim, 2005).

[208] F. Krzakała, A. Montanari, F. Ricci-Tersenghi, G. Semerjian, and L. Zdeborová, "Gibbs states and the set of solutions of random constraint satisfaction problems", Proc. Natl. Acad. Sci. USA **104**, 10318–10323 (2007).

[209] M. Mézard, G. Parisi, and R. Zecchina, "Analytic and Algorithmic Solution of Random Satisfiability Problems", Science **297**, 812–815 (2002).

[210] M. Mézard and R. Zecchina, "Random K-satisfiability problem: From an analytic solution to an efficient algorithm", Phys. Rev. E **66**, 056126 (2002).

[211] M. Bernaschi, M. Bisson, M. Fatica, E. Marinari, V. Martin-Mayor, G. Parisi, and F. Ricci-Tersenghi, "How we are leading a 3-XORSAT challenge: From the energy landscape to the algorithm and its efficient implementation on GPUs", Europhys. Lett. **133**, 60005 (2021).

[212] P. Charbonneau, J. Kurchan, G. Parisi, P. Urbani, and F. Zamponi, "Fractal free energy landscapes in structural glasses", Nat. Commun. **5**, 3725 (2014).

[213] P. Charbonneau, J. Kurchan, G. Parisi, P. Urbani, and F. Zamponi, "Glass and jamming transitions: From exact results to finite-dimensional descriptions", Annu. Rev. Condens. Matter Phys. **8**, 265 (2017).

[214] L. Berthier, G. Biroli, P. Charbonneau, E. I. Corwin, S. Franz, and F. Zamponi, "Gardner physics in amorphous solids and beyond", J. Chem. Phys. **151**, 010901 (2019).

[215] A. J. Liu and S. R. Nagel, "Nonlinear dynamics: Jamming is not just cool any more", Nature **396**, 21 (1998).

[216] S. Torquato, T. M. Truskett, and P. G. Debenedetti, "Is Random Close Packing of Spheres Well Defined?", Phys. Rev. Lett. **84**, 2064 (2000).

[217] A. J. Liu, S. R. Nagel, W. van Saarloos, and M. Wyart, "The jamming scenario - an introduction and outlook", arXiv:1006.2365 (2010).

[218] S. Torquato and F. H. Stillinger, "Jammed hard-particle packings: From Kepler to Bernal and beyond", Rev. Mod. Phys. **82**, 2633–2672 (2010).

[219] E. DeGiuli, E. Lerner, C. Brito, and M. Wyart, "Force distribution affects vibrational properties in hard-sphere glasses", Proc. Natl. Acad. Sci. USA **111**, 17054–17059 (2014).

[220] R. C. Dennis and E. I. Corwin, "Jamming Energy Landscape is Hierarchical and Ultrametric", Phys. Rev. Lett. **124**, 078002 (2020).

[221] S. Franz, G. Parisi, P. Urbani, and F. Zamponi, "Universal spectrum of normal modes in low-temperature glasses", Proc. Natl. Acad. Sci. USA **112**, 14539–14544 (2015).

[222] S. Franz and G. Parisi, "The simplest model of jamming", J. Phys. A **49**, 145001 (2016).

[223] A. Altieri, S. Franz, and G. Parisi, "The jamming transition in high dimension: an analytical study of the TAP equations and the effective thermodynamic potential", J. Stat. Mech. Theory Exp., 093301 (2016).

[224] S. Franz, G. Parisi, M. Sevelev, P. Urbani, and F. Zamponi, "Universality of the SAT-UNSAT (jamming) threshold in non-convex continuous constraint satisfaction problems", SciPost Phys. **2**, 019 (2017).

[225] E. Agoritsas, G. Biroli, P. Urbani, and F. Zamponi, "Out-of-equilibrium dynamical mean-field equations for the perceptron model", J. Phys. A **51**, 085002 (2018).

[226] F. Rosenblatt, "The perceptron: A probabilistic model for information storage and organization in the brain", Psychol. Rev. **65**, 386–408 (1958).

[227] E. Gardner, "The space of interactions in neural network models", J. Phys. A **21**, 257 (1988).

[228] E. Gardner and B. Derrida, "Optimal storage properties of neural network models", J. Phys. A **21**, 271 (1988).

[229] A. Battista and R. Monasson, "Capacity-Resolution Trade-Off in the Optimal Learning of Multiple Low-Dimensional Manifolds by Attractor Neural Networks", Phys. Rev. Lett. **124**, 048302 (2020).

[230] F. Benatti, G. Gramegna, and S. Mancini, "Pattern capacity of a single quantum perceptron", J. Phys. A **55**, 155301 (2022).

[231] A. Bray and M. Moore, "Replica theory of quantum spin glasses", J. Phys. C **13**, L655 (1980).

[232] J. Miller and D. A. Huse, "Zero-temperature critical behavior of the infinite-range quantum Ising spin glass", Phys. Rev. Lett. **70**, 3147 (1993).

[233] S. Sachdev, "Quantum Phase Transitions" (Cambridge University Press, 2000).

[234] L. F. Cugliandolo, D. R. Grempel, and C. A. da Silva Santos, "Imaginary-time replica formalism study of a quantum spherical p-spin-glass model", Phys. Rev. B **64**, 014403 (2001).

[235] G. Biroli and L. F. Cugliandolo, "Quantum Thouless-Anderson-Palmer equations for glassy systems", Phys. Rev. B **64**, 014206 (2001).

[236] C. Laumann, A. Scardicchio, and S. L. Sondhi, "Cavity method for quantum spin glasses on the Bethe lattice", Phys. Rev. B **78**, 134424 (2008).

[237] A. Andreanov and M. Müller, "Long-Range Quantum Ising Spin Glasses at $T = 0$: Gapless Collective Excitations and Universality", Phys. Rev. Lett. **109**, 177201 (2012).

[238] B. Altshuler, H. Krovi, and J. Roland, "Anderson localization makes adiabatic quantum optimization fail", Proc. Natl. Acad. Sci. USA **107**, 12446–12450 (2010).

[239] C. R. Laumann, A. Pal, and A. Scardicchio, "Many-Body Mobility Edge in a Mean-Field Quantum Spin Glass", Phys. Rev. Lett. **113**, 200405 (2014).

[240] C. R. Laumann, R. Moessner, A. Scardicchio, and S. L. Sondhi, "Quantum annealing: The fastest route to quantum computation?", Eur. Phys. J. Spec. Top. **224**, 75–88 (2015).

[241] G. Mossi and A. Scardicchio, "Ergodic and localized regions in quantum spin glasses on the Bethe lattice", Philos. Trans. R. Soc. A **375**, 20160424 (2017).

[242] V. N. Smelyanskiy, K. Kechedzhi, S. Boixo, S. V. Isakov, H. Neven, and B. Altshuler, "Nonergodic Delocalized States for Efficient Population Transfer within a Narrow Band of the Energy Landscape", Phys. Rev. X **10**, 011017 (2020).

[243] Z. Nussinov, P. Johnson, M. J. Graf, and A. V. Balatsky, "Mapping between finite temperature classical and zero temperature quantum systems: Quantum critical jamming and quantum dynamical heterogeneities", Phys. Rev. B **87**, 184202 (2013).

[244] S. Franz, T. Maimbourg, G. Parisi, and A. Scardicchio, "Impact of jamming criticality on low-temperature anomalies in structural glasses", Proc. Natl. Acad. Sci. USA **116**, 13768 (2019).

[245] A. Georges, G. Kotliar, W. Krauth, and M. J. Rozenberg, "Dynamical mean-field theory of strongly correlated fermion systems and the limit of infinite dimensions", Rev. Mod. Phys. **68**, 13–125 (1996).

[246] J. Reinisch and A. Heuer, "Local properties of the potential-energy landscape of a model glass: Understanding the low-temperature anomalies", Phys. Rev. B **70**, 064201 (2004).

[247] J. Reinisch and A. Heuer, "What Is Moving in Silica at 1 K? A Computer Study of the Low-Temperature Anomalies", Phys. Rev. Lett. **95**, 155502 (2005).

[248] D. Khomenko, C. Scalliet, L. Berthier, D. R. Reichman, and F. Zamponi, "Depletion of Two-Level Systems in Ultrastable Computer-Generated Glasses", Phys. Rev. Lett. **124**, 225901 (2020).

[249] T. Cretegny, T. Dauxois, S. Ruffo, and A. Torcini, "Localization and equipartition of energy in the β-FPU chain: Chaotic breathers", Physica D **121**, 109–126 (1998).

[250] G. Berman and F. Izrailev, "The Fermi–Pasta–Ulam problem: Fifty years of progress", Chaos **15**, 015104 (2005).

[251] T. Dauxois and S. Ruffo, "Fermi-Pasta-Ulam nonlinear lattice oscillations", Scholarpedia **3**, 5538 (2008).

[252] G. Gallavotti, ed., "The Fermi-Pasta-Ulam Problem: A Status Report" (Springer, Berlin, Heidelberg, 2008).

[253] P. G. Drazin and R. S. Johnson, "Solitons: An Introduction", 2nd ed. (Cambridge University Press, 1989).

[254] E. Fucito, F. Marchesoni, E. Marinari, G. Parisi, L. Peliti, S. Ruffo, and A. Vulpiani, " Approach to equilibrium in a chain of nonlinear oscillators", J. Physique **43**, 707–713 (1982).

[255] G. Parisi, "On the approach to equilibrium of a Hamiltonian chain of anharmonic oscillators", Europhys. Lett. **40**, 357–362 (1997).

[256] A. Carati and L. Galgani, "On the Specific Heat of Fermi–Pasta–Ulam Systems and Their Glassy Behavior", J. Stat. Phys. **94**, 859–869 (1999).

[257] D. Bambusi and A. Ponno, "On Metastability in FPU", Commun. Math. Phys. **264**, 539–561 (2006).

[258] A. Carati, A. Maiocchi, L. Galgani, and G. Amati, "The Fermi–Pasta–Ulam System as a Model for Glasses", Math. Phys., Anal. and Geom. **18**, 31 (2015).

[259] M. Ablowitz and B. Prinari, "Nonlinear Schrödinger systems: continuous and discrete", Scholarpedia **3**, 5561 (2008).

[260] H. Spohn, "Hydrodynamic equations for the Ablowitz-Ladik discretization of the nonlinear Schrödinger equation", J. Math. Phys. **63**, 033305 (2022).

[261] K. Ø. Rasmussen, T. Cretegny, P. G. Kevrekidis, and N. Grønbech-Jensen, "Statistical Mechanics of a Discrete Nonlinear System", Phys. Rev. Lett. **84**, 3740 (2000).

[262] T. Mithun, Y. Kati, C. Danieli, and S. Flach, "Weakly Nonergodic Dynamics in the Gross-Pitaevskii Lattice", Phys. Rev. Lett. **120**, 184101 (2018).

[263] S. Iubini, L. Chirondojan, G.-L. Oppo, A. Politi, and P. Politi, "Dynamical Freezing of Relaxation to Equilibrium", Phys. Rev. Lett. **122**, 084102 (2019).

[264] G. Gotti, S. Iubini, and P. Politi, "Finite-size localization scenarios in condensation transitions", Phys. Rev. E **103**, 052133 (2021).

[265] B. Rumpf, "Simple statistical explanation for the localization of energy in nonlinear lattices with two conserved quantities", Phys. Rev. E **69**, 016618 (2004).

[266] B. Rumpf, "Growth and erosion of a discrete breather interacting with Rayleigh-Jeans distributed phonons", Europhys. Lett. **78**, 26001 (2007).

[267] B. Rumpf, "Transition behavior of the discrete nonlinear Schrödinger equation", Phys. Rev. E **77**, 036606 (2008).

[268] B. Rumpf, "Stable and metastable states and the formation and destruction of breathers in the discrete nonlinear Schrödinger equation", Physica D **238**, 2067–2077 (2009).

[269] S. Iubini, R. Franzosi, R. Livi, G.-L. Oppo, and A. Politi, "Discrete breathers and negative-temperature states", New J. Phys. **15**, 023032 (2013).

[270] S. Iubini, A. Politi, and P. Politi, "Coarsening Dynamics in a Simplified DNLS Model", J. Stat. Phys. **154**, 1057–1073 (2014).

[271] J.-P. Eckmann and C. E. Wayne, "Breathers as metastable states for the discrete NLS equation", Discr. & Cont. Dyn. Syst. A **38**, 6091 (2018).

[272] W. De Roeck and F. Huveneers, "Asymptotic Quantum Many-Body Localization from Thermal Disorder", Commun. Math. Phys. **332**, 1017–1082 (2014).

[273] F. Huveneers and E. Theil, "Equivalence of Ensembles, Condensation and Glassy Dynamics in the Bose–Hubbard Hamiltonian", J. Stat. Phys. **177**, 917–935 (2019).

[274] W. De Roeck and F. Huveneers, "Asymptotic Localization of Energy in Nondisordered Oscillator Chains", Commun. Pure Appl. Math. **68**, 1532–1568 (2015).

[275] B. Eiermann, T. Anker, M. Albiez, M. Taglieber, P. Treutlein, K.-P. Marzlin, and M. K. Oberthaler, "Bright Bose-Einstein Gap Solitons of Atoms with Repulsive Interaction", Phys. Rev. Lett. **92**, 230401 (2004).

[276] M. Pino, L. B. Ioffe, and B. L. Altshuler, "Nonergodic metallic and insulating phases of Josephson junction chains", Proc. Natl. Acad. Sci. USA **113**, 536–541 (2016).

[277] M. Pino, V. Kravtsov, B. Altshuler, and L. Ioffe, "Multifractal metal in a disordered Josephson junctions array", Phys. Rev. B **96**, 214205 (2017).

[278] D. Basko, "Weak chaos in the disordered nonlinear Schrödinger chain: Destruction of Anderson localization by Arnold diffusion", Ann. Phys. (Amsterdam) **326**, 1577–1655 (2011).

[279] W. De Roeck and F. Huveneers, "Glassy dynamics in strongly anharmonic chains of oscillators", Comptes Rendus Physique **20**, 419–428 (2019).

[280] Y. Kati, X. Yu, and S. Flach, "Density Resolved Wave Packet Spreading in Disordered Gross-Pitaevskii Lattices", SciPost Phys. Core **3**, 6 (2020).

[281] A. Y. Cherny, T. Engl, and S. Flach, "Non-Gibbs states on a Bose-Hubbard lattice", Phys. Rev. A **99**, 023603 (2019).

[282] G. Gradenigo, S. Iubini, R. Livi, and S. N. Majumdar, "Localization transition in the discrete nonlinear Schrödinger equation: ensembles inequivalence and negative temperatures", J. Stat. Mech. Theory Exp. **2021**, 023201 (2021).

[283] G. Gradenigo, S. Iubini, R. Livi, and S. N. Majumdar, "Condensation transition and ensemble inequivalence in the discrete nonlinear Schrödinger equation", Eur. Phys. J. E **44**, 29 (2021).

[284] M. Johansson and K. Ø. Rasmussen, "Statistical mechanics of general discrete nonlinear Schrödinger models: Localization transition and its relevance for Klein-Gordon lattices", Phys. Rev. E **70**, 066610 (2004).

[285] M. R. Samuelsen, A. Khare, A. Saxena, and K. Ø. Rasmussen, "Statistical mechanics of a discrete Schrödinger equation with saturable nonlinearity", Phys. Rev. E **87**, 044901 (2013).

[286] D. J. Thouless, P. W. Anderson, and R. G. Palmer, "Solution of 'Solvable model of a spin glass'", Philos. Mag. **35**, 593–601 (1977).

[287] Y. Kuramoto, "Self-Entrainment of a Population of Coupled Non-Linear Oscillators", in International Symposium on Mathematical Problems in Theoretical Physics (Springer, 1975), pp. 420–422.

[288] J. A. Acebrón, L. L. Bonilla, C. J. Pérez Vicente, F. Ritort, and R. Spigler, "The Kuramoto model: A simple paradigm for synchronization phenomena", Rev. Mod. Phys. **77**, 137–185 (2005).

[289] S. Chatterjee, "A note about the uniform distribution on the intersection of a simplex and a sphere", J. Topol. Anal. **09**, 717–738 (2017).

[290] A. Auffinger and G. B. Arous, "Complexity of random smooth functions on the high-dimensional sphere", Ann. Prob. **41**, 4214–4247 (2013).

[291] A. Auffinger, G. B. Arous, and J. Černý, "Random Matrices and Complexity of Spin Glasses", Commun. Pure Appl. Math. **66**, 165–201 (2013).

[292] M. Bellitti, F. Ricci-Tersenghi, and A. Scardicchio, "Entropic barriers as a reason for hardness in both classical and quantum algorithms", Phys. Rev. Research **3**, 043015 (2021).

[293] U. C. Täuber, "Critical Dynamics: A Field Theory Approach to Equilibrium and Non-Equilibrium Scaling Behavior" (Cambridge University Press, 2014).

[294] M. Bernaschi, A. Billoire, A. Maiorano, G. Parisi, and F. Ricci-Tersenghi, "Strong ergodicity breaking in aging of mean-field spin glasses", Proc. Natl. Acad. Sci. USA **117**, 17522–17527 (2020).

[295] V. Ros, G. Ben Arous, G. Biroli, and C. Cammarota, "Complex Energy Landscapes in Spiked-Tensor and Simple Glassy Models: Ruggedness, Arrangements of Local Minima, and Phase Transitions", Phys. Rev. X **9**, 011003 (2019).

[296] V. Ros, G. Biroli, and C. Cammarota, "Complexity of energy barriers in mean-field glassy systems", Europhys. Lett. **126**, 20003 (2019).

[297] V. Ros, G. Biroli, and C. Cammarota, "Dynamical Instantons and Activated Processes in Mean-Field Glass Models", SciPost Phys. **10**, 2 (2021).

[298] "Geometry and Topology in Hamiltonian Dynamics and Statistical Mechanics" (Springer, New York, 2007).

[299] M. Gori, R. Franzosi, and M. Pettini, "Topological origin of phase transitions in the absence of critical points of the energy landscape", J. Stat. Mech. Theory Exp. **2018**, 093204 (2018).

[300] O. B. Ericok and J. K. Mason, "A geometric conjecture about phase transitions", arXiv:2203.03154 (2022).

[301] A. Chandran, I. H. Kim, G. Vidal, and D. A. Abanin, "Constructing local integrals of motion in the many-body localized phase", Phys. Rev. B **91**, 085425 (2015).

[302] T. E. O'Brien, D. A. Abanin, G. Vidal, and Z. Papić, "Explicit construction of local conserved operators in disordered many-body systems", Phys. Rev. B **94**, 144208 (2016).

[303] L. Rademaker and M. Ortuño, "Explicit Local Integrals of Motion for the Many-Body Localized State", Phys. Rev. Lett. **116**, 010404 (2016).

[304] Y.-Z. You, X.-L. Qi, and C. Xu, "Entanglement holographic mapping of many-body localized system by spectrum bifurcation renormalization group", Phys. Rev. B **93**, 104205 (2016).

[305] D. Pekker, B. K. Clark, V. Oganesyan, and G. Refael, "Fixed Points of Wegner-Wilson Flows and Many-Body Localization", Phys. Rev. Lett. **119**, 075701 (2017).

[306] A. K. Kulshreshtha, A. Pal, T. B. Wahl, and S. H. Simon, "Approximating observables on eigenstates of large many-body localized systems", Phys. Rev. B **99**, 104201 (2019).

[307] P. Peng, Z. Li, H. Yan, K. X. Wei, and P. Cappellaro, "Comparing many-body localization lengths via nonperturbative construction of local integrals of motion", Phys. Rev. B **100**, 214203 (2019).

[308] A. Chandran, A. Pal, C. R. Laumann, and A. Scardicchio, "Many-body localization beyond eigenstates in all dimensions", Phys. Rev. B **94**, 144203 (2016).

[309] S. C. Glotzer, N. Jan, T. Lookman, A. B. MacIsaac, and P. H. Poole, "Dynamical heterogeneity in the Ising spin glass", Phys. Rev. E **57**, 7350 (1998).

[310] M. D. Ediger, "Spatially Heterogeneous Dynamics in Supercooled Liquids", Annu. Rev. Phys. Chem. **51**, 99–128 (2000).

[311] S. C. Glotzer, "Spatially heterogeneous dynamics in liquids: insights from simulation", J. Non-Cryst. Solids **274**, 342–355 (2000).

[312] B. Olmos, I. Lesanovsky, and J. P. Garrahan, "Facilitated Spin Models of Dissipative Quantum Glasses", Phys. Rev. Lett. **109**, 020403 (2012).

[313] S. Hill and W. K. Wootters, "Entanglement of a Pair of Quantum Bits", Phys. Rev. Lett. **78**, 5022–5025 (1997).

[314] W. K. Wootters, "Entanglement of Formation of an Arbitrary State of Two Qubits", Phys. Rev. Lett. **80**, 2245–2248 (1998).

[315] P. Facchi, G. Florio, G. Parisi, and S. Pascazio, "Maximally multipartite entangled states", Phys. Rev. A **77**, 060304 (2008).

[316] P. Facchi, G. Florio, U. Marzolino, G. Parisi, and S. Pascazio, "Multipartite entanglement and frustration", New J. Phys. **12**, 025015 (2010).

[317] L. Amico, R. Fazio, A. Osterloh, and V. Vedral, "Entanglement in many-body systems", Rev. Mod. Phys. **80**, 517–576 (2008).

[318] N. Laflorencie, "Quantum entanglement in condensed matter systems", Phys. Rep. **646**, 1–59 (2016).

[319] M. Serbyn, Z. Papić, and D. A. Abanin, "Universal Slow Growth of Entanglement in Interacting Strongly Disordered Systems", Phys. Rev. Lett. **110**, 260601 (2013).

[320] F. Pietracaprina, G. Parisi, A. Mariano, S. Pascazio, and A. Scardicchio, "Entanglement critical length at the many-body localization transition", J. Stat. Mech. Theory Exp. **2017**, 113102 (2017).

[321] J. Goold, C. Gogolin, S. R. Clark, J. Eisert, A. Scardicchio, and A. Silva, "Total correlations of the diagonal ensemble herald the many-body localization transition", Phys. Rev. B **92**, 180202 (2015).

[322] G. De Tomasi, S. Bera, J. H. Bardarson, and F. Pollmann, "Quantum Mutual Information as a Probe for Many-Body Localization", Phys. Rev. Lett. **118**, 016804 (2017).

[323] G. De Tomasi, F. Pollmann, and M. Heyl, "Efficiently solving the dynamics of many-body localized systems at strong disorder", Phys. Rev. B **99**, 241114 (2019).

[324] L. Herviou, S. Bera, and J. H. Bardarson, "Multiscale entanglement clusters at the many-body localization phase transition", Phys. Rev. B **99**, 134205 (2019).

[325] F. Iemini, A. Russomanno, D. Rossini, A. Scardicchio, and R. Fazio, "Signatures of many-body localization in the dynamics of two-site entanglement", Phys. Rev. B **94**, 214206 (2016).

[326] P. Jurcevic, B. P. Lanyon, P. Hauke, C. Hempel, P. Zoller, R. Blatt, and C. F. Roos, "Quasiparticle engineering and entanglement propagation in a quantum many-body system", Nature **511**, 202–205 (2014).

[327] T. Fukuhara, S. Hild, J. Zeiher, P. Schauß, I. Bloch, M. Endres, and C. Gross, "Spatially Resolved Detection of a Spin-Entanglement Wave in a Bose-Hubbard Chain", Phys. Rev. Lett. **115**, 035302 (2015).

[328] J. Z. Imbrie, V. Ros, and A. Scardicchio, "Local integrals of motion in many-body localized systems", Ann. Phys. (Berlin) **529**, 1600278 (2017).

[329] V. K. Varma, A. Raj, S. Gopalakrishnan, V. Oganesyan, and D. Pekker, "Length scales in the many-body localized phase and their spectral signatures", Phys. Rev. B **100**, 115136 (2019).

[330] F. Alet and N. Laflorencie, "Many-body localization: An introduction and selected topics", Comptes Rendus Physique **19**, 498–525 (2018).

[331] R. Nandkishore and D. A. Huse, "Many-Body Localization and Thermalization in Quantum Statistical Mechanics", Annu. Rev. Condens. Matt. Phys. **6**, 15–38 (2015).

[332] T. Yu and J. H. Eberly, "Evolution from Entanglement to Decoherence of Bipartite Mixed "X" States", Quantum Info. Comput. **7**, 459–468 (2007).

[333] R. B. Sidje, "Expokit: A Software Package for Computing Matrix Exponentials", ACM Trans. Math. Softw. **24**, 130–156 (1998).

[334] R. Nandkishore, S. Gopalakrishnan, and D. A. Huse, "Spectral features of a many-body-localized system weakly coupled to a bath", Phys. Rev. B **90**, 064203 (2014).

[335] E. Levi, M. Heyl, I. Lesanovsky, and J. P. Garrahan, "Robustness of Many-Body Localization in the Presence of Dissipation", Phys. Rev. Lett. **116**, 237203 (2016).

[336] M. V. Medvedyeva, T. Prosen, and M. Žnidarič, "Influence of dephasing on many-body localization", Phys. Rev. B **93**, 094205 (2016).

[337] B. Everest, I. Lesanovsky, J. P. Garrahan, and E. Levi, "Role of interactions in a dissipative many-body localized system", Phys. Rev. B **95**, 024310 (2017).

[338] R. Nandkishore and S. Gopalakrishnan, "Many body localized systems weakly coupled to baths", Ann. Phys. (Berlin) **529**, 1600181 (2017).

[339] I. Vakulchyk, I. Yusipov, M. Ivanchenko, S. Flach, and S. Denisov, "Signatures of many-body localization in steady states of open quantum systems", Phys. Rev. B **98**, 020202 (2018).

[340] E. Wybo, M. Knap, and F. Pollmann, "Entanglement dynamics of a many-body localized system coupled to a bath", Phys. Rev. B **102**, 064304 (2020).

[341] S. S. Kondov, W. R. McGehee, W. Xu, and B. DeMarco, "Disorder-Induced Localization in a Strongly Correlated Atomic Hubbard Gas", Phys. Rev. Lett. **114**, 083002 (2015).

[342] J.-y. Choi et al., "Exploring the many-body localization transition in two dimensions", Science **352**, 1547–1552 (2016).

[343] P. Bordia, H. Lüschen, S. Scherg, S. Gopalakrishnan, M. Knap, U. Schneider, and I. Bloch, "Probing Slow Relaxation and Many-Body Localization in Two-Dimensional Quasiperiodic Systems", Phys. Rev. X **7**, 041047 (2017).

[344] I.-D. Potirniche, S. Banerjee, and E. Altman, "Exploration of the stability of many-body localization in $d > 1$", Phys. Rev. B **99**, 205149 (2019).

[345] T. B. Wahl, A. Pal, and S. H. Simon, "Signatures of the many-body localized regime in two dimensions", Nat. Phys. **15**, 164–169 (2019).

[346] H. Théveniaut, Z. Lan, G. Meyer, and F. Alet, "Transition to a many-body localized regime in a two-dimensional disordered quantum dimer model", Phys. Rev. Research **2**, 033154 (2020).

[347] M. A. Ramos, "Are universal "anomalous" properties of glasses at low temperatures truly universal?", Low Temp. Phys. **46**, 104–110 (2020).

[348] A. J. Leggett and C. C. Yu, "Low temperature properties of amorphous materials: Through a glass darkly", Comments Condens. Matter Phys. **14**, 231 (1988).

[349] A. J. Leggett, "Amorphous materials at low temperatures: why are they so similar?", Physica B **169**, 322–327 (1991).

[350] A. J. Leggett and D. C. Vural, ""Tunneling Two-Level Systems" Model of the Low-Temperature Properties of Glasses: Are "Smoking-Gun" Tests Possible?", J. Phys. Chem. B **117**, 12966–12971 (2013).

[351] C. Enss and S. Hunklinger, "Low-Temperature Physics" (Springer, Berlin, Heidelberg, 2005).

[352] W. Arnold and S. Hunklinger, "Experimental evidence for the direct interaction between two-level systems in glasses at very low temperatures", Solid State Commun. **17**, 883–886 (1975).

[353] J. Joffrin and A. Levelut, "Virtual phonon exchange in glasses", J. Physique **36**, 811–822 (1975).

[354] J. L. Black and B. I. Halperin, "Spectral diffusion, phonon echoes, and saturation recovery in glasses at low temperatures", Phys. Rev. B **16**, 2879–2895 (1977).

[355] A.-M. Boiron, P. Tamarat, B. Lounis, R. Brown, and M. Orrit, "Are the spectral trails of single molecules consistent with the standard two-level system model of glasses at low temperatures?", Chem. Phys. **247**, 119–132 (1999).

[356] J. Lisenfeld, G. J. Grabovskij, C. Müller, J. H. Cole, G. Weiss, and A. V. Ustinov, "Observation of directly interacting coherent two-level systems in an amorphous material", Nat. Commun. **6**, 6182 (2015).

[357] K. Kassner and R. Silbey, "Interactions of two-level systems in glasses", J. Phys. Condens. Matter **1**, 4599–4610 (1989).

[358] A. L. Burin, "Dipole gap effects in low energy excitation spectrum of amorphous solids. Theory for dielectric relaxation", J. Low Temp. Phys. **100**, 309–337 (1995).

[359] A. Burin and Y. Kagan, "On the nature of the universal properties of amorphous solids", Phys. Lett. A **215**, 191–196 (1996).

[360] S. Rogge, D. Natelson, and D. D. Osheroff, "Evidence for the Importance of Interactions between Active Defects in Glasses", Phys. Rev. Lett. **76**, 3136–3139 (1996).

[361] C. Enss and S. Hunklinger, "Incoherent Tunneling in Glasses at Very Low Temperatures", Phys. Rev. Lett. **79**, 2831–2834 (1997).

[362] D. Natelson, D. Rosenberg, and D. D. Osheroff, "Evidence for Growth of Collective Excitations in Glasses at Low Temperatures", Phys. Rev. Lett. **80**, 4689–4692 (1998).

[363] D. C. Vural and A. J. Leggett, "Universal sound absorption in amorphous solids: A theory of elastically coupled generic blocks", J. Non-Crystalline Solids **357**, 3528–3537 (2011).

[364] O. Asban, A. Amir, Y. Imry, and M. Schechter, "Effect of interactions and disorder on the relaxation of two-level systems in amorphous solids", Phys. Rev. B **95**, 144207 (2017).

[365] H. M. Carruzzo and C. C. Yu, "Why Phonon Scattering in Glasses is Universally Small at Low Temperatures", Phys. Rev. Lett. **124**, 075902 (2020).

[366] M. H. Fischer, M. Maksymenko, and E. Altman, "Dynamics of a Many-Body-Localized System Coupled to a Bath", Phys. Rev. Lett. **116**, 160401 (2016).

[367] H. P. Lüschen et al., "Signatures of Many-Body Localization in a Controlled Open Quantum System", Phys. Rev. X **7**, 011034 (2017).

[368] J. F. Berret and M. Meißner, "How Universal are the Low Temperature Acoustic Properties of Glasses?", Z. Phys. B **70**, 65–72 (1988).

[369] P. Strehlow, C. Enss, and S. Hunklinger, "Evidence for a Phase Transition in Glasses at Very Low Temperature: A Macroscopic Quantum State of Tunneling Systems?", Phys. Rev. Lett. **80**, 5361–5364 (1998).

[370] H.-P. Breuer and F. Petruccione, "The Theory of Open Quantum Systems" (Oxford University Press, Oxford, 2007), p. 656.

[371] D. Manzano, "A short introduction to the Lindblad master equation", AIP Adv. **10**, 025106 (2020).

[372] N. Y. Yao, C. R. Laumann, S. Gopalakrishnan, M. Knap, M. Müller, E. A. Demler, and M. D. Lukin, "Many-Body Localization in Dipolar Systems", Phys. Rev. Lett. **113**, 243002 (2014).

[373] A. L. Burin, "Many-body delocalization in a strongly disordered system with long-range interactions: Finite-size scaling", Phys. Rev. B **91**, 094202 (2015).

[374] X. Deng, A. L. Burin, and I. M. Khaymovich, "Anisotropy-mediated reentrant localization", arXiv:2002.00013 (2020).

[375] M. Pino, "Entanglement growth in many-body localized systems with long-range interactions", Phys. Rev. B **90**, 174204 (2014).

[376] M. Rigol, V. Dunjko, and M. Olshanii, "Thermalization and its mechanism for generic isolated quantum systems", Nature **452**, 854–858 (2008).

[377] A. Polkovnikov, K. Sengupta, A. Silva, and M. Vengalattore, "*Colloquium*: nonequilibrium dynamics of closed interacting quantum systems", Rev. Mod. Phys. **83**, 863–883 (2011).

[378] M. Schulz, C. A. Hooley, R. Moessner, and F. Pollmann, "Stark Many-Body Localization", Phys. Rev. Lett. **122**, 040606 (2019).

[379] E. van Nieuwenburg, Y. Baum, and G. Refael, "From Bloch oscillations to many-body localization in clean interacting systems", Proc. Natl. Acad. Sci. USA **116**, 9269–9274 (2019).

[380] A. Bray, "Theory of phase-ordering kinetics", Adv. Phys. **43**, 357–459 (1994).

[381] A. Onuki, "Phase Transition Dynamics" (Cambridge University Press, 2002).

[382] S. Karthika, T. K. Radhakrishnan, and P. Kalaichelvi, "A Review of Classical and Nonclassical Nucleation Theories", Crystal Growth & Design **16**, 6663–6681 (2016).

[383] I. Y. Kobzarev, L. B. Okun, and M. B. Voloshin, "Bubbles in Metastable Vacuum", Yad. Fiz. **20**, 1229–1234 (1974).

[384] S. Coleman, "Fate of the false vacuum: Semiclassical theory", Phys. Rev. D **15**, 2929–2936 (1977).

[385] C. G. Callan and S. Coleman, "Fate of the false vacuum. II. First quantum corrections", Phys. Rev. D **16**, 1762–1768 (1977).

[386] S. Coleman, "Aspects of Symmetry: Selected Erice Lectures" (Cambridge University Press, 1985).

[387] A. H. Guth, "Inflation and eternal inflation", Phys. Rep. **333**, 555–574 (2000).

[388] B. Song, S. Dutta, S. Bhave, J.-C. Yu, E. Carter, N. Cooper, and U. Schneider, "Realizing discontinuous quantum phase transitions in a strongly correlated driven optical lattice", Nat. Phys. **18**, 259–264 (2022).

[389] E. Farhi, J. Goldstone, S. Gutmann, J. Lapan, A. Lundgren, and D. Preda, "A quantum adiabatic evolution algorithm applied to random instances of an NP-complete problem", Science **292**, 472–475 (2001).

[390] E. Crosson, E. Farhi, C. Y.-Y. Lin, H.-H. Lin, and P. Shor, "Different strategies for optimization using the quantum adiabatic algorithm", arXiv:1401.7320 (2014).

[391] V. Bapst, L. Foini, F. Krzakala, G. Semerjian, and F. Zamponi, "The quantum adiabatic algorithm applied to random optimization problems: The quantum spin glass perspective", Phys. Rep. **523**, 127–205 (2013).

[392] A. Yoshinaga, H. Hakoshima, T. Imoto, Y. Matsuzaki, and R. Hamazaki, "Emergence of Hilbert Space Fragmentation in Ising Models with a Weak Transverse Field", arXiv:2111.05586 (2021).

[393] O. Hart and R. Nandkishore, "Hilbert space shattering and dynamical freezing in the quantum Ising model", arXiv:2203.06188 (2022).

[394] J. Maldacena, "The Large-N Limit of Superconformal Field Theories and Supergravity", Intl. J. Theor. Phys. **38**, 1113–1133 (1999).

[395] S. Gubser, I. Klebanov, and A. Polyakov, "Gauge theory correlators from noncritical string theory", Phys. Lett. B **428**, 105–114 (1998).

[396] E. Witten, "Anti De Sitter Space And Holography", Adv. Theor. Math. Phys. **2**, 253 (1998).

[397] B. F. Logan and L. A. Shepp, "A variational problem for random Young tableaux", Adv. Math. **26**, 206–222 (1977).

[398] A. Vershik and S. Kerov, "Asymptotics of the Plancherel measure of the symmetric group and the limit form of Young tableaux", Sov. Math. Dokl. **18**, 527–531 (1977).

[399] A. Vershik and S. Kerov, "Asymptotics of the maximal and typical dimension of irreducible representations of symmetric group", Funct. Anal. Appl. **19** (1985).

[400] A. Okounkov, "Random matrices and random permutations", Intl. Math. Res. Not. **2000**, 1043–1095 (2000).

[401] A. Okounkov, "Infinite wedge and random partitions", Sel. Math. **7**, 57 (2001).

[402] A. Okounkov, "The uses of random partitions", arXiv:math-ph/0309015 (2003).

[403] A. Okounkov and N. Reshetikhin, "Correlation function of Schur process with application to local geometry of a random 3-dimensional Young diagram", J. Amer. Math. Soc. **16**, 581–603 (2003).

[404] P. L. Ferrari and H. Spohn, "Step Fluctuations for a Faceted Crystal", J. Stat. Phys. **113**, 1–46 (2003).

[405] H. Spohn, "Exact solutions for KPZ-type growth processes, random matrices, and equilibrium shapes of crystals", Physica A **369**, 71–99 (2006).

[406] A. Okounkov, N. Reshetikhin, and C. Vafa, "Quantum Calabi-Yau and classical crystals", in *The unity of mathematics* (Springer, 2006), pp. 597–618.

[407] H. Ooguri and M. Yamazaki, "Crystal Melting and Toric Calabi-Yau Manifolds", Commun. Math. Phys. **292**, 179–199 (2009).

[408] K. Agarwal, S. Gopalakrishnan, M. Knap, M. Müller, and E. Demler, "Anomalous Diffusion and Griffiths Effects Near the Many-Body Localization Transition", Phys. Rev. Lett. **114**, 160401 (2015).

[409] M. Žnidarič, A. Scardicchio, and V. K. Varma, "Diffusive and Subdiffusive Spin Transport in the Ergodic Phase of a Many-Body Localizable System", Phys. Rev. Lett. **117**, 040601 (2016).

[410] D. J. Luitz and Y. B. Lev, "The ergodic side of the many-body localization transition", Ann. Phys. (Berlin) **529**, 1600350 (2017).

[411] S. R. Taylor and A. Scardicchio, "Subdiffusion in a one-dimensional Anderson insulator with random dephasing: Finite-size scaling, Griffiths effects, and possible implications for many-body localization", Phys. Rev. B **103**, 184202 (2021).

[412] S. Gopalakrishnan and D. A. Huse, "Instability of many-body localized systems as a phase transition in a nonstandard thermodynamic limit", Phys. Rev. B **99**, 134305 (2019).

[413] F. Pietracaprina and F. Alet, "Probing many-body localization in a disordered quantum dimer model on the honeycomb lattice", SciPost Phys. **10**, 44 (2021).

[414] H. Aoki, N. Tsuji, M. Eckstein, M. Kollar, T. Oka, and P. Werner, "Nonequilibrium dynamical mean-field theory and its applications", Rev. Mod. Phys. **86**, 779–837 (2014).

[415] H. Spohn, "Kinetic Equations for Quantum Many-Particle Systems", arXiv: 0706.0807 (2007).

[416] C. J. Turner, A. A. Michailidis, D. A. Abanin, M. Serbyn, and Z. Papić, "Quantum scarred eigenstates in a Rydberg atom chain: Entanglement, breakdown of thermalization, and stability to perturbations", Phys. Rev. B **98**, 155134 (2018).

[417] J. R. Schrieffer and P. A. Wolff, "Relation between the Anderson and Kondo Hamiltonians", Phys. Rev. **149**, 491–492 (1966).

[418] P. Schauß et al., "Observation of spatially ordered structures in a two-dimensional Rydberg gas", Nature **491**, 87–91 (2012).

[419] S. Ebadi et al., "Quantum phases of matter on a 256-atom programmable quantum simulator", Nature **595**, 227–232 (2021).

[420] N. Chepiga and F. Mila, "Kibble-Zurek exponent and chiral transition of the period-4 phase of Rydberg chains", Nat. Commun. **12**, 414 (2021).

[421] M. Schecter and T. Iadecola, "Many-body spectral reflection symmetry and protected infinite-temperature degeneracy", Phys. Rev. B **98**, 035139 (2018).

[422] H. Rost, "Non-equilibrium behaviour of a many particle process: Density profile and local equilibria", Zeit. Wahrscheinlichkeitstheorie und Verwandte Gebiete **58**, 41–53 (1981).

[423] T. M. Liggett, "Stochastic Interacting Systems: Contact, Voter and Exclusion Processes" (Springer, Berlin, Heidelberg, 1999), pp. 209–316.

[424] G. Schütz, "Exactly Solvable Models for Many-Body Systems Far from Equilibrium", in *Phase Transitions and Critical Phenomena*, Vol. 19, edited by C. Domb and J. Lebowitz (Academic Press, 2001), pp. 1–251.

[425] G. Grosso and G. Pastori Parravicini, "Solid State Physics", Second Edition (Academic Press, Amsterdam, 2014).

[426] D. Richardson, "Random growth in a tessellation", Math. Proc. Cambridge Phil. Soc. **74**, 515–528 (1973).

[427] J. Krug and H. Spohn, "Kinetic Roughening of Growing Interfaces", in *Solids Far from Equilibrium*, edited by C. Godrèche (Cambridge University Press, 1991), pp. 479–572.

[428] R. Dijkgraaf, D. Orlando, and S. Reffert, "Quantum crystals and spin chains", Nucl. Phys. **B811**, 463–490 (2009).

[429] T. Araujo, D. Orlando, and S. Reffert, "Quantum crystals, Kagome lattice, and plane partitions fermion-boson duality", Phys. Rev. D **103**, 026020 (2021).

[430] A. Borodin, A. Okounkov, and G. Olshanski, "Asymptotics of Plancherel measures for symmetric groups", J. Amer. Math. Soc. **13**, 481–515 (2000).

[431] E. Fradkin, M. Srednicki, and L. Susskind, "Fermion representation for the Z_2 lattice gauge theory in 2+1 dimensions", Phys. Rev. D **21**, 2885–2891 (1980).

[432] A. Polyakov, "Quantum geometry of fermionic strings", Phys. Lett. B **103**, 211–213 (1981).

[433] N. Iqbal and J. McGreevy, "Toward a 3d Ising model with a weakly-coupled string theory dual", SciPost Phys. **9**, 19 (2020).

[434] T. Antal, Z. Rácz, A. Rákos, and G. M. Schütz, "Transport in the XX chain at zero temperature: Emergence of flat magnetization profiles", Phys. Rev. E **59**, 4912–4918 (1999).

[435] B. Derrida, M. R. Evans, V. Hakim, and V. Pasquier, "Exact solution of a 1D asymmetric exclusion model using a matrix formulation", J. Phys. A **26**, 1493–1517 (1993).

[436] B. Derrida, "An exactly soluble non-equilibrium system: The asymmetric simple exclusion process", Phys. Rep. **301**, 65–83 (1998).

[437] O. Golinelli and K. Mallick, "The asymmetric simple exclusion process: an integrable model for non-equilibrium statistical mechanics", J. Phys. A **39**, 12679–12705 (2006).

[438] C. A. Tracy and H. Widom, "Level spacing distributions and the Bessel kernel", Commun. Math. Phys. **161**, 289–309 (1994).

[439] M. L. Mehta, "Random Matrices" (Elsevier, 2004).

[440] I. Peschel and V. Eisler, "Reduced density matrices and entanglement entropy in free lattice models", J. Phys. A **42**, 504003 (2009).

[441] C. A. Tracy and H. Widom, "Level-spacing distributions and the Airy kernel", Phys. Lett. B **305**, 115–118 (1993).

[442] C. A. Tracy and H. Widom, "Level-spacing distributions and the Airy kernel", Commun. Math. Phys. **159**, 151–174 (1994).

[443] B. Doyon, "Lecture Notes On Generalised Hydrodynamics", SciPost Phys. Lect. Notes, 18 (2020).

[444] V. Eisler, G. D. Giulio, E. Tonni, and I. Peschel, "Entanglement Hamiltonians for non-critical quantum chains", J. Stat. Mech. Theory Exp. **2020**, 103102 (2020).

[445] V. Eisler and Z. Rácz, "Full Counting Statistics in a Propagating Quantum Front and Random Matrix Spectra", Phys. Rev. Lett. **110**, 060602 (2013).

[446] V. Eisler, F. Iglói, and I. Peschel, "Entanglement in spin chains with gradients", J. Stat. Mech. **2009**, P02011 (2009).

[447] I. Peschel, "On the reduced density matrix for a chain of free electrons", J. Stat. Mech. Theory Exp. **2004**, P06004 (2004).

[448] I. Peschel, "Calculation of reduced density matrices from correlation functions", J. Phys. A **36**, L205–L208 (2003).

[449] S.-A. Cheong and C. L. Henley, "Many-body density matrices for free fermions", Phys. Rev. B **69**, 075111 (2004).

[450] J. Dubail, J.-M. Stéphan, J. Viti, and P. Calabrese, "Conformal Field Theory for Inhomogeneous One-dimensional Quantum Systems: the Example of Non-Interacting Fermi Gases", SciPost Phys. **2**, 002 (2017).

[451] S. Scopa, P. Calabrese, and J. Dubail, "Exact hydrodynamic solution of a double domain wall melting in the spin-1/2 XXZ model", SciPost Phys. **12**, 207 (2022).

[452] W. Fulton, "Young Tableaux" (Cambridge University Press, 1996).

[453] F. Pietracaprina, V. Ros, and A. Scardicchio, "Forward approximation as a mean-field approximation for the Anderson and many-body localization transitions", Phys. Rev. B **93**, 054201 (2016).

[454] A. Scardicchio and T. Thiery, "Perturbation theory approaches to Anderson and Many-Body Localization: some lecture notes", arXiv:1710.01234 (2017).

[455] D. Abanin, W. De Roeck, W. W. Ho, and F. Huveneers, "A Rigorous Theory of Many-Body Prethermalization for Periodically Driven and Closed Quantum Systems", Commun. Math. Phys. **354**, 809–827 (2017).

[456] W. Morong et al., "Observation of Stark many-body localization without disorder", Nature **599**, 393–398 (2021).

[457] F. W. J. Olver et al., eds., "NIST Digital Library of Mathematical Functions", Release 1.1.6 (2022).

[458] S. Sachdev and J. Ye, "Gapless spin-fluid ground state in a random quantum Heisenberg magnet", Phys. Rev. Lett. **70**, 3339–3342 (1993).

[459] A. Kitaev, *A simple model of quantum holography*, `http://online.kitp.ucsb.edu/online/entangled15/kitaev/`, `http://online.kitp.ucsb.edu/online/entangled15/kitaev2/`, 2015.

[460] GitHub repository at `https://github.com/fbaldux/Ising-Melting-dis`.

[461] P. Sierant, M. Lewenstein, and A. Scardicchio, "Universality in Anderson localization on random graphs with varying connectivity", arXiv:2205.14614 (2022).

[462] B. Li and J. Wang, "Anomalous Heat Conduction and Anomalous Diffusion in One-Dimensional Systems", Phys. Rev. Lett. **91**, 044301 (2003).

[463] J. J. Mendoza-Arenas, M. Žnidarič, V. K. Varma, J. Goold, S. R. Clark, and A. Scardicchio, "Asymmetry in energy versus spin transport in certain interacting disordered systems", Phys. Rev. B **99**, 094435 (2019).

[464] A. Nahum, J. Ruhman, S. Vijay, and J. Haah, "Quantum Entanglement Growth under Random Unitary Dynamics", Phys. Rev. X **7**, 031016 (2017).

[465] A. Nahum, S. Vijay, and J. Haah, "Operator Spreading in Random Unitary Circuits", Phys. Rev. X **8**, 021014 (2018).

[466] A. Chan, A. De Luca, and J. T. Chalker, "Solution of a Minimal Model for Many-Body Quantum Chaos", Phys. Rev. X **8**, 041019 (2018).

[467] R. Jose, C. Arita, and L. Santen, "Bidirectional non-Markovian exclusion processes", J. Stat. Mech. Theory Exp. **2020**, 033207 (2020).

[468] D. D'Alessandro, "Introduction to Quantum Control and Dynamics" (Chapman and Hall, 2007).

[469] S. J. Glaser et al., "Training Schrödinger's cat: quantum optimal control", The European Physical Journal D **69**, 279 (2015).

[470] U. Boscain, M. Sigalotti, and D. Sugny, "Introduction to the Pontryagin Maximum Principle for Quantum Optimal Control", PRX Quantum **2**, 030203 (2021).

[471] C. P. Koch et al., "Quantum optimal control in quantum technologies. Strategic report on current status, visions and goals for research in Europe", arXiv: 2205.12110 (2022).

[472] N. Khaneja, S. J. Glaser, and R. Brockett, "Sub-Riemannian geometry and time optimal control of three spin systems: Quantum gates and coherence transfer", Phys. Rev. A **65**, 032301 (2002).

[473] P. Treutlein, T. W. Hänsch, J. Reichel, A. Negretti, M. A. Cirone, and T. Calarco, "Microwave potentials and optimal control for robust quantum gates on an atom chip", Phys. Rev. A **74**, 022312 (2006).

[474] M. Grace, C. Brif, H. Rabitz, I. A. Walmsley, R. L. Kosut, and D. A. Lidar, "Optimal control of quantum gates and suppression of decoherence in a system of interacting two-level particles", J. Phys. B **40**, S103–S125 (2007).

[475] T. Schulte-Herbrüggen, A. Spörl, N. Khaneja, and S. J. Glaser, "Optimal control for generating quantum gates in open dissipative systems", J. Phys. B **44**, 154013 (2011).

[476] A. Choquette, A. Di Paolo, P. K. Barkoutsos, D. Sénéchal, I. Tavernelli, and A. Blais, "Quantum-optimal-control-inspired ansatz for variational quantum algorithms", Phys. Rev. Research **3**, 023092 (2021).

[477] A. B. Magann, C. Arenz, M. D. Grace, T.-S. Ho, R. L. Kosut, J. R. McClean, H. A. Rabitz, and M. Sarovar, "From Pulses to Circuits and Back Again: A Quantum Optimal Control Perspective on Variational Quantum Algorithms", PRX Quantum **2**, 010101 (2021).

[478] V. Giovannetti, S. Lloyd, and L. Maccone, "Quantum-Enhanced Measurements: Beating the Standard Quantum Limit", Science **306**, 1330–1336 (2004).

[479] L. Viola and S. Lloyd, "Dynamical suppression of decoherence in two-state quantum systems", Phys. Rev. A **58**, 2733–2744 (1998).

[480] L. Viola, E. Knill, and S. Lloyd, "Dynamical Decoupling of Open Quantum Systems", Phys. Rev. Lett. **82**, 2417–2421 (1999).

[481] P. Facchi, S. Tasaki, S. Pascazio, H. Nakazato, A. Tokuse, and D. A. Lidar, "Control of decoherence: Analysis and comparison of three different strategies", Phys. Rev. A **71**, 022302 (2005).

[482] G. S. Uhrig, "Keeping a Quantum Bit Alive by Optimized π-Pulse Sequences", Phys. Rev. Lett. **98**, 100504 (2007).

[483] G. de Lange, Z. H. Wang, D. Ristè, V. V. Dobrovitski, and R. Hanson, "Universal Dynamical Decoupling of a Single Solid-State Spin from a Spin Bath", Science **330**, 60–63 (2010).

[484] J. M. Taylor et al., "High-sensitivity diamond magnetometer with nanoscale resolution", Nat. Phys. **4**, 810–816 (2008).

[485] L. M. Pham et al., "Magnetic field imaging with nitrogen-vacancy ensembles", New J. Phys. **13**, 045021 (2011).

[486] F. Dolde et al., "Electric-field sensing using single diamond spins", Nat. Phys. **7**, 459–463 (2011).

[487] N. Bar-Gill, L. M. Pham, A. Jarmola, D. Budker, and R. L. Walsworth, "Solid-state electronic spin coherence time approaching one second", Nat. Commun. **4**, 1743 (2013).

[488] G. Thiering and A. Gali, "Color centers in diamond for quantum applications", in *Diamond for Quantum Applications (Part 1)*, Vol. 103, edited by C. E. Nebel, I. Aharonovich, N. Mizuochi, and M. Hatano, Semiconductors and Semimetals (Elsevier, 2020), pp. 1–36.

[489] C. R. Laumann, A. M. Läuchli, R. Moessner, A. Scardicchio, and S. L. Sondhi, "Product, generic, and random generic quantum satisfiability", Phys. Rev. A **81**, 062345 (2010).

[490] M. P. Harrigan et al., "Quantum approximate optimization of non-planar graph problems on a planar superconducting processor", Nat. Phys. **17**, 332–336 (2021).

[491] A. G. R. Day, M. Bukov, P. Weinberg, P. Mehta, and D. Sels, "Glassy Phase of Optimal Quantum Control", Phys. Rev. Lett. **122**, 020601 (2019).

[492] P. J. Van Laarhoven and E. H. Aarts, "Simulated annealing", in *Simulated annealing: Theory and applications* (Springer, 1987), pp. 7–15.

[493] D. Bertsimas and J. Tsitsiklis, "Simulated annealing", Statistical Science **8**, 10–15 (1993).

[494] E. L. Hahn, "Spin Echoes", Phys. Rev. **80**, 580–594 (1950).

[495] H. Y. Carr and E. M. Purcell, "Effects of Diffusion on Free Precession in Nuclear Magnetic Resonance Experiments", Phys. Rev. **94**, 630–638 (1954).

[496] S. Meiboom and D. Gill, "Modified Spin-Echo Method for Measuring Nuclear Relaxation Times", Rev. Sci. Instrum. **29**, 688–691 (1958).

[497] S. Hernández-Gómez and N. Fabbri, "Quantum control for nanoscale spectroscopy with diamond NV centers: A short review", Frontiers in Physics **8**, 610868 (2021).

[498] N. Zhao, J.-L. Hu, S.-W. Ho, J. T. K. Wan, and R. B. Liu, "Atomic-scale magnetometry of distant nuclear spin clusters via nitrogen-vacancy spin in diamond", Nat. Nanotech. **6**, 242–246 (2011).

[499] J. Casanova, Z.-Y. Wang, J. F. Haase, and M. B. Plenio, "Robust dynamical decoupling sequences for individual-nuclear-spin addressing", Phys. Rev. A **92**, 042304 (2015).

[500] F. Poggiali, P. Cappellaro, and N. Fabbri, "Optimal Control for One-Qubit Quantum Sensing", Phys. Rev. X **8**, 021059 (2018).

[501] L. F. Cugliandolo and D. S. Dean, "Full dynamical solution for a spherical spin-glass model", J. Phys. A **28**, 4213–4234 (1995).

[502] F. Reinhard et al., "Tuning a Spin Bath through the Quantum-Classical Transition", Phys. Rev. Lett. **108**, 200402 (2012).

[503] S. Hernández-Gómez, F. Poggiali, P. Cappellaro, and N. Fabbri, "Noise spectroscopy of a quantum-classical environment with a diamond qubit", Phys. Rev. B **98**, 214307 (2018).

[504] J. Pokorný, J. Pokorný, and J. Vrba, "Generation of Electromagnetic Field by Microtubules", Intl. J. Molecular Sciences **22** (2021).

[505] S. Sahu, S. Ghosh, B. Ghosh, K. Aswani, K. Hirata, D. Fujita, and A. Bandyopadhyay, "Atomic water channel controlling remarkable properties of a single brain microtubule: Correlating single protein to its supramolecular assembly", Biosensors and Bioelectronics **47**, 141–148 (2013).

[506] P. Szendro, G. Vincze, and A. Szasz, "Pink-noise behaviour of biosystems", Eur. Biophys. J. **30**, 227–231 (2001).

[507] O. Szasz, G. P. Szigeti, and A. Szasz, "Intrinsic Noise Monitoring of Complex Systems", Open J. Biophys. **7**, 197 (2017).

[508] B. Derrida, "Random-energy model: An exactly solvable model of disordered systems", Phys. Rev. B **24**, 2613–2626 (1981).

[509] S. Lloyd and H. Pagels, "Complexity as thermodynamic depth", Ann. Phys. (Amsterdam) **188**, 186–213 (1988).

[510] D. N. Page, "Average entropy of a subsystem", Phys. Rev. Lett. **71**, 1291–1294 (1993).

[511] T. Antal, P. L. Krapivsky, and A. Rákos, "Logarithmic current fluctuations in nonequilibrium quantum spin chains", Phys. Rev. E **78**, 061115 (2008).

[512] M. Abramowitz and I. A. Stegun, "Handbook of Mathematical Functions", 9th (Dover, New York, 1964).

[513] S. L. Braunstein and C. M. Caves, "Statistical distance and the geometry of quantum states", Phys. Rev. Lett. **72**, 3439 (1994).